



IntechOpen

Tribology of Machine Elements

Fundamentals and Applications

*Edited by Giuseppe Pintaude,
Tiago Cousseau and Anna Rudawska*



Tribology of Machine Elements - Fundamentals and Applications

*Edited by Giuseppe Pintaude,
Tiago Cousseau and Anna Rudawska*

Published in London, United Kingdom



IntechOpen





Supporting open minds since 2005



Tribology of Machine Elements - Fundamentals and Applications
<http://dx.doi.org/10.5772/intechopen.95156>
Edited by Giuseppe Pintaude, Tiago Cousseau and Anna Rudawska

Contributors

Farouk Maaboudallah, Mohammed Najah, Nouredine Atalla, Mahesh M. Manohar Sonekar, Walmik S. Rathod, Sung-Ho Hong, Naofumi Hiraoka, Guido Boidi, Markus Varga, Francisco J. Profito, Izabel F. Machado, Márcio Rodrigues Da Silva, Philipp G. Grützmacher, Carsten Gachot, Daniele Dini, Christian Ortiz, Erick Hernández, Julio Caicedo, Rodrigo Santiago Coelho, Luis Fernando Folle, Bruno Caetano Dos Santos Silva, Gilmar Ferreira Batalha, Masayuki Ochiai, Yuki Sato, Giuseppe Pintaude, Tiago Cousseau, Anna Stoynova, Irina Aleksandrova, Anatoly Aleksandrov, Takenori Ono, Dagmar Draganovská, Anna Guzanová, Janette Brezinová

© The Editor(s) and the Author(s) 2022

The rights of the editor(s) and the author(s) have been asserted in accordance with the Copyright, Designs and Patents Act 1988. All rights to the book as a whole are reserved by INTECHOPEN LIMITED. The book as a whole (compilation) cannot be reproduced, distributed or used for commercial or non-commercial purposes without INTECHOPEN LIMITED's written permission. Enquiries concerning the use of the book should be directed to INTECHOPEN LIMITED rights and permissions department (permissions@intechopen.com).

Violations are liable to prosecution under the governing Copyright Law.



Individual chapters of this publication are distributed under the terms of the Creative Commons Attribution 3.0 Unported License which permits commercial use, distribution and reproduction of the individual chapters, provided the original author(s) and source publication are appropriately acknowledged. If so indicated, certain images may not be included under the Creative Commons license. In such cases users will need to obtain permission from the license holder to reproduce the material. More details and guidelines concerning content reuse and adaptation can be found at <http://www.intechopen.com/copyright-policy.html>.

Notice

Statements and opinions expressed in the chapters are these of the individual contributors and not necessarily those of the editors or publisher. No responsibility is accepted for the accuracy of information contained in the published chapters. The publisher assumes no responsibility for any damage or injury to persons or property arising out of the use of any materials, instructions, methods or ideas contained in the book.

First published in London, United Kingdom, 2022 by IntechOpen
IntechOpen is the global imprint of INTECHOPEN LIMITED, registered in England and Wales, registration number: 11086078, 5 Princes Gate Court, London, SW7 2QJ, United Kingdom
Printed in Croatia

British Library Cataloguing-in-Publication Data

A catalogue record for this book is available from the British Library

Additional hard and PDF copies can be obtained from orders@intechopen.com

Tribology of Machine Elements - Fundamentals and Applications
Edited by Giuseppe Pintaude, Tiago Cousseau and Anna Rudawska
p. cm.
Print ISBN 978-1-83969-893-4
Online ISBN 978-1-83969-894-1
eBook (PDF) ISBN 978-1-83969-895-8

We are IntechOpen, the world's leading publisher of Open Access books Built by scientists, for scientists

5,800+

Open access books available

144,000+

International authors and editors

180M+

Downloads

156

Countries delivered to

Our authors are among the
Top 1%

most cited scientists

12.2%

Contributors from top 500 universities



WEB OF SCIENCE™

Selection of our books indexed in the Book Citation Index (BKCI)
in Web of Science Core Collection™

Interested in publishing with us?
Contact book.department@intechopen.com

Numbers displayed above are based on latest data collected.
For more information visit www.intechopen.com



Meet the editors



Giuseppe Pintaude, Ph.D., is a Professor of Tribology and Mechanical Behavior of Materials at the Universidade Tecnológica Federal do Paraná, Curitiba/PR, Brazil. He was one of the primary organizers of TriboBR conferences, the International Brazilian Conference on Tribology. His research activities are well correlated to industry demands, especially in line with the automotive sector. He belongs to an Excellence Research Nucleus of plasma-assisted processes to reduce wear and corrosion, bringing his experience as a visiting researcher at the University of Birmingham, England. He is a recognized researcher by CNPq - The Brazilian National Council for Scientific and Technological Development. He is a subeditor of *Matéria* and served as a guest editor for *SN Applied Sciences* and *Industrial Lubrication Tribology*.



Tiago Cousseau, Ph.D., is a Professor of Contact Mechanics and Lubrication at the Universidade Tecnológica Federal do Paraná, Curitiba/PR, Brazil. He obtained a Ph.D. in Mechanical Engineering from the University of Porto, Portugal, in 2013 in grease-lubricated ball bearings. Part of his research was conducted at the Luleå University of Technology, Sweden, and the SKF Engineering and Research Center. Since then, his research has focused on the efficiency and reliability of lubricated components. The main outcome of his research work is the development of bench tests and test methods for proper lubricant selection and formulation.



Prof. Anna Rudawska, Ph.D., DSc, Eng, works in the Faculty of Mechanical Engineering, Lublin University of Technology, Poland. She is an author or co-author of 300 scientific publications in Polish, English, Ukrainian, and Slovak, several monographs and book chapters, and patents and patent applications. Her research focuses on the influence of technological and structural factors on the strength of polymer and metal adhesive joints, design of bonding technology, surface treatment of adherents, properties of adhesives for increasing the strength of adhesive joints, and the modification of epoxy adhesive compounds.

Contents

Preface	XIII
Section 1 Fundamentals	1
Chapter 1 Remarks on Wear Transitions Related to Hardness and Size of Abrasive Particles <i>by Giuseppe Pintaude</i>	3
Chapter 2 Grease Lubrication: Formulation Effects on Tribological Performance <i>by Tiago Cousseau</i>	17
Chapter 3 A Review on the Contact Mechanics Modeling of Rough Surfaces in the Elastic Regime: Fundamentals, Theories, and Numerical Implementations <i>by Farouk Maaboudallah, Mohamed Najah and Noureddine Atalla</i>	41
Chapter 4 Remote Nondestructive Thermal Control of Elastic Abrasive Cutting <i>by Anna Stoyanova, Irina Aleksandrova and Anatoliy Aleksandrov</i>	71
Chapter 5 Analysis of the Tribological Evolution of Nitride-Based Coatings <i>by Christian Ortiz Ortiz, Erick Hernandez-Rengifo and Julio Cesar Caicedo</i>	95
Chapter 6 Wear Life of Bonded MoS ₂ Film Lubricant <i>by Naofumi Hiraoka</i>	115
Section 2 Applications	131
Chapter 7 Tribology in Marine Diesel Engines <i>by Sung-Ho Hong</i>	133

Chapter 8	159
The Role of Friction on Metal Forming Processes <i>by Luis Fernando Folle, Bruno Caetano dos Santos Silva, Gilmar Ferreira Batalha and Rodrigo Santiago Coelho</i>	
Chapter 9	179
Groove Shape Optimization on Dry Gas Seals <i>by Masayuki Ochiai and Yuki Sato</i>	
Chapter 10	197
Surface Characterization after Blasting <i>by Dagmar Draganovská, Janette Brezinová and Anna Guzanová</i>	
Chapter 11	215
Tribological Performance of Random Sinter Pores vs. Deterministic Laser Surface Textures: An Experimental and Machine Learning Approach <i>by Guido Boidi, Philipp G. Grützmacher, Markus Varga, Márcio Rodrigues da Silva, Carsten Gachot, Daniele Dini, Francisco J. Profito and Izabel F. Machado</i>	
Chapter 12	237
Tribological Behavior of Atmospheric Plasma Sprayed HA-CNT Coatings of Biomaterials <i>by Mahesh M. Sonekar and Walmik S. Rathod</i>	
Chapter 13	257
Estimation of the Grain Trajectory and Engaging on the Material <i>by Takenori Ono</i>	

Preface

Tribology is a branch of science that deals with machine elements and their friction, wear, and lubrication.

This book presents the fundamentals of tribology, with chapters on its applications in engines, metal forming, seals, blasting, sintering, laser texture, biomaterials, and grinding.

In Section 1, Chapter 1, discusses how abrasion can be controlled through the variables of hardness and size. Chapter 2, is fundamental for understanding how current raw materials can be manipulated to improve the performance of machine elements. Chapter 3 examines models of contact mechanics to combat elastic deformation. Chapter 4 discusses thermal control during abrasive conditions. Chapter 5 discusses the use of nitride-based coatings to protect against harsh machining operations and Chapter 6 discusses the use of molybdenum disulfide to promote solid lubricant.

In Section 2, Chapter 7 introduces the main issues associated with marine diesel engines. Chapter 8 discusses the friction determination observed in metal forming, and Chapter 9 examines how to optimize dry gas seals through groove shape. Chapter 10 presents how to characterize a surface after blasting. Chapter 11 compares two routes to improve tribological performance using random or deterministic textures. Chapter 12 examines the application of a coating to biomaterials and Chapter 13 shows how to estimate the grain trajectory for abrasive machining.

Giuseppe Pintaude and Tiago Cousseau

Academic Department of Mechanics,
Universidade Tecnológica Federal do Paraná,
Curitiba, Brazil

Anna Rudawska

Faculty of Mechanical Engineering,
Lublin University of Technology,
Lublin, Poland

Section 1

Fundamentals

Remarks on Wear Transitions Related to Hardness and Size of Abrasive Particles

Giuseppe Pintaude

Abstract

Abrasive wear is highly dependent on the characteristics and properties of abrasive particles. Their hardness and size can define the severity of abrasion in terms of wear rates. Typically, critical values have been empirically determined to define the transition between mild and severe wear. This review aims to update some of the issues related to these critical values and their relations to abrasive wear. After presenting the current state-of-art, the following items are discussed: a) the scratchability of materials; b) the particle fragmentation associated with size effects; and c) description of abrasion severity.

Keywords: abrasive wear, hardness, particle size effect, fragmentation, wear severity

1. Introduction

Probably the most recognized property associated with abrasivity, i.e., “the ability of a material or substance to cause abrasive wear” [1], is hardness. An unambiguous proof of this relation is the possibility to define hardness by employing the wear that a particle can promote on a surface, as postulated former by Tonn [2].

The relation between hardness and wear depends on the level of severity imposed by the tribological system. In this sense, the mild and severe regimes of abrasion [3] can be associated with the abrasive particle/worn material hardness ratio [4]. For a better understanding, here, this tribological pair will be called ‘indenter/worn material’ because some examples will be associated with the scratching process. For this reason, the hardness ratio will be referred to as H_i/H_w .

For rescuing the historical information, one could ask when the effect of the H_i/H_w ratio on the abrasive wear was first experimentally determined. For that reason, five manuscripts were consulted to check the cited references on the topic. A summary of these experimental investigations can be shown in **Table 1**.

Based on data presented in **Table 1**, one can note that the investigations performed by Nathan and Jones [6] and Richardson [7] were most cited, but the former one can be considered that conducted by Wahl in 1951 [12].

For exemplifying the effect of the H_i/H_w ratio on friction, it is fashionable to mention the findings of Tabor [15]. He conducted an unusual experiment using a scratch device for investigating the existence of a critical value of the H_i/H_w ratio. The experiment consisted of a metal with a sharp point at this end (indenter role)

Manuscript/Year	Aim	Experimental results cited for H_i/H_w ratio
Moore, 1978 [5]	Review	Nathan & Jones, 1966 [6]; Richardson, 1968 [7]
Torrance, 1981 [8]	Modeling	Richardson, 1968 [7]
Misra/Finnie, 1982 [9]	Review	Wahl, 1954 [10]
Tylczak, 1992 [11]	Review	Wahl, 1951 [12]; Nathan & Jones, 1966 [6]
Magnee, 1993 [13]	Modeling	Kruschov, 1958 [14]

Table 1.

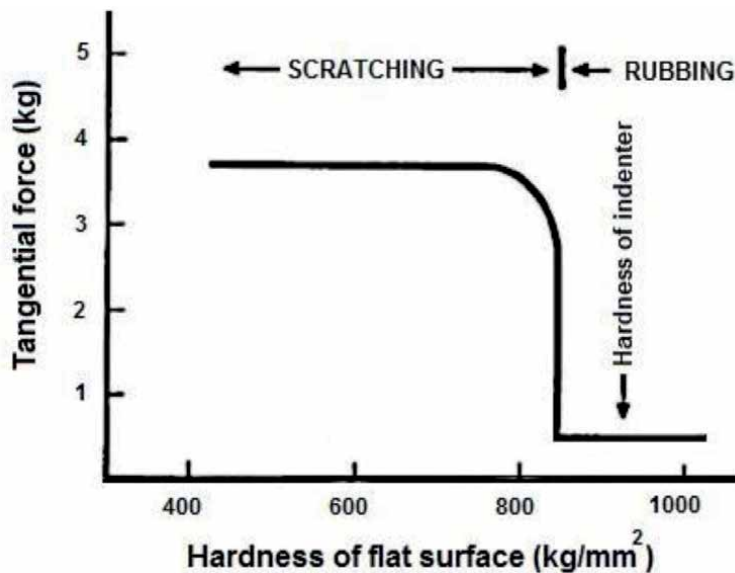
References cited on the experimental values of the H_i/H_w ratio.

scratching a sheet with variable hardness along its length, obtained by suitable heat treatment. The measurement of tangential force was able to define the mode of contact during the scratching, i.e., if the sharp point was able to scratch the metallic surface or not.

The indenter hardness indicated in **Figure 1** allows concluding that it will scratch the sheet's surface only if $H_i/H_w \geq 1.2$. Here this value is referred to as critical hardness ratio $(H_i/H_w)_{\text{CRIT}}$. Magnee [13], in his model formulation, called it a lethal abrasion coefficient.

The relation between the $(H_i/H_w)_{\text{CRIT}}$ and the abrasion regime - mild or severe wear - only makes sense if the wear mechanisms and observed damages on bodies' surfaces are well related. This task was done by Pintaude et al. [4], and it is summarized in **Figure 2**. Besides the findings described in [4], the detailed description of wear mechanisms could be found in Piazzetta et al. [16], who performed a Cherchar abrasivity test, sliding on nine rocks.

Considering the previous overview published [17], this review intends to incorporate experimental results to understand the concept of critical hardness ratio. The manuscript will be divided into three sections: i) the scratchability of materials, ii) the fragmentation of abrasive particles and size effects, and iii) the description of abrasion severity.

**Figure 1.**

Friction force determined between a metal point and a metal sheet of varying hardness [15].

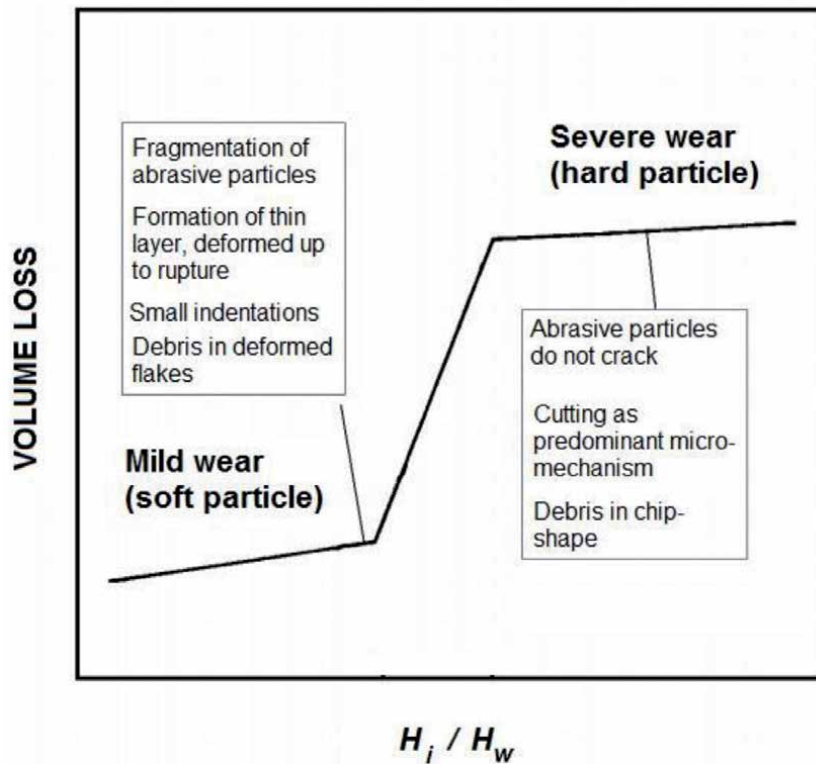


Figure 2.
Summary of wear mechanisms and surface damages on surfaces associated with each wear regime of abrasion, separated by the hardness ratio H_i/H_w , following [4].

2. Scratchability of materials: looking for an indicator of hardness differential

In his historical overview of indentation hardness, Walley [18] described the Mohs scale of hardness as the first to define hardness. Other researchers also published the idea of mutual scratchability. For instance, Shires [19] reported that the development of the sclerometry technique began in 1886 for defining scratch hardness. Regarding the Mohs scale, Petrescu [20] pointed out that a question arises if the standard minerals represent an arbitrary selection of increasing hardness substances or obeying a mathematical rule. Based on a series of experimental and independent data, this author concluded that a hypothetical mathematical relationship would need better experimental support. The possibility of a mathematical law would be very relevant to defining a critical value of hardness ratio for defining mild–severe wear transition, as observed by Tabor [15]. For this purpose, some investigations will be discussed based on the indentation hardness of Mohs minerals.

Masuda et al. [21] determined the Meyer hardness for nine minerals of the Mohs scale. The hardness ratio for each pair of minerals up to corundum (mineral number 9) can be calculated, besides data presented elsewhere [14], which was determined by Broz et al. [22]. This summary is presented in **Figure 3**.

The similarity of values between the two investigations observed in **Figure 3** could be discussed in their crystallographic orientations. However, Masuda et al. [21] were unable to describe the crystallographic orientation of 7 tested minerals. Based on this fact, the similarity of values can be considered surprisingly high, except for pairs 2 and 4.

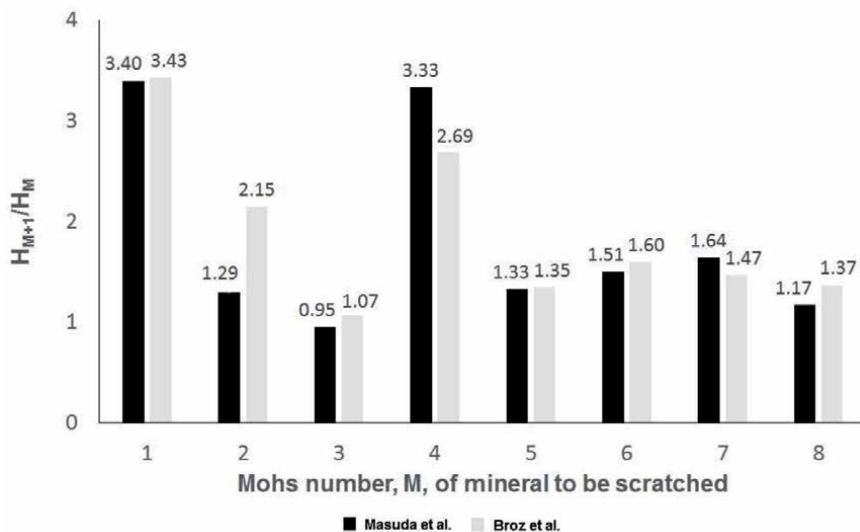


Figure 3. Hardness ratios for Mohs mineral pairs as measured by Masuda et al. [21] and Broz et al. [22]. Both references used depth-sensing techniques.

Pintaude [17] concluded that any constant value could be defined as the hardness differential required to produce scratches. Therefore, using minerals of the Mohs scale to find a critical value during scratch should be definitively abandoned. Also, using a scratch device to investigate the abrasive wear transition becomes impossible using only common indenters, such as diamond and hardmetal. These hard materials put the scratch process only in severe wear mode. Then, the question is: how do we manufacture relatively soft indenters?

Indentation experiments using varied metallic materials can be easily found [23–25], but soft and sharp non-metallic indenters are much rarer in the literature. In this fashion, the experiments conducted by Engelder and Scholz [26] and their results deserve special attention. These researchers prepared scratch tips with 0.3 mm of curvature made of apatite, orthoclase, quartz, topaz, and corundum. Controlling the normal load, they measured the tangential force during the scratching on different polished surfaces of quartz, microcline, and fused silica. Unfortunately, they did not report the indentation hardness of all minerals but described them in the Mohs scale. We can consider Vickers hardness's data reported by Broz et al. [22] for topaz, quartz, and orthoclase, and considering the value of 7.3 GPa for fused silica presented in [27]. The relative hardness of scratch tips to fused silica is included in **Figure 4** for clarification. (2.4; 1.7; and 0.9).

The variation of friction coefficient with the normal load obtained by Engelder and Scholz [26] is very intriguing. These authors noted a transition from the deformation to the fracture mode of scratch as the load was increased. Under low loads, friction behavior tends to be similar, independent of the relative hardness of the pair. On the other hand, when the fracture is a predominant mechanism, the relative hardness is essential, being the friction coefficient more significant for high values of relative hardness, which was expected.

Two speculations can be made from the above-described results. First, the scratch capacity of tested fused silica is only associated with the fracture behavior, a point of view supported by Akono et al. [28]. For these authors, scratching is a fracture process for all materials. Second, when the fracture acts in favor of the scratching process, some minerals can behave like metals, as described by Tabor [15].

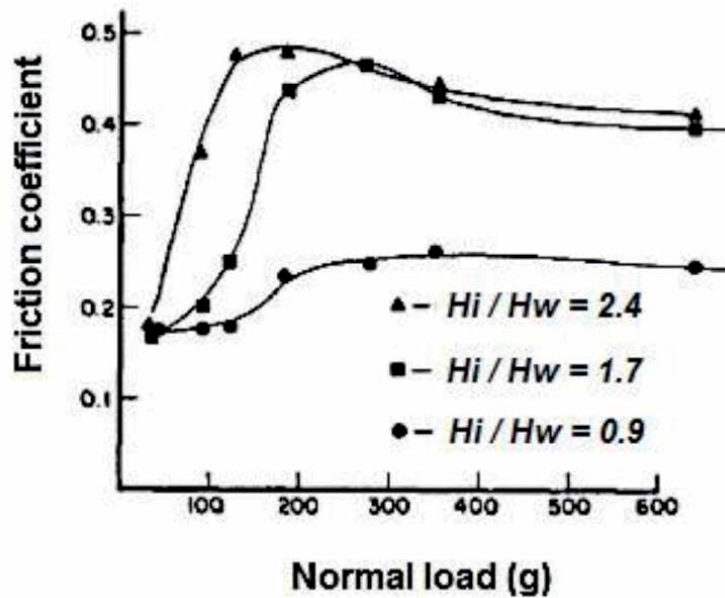


Figure 4. Friction coefficient as a function of normal load during sliding on fused silica by three minerals [26].

It is worthwhile in **Figure 4** the similar behavior between topaz and quartz scratching fused silica, i.e., for H_i/H_w of 1.7 and 2.4, the friction behavior was the same. In contrast, when a hardness ratio is smaller than 1, the friction value is much smaller than those obtained with other pairs. It opens the possibility to extend the range of tested materials by [26] to verify a transition on scratchability.

3. Particle fragmentation and size effects

An experimental observation during mild abrasion, related by Pintaude et al. [29], is the fragmentation of abrasive particles. The cracking of particles is a combination of fracture toughness and the level of stress imposed by the contact. A consequence is the particle size reduction during the wear process. Smaller particles cause less wear, being the particle size effect a well-known phenomenon in abrasive wear [30–40]. Therefore, the fragmentation of particles and size effects are characteristics of events during mild abrasion.

A question arises from this issue: if the wear rate changes for smaller particles, would there be a suitable hardness to express the worn surface? The answer is not simple once the size effect is present in the indentation event, called the indentation size effect (ISE) [41–47]. For example, Pintaude et al. [48] showed that the indentation size observed in steel could change the $(H_i/H_w)_{\text{CRIT}}$ value.

Pintaude [49] proposed a route (**Figure 5**) to define an adequate hardness measurement for the wearing event, defined by determining the abraded surface's R_z parameter. The results described in [49] were associated with the active force made by a single abrasive particle during the abrasion process. Applying the methodology described in **Figure 5**, maximum force values are obtained (**Table 2**), which correspond to the forces applied by abrasive particles. This equivalency is checked by looking at the resulted values from the model formulated by Bulsara et al. [50], which matched with those reported in **Table 2**.

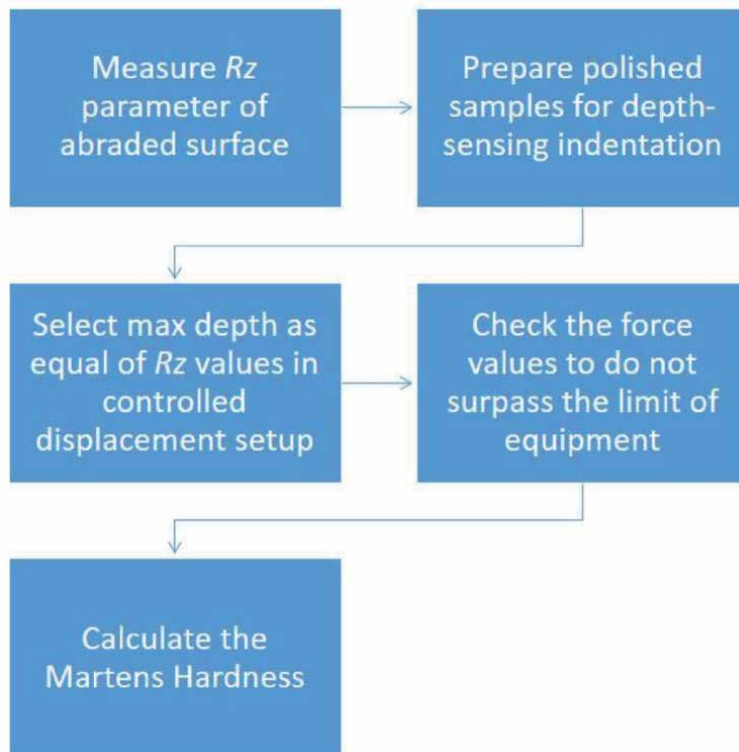


Figure 5.

Flowchart for determining a suitable hardness based on the characteristic left by an abrasion event.

Material	Rz produced by 0.06-mm particle	Rz produced by 0.2-mm particle	Max force (N) resulted
52100 steel	1.4 ± 0.2	2.9 ± 0.5	0.743 ± 0.006
HCCI	0.34 ± 0.03	1.7 ± 0.5	0.25 ± 0.02

Table 2.

Rz parameter (μm) of abraded surfaces, after tests using glass coated paper and the resulting forces (N) from the displacement control indentation (following Figure 5).

The Rz parameter can be roughly associated with the depth of penetration caused by an individual particle. This depth results from the combination between the applied normal load and the abrasive size [51].

A suitable coincidence between tested materials (high-chromium cast iron (HCCI) and the wire drawing 52100 steel) presented in Table 2 is that both have the same micro-hardness value, considering only their metallic matrices. Thus, the superior wear resistance of HCCI can be explained by a good action of its second hard phase [4]. When a glass paper with 0.2 mm particle size abraded these materials, the wear resistance of HCCI was approximately 30 times larger than that observed for 52100 steel. The hardness of HCCI promoted a reduction of 70% in the Rz parameter, considering particles of 0.2 mm. A much more dramatic decrease is noted in tests performed with abrasives of 0.06 mm, approximately four times. One can conclude that penetration depth was much more reduced in tests performed with smaller particle sizes.

The wear transition in abrasion is directly related to the capacity of particles to scratch the surfaces. For the same H_i/H_w ratio, scratch capacity is altered by the particle size or applied load if any of these variables are diminished. Consequently,

abrasive wear is subject to the size effect, and the best scale of hardness to express the wear behavior is that in its equivalent scale, evaluating by wear depth or wear width.

The initial question at the beginning of this section can also be discussed in the light of Graça et al. [52] findings. These researchers promoted nanoabrasive wear of Ni, Ni-85%Co, and Co using a diamond tip mounted in an atomic force microscope in nanoscale. The wear behavior was better related to their nanohardness and not to their conventional microhardness. On another extreme scale, the findings reported by Bryggman et al. [53] may be included here. Performing field tests measuring the wear of excavator bucket teeth, these authors concluded that the bulk hardness (HV300) was the best indicator of wear resistance.

Considering now the scratching test, the necessity to investigate a relationship between wear and hardness, both affected by size effects, the findings of Kareer et al. [54] bring a new concept. This investigation demonstrated a lateral size effect (LSE), which remains open to the use of hardness as an indicator of wear performance. These researchers performed scratch tests with the Berkovich indenter aligned either edge forward or face forward to the scratch direction. The scratch hardness was highly dependent on the tip orientation, resulting in a size effect much higher than that observed for the indentation hardness. This phenomenon should be more explored in the future for adjusting the scale for relating hardness and wear.

The discussion made in this section can be completed by analyzing the severity levels caused by abrasion in terms of hardness or size variations observed in abrasive particles.

4. Description of abrasion severity

The wear coefficient (K) concept can be associated with system variables not explicit in Archard's equation (applied load, sliding distance, and hardness of worn material). Zum-Gahr [55] described for dry systems possible ranges of K values for two- (10^{-1} – 10^{-4}) and three-body abrasion (10^{-2} – 10^{-5}). Indeed, the hardness and size of abrasive particles significantly affect these values, independent of the system configuration.

The first values of K to be considered in this discussion is reported by Pintaude et al. [4]. For the hardest tested material studied by these researchers (706 HV), under mild condition - $(H_i/H_w)_{\text{CRIT}} < 1.2$ – the wear coefficient found was 4.5×10^{-5} . Severe wear begging at approximately $K = 1.5 \times 10^{-2}$.

A vast variation in particle size was studied by Sasada et al. [56]. These authors measured the wear caused by SiC particles range from 3 up to 150 μm under three-body configuration, constantly testing similar body and counter-body material. They described three wear regimes as a function of SiC particle size, as shown in **Figure 6** for commercially pure iron as wear bodies.

Looking at **Figure 6**, a wear coefficient of 1.5×10^{-2} was determined for minor sizes. It is the same value reported for severe wear following the results of ref. [4]. On the opposite, Sasada et al. [56] claimed that the wear mechanism is adhesive wear because the particle sizes ($< d_t$) are smaller than the debris dimensions. In those cases, particles could not impede the metallic transfer, resulting in an adhesion mechanism. When this mechanism became operational, minimum wear was reached, meaning a $K \sim 2.5 \times 10^{-5}$, equivalent to a mild regime.

Therefore, both the hardness and size of abrasive particles can change the wear regime. However, when the investigation of Sasada et al. [56] was published, wear results determined under microscale abrasion test were very incipient [57]. Typical sizes used in microscale fall within the small range of values used in [56], then the comparison between their wear coefficient values seems to be a helpful exercise.

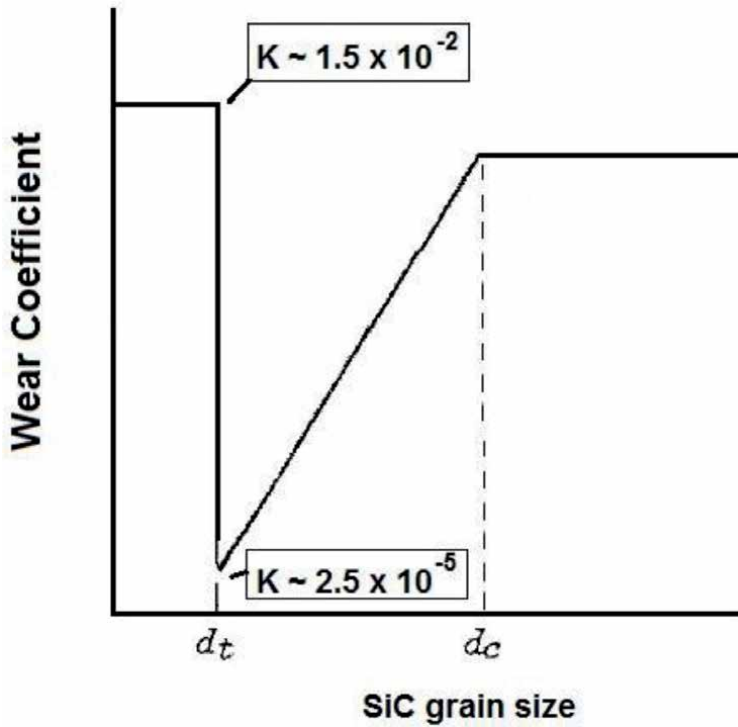


Figure 6.
Variation of wear coefficient as a function of SiC grain size, based on reference [56].

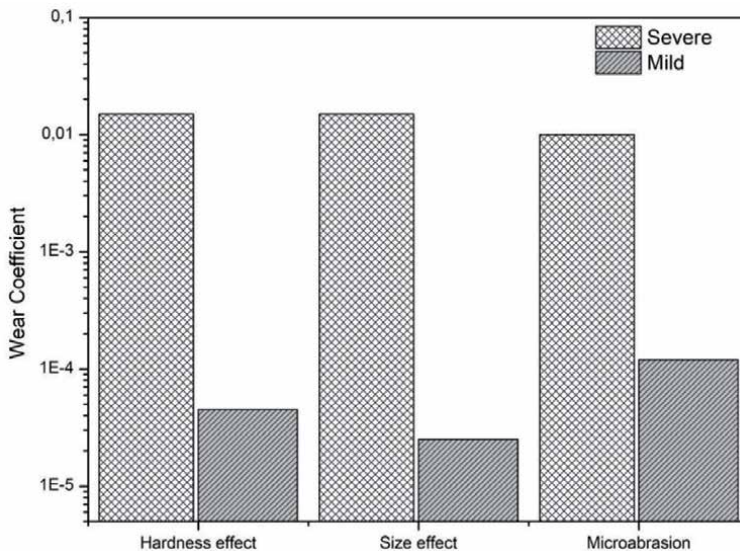


Figure 7.
Summary of wear coefficient limits, considering the effects of particle hardness [4], particle size [56], and microscale abrasion test [58, 59].

Here two investigations [58, 59] conducted under microscale abrasion deserve attention. They are interesting because the abrasive particles and micro-constituents of worn material had very different hardness.

Badisch and Mitterer [58] used three abrasive materials (SiC, alumina, and zirconia), 4–5 μm average size, using 0.3 N load. Testing three steels, they found

two levels of wear, which can express by $K = 10^{-2}$ for the high-wear, and $K = 3 \times 10^{-3}$ for low-level. Colaço [59] used alumina or silica particles against six hardfacing alloys under 0.8 N load. Values of 2.5×10^{-3} and 1.2×10^{-4} of wear coefficient can be reported taking the extremum values determined in his investigation. The order of magnitude using alumina is similar to that determined by [58]. Therefore, it is possible to consider limit values obtained with SiC (high-level of severity) and silica (low-level of severity).

Summarizing all described results, **Figure 7** shows the effects caused by particle hardness, particle size, and those verified using microscale abrasion test on the wear coefficients. The range of values determined using microabrasion is not entirely understood yet, taking the restricted and minor sizes used in this system.

The dynamics of a relatively soft and small abrasive should be better understood under the microscale abrasion test. It seems to be the challenge opened by Esteves et al. [60], who studied many combinations between load conditions, concentrations of the abrasive slurry, and hardness ratios of the sample and ball. A future model should consider the number of active particles and the effective force on each grain.

5. Conclusions

In this review, some aspects regarding the critical hardness ratio used to define the mild–severe wear transition in abrasion were presented. Based on the approaches described during the article, the following conclusions can be forward:

1. Scratchability of materials can be helpful to investigate the transition of soft-to-hard abrasion. In this sense, an extension of the results produced by Engelder and Scholz [26] is very promising;
2. The critical hardness ratio is a value influenced by size effects. For choosing a suitable scale of hardness, a route has been proposed, based on the features left by the abrasion process; and
3. Although the particle size effect can change the abrasion severity, wear coefficient values obtained under the microscale abrasion test deserve better comprehension.

Acknowledgements

The author acknowledges CNPq for his scholarship funding through process 310523/2020-6.

Nomenclature

H_i	indenter hardness
$(H_i/H_w)_{\text{CRIT}}$	critical hardness ratio
H_w	worn material hardness
HCCI	high-chromium cast iron
ISE	indentation size effect
K	wear coefficient
LSE	lateral size effect
Rz	average maximum height of the profile

Author details

Giuseppe Pintaude
Federal University of Technology - Paraná, Curitiba, Brazil

*Address all correspondence to: pintaude@utfpr.edu.br

IntechOpen

© 2021 The Author(s). Licensee IntechOpen. This chapter is distributed under the terms of the Creative Commons Attribution License (<http://creativecommons.org/licenses/by/3.0>), which permits unrestricted use, distribution, and reproduction in any medium, provided the original work is properly cited. 

References

- [1] ASTM. Standard Terminology Relating to Wear and Erosion; ASTM G40-17; ASTM International: West Conshohocken, EUA, 2017.
- [2] Tonn W. Beitrag zur Kenntnis des Verschleissvorganges beim Kurzversuch am Beispiel der reinen Metalle. *Zeitschrift für Metallkunde* 1937; 29:196-198.
- [3] Gates JD. Two-body and three-body abrasion: a critical discussion. *Wear* 1998;214:139-146. DOI: 10.1016/S0043-1648(97)00188-9
- [4] Pintaude G, Bernardes FG, Santos MM, et al. Mild and severe wear of steels and cast irons in sliding abrasion. *Wear*. 2009;267:19-25. DOI: 10.1016/j.wear.2008.12.099
- [5] Moore MA. Abrasive wear. *Int J Mater Eng Appl*. 1978;1:97-111. DOI: 10.1016/S0141-5530(78)90054-7
- [6] Nathan GK, Jones WD. Influence of the Hardness of Abrasives on the Abrasive Wear of Metals. *Proc Inst Mech Eng*. 1966;181:215-221. DOI: 10.1243/PIME_CONF_1966_181_317_02
- [7] Richardson RCD. The wear of metals by relatively soft abrasives. *Wear*. 1968;11:245-275. DOI: 10.1016/0043-1648(68)90175-0
- [8] Torrance AA. An Explanation of the Hardness Differential Needed for Abrasion. *Wear*. 1981;68:263-266. DOI: 10.1016/0043-1648(81)90096-X
- [9] Misra A, Finnie I. A review of the abrasive wear of metals. *J Eng Mater Technol*. 1982;104:94-101. DOI: 10.1115/1.3225058
- [10] Wahl H. Querschnitt durch das Verschleißgebiet. *Metallen*. 1954;9:4-6.
- [11] Tylczak JH. Abrasive wear. In: Totten GE, editor. *ASM Handbook* 18, Friction, Lubrication and Wear Technology, 2nd ed. Cleveland: ASM International; 1992. p. 184-190.
- [12] Wahl H. Verschleissprobleme im Braunkohlenbergbad. *Braunkohle Wärme Energie*. 1951;5/6:75-87.
- [13] Magneè A. Modelization of Damage by Abrasion. *Wear*. 1993;162-164:848-855. DOI: 10.1016/0043-1648(93)90086-2
- [14] Khrushchov MM. Resistance of Metal to Wear by Abrasion as Related to Hardness. In: *Proceedings of Conference on Lubrication and Wear*; 1-3 October 1957; London. London: Institution of Mechanical Engineers; 1958. p. 635-639.
- [15] Tabor D. Moh's Hardness Scale - A Physical Interpretation. *Proc Phys Soc London B*. 1954;67:249-257. DOI: 10.1088/0370-1301/67/3/310
- [16] Piazzetta GR, Lagoeiro LE, Figueira IFR, et al. Identification of abrasion regimes based on mechanisms of wear on the steel stylus used in the Cerchar abrasiveness test. *Wear*. 2018;410:181-189. DOI: 10.1016/j.wear.2018.07.009
- [17] Pintaude G. An overview of the hardness differential required for abrasion. *J Tribol*. 2010;132:034502. DOI: 10.1115/1.4001896
- [18] Walley SM. Historical origins of indentation hardness testing. *Mater Sci Technol*. 2012;28:1028-1044. DOI: 10.1179/1743284711Y.0000000127
- [19] Shires GA. Hardness Tests Research: Some Practical Aspects of the Scratch Test for Hardness. *Proc Inst Mech Eng*. 1925;108:647-687. DOI:10.1243/PIME_PROC_1925_108_028_02
- [20] Petrescu MI. Quantitative possibilities for converting the Mohs

- mineralogical hardness numbers into microhardness values obtained by indentation techniques. *UPB Sci Bull Series B: Chem Mater Sci.* 1999;61: 223-231.
- [21] Masuda T, Omori Y, Sakurai R, et al. Loop energy: A useful indicator of the hardness of minerals from depth-sensing indentation tests. *J Struc Geol.* 2018;117:96-104. DOI: 10.1016/j.jsg.2018.09.004
- [22] Broz ME, Cook RF, Whitney DL. Microhardness, toughness, and modulus of Mohs scale minerals. *Am Mineralogist.* 2006;91:135-142. DOI: 10.2138/am.2006.1844
- [23] Kayaba T, Hokkirigawa K, Kato K. Experimental Analysis of Yield Criterion for a Hard Asperity Sliding on a Soft Flat Surface. *Wear.* 1984;96:255-265. DOI: 10.1016/0043-1648(84)90040-1
- [24] Jamari J, Schipper DJ. Experimental investigation of fully plastic contact of a sphere against a hard flat. *J Tribol.* 2006;128:230-235. DOI: 10.1115/1.2164470
- [25] Pawlus P, Zelasko W, Dzierwa A, et al. Experimental Investigation of a Hemisphere Contact with a Hard Flat. *Tehnički vjesnik.* 2018;25:40-46. DOI: 10.17559/TV-20160720235706
- [26] Engelder JT, Scholz CH. The role of asperity indentation and ploughing in rock friction—II: Influence of relative hardness and normal load. *Int J Rock Mech Mining Sci & Geomech Abst.* 1976;13:155-163. DOI: 10.1016/0148-9062(76)90820-2
- [27] Michel MD, Serbena, FC, Lepienski CM. Effect of temperature on hardness and indentation cracking of fused silica. *J Non-Crystal Solids* 2006;352:3550-3555. DOI: 10.1016/j.jnoncrysol.2006.02.113
- [28] Akono AT, Reis PM, Ulm F J. Scratching as a fracture process: From butter to steel. *Phys Rev Lett.* 2011;106:204302. DOI: 10.1103/PhysRevLett.106.204302
- [29] Pintaude G, Tanaka DK, Sinatora A. The effects of abrasive particle size on the sliding friction coefficient of steel using a spiral pin-on-disk apparatus. *Wear.* 2003;255:55-59. DOI: 10.1016/S0043-1648(03)00212-6
- [30] Coronado JJ. Abrasive size effect on friction coefficient of AISI 1045 steel and 6061-T6 aluminium alloy in two-body abrasive wear. *Tribol Lett.* 2015;60(3):40. DOI: 10.1007/s11249-015-0615-1
- [31] Coronado JJ, Sinatora A. Effect of abrasive size on wear of metallic materials and its relationship with microchips morphology and wear micromechanisms: Part 1. *Wear.* 2011;271(9-10):1794-1803. DOI: 10.1016/j.wear.2011.01.078
- [32] Coronado JJ, Sinatora A. Effect of abrasive size on wear of metallic materials and its relationship with microchips morphology and wear micromechanisms: Part 2. *Wear* 2011;271(9-10):1804-1812. DOI: 10.1016/j.wear.2011.05.036
- [33] Coronado JJ, Sinatora A. Particle size effect on abrasion resistance of mottled cast iron with different retained austenite contents. *Wear.* 2009;267(11): 2077-2082. DOI: 10.1016/j.wear.2009.08.011
- [34] De Pellegrin DV, Torrance AA, Haran E. Wear mechanisms and scale effects in two-body abrasion. *Wear.* 2009;266(1-2):13-20. DOI: 10.1016/j.wear.2008.05.015
- [35] Sevim I, Eryurek IB. Effect of abrasive particle size on wear resistance in steels. *Materials & Design.*

2006;27(3):173-181. DOI: 10.1016/j.matdes.2004.10.010

[36] Pintaude G, Tschiptschin AP, Tanaka DK, et al. The particle size effect on abrasive wear of high-chromium white cast iron mill balls. *Wear*. 2001;250(1-12):66-70. DOI: 10.1016/S0043-1648(01)00663-9

[37] Gählin R, Jacobson S. The particle size effect in abrasion studied by controlled abrasive surfaces. *Wear*. 1999;224(1):118-125. DOI: 10.1016/S0043-1648(98)00344-5

[38] Chandrasekaran T, Kishore. Grinding abrasive wear and associated particle size effect. *Mater Sci Technol*. 1992;8(8):722-728. DOI: 10.1179/mst.1992.8.8.722

[39] Misra A, Finnie I. On the size effect in abrasive and erosive wear. *Wear*. 1981;65(3):359-373. DOI: 10.1016/0043-1648(81)90062-4

[40] Sin H, Saka N, Suh NP. Abrasive wear mechanisms and the grit size effect. *Wear*. 1979;55:163-190. DOI: 10.1016/0043-1648(79)90188-1

[41] Ruiz-Moreno A, Hähner P, Kurpaska L, et al. Round Robin into Best Practices for the Determination of Indentation Size Effects. *Nanomaterials*. 2020;10:130. DOI: 10.3390/nano10010130.

[42] Durst K, Göken M, Pharr GM. Indentation size effect in spherical and pyramidal indentations. *J Phys D: Appl Phys*. 2008;41(7):074005. DOI: 10.1088/0022-3727/41/7/074005

[43] Kim JY, Kang SK, Lee JJ, et al. Influence of surface-roughness on indentation size effect. *Acta Mater*. 2007;55(10):3555-3562. DOI: j.actamat.2007.02.006

[44] Huang Y, Zhang F, Hwang KC, et al. A model of size effects in

nano-indentation. *J Mech Phys. Solids*. 2006;54(8):1668-1686. DOI: 10.1016/j.jmps.2006.02.002

[45] Bull SJ. On the origins and mechanisms of the indentation size effect. *Zeitschrift für Metallkunde*. 2003;94(7):787-792. DOI: 10.3139/146.030787

[46] Iost A, Bigot R. Indentation size effect: reality or artefact? *J Mater Sci*. 1996;31(13):3573-3577. DOI: 10.1007/BF00360764

[47] Li H, Ghosh A, Han YH, Bradt RC. The frictional component of the indentation size effect in low load microhardness testing. *J Mater Res*. 1993;8(5):1028-1032. DOI: 10.1557/JMR.1993.1028

[48] Pintaude G, Tanaka DK, Sinatora A. Effect of indentation size and microhardness calculation on abrasive wear severity. *Scripta Mater*. 2001;44:659-663. DOI: 10.1016/S1359-6462(00)00633-3

[49] Pintaude, G. Application of instrumented indentation testing under micrometric range (in Portuguese). *Metalurgia & Materiais*. 2003;59(530): 96-8. DOI:

[50] Bulsara, V. H., Ahn, Y., Chandrasekar, S. et al. Mechanics of polishing. *J Appl Mech*. 1998;65(2):410-416. DOI: 10.1115/1.2789069

[51] Moore MA, Douthwaite RM. Plastic deformation below worn surfaces. *Metallurgical Trans. A*. 1976;7A:1833-1839. DOI: 10.1007/BF02659813

[52] Graça S, Vilar R, Colaço R. The role of indentation size effect on the abrasive wear behaviour of ductile metallic materials: A nanotribological study. *Wear*. 2010;268:931-938. DOI: 10.1016/j.wear.2009.12.019

[53] Bryggman U, Hogmark S, Vingsbo O. Prediction of gouging

abrasion resistance of steel by pendulum grooving and other laboratory test methods. *Wear*. 1987; 115:203-213. DOI: 10.1016/0043-1648(87)90210-9

[54] Kareer A, Hou XD, Jennett NM, et al. The existence of a lateral size effect and the relationship between indentation and scratch hardness in copper. *Philos Mag*. 2016;96:3396-3413. DOI: 10.1080/14786435.2016.1146828

[55] Zum Gahr KH, Wear by hard particles. *Tribol Int*. 1998;31:587-596. DOI: 10.1016/s0301-679x(98)00079-6

[56] Sasada T, Oike M, Emori N. The effect of abrasive grain size on the transition between abrasive and adhesive wear. *Wear*. 1984;97:291-302. DOI: 10.1016/0043-1648(84)90155-8

[57] Gant AJ, Gee MG. A review of micro-scale abrasion testing. *Journal of Physics D: Applied Physics*. 2011;44:073001. DOI: 10.1088/0022-3727/44/7/073001

[58] Badisch, E, Mitterer, C. Abrasive wear of high speed steels: influence of abrasive particles and primary carbides on wear resistance. *Tribol Int*. 2003;36:765-770. DOI: 10.1016/S0301-679X(03)00058-6

[59] Colaço, FHG. Study of abrasion behavior and formation of coatings applied by GTAW with double feeding of tubular wires (in Portuguese) [thesis]. Curitiba: Federal University of Technology - Paraná; 2021.

[60] Esteves PJ, Seriacopi V, de Macêdo MC, Souza RM, Scandian C. Combined effect of abrasive particle size distribution and ball material on the wear coefficient in micro-scale abrasive wear tests. *Wear*. DOI: 10.1016/j.wear.2021.203639

Grease Lubrication: Formulation Effects on Tribological Performance

Tiago Cousseau

Abstract

Grease lubrication performance prediction is challenging. Only recently that empirical equations to predict grease film thickness for prevailing rolling conditions under fully flooded lubrication taking into account thickener properties and content for low, moderate, and high speeds were developed. At starved lubrication, although new insights about the supply and loss mechanisms that govern film formation have been published, contact replenishment and, consequently, film thickness predictions for long-term operation are still not available. Prediction of components efficiency requires film thickness values and properties, including film's molecular structure, which makes it even more challenging. When it comes to prevailing sliding conditions, the literature is scarce and most of the knowledge developed for prevailing rolling conditions is not applicable. During the sliding of the contacting bodies, boundary and mixed lubrication regimes are expected. In this situation, the tribological response is primarily defined by grease thickener and additives physicochemical interaction with the surface. This complexity leads many researchers to seek simpler relationships between grease formulation and properties with its performance. This review aims to present the state-of-art on grease lubrication and update some of these relationships.

Keywords: grease components, grease properties, grease performance, friction, wear, rolling contact fatigue

1. Introduction

The most common definition of lubricating grease is the one put forward by ASTM D 288: "A solid to semifluid product of a thickening agent in a liquid lubricant, other ingredients imparting special properties may be included" [1]. This means that grease is a thickened (not a thick) oil. It also states that lubricating grease is based on a multiphase system consisting of at least two well-defined components, namely a thickener and a lubricant fluid. The "other ingredients" refer to additives. The distribution of these components depends on the application but typically is 65–95 wt % base oil, from 5 to 35 wt % thickener, and from 0 to 15% additives. These separate components form a multiphase matrix, in which the thickener forms a structure that holds the base oil and the additives. This multiphase matrix endows the grease with a certain consistency and a yield pseudoplastic behavior that gives it many advantages over lubricant fluids, such as

ease of use (it will not easily leak out due to its consistency), inherent sealing action, low friction, and protection against corrosion [2]. However, it also makes it quite difficult to characterize or model the individual influence of each of its components on the grease overall performance because their effectiveness depends on their interaction [3, 4], manufacturing process [5, 6], and system operating conditions, as observed with calcium sulfonate thickened greases that show excellent wear resistance in pure sliding tests [7, 8] but reduced rolling contact fatigue life in prevailing rolling conditions [9, 10].

The synergic effect among grease components (base oil, thickener, and additives) along with its properties dependency on the manufacturing process, pose significant challenges on modeling grease behavior in a tribological system. Consequently, there are very few scientific works modeling grease behavior as a multiphase fluid [11, 12], and most of the experimental work focuses on the comparison between grease performance with its composition or properties.

The available work modeling lubricating greases as a multiphase fluid is very promising and may bring significant new insights about grease performance, such as the grease lubricating phase (variation of volume fraction distribution of oil and thickener in the contact) as a function of time and position [11], and the rheological changes of lubricating greases as a function of thickener distribution and deformation [12]. Unfortunately, such models were not yet employed to compare different grease formulations with their flow and tribological responses. Analytical solutions to predict grease-lubricated rolling bearing life, such as ISO 281, still do not take into account the thickener type, although grease response depends on it.

The experimental work evaluating grease performance is abundant under operating conditions that resemble the ones from rolling bearings (low slide to roll ratio, SRR), which are the main grease application. Tests have been performed over the years by many researchers under such conditions with several lubricating greases. Their main outcomes—film thickness, friction, wear, and rolling contact fatigue—have been related to grease characteristics. By today, it is well known that under fully flooded conditions, grease does not always follow the film thickness predicted by the traditional elastohydrodynamic lubrication (EHL) theory [13] nor the coefficient of friction is depicted by the Stribeck curve [14]. This divergence is attributed to the presence of thickener in the contact [15] and depends on the operating conditions, in particular the lubrication regime [16]. In fact, it has been shown that thickener changes film thickness [13], coefficient of friction [14], crack propagation rate [15], and play a significant role in the lubricant supply to the contact under starved lubrication [17]. Although a good agreement between thickener content and morphology with film thickness measurements under fully flooded conditions was observed [13], its effect on friction, wear and crack propagation is still not well known [15].

Different from prevailing rolling contacts, when it comes to grease evaluation under pure sliding conditions, the literature is scarce and the effect of thickener and base oil on grease tribological response is unknown for most grease formulations. At typical concentrated sliding contact conditions, hydrodynamic lubrication is not prone to occur and the lubrication regime is the boundary or mixed [18]. In this situation, the thin film covering the surfaces is mostly composed of thickener and/or additives. Consequently, the thickener used to play a more significant role than the base oil viscosity on grease performance [19]. Most of the existent work under sliding conditions focuses on the development and evaluation of extreme pressure/anti-wear (EP/AW) additives and nanoparticles to control friction and wear [20–22]. Studying the effect of one specific additive or nanoparticle on grease performance is complicated by the presence of other additives and it is often most appropriate to consider the additive package since one additive can have a

synergistic or an antagonistic effect on another one [20]. Furthermore, the additives performance also depends on the thickener type, which interferes with their mobility toward the surface through chemical interactions or attractive forces [21]. Consequently, it is difficult to observe general trends for the tribological response of a specific additive. Besides that, only general information about the additive package is provided by grease manufacturers.

In order to clarify the role of thickener type and base oil viscosity on grease film thickness, friction and wear, this review presents a compilation of the literature for prevailing rolling and prevailing sliding conditions through schematic graphics along with a ranking of the thickeners and base oils that contribute the most on the tribological response of the greases.

2. The role of thickener and base oil in prevailing rolling contacts

Lubricating grease is mostly used in prevailing rolling contacts, such as in rolling bearings and gears [23]. Therefore, most of the knowledge on grease lubrication is related to tests performed under the low slide-to-roll ratios. In these operating conditions, lubricating greases are prone to form elastohydrodynamic films that separate the contacting surfaces, and therefore, the study of film formation, friction, and rolling contact fatigue is of particular interest. The tests reported in the literature can be divided into many ways. Here, they are divided into two ways—fully flooded and starved contacts.

2.1 Fully flooded conditions

The large majority of grease film thickness and coefficient of friction measurements reported in the literature comes from the ball-on-disc experiments using a device that forces the grease back to the contact and ensures a fully flooded condition. A schematic view of this device is well depicted in [24]. In this situation, lubricating greases present different behavior than lubricating oils. **Figure 1** presents typical center film thickness measurements as a function of the entrainment speed for a lubricating grease and its base oil. The film thickness increases proportionally to entrainment speed ($h_{ff} \propto U^{0.67}$) for the oils, as predicted by EHL theory

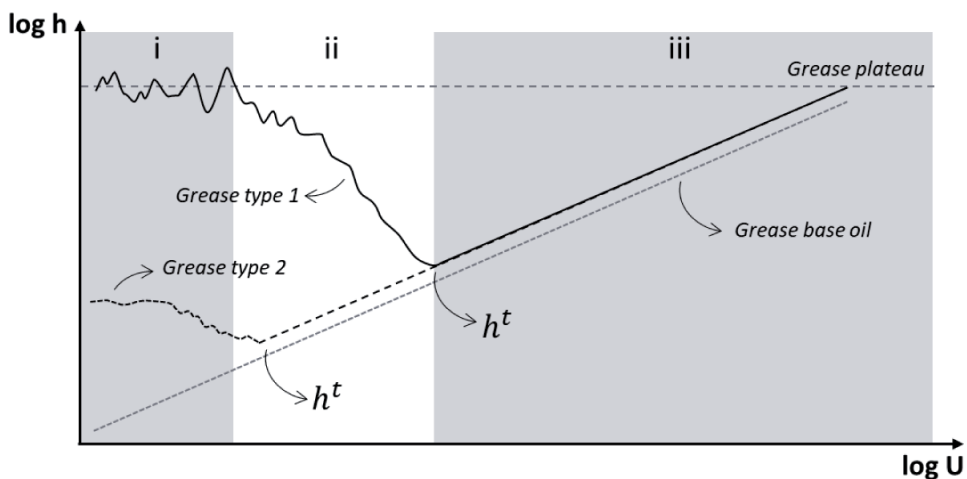


Figure 1. Typical film thickness versus entrainment speed curves for grease and its base under fully flooded lubrication and low SRR.

for point contacts and fully flooded lubrication (Eq. (1)) [25], while lubricating greases present the well-known “V-shape” curve [15]. That difference is attributed to the thickener effect on film formation. At medium to high speeds grease presents the same behavior of its base oil (region iii) and used to be modeled with Eq. (1), although in general, it presents slightly higher film thickness. The difference was found to be proportional to the ratio of the thickener concentration (φ) to the average volume of the individual thickener particles (V), as shown by Eq. (2), which presented a good agreement with experimental results and better predicts lubricating grease film thickness [13]. The grease film thickness predicted with Eq. (2) was found to be 3–40% higher than the ones predicted with Eq. 1 [14], which shows the importance to take into account the thickener on film thickness prediction.

$$h_{ff} = 2.69R_x(1 - 0.6e^{-0.73k})(E'\alpha)^{0.53}\left(\frac{\bar{u}\eta_0}{E'R_x}\right)^{0.67}\left(\frac{F}{E'R_x}\right)^{-0.067} \quad (1)$$

$$h_g = h_{ff}\left[\left(0.61\left(\frac{\varphi}{V}\right) + 1.97\right) + 1\right] \quad (2)$$

As the entrainment speed is reduced, a transition occurs (h^t) and the grease does not follow the conventional EHL theory anymore (region ii). In this region, the film thickness is dominated by thickener material trapped on the contact interface and increases as the entrainment speed is further reduced. At very low speeds most lubricating greases reach a plateau with very high film thickness (region i). In these regions (i and ii), the measurements fluctuate significantly due to the thickener material crossing the contact [26, 27], and qualitative relationship among film thickness and thickener content, morphology, and properties have been presented [26–28]. The observed transition (h^t) occurs, for each type of grease, at a different specific film thickness [26]. Kanazawa et al. [16, 29] showed strong evidence that (h^t) is related to the ratio between film thickness and thickener particles size, and that colloidal nanoparticle dispersions present the same behavior. This should lead to new research lines in which grease film thickness must be modeled as a multiphase fluid and thickener characteristics should be taken into account. While such research lines are emerging, engineering solutions have been proposed. Morales et al. [30] modeled the trends observed in regions i and ii with good agreement with the experimental results. To do so, first film thickness measurements h_g are used to estimate the effective grease viscosity by solving Hamrock and Dowson equation for the dynamic viscosity η_0 at every speed \bar{u} value (Eq. (1) [25]). The grease effective viscosity $\eta_{g,eff}$ is then approximated by a simple model described by Eq. (3), in which the constants A and f are obtained by applying a collocation method using one speed below and one at the transition (h^t). Finally, the grease effective viscosity ($\eta_{g,eff}$) is used instead of the grease base oil viscosity (η_0) in Eq. (1) to predict film thickness.

$$\eta_{g,eff} = \eta_{0,oil}[\coth(A\bar{u})]^f \quad (3)$$

These empirical equations are the state-of-art to predict grease film thickness under fully flooded conditions using analytical solutions for the three regions presented in **Figure 1**. At the oil-dominated region (iii), the film thickness can be reasonably predicted using only the base oil type and viscosity (Eq. (1)), which are provided by grease suppliers, although more accurate predictions can be done if thickener morphology and content are taken into account (Eq. (2)). At the

thickener-dominated regions (i and ii) film thickness can only be predicted if prior film thickness measurements are carried out (Eq. (3)). Since thickener characterization and film thickness measurements are, in general, not available for end users, several researchers have presented qualitative relationships between grease type and film thickness that are quite useful [14, 26, 28, 30–35]. These observations show that—(i) mineral oils (M) present higher film thickness values than synthetic oils (S) with the same viscosity due to their greater pressure-viscosity coefficient [25]; (ii) film thickness increases with thickener content [36]; (iii) in general, thickeners that enhance grease film thickness the most in comparison to the corresponding base oil for lubricating greases formulated with mineral oils, above and below the transition (h^t), are as follows—calcium (C) > polyurea (Pu) > lithium (L); (iv) for lubricating greases formulated with synthetic oils—polypropylene (P) > lithium complex (Lc) > polyurea (Pu). Although lubricating greases formulated with synthetic oils present similar behavior, PAO-based greases present higher film thickness than ester-based greases. This response is attributed to the thickener structure, which is smaller for ester-based greases processed with the same thickener type [37].

From the aforementioned summary, in **Figure 1**, “grease type 1” refers to PS, LcS, and CM, while “grease type 2” refers to LM and PuM. However, it is important to stress that this general trend might not be always observed. Depending on the combination of thickener and base oil types, along with the manufacturing process, the thickener morphology changes [3, 6, 38], and consequently the film thickness response also changes [37].

The operating conditions also affect the trends presented in **Figure 1**. Temperature variation affects grease base oil viscosity, which in turn affects film thickness in a similar manner as the entrainment speed does. Therefore, the transition (h^t) occurs at higher speeds with an increase in temperature, but its value stays fairly constant [39]. Load and slip ratio variation were shown to have a minor effect on film thickness values, as predicted by standard EHL theory [39].

Figure 2 presents the typical coefficient of friction measurements as a function of the entrainment speed for lubricating grease and its base oil. The base oil coefficient of friction follows the Stribeck curve, which is characterized by high friction values at low speeds (low specific film thickness) due to asperities contact (region i), followed by a reduction of the coefficient of friction as the speed increases (region ii), up to a point in which the friction does not vary significantly (region iii).

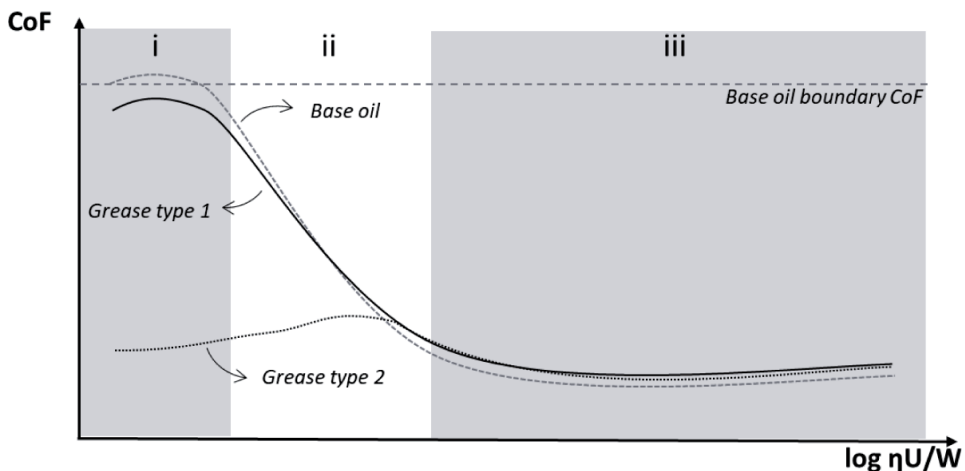


Figure 2. Typical coefficient of friction versus entrainment speed curves for grease and its base oil under fully flooded lubrication and low SRR.

Different than their base oils, some lubricating greases do not follow Stribeck curve and present friction reduction as the speed is reduced from region iii to region i. That difference is also attributed to the thickener. At high speeds (region iii) greases and their base oils present the same behavior, although lubricating greases used to present friction values slightly different (lower) than their base oils. At low speeds (regions i and ii), at the thickener dominated region, two different trends are observed—(i) lubricating greases “type 1” follow the Stribeck curve and might present slightly higher friction values than their base oils as the speed is reduced; (ii) lubricating greases “type 2” present moderate friction increase followed by its stabilization or reduction as the speed is reduced. It is very important to mention the coefficient of friction does not necessarily reduce as film thickness increases. This is well depicted by calcium greases, which present very high film thickness, but also a high coefficient of friction, at the low-speed region [14, 15]. This occurs because the friction depends on the film properties and does not only on its thickness, and therefore, the typical coefficient of friction versus specific film thickness curves observed for base oils are not always observed for greases.

The grease coefficient of friction under EHL conditions depends on grease film thickness, thus, all the uncertainties around film thickness prediction are observed for the coefficient of friction prediction. Besides that, while film thickness formation is mostly governed by two “macro” properties above the transition (h^*)—ambient pressure viscosity η_0 and pressure viscosity coefficient α , friction has its origins in the lubricant molecular structure [40], including molecular shape and flexibility [41], which is obviously a much more complicated matter. Therefore, most of the published work focused on the qualitative relationship between grease type and friction [14, 16, 27, 28, 32, 35, 37, 42]. The summary of these works shows that—(i) mineral oils present a higher coefficient of friction than synthetic oils with the same viscosity due to their greater pressure-viscosity coefficient, which seems to be related to their limiting shear strength and viscosity index [14, 37]; (ii) greases formulated with PAO base oils seem to provide the lowest friction followed, in order, by ester, mineral paraffinic, and naphthenic base oils [43–46]; (iii) the higher the thickener content the smaller is the CoF for lubricating greases of “type 2” [35, 47] (see **Figure 2**) due to the increased probability of thickener crossing the contact and depositing on the surface; (iv) the low-pressure rheological properties (viscous and viscoelastic) are not the main influential factor in determining friction [48]; (v) in general, thickeners that reduce the coefficient of friction the most in comparison to the corresponding base oil for lubricating greases formulated with mineral oils are as follows—lithium (L) > polyurea (Pu) > calcium (C); (vi) for lubricating greases formulated with synthetic oils—polypropylene (P) > lithium complex (Lc) > polyurea (Pu).

Based on the aforementioned summary, in **Figure 2**, “grease type 1” refers to CM, PM + S, LM, while “grease type 2” refers to PS, LcS, and PuS. However, as mentioned before, the coefficient of friction depends on the properties of the separating film, which in turn depends on the combination of thickener, base oil, and the manufacturing process, hence caution should be taken while using these qualitative rankings.

The trends presented in **Figures 1** and **2** are of utmost importance for grease selection because rolling bearing life and efficiency are directly related to film thickness and friction. The current procedures for grease selection, based on ISO 281, and rolling bearing efficiency, based on tools provided by bearing manufactures [49], only take into account grease base oil viscosity. These current practices would lead to the selection of lubricating greases with very high base oil viscosity to ensure adequate lubrication (high specific film thickness—region iii of **Figures 1** and **2**) for rolling bearings operating at low speeds, which are usually observed in

large-size bearings. However, high viscous greases used to present very low bleeding properties which can generate premature failure due to starvation [50], as discussed in the next section. An alternative is the selection of lubricating greases that generate high film thickness and low friction under low entrainment speed (low specific film thickness), such as lubricating greases formulated with PAO base oil and thickened with polypropylene or lithium complex (PS or LcS). Obviously, other parameters, out of the scope of this chapter, should be verified, such as environmental and operating factors.

Similar trends presented in **Figures 1** and **2** are also observed in full rolling bearing tests [27, 29, 30, 51–57] under fully flooded conditions or a short period of test, situations in which starvation and grease degradation do not take place. Under these operating conditions, if the rolling bearing is properly selected, the main source of failure is fatigue or grease degradation. In case of fatigue, a thickener type that has a high affinity with the bearing material and a morphology resembling small particles, such as calcium sulfonate, is more likely to enter the pre-formed cracks and propagate them faster, leading to severe wear [15].

2.2 Starved conditions

Although most of the published studies on grease lubrication are performed under fully flooded conditions, it is well known that most greased components, such as rolling bearings, operate under starved conditions. Therefore, it is crucial to understand the key aspects controlling the lubrication process when the lubricant is not available in abundance to the contact. Starved conditions are usually evaluated in ball-on-disc test rigs without the use of a device to channel the grease back to the contact or in long-duration rolling bearing tests. Generally, these tests are performed at a constant speed to evaluate grease film thickness variation over time, which is governed by competing for lubricant supply and loss mechanisms. This balance, which is not constant in time and can present a chaotic behavior [58], has not been modeled yet due to its dependence on a number of factors, such as—(i) centrifugal forces [59, 60]; (ii) surface tension [60, 61]; (iii) capillary forces [62]; (iv) contact forces between contacting bodies [63]; (v) transient operating conditions [63]; (vi) cage geometry and material [17]; (vii) bleed oil properties [17, 28]; (viii) grease rheology, in particular, its yield stress [50], (ix) grease bleeding [50] and (x) mechanical stability [50]. However, several of these individual factors have already been modeled and validated with experimental results. For instance, the grease-free flow due to centrifugal forces was shown to be dependent on the Herschel-Bulkley rheological parameters (τ_0 , K , n) when oil separation is low (low temperatures), and also on the bleed oil properties when oil separation is high [64]. Grease bleeding due to centrifugal forces was numerically modeled for greases with fibrous structure, such as lithium thickened greases. This model considers grease base oil viscosity and density, thickener fiber diameter, and mass [65]. Static oil bleed, representing the oil bleeding from the grease settle at the outer ring shoulder and on the seal was recently described using a Washburn-like model based on Darcy's law with the great agreement with five lubricating greases [66]. Shear degradation at different temperatures was modeled for fibrous structured greases and the results were validated using grease collected from a grease worker and rolling bearings [67]. Due to these recent advances in the prediction of grease shear aging and oil bleeding, it is expected that soon all these models will be placed together and better predictions of grease film thickness under starved conditions will be available.

Figure 3 presents grease film thickness as a function of time for entrainment speeds higher than the transition thickness (h^t) in a log-log scale (see **Figure 1**).

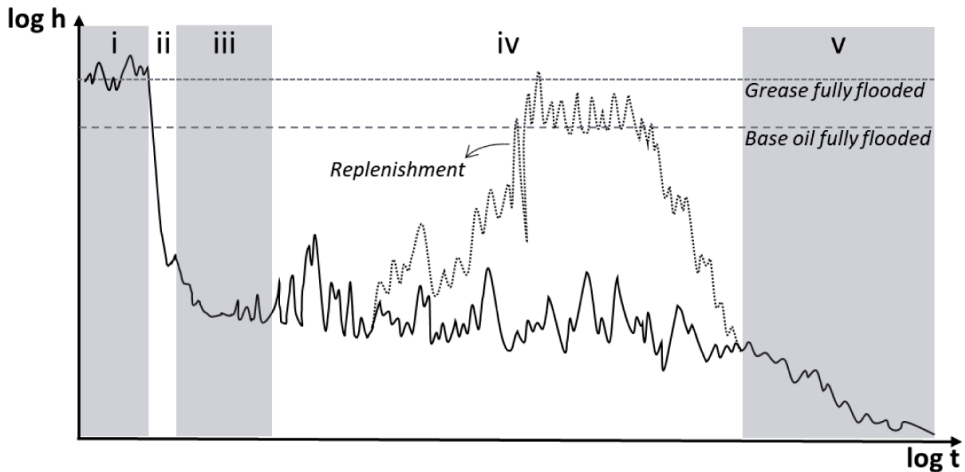


Figure 3.

Typical film thickness versus time curves for lubricating grease under starved lubrication and low SRR.

Two dashed lines representing grease and its base oil film thicknesses under fully flooded lubrication are also presented. Besides, the curve is divided into five stages—(i) at the beginning of the test the contact is fully supplied with grease and the same trends reported in Section 2.1 are observed, that is, most lubricating greases present higher film thickness than their base oils due to thickener contribution; (ii) as time progresses film thickness drops quickly; (iii) after that the film thickness decay rate slows considerably, (iv) up to the moment it reaches a stable value that might remain for a long period of time (hours). In this stage, the film thickness, which is formed by a thin layer of highly worked grease deposited on the track, changes little with time, and it may decrease or increase very slowly unless replenishment by grease or its bleed-oil improves and increases film thickness considerably (dotted line). In this stage, the base oil viscosity is not directly related to film thickness values [50]; (v) at some point the lubrication availability to the contact becomes scarce and asperities contact takes place.

In every stage, the film thickness curve is characterized by significant scatter due to sudden local increases caused by thickener lumps crossing the contact. Such local increases occur at different rates and reach different thickness values depending on the thickener morphology [28, 68]. The duration, or even the existence, of each stage depends on the competing lubricant supply and loss mechanisms aforementioned. Therefore, some greases might not present the stabilization stage (iv) and quickly reach asperities contact (v), while others might present several replenishment cycles before reaching asperities contact. In terms of film thickness prediction, the first stage can be modeled using Eq. (2) since fully flooded lubrication occurs. Then, as starvation proceeds, which occurs in a few hours, the steady grease film thickness at the end of stage (iii) can be predicted by Eq. (4), which is related to the product of speed (U , m/s), dynamic viscosity (η , Pa s), and half-contact width (a , m).

$$h_{g_starve} = h_{ff} \cdot b \cdot (U \cdot \eta \cdot a)^{-c} \quad (4)$$

This equation was validated in a full bearing test rig instrumented to measure film thickness [17]. The tests were performed with a deep-groove ball bearing 6309-2Z/C3 with a steel cage with 10 balls (full bearing) and 05 balls, and with a DGBB 6309-2Z/TN99 with a glass fiber reinforced polyamide 66 cage with 10 balls (full bearing) and 05 balls. Three lubricating greases with different thickener

(Li, LiC, and Pu) and base oil (M, E, and PAO) types were tested for several rotational speeds and loads. The results clearly showed that whatever is the effect of grease formulation, rheology, bleeding properties, number of balls in a bearing (overrolling time), cage geometry, and type of surface tension, all the experiments collapsed into a single curve represented by Eq. (4), which suggests that they are secondary at this stage. However, some spread between model and experiments was observed and attributed to these secondary effects, although it could also be related to the use of the fully flooded oil film thickness (h_{ff} , Eq. (1)) instead of the fully flooded grease film thickness (h_g , Eq. (2)) into Eq. (4).

It is also important to state that Eq. (4) is not a general film thickness equation for starved lubricated contacts since the values of the constants “b” and “c” were shown to be dependent on the tribological system (ball-on-disc, rolling bearing type) and might be affected by load direction (axial, radial, or combined) [17]. This equation clearly shows that starvation increases with speed, viscosity, and half-contact width. High speeds lead to faster starvation due to grease being pushed away from the contact and having less time for the film to recover [17, 62]. However, since the centrifugal force acting on the side reservoirs of grease increases with speed, bleeding increases, and the replenishment of grease and its bled oil also takes place more often. Such effect was not observed in the experiments due to their short duration (20 h). High base oil viscosity reduces replenishment and oil bleeding due to a reduction of oil mobility [62]. Increasing half-contact width requires more time for replenishments to the center of the contact [17].

As the time further progresses and stage (iv) is reached, grease properties and formulation effect on film formation become relevant. Long-term tests (100 h) were performed with full deep groove ball bearing 6209-2Z/C3 at constant axial load and rotational speed for six lubricating greases with different thickeners (Cs, L, Lc, Pu) and base oil (M, E, PAO, SS) types. Grease rheological parameters, shear stability, and bleeding properties were all different. The measured film thickness results clearly showed that lubricating greases with low shear stability and high oil bleeding were able to replenish the contact within the tested time, and therefore to present higher film thickness values, which were closer or higher to the oil fully flooded film thickness prediction. Grease shear aging caused an increase in oil separation and a decrease in the thickener particle size. This led to a reduction of the yield stress which enhanced the mobility of the grease. Furthermore, smaller thickener particles contribute the most to film thickness enhancement as shown by Eq. (2). Other researchers also observed improved replenishment for lubricating grease with a higher oil-bleed rate, lower viscosity, consistency, and mechanical stability [50, 55, 69]. From these results, it is verified that replenishment at stage (iv) is mainly driven by oil bleeding and grease shear aging, being the other aforementioned effects secondary [50]. Although 100 h may be long for a lab test, it is extremely short compared to the expected life of rolling bearings. Therefore, grease quality should not be associated with low mechanical stability and high oil bleeding rate, since it may cause severe starvation in the long run due to grease leakage [50]. Film thickness variations during stages (iv) and (v) have been only qualitatively presented and numerical models to predict grease contact replenishment are not available yet.

The schematic film thickness curve presented in **Figure 3** changes with the operating conditions and grease type. As temperature increases, the decay rate decreases leading to later starvation and better replenishment due to decreased consistency, reduced bled oil viscosity, and improved oil bleeding [50]. The scatter on the results increases significantly at higher temperatures, which indicates the thickener lumps are crossing the contact at a higher rate. Load reduction reduces the Hertzian half-contact width which slows down the onset of starvation [50]. Ball

spin was also shown to improve replenishment by dragging the grease and bleed-oil of the sidetrack into the contact inlet [55].

In terms of grease formulation, some thickeners produce higher film thickness values and enter the contact much more often than others at stage (iv), without considering replenishment effects. Here, the same trends observed for fully flooded conditions were detected. In general, thickeners that enhance grease film thickness the most are as follows—polypropylene (P) > calcium (C) > polyurea (Pu) \approx lithium (L) [28, 33, 34, 39, 68, 70].

Friction measurements performed under starved conditions in a ball-on-disc test rig at entrainment speeds higher than the transition thickness (h^t) also present 05 stages, as shown in **Figure 4**—(i) at the very beginning of the test (first seconds) the contact is fully supplied with grease, and the same trends reported in Section 2.1 are observed, that is, lubricating greases present similar coefficient of friction than their base oils under fully flooded conditions; (ii) as time progresses coefficient of friction increases quickly (few minutes); (iii) after that the friction coefficient increase rate slows considerably, (iv) up to the moment, it reaches a stable value that remains for a long period of time (hours); (v) and finally the grease is gradually expelled from the contact and friction tends to asperities friction values (dry CoF).

The coefficient of friction curve presented in **Figure 4** changes with the operating conditions and grease type. In terms of operating conditions, by increasing the entrainment speed, the CoF grows quicker and its value in the stabilization zone is higher than that at lower entrainment speeds, which should be due to stronger starvation. The same effect is observed for tests performed at higher SRR values, but in this case, the value of the CoF in the stabilization zone is even higher. On the other hand, at higher operating temperatures lower CoF values are observed due to the decrease in the viscous friction and better replenishment due to the reduced grease consistency and improved oil bleeding [68]. Lewis et al. [71] showed the time required to reach stage (v) (dry coefficient of friction) depends more on samples' roughness than on grease properties. Samples with low roughness ($R_a < 2 \mu\text{m}$) reach stage (v) up to four times later than samples with high roughness ($R_a > 3 \mu\text{m}$).

In terms of grease formulation, it is known that lubricating greases formulated with mineral and high viscous oils produce higher friction than the ones formulated

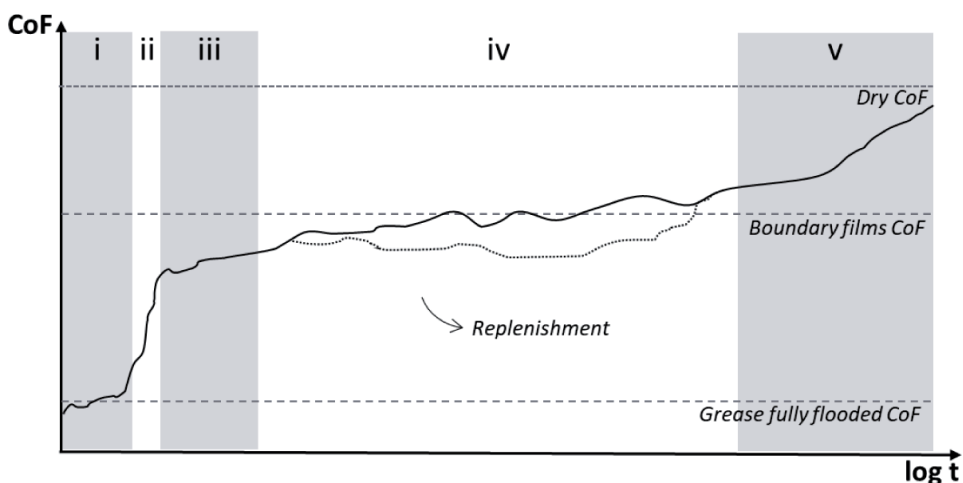


Figure 4. Typical coefficient of friction versus time curves for lubricating grease under starved lubrication and low SRR.

with synthetic and low viscous oils [14, 72]. When it comes to the thickener, similar to fully flooded lubrication, lower friction values are observed for polypropylene (P) > polyurea (Pu) > lithium (L) > calcium (C). This occurs because the coefficient of friction is a response of the boundary films, which are mainly formed by sheared thickener. As discussed in Section 2.1, some thickener types present high friction properties, while others present low friction properties, such as calcium and polypropylene, respectively.

Analogously to the closure of Section 2.1, grease selection for applications that run under starved lubrication should not blindly follow the procedure defined by ISO 281, since it does not take into account the thickener type, nor critical grease properties such as oil bleeding. In fact, the starved film thickness, before any mechanism of grease/bleed-oil supply to the contact takes place, does not present any trend with the base oil viscosity, but with grease formulation (thickener and base oil type). Higher film thickness values are observed for synthetic oils thickened with polypropylene, lithium complex, or polyurea [50]. These formulations also present lower friction values and higher efficiency. The maintenance of this film depends on contact replenishment, which in turn depends on grease rheological properties, shear stability, and bleeding rate. All these properties can be changed by playing with the thickener content and grease manufacturing process. However, at the moment, there are no tools or models to provide end users with optimum values of these properties for specific applications. The general advice is to look for the unworked and worked grease consistency (related to its rheology and mechanical stability), the oil bleeding rate, thickener type, and operating temperature of lubricating greases that operate successfully in similar applications to establish reference values. Alternatively, bearing manufacturers could be contacted to assist user needs.

3. The role of grease components in sliding contacts

Grease is used in a wide range of applications. Its usage in components that operate under prevailing sliding conditions, such as railway lubrication, represents just a small fraction of grease usage. This explains the short amount of systematic research on grease lubricated sliding contacts. In these conditions, lubricating greases are not prone to form full films, thus boundary and mixed lubrication regimes are expected. Therefore, the study of wear and friction is of particular interest and reported in the following sections considering fully flooded and starved contacts.

3.1 Fully flooded conditions

Under sliding conditions, lubricating greases are mainly evaluated in four-ball machines or pin-on-disc test rigs under unidirectional or reciprocating motions. These types of tests are, in general, not instrumented to measure film thickness, although electric methods (capacitance, resistance) are sometimes employed as an indirect measure of film thickness. Alternatively, the lubrication regime is qualitatively evaluated based on friction and wear analysis.

Figure 5 shows the coefficient of friction as a function of time in a grease-lubricated pin-on-disc test under low contact pressures. The general trend is high friction at the very beginning of the test (region i) to overcome the static condition followed by a stable regime (ii) in which some scatter is observed due to thickener crossing the contact and eventual asperity contact since mixed lubrication regime is expected. At this stage, if the grease supply fails, a rapid increase in friction is

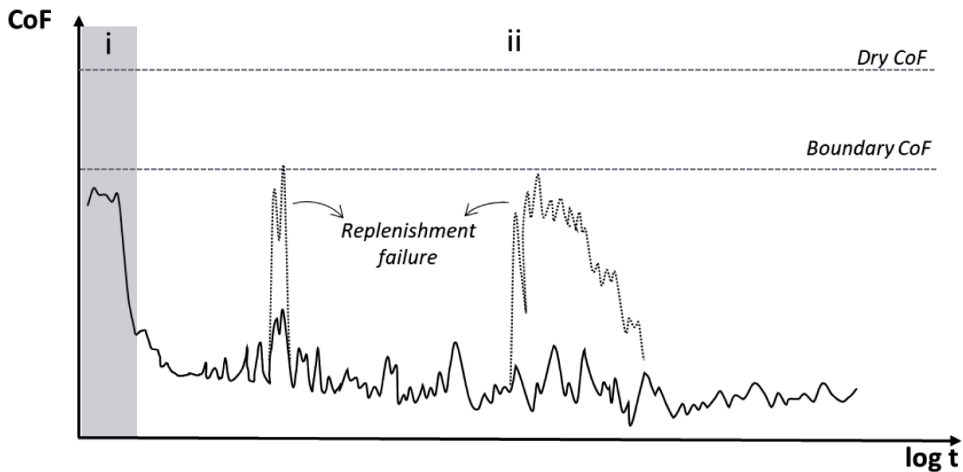


Figure 5. Typical coefficient of friction versus time curves for lubricating grease under fully flooded lubrication and pure sliding condition.

observed. Here, the coefficient of friction results from shearing a thin layer of grease, mostly composed of thickener deposited onto the surfaces, and/or reactions films composed by additives (boundary CoF). These trends are observed for lubricating greases whatever is their formulation [18, 19]. Even with constant grease supply to the contact, sometimes replenishment failure occurs because the parallel contacting surfaces are not prone to hydrodynamic film formation.

Figure 6 shows a schematic representation of the coefficient of friction as a function of the Hersey parameter under pure sliding conditions for two grease types. These trends were obtained from the pin-on-disc evaluation of six in-house fully formulated NLGI 2 greases formulated with a commercial additive package for EP application and mineral base oil. The two most common thickener types, lithium and calcium, and three base oil viscosities, 50 mm²/s, 200 mm²/s e 500 mm²/s, were used in the formulations. More details about these lubricating greases can be found in [15]. The pin-on-disc tests were performed under a constant sliding speed of

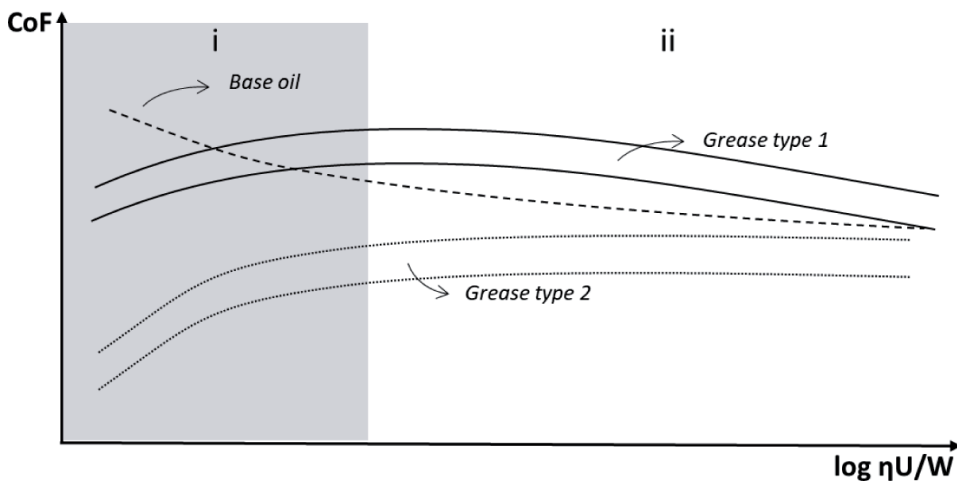


Figure 6. Typical coefficient of friction versus Hersey number curves for lubricating grease under fully flooded lubrication and pure sliding condition.

0.5 m/s and contact pressure of 2.5 MPa for 60 min. The flat-tip pins and discs were manufactured from pearlitic steel with a hardness of 360 HV and composite roughness of $S_q = 1.2 \mu\text{m}$ [19]. Different from the observations from prevailing rolling conditions the coefficient of friction does not vary significantly with the product of speed and viscosity [19, 45]. This occurs because pin-on-disc tests performed under pure sliding conditions are not prone to build thick films due to their parallel surfaces. The surfaces are either parallel from the beginning of the test when flat-tip pins are used, or they quickly turn flat and parallel due to wear when round-tip pins are used [18]. Therefore, the usual lubrication regimes are boundary (stage i) and early mixed lubrication (stage ii) for usual engineering surface finishing and contact pressure. In the case of very smooth surfaces, low loads, high speeds, and fully flooded conditions, the coefficient of the friction may resemble the one from **Figure 2**. Although, in general, the effect of speed, viscosity, and load on friction coefficient is rather small [19, 22, 73].

Under boundary lubrication conditions (stage i), the film is composed mainly of thickeners under moderate loads, and therefore, the coefficient of friction depends on its properties. In this situation, lubricating greases thickened with calcium (grease type 1) are used to present higher friction values than greases thickened with lithium (grease type 2) [7, 8, 19]. This is also observed under prevailing rolling conditions and fully flooded lubrication [74]. As the base oil viscosity or speed increases (region ii) the effect of thickener on the coefficient of friction becomes slightly less relevant, as in this region the film is also composed of base oil. The friction variation from regions i to ii is small and depends pretty much on the grease formulation. Lithium thickened greases in general present lower shear resistance than their corresponding base oil and, therefore, the coefficient of friction is lower when the film is mostly formed by thickener (low Hersey number) [7, 8, 19]. Calcium thickened greases, on the other hand, in general present similar shear resistance to its base oil, and therefore, the coefficient of friction varies little as a function of the film composition (%thickener + %oil) [7, 8, 19].

Figure 7 shows the sum of the mass loss of the tested pins and discs as a function of the Hersey parameter under fully flooded lubrication and pure sliding conditions. Analogously to **Figure 6** the zones i and ii correspond to the boundary and early mixed lubrication regime, respectively. The dominant wear mechanism under these operating conditions is two-body abrasion since the adhesive forces between

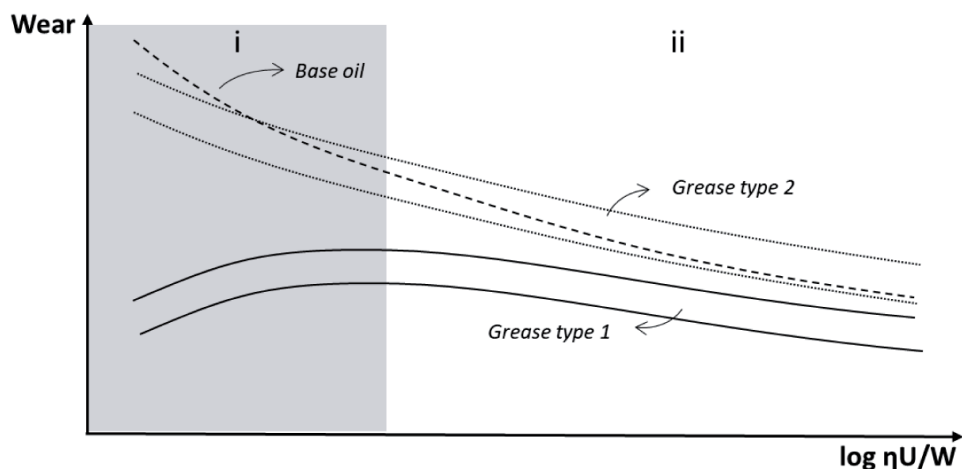


Figure 7. Typical mass loss versus Hersey number curves for lubricating grease under fully flooded lubrication and pure sliding condition.

contacting asperities are reduced substantially by the introduction of grease [18]. In these conditions calcium greases (grease type 1) present lower wear than lithium greases (grease type 2), as also observed by [7]. As the base oil viscosity increases (region ii), the effect of thickener on wear becomes less relevant and similar wear values are observed for both greases, as in this region the film is also composed of base oil. The wear variation from regions i to ii depends on grease formulation. Lithium thickened greases present wear reduction due to a slight increase in film thickness, which reduces the contact severity. At region i, wear is quite high because of the poor anti-wear properties of lithium thickener [15, 75]. Calcium-thickened greases present similar wear values for the whole range of the Hersey number. This occurs because as viscosity decreases (transition from regime ii to regime i) the film composition becomes dominated by calcium thickener that minimizes wear under boundary lubrication due to its well-known anti-wear properties [8, 76].

3.2 Starved conditions

Figure 8 shows the coefficient of friction as a function of time under pure sliding conditions and starved lubrication. Three-dashed lines representing the coefficient of friction measured without lubrication (dry), the coefficient of friction resulting from tribofilms derived from thickener and/or additives (boundary CoF), and the coefficient of friction measured when grease supply to the contact is abundant (grease fully flooded lubrication) are also presented. Besides, the curve is divided into five stages—(i) at the beginning of the test, static friction is overcome and the lubricant between the contacting bodies accommodates, thus high friction values are observed. This period lasts a few seconds and it is followed by (ii) very low friction values, which are equivalent to the fully flooded lubrication presented in **Figure 5** since at this stage, there is lubricant enough to supply the contact. This stage also used to last a few seconds [77]; (iii) as time progresses starvation proceeds and the coefficient of friction increases up to its stabilization at stage (iv). In this stage, that last several hours [78], the coefficient of friction, which is governed by a thin layer of highly worked grease deposited in the track and/or tribofilms derived from chemical reactions between additives and the surface, changes little with time, and it may decrease or increase very slowly unless replenishment occurs and the

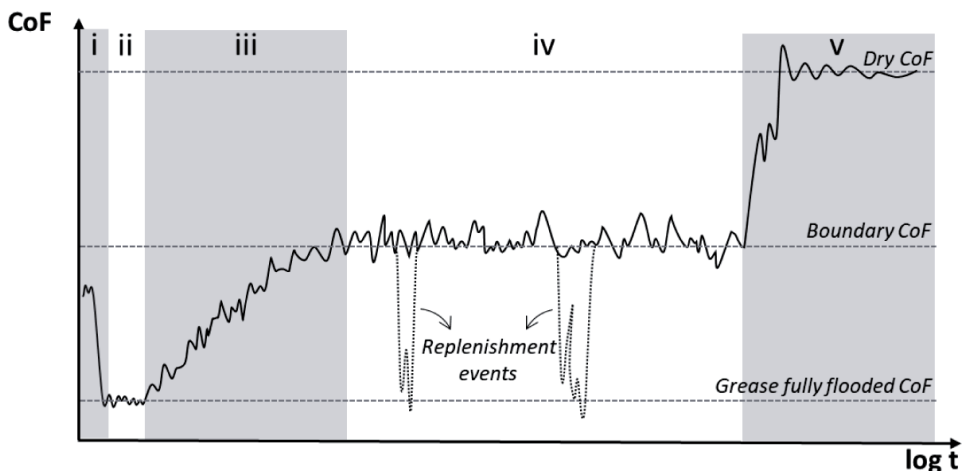


Figure 8. Typical coefficient of friction versus time curves for lubricating grease under starved lubrication and pure sliding condition.

coefficient of friction reduces considerably (dotted lines); (v) at some point the tribofilm derived from thickener and/or additives wears off and the coefficient of friction quickly reaches dry friction values, that phenomena are usually reported as film breakdown [78]. The duration, or even the existence, of each stage presented in **Figure 8** depends on the competing lubricant supply and loss mechanisms, as well as the formation of reaction films. Therefore, some greases might not present the boundary stage (iv) and quickly reach asperities contact (v), while others might present several replenishment cycles before reaching asperities contact. The transition from stages (ii) to (iv) and from stages (iv) to (v) are defined as lubricant film breakdown [77, 78], although the related phenomena are different. The transition from stages (ii) to (iv), defined from here on as lube film breakdown, describes the starvation process, that is, the progressive absence of lubricant supply to the contact. The transition from stages (iv) to (v), defined from here on as boundary film breakdown, described the wear process of the boundary film formed from physical and or chemical interaction of thickener and additives with the contacting surfaces.

The schematic film thickness curve presented in **Figure 8** changes with operating conditions and grease type. In terms of operating conditions, a low coefficient of friction is observed for a longer period of time (stage ii) for the greater initial amount of lubricating grease, lower contact pressure, and higher sliding speed [77]. According to Hersey number and Stribeck curve, higher load (thus higher contact pressure) and lower speed will generate nominal thinner films (**Figures 1 and 2**), leading to premature lube film breakdown and a high coefficient of friction. This, however, only occurs at very low speeds. At high speeds, a significant decrease in load carrying capacity occurs due to the effect of frictional heating in the contact zone, causing an appreciable decrease in effective lubricant viscosity [79], and due to low replenishment as a result of grease being pushed away from the contact and having less time for the film to recover [62]. Lundberg [80] showed that low roughness increases the period in stage (ii), which is in agreement with the observations under prevailing rolling conditions [71]. In this case, low roughness indicates thicker film, and therefore, a larger period of time to occur lube film breakdown. It is important to point out the replenishment events presented in **Figure 8** occur less often under pure sliding than under rolling conditions, mainly because grease or bleed-oil that might flow into the contact is more likely to be ejected than to find its way back in between the contact bodies due to the flat contact geometry. Besides that, the influence of operating conditions on the replenishment events follows the ones described in Section 2.2.

In terms of grease formulation, base oil nature, thickener type, and additive package play a major role in the starved coefficient of friction. For lubricating greases formulated with the same additive package, calcium greases present a higher coefficient of friction and reach stage (iv) faster than lithium greases, just like observed in **Figures 2 and 6**, and also for the same reasons. At stage (iv), calcium greases continue to present higher friction values than lithium greases, however, the tribofilms derived from calcium thickened greases last much longer. Considering the goal of lubricating greases is to prevent or minimize the chances to reach stage (v), associate with severe wear [78], and the time between stages (i) and (iii) used to be just a fraction of the time spent in stage (iv), one can conclude that calcium greases, in particular calcium sulfonate greases, present higher performance than lithium greases under concentrated sliding contacts. Therefore, for starved sliding contacts, lubricating greases that are highly reactive to the surface are used to present better performance [7, 8].

Mass loss of pins and discs under pure sliding conditions and starved lubrication depends on the five stages presented in **Figure 8**. The mass loss might be quite high at stage (i), but it drops rapidly and remains low at stage (ii). At these stages, the

surfaces are partially separated and the dimensional wear coefficient used to be less than $k \approx 10^{-9} \text{ mm}^3 (\text{N m})^{-1}$. During this period the separation might increase due to surface smoothing, which keeps the wear under low levels. At stages (iii) and (iv), the mass loss is higher but still acceptable for many engineering applications— $k \approx 10^{-6}$ to $10^{-8} \text{ m}^3 (\text{N m})^{-1}$. At these stages, there is a thin film of lubricant material (thickener and/or additives) adsorbed to the surface that controls wear. Since these films are sparse and do not cover the whole contacting area, asperities contact is expected. In general, stages (i)–(iv) are oxidative in character, although some adhesive mechanisms related to unprotected asperity contacts might occur. As time progresses, these films are worn off up to the moment the metallic contact takes place, generating high wear rates, with dimensional wear coefficient typically greater than $k \approx 10^{-5} \text{ mm}^3 (\text{N m})^{-1}$. High loads and high speeds increase the severity of the contact leading to premature scuffing (stage v). Wear resistance in pure sliding conditions depends on the likelihood of thickener and additives to get onto the contacting surfaces and form tribofilms. This is achieved using lubricating greases with high chemical affinity with the contact bodies and small size thickener particles, such as greases thickened with calcium sulfonate, formulated with ester base oil, and additives with high load-carrying capacity based on sulfur and phosphorus.

4. Conclusions

Lubricating greases play a significant role in the component's life and efficiency. In order to maximize this role, they must meet specific performance requirements. However, defining such specifications is challenging because they are system-dependent and their simulation in the laboratory might require elaborate equipment and tests with a long duration (>100 h).

Under prevailing rolling conditions and fully flooded lubrication, the current practice, which works reasonably well, is to predict film thickness using traditional EHL theory for oil lubrication (Eq. (1)) when the operating conditions lead to film thickness higher than the transition film thickness (h^t). Although an improved film thickness equation for grease-lubricated contacts that account for the thickener effect (Eq. (2)) was developed and more accurate results can be achieved. These equations are reliable to predict film thickness in situations in which fully flooded conditions are expected, such as in rolling bearings lubricated by centralized systems or during the first days of operation of sealed for life rolling bearings. Below the transition film thickness (h^t), typically observed in large size bearings running under low rotational speeds, grease and oil behavior differs the most. In this condition, the film thickness can only be predicted based on previous film thickness measurements (Eq. (3)). Due to the costs related to large-size bearings maintenance, further research on film formation below the transition speed is of utmost importance.

When it comes to starved lubrication, which is the operating condition of rolling bearings sealed for life during most of their lifetime, several phenomena occur simultaneously and grease film thickness prediction is challenging. Initially (first few minutes), grease film thickness is larger than the fully flooded base oil, indicating fully flooded conditions with thickener contribution. At this stage, Eq. (2) can be used to predict grease film thickness. Then film thickness decreases due to starvation (first hour) and remains stable for a few more hours. At this stage, the grease film thickness can be predicted with Eq. (4). At a certain moment, grease film thickness increases again to values similar or higher than its

fully flooded base oil, mostly, due to oil bleeding, and grease shear aging. This stage strongly depends on grease type, particularly on its bleed properties and mechanical stability (rheological behavior). The higher is the bleed rate and the lowest in the mechanical stability the faster grease film recovery is observed. However, it does not mean that a high bleed rate and low mechanical stability properties are desired for lubricating greases since their long-term effects (after 100 h) are not known. This last stage has not been modeled yet because it requires more accurate bleeding and shear aging models to be implemented along with film thickness predictions.

The coefficient of friction prediction depends on grease film thickness and properties (molecular structure). Consequently, all uncertainties around film thickness prediction impact friction. Besides, the need to include the film properties at the high-pressure zone makes it a much more complicated matter. In the case of mixed and boundary lubrication, the role of surface topography and properties on the physicochemical reactions with additives and thickener must be also taken into account. Therefore, the existent numerical models, to predict coefficient of friction, are far less developed than the ones to predict film thickness and still do not take into consideration the role of thickener.

All these challenges related to film thickness and coefficient of friction prediction lead several researchers to evaluate formulations and properties of lubricating greases that promote high film thickness and low coefficient of friction over a wide range of operating conditions. The results point out for lubricating greases formulated with low viscosity synthetic oils, in particular PAO, thickened with polypropylene, polyurea, or lithium. These combinations, in particular PAO with polypropylene or polyurea, also lead to long grease life at moderate temperatures [81]. Obviously, the grease properties such as oil bleeding and mechanical stability, which can be adjusted during the manufacturing process, must match the application. Those general trends do not qualify PPAO, PuPAO, or LPAO as a multiuse grease. In fact, for specific situations, that is, very low speeds, high loads, high temperature, and humid environment, over based calcium sulfonate complex greases, are the best option due to their high dropping point, excellent EP/AW characteristics, and water resistance [81].


Under prevailing sliding conditions, the lubrication regime for usual engineering surfaces is mainly boundary and mixed lubrication, whatever the contact is fully flooded or starved since the contact conditions are less prone to film formation. Thus, the research lies mostly on the effect of grease type and properties on wear and friction, instead of film thickness. Comparatively to prevailing rolling conditions, the effect of base oil viscosity, speed, and load on the coefficient of friction is rather small since lubrication regime transitions are less likely to occur. In this situation, in which nominal specific film thickness is low, the film that partially separates the surfaces is mainly composed of grease thickener and/or additives, which primarily govern the friction and wear response of the system. Thickener types used to be qualified by their thermomechanical stability, water resistance, load carrying capacity, lubricity (friction), additive response, and compatibility with other greases by grease manufacture. As discussed earlier, as grease properties depend on their constituents, interaction, and the manufacturing process, the thickener properties do not necessarily translate the grease properties. Still, in the large majority of the evaluations reported in the literature, calcium greases present higher load carrying capacity (wear resistance) but slightly lower lubricity (friction) than lithium greases in tribological tests, which is in agreement with the general classification provided by grease suppliers. The durability of the films formed by thickeners and/or additives on the surface is still an open topic that requires further investigation.

Author details

Tiago Cousseau
Federal University of Technology, Curitiba, Paraná, Brazil

*Address all correspondence to: tcousseau@utfpr.edu.br

IntechOpen

© 2021 The Author(s). Licensee IntechOpen. This chapter is distributed under the terms of the Creative Commons Attribution License (<http://creativecommons.org/licenses/by/3.0>), which permits unrestricted use, distribution, and reproduction in any medium, provided the original work is properly cited. 

References

- [1] ASTM standard D288-61. Definitions of terms relating to petroleum (withdrawn 1980). 1978
- [2] Lugt PM. A review on grease lubrication in rolling bearings. *Tribology Transactions*. 2009;**52**(4):470-480
- [3] Salomonsson L, Stang G, Zhmud B. Oil/thickener interactions and rheology of lubricating greases. *Tribology Transactions*. 2007;**50**(3):302-309
- [4] Kaperick JP. Timken OK load—media bias? A comparison of Timken response to similar additive systems in both grease and oil formulations. In: *NLGI Spokesman-Including NLGI Annual Meeting*. Vol. 71. Kansas City, Mo: National Lubricating Grease Institute; 2007. No. 5. pp. 13-17
- [5] Franco JM, Delgado MA, Valencia C, Sánchez MC, Gallegos C. Mixing rheometry for studying the manufacture of lubricating greases. *Chemical Engineering Science*. 2005;**60**(8-9): 2409-2418
- [6] Xu N, Li W, Zhang M, Zhao G, Wang X. New insight to the tribology-structure interrelationship of lubricating grease by a rheological method. *RSC Advances*. 2015;**5**(67):54202-54210
- [7] Fan X, Li W, Li H, Zhu M, Xia Y, Wang J. Probing the effect of thickener on tribological properties of lubricating greases. *Tribology International*. 2018; **118**:128-139
- [8] Xia Y, Wen Z, Feng X. Tribological properties of a lithium-calcium grease. *Chemistry and Technology of Fuels and Oils*. 2015;**51**(1):10-16
- [9] Richardson AD, Evans MH, Wang L, Ingram M, Rowland Z, Llanos G, et al. The effect of over-based calcium sulfonate detergent additives on white etching crack (WEC) formation in rolling contact fatigue tested 100Cr6 steel. *Tribology International*. 2019;**133**: 246-262
- [10] Popinceanu NG, Gafițanu MD, Crețu SS, Diaconescu EN, Hostiu LT. Rolling bearing fatigue life and EHL theory. *Wear*. 1977;**45**(1):17-32
- [11] Raj A, Sarkar C, Pathak M. Thermal and multiphase flow simulations of polytetrafluoroethylene-based grease flow in restricted geometry. *Proceedings of the Institution of Mechanical Engineers, Part J: Journal of Engineering Tribology*. 2022;**236**(1):80-89. DOI: 10.1177/13506501211009406
- [12] Hamedi N, Westerberg L-G. On the deformation of fibrous suspensions. In: *Nordic Rheology Conference*; Gothenburg, Aug 21–23, 2019. Vol. 27. Sweden: Nordic Rheology Society; 2019
- [13] Cyriac F, Lugt PM, Bosman R, Padberg CJ, Venner CH. Effect of thickener particle geometry and concentration on the grease EHL film thickness at medium speeds. *Tribology Letters*. 2016;**61**(2):18
- [14] De Laurentis N, Kadiric A, Lugt P, Cann P. The influence of bearing grease composition on friction in rolling/sliding concentrated contacts. *Tribology International*. 2016;**94**:624-632
- [15] Biazon L, Ferrer BP, Toro A, Cousseau T. Correlations between rail grease formulation and friction, wear and RCF of a wheel/rail tribological pair. *Tribology International*. 2021;**153**: 106566
- [16] Kanazawa Y, Sayles RS, Kadiric A. Film formation and friction in grease lubricated rolling-sliding non-conformal contacts. *Tribology International*. 2017; **109**:505-518
- [17] Cen H, Lugt PM. Replenishment of the EHL contacts in a grease lubricated

- ball bearing. *Tribology International*. 2020;**146**:106064
- [18] Sundh J, Olofsson U, Sundvall K. Seizure and wear rate testing of wheel-rail contacts under lubricated conditions using pin-on-disc methodology. *Wear*. 2008;**265**(9-10):1425-1430
- [19] Ferrer BP. Avaliação em laboratório do efeito da formulação e das propriedades de graxas lubrificantes no desempenho tribológico do contato roda-trilho [Master's thesis]. Parana, Brazil: Universidade Tecnológica Federal do Paraná; 2020
- [20] Braun J, Omeis J. Chapter 6—Additives. In: Mang T, Dresel W, editors. *Lubricants and Lubrication*. Weinheim, Germany: John Wiley & Sons; 2007
- [21] Kaperick JP. Timken OK load—Media bias? A comparison of Timken response to similar additive systems in both grease and oil formulations. *NLGI Spokesman*. 2007;**71**(5):13-17
- [22] Nabhan A, Rashed A, Ghazaly NM, Abdo J, Haneef M. Tribological properties of Al₂O₃ nanoparticles as lithium grease additives. *Lubricants*. 2021;**9**(1):9
- [23] Lugt PM. *Grease Lubrication in Rolling Bearings*. The Atrium, Southern Gate, Chichester, West Sussex, United Kingdom: John Wiley & Sons; 2012
- [24] Fischer D, Jacobs G, Stratmann A, Burghardt G. Effect of base oil type in grease composition on the lubricating film formation in EHD contacts. *Lubricants*. 2018;**6**(2):32
- [25] Hamrock BJ, Dowson D. Isothermal elastohydrodynamic lubrication of point contacts: Part III—Fully flooded results. *Journal of Tribology*. 1977;**99**(2):264-275
- [26] Cen H, Lugt PM, Morales-Espejel G. Film thickness of mechanically worked lubricating grease at very low speeds. *Tribology Transactions*. 2014;**57**(6):1066-1071
- [27] Gonçalves D, Graça B, Campos AV, Seabra J, Leckner J, Westbroek R. On the film thickness behaviour of polymer greases at low and high speeds. *Tribology International*. 2015;**90**:435-444
- [28] Cousseau T, Graça B, Campos A, Seabra J. Grease aging effects on film formation under fully-flooded and starved lubrication. *Lubricants*. 2015;**3**(2):197-221
- [29] Kanazawa Y, De Laurentis N, Kadiric A. Studies of friction in grease-lubricated rolling bearings using ball-on-disc and full bearing tests. *Tribology Transactions*. 2020;**63**(1):77-89
- [30] Morales-Espejel GE, Lugt PM, Pasaribu HR, Cen H. Film thickness in grease lubricated slow rotating rolling bearings. *Tribology International*. 2014;**74**:7-19
- [31] Goncalves D, Cousseau T, Gama A, Campos AV, Seabra JH. Friction torque in thrust roller bearings lubricated with greases, their base oils and bleed-oils. *Tribology International*. 2017;**107**:306-319
- [32] Vengudusamy B, Enekes C, Spallek R. On the film forming and friction behaviour of greases in rolling/sliding contacts. *Tribology International*. 2019;**129**:323-337
- [33] Cann PM, Williamson BP, Coy RC, Spikes HA. The behaviour of greases in elastohydrodynamic contacts. *Journal of Physics D: Applied Physics*. 1992;**25**(1A):A124
- [34] Couronné ID, Vergne P, Mazuyer D, Truong-Dinh N, Girodin D. Effects of grease composition and

- structure on film thickness in rolling contact. *Tribology Transactions*. 2003; **46**(1):31-36
- [35] Gonçalves D, Vieira A, Carneiro A, Campos AV, Seabra JH. Film thickness and friction relationship in grease lubricated rough contacts. *Lubricants*. 2017; **5**(3):34
- [36] Williamson BP. An optical study of grease rheology in an elastohydrodynamic point contact under fully flooded and starvation conditions. *Proceedings of the Institution of Mechanical Engineers, Part J: Journal of Engineering Tribology*. 1995; **209**(1):63-74
- [37] De Laurentis N, Cann P, Lugt PM, Kadiric A. The influence of base oil properties on the friction behaviour of lithium greases in rolling/sliding concentrated contacts. *Tribology Letters*. 2017; **65**(4):1-6
- [38] Roman C, Valencia C, Franco JM. AFM and SEM assessment of lubricating grease microstructures: Influence of sample preparation protocol, frictional working conditions and composition. *Tribology Letters*. 2016; **63**(2):1-2
- [39] Cen H, Lugt PM, Morales-Espejel G. On the film thickness of grease-lubricated contacts at low speeds. *Tribology Transactions*. 2014; **57**(4):668-678
- [40] Günsel S, Korček S, Smeeth M, Spikes HA. The elastohydrodynamic friction and film forming properties of lubricant base oils. *Tribology Transactions*. 1999; **42**(3):559-569
- [41] Spikes H. Basics of EHL for practical application. *Lubrication Science*. 2015; **27**(1):45-67
- [42] Vengudusamy B, Enekes C, Spallek R. EHD friction properties of ISO VG 320 gear oils with smooth and rough surfaces. *Friction*. 2020; **8**(1):11
- [43] Wikström V, Höglund E. Starting and steady-state friction torque of grease-lubricated rolling element bearings at low temperatures—Part I: A parameter study. *Tribology Transactions*. 1996; **39**(3):517-526
- [44] Wikström V, Höglund E. Starting and steady-state friction torque of grease-lubricated rolling element bearings at low temperatures—Part II: Correlation with less-complex test methods. *Tribology Transactions*. 1996; **39**(3):684-690
- [45] Cousseau T, Graça BM, Campos AV, Seabra JH. Influence of grease formulation on thrust bearings power loss. *Proceedings of the Institution of Mechanical Engineers, Part J: Journal of Engineering Tribology*. 2010; **224**(9):935-946
- [46] Yamamoto M, Imai J. Development of grease focusing on improved energy efficiency. *NLGI Spokesman*. 2014; **78**(4):18-29
- [47] Cann P. Greases Film Thickness and Friction in EHL Contacts. *WTC* 159-164. 2001
- [48] Delgado MA, Franco JM, Kuhn E. Effect of rheological behaviour of lithium greases on the friction process. *Industrial Lubrication and Tribology*. 2008; **60**(1):37-45
- [49] Guillermo ME. Using a friction model as an engineering tool. *Evolution SKF*. 2006; **2**:27-30
- [50] Zhou Y, Bosman R, Lugt PM. An experimental study on film thickness in a rolling bearing for fresh and mechanically aged lubricating greases. *Tribology Transactions*. 2019; **62**(4):557-566
- [51] Zhang X, Glovnea R. Grease film thickness measurement in rolling bearing contacts. *Proceedings of the Institution of Mechanical Engineers*,

- Part J: Journal of Engineering Tribology. 2021;235(7):1430-1439
- [52] Ward P, Leveille A, Frantz P. Measuring the EHD film thickness in a rotating ball bearing. In: Proc. 39th Aerospace Mechanisms Symposium. Vol. 107. NASA, Hanover, MD; 2008
- [53] Cen H, Lugt PM. Film thickness in a grease lubricated ball bearing. *Tribology International*. 2019;134:26-35
- [54] Baly H, Poll G, Cann PM, Lubrecht AA. Correlation between model test devices and full bearing tests under grease lubricated conditions. In: IUTAM Symposium on Elastohydrodynamics and Micro-Elastohydrodynamics. Dordrecht: Springer; 2006. pp. 229-240
- [55] Cann PM, Lubrecht AA. Bearing performance limits with grease lubrication: The interaction of bearing design, operating conditions and grease properties. *Journal of Physics D: Applied Physics*. 2007;40(18):5446
- [56] Cousseau T, Graça B, Campos A, Seabra J. Friction and wear in thrust ball bearings lubricated with biodegradable greases. *Proceedings of the Institution of Mechanical Engineers, Part J: Journal of Engineering Tribology*. 2011;225(7):627-639
- [57] Muennich HC, Gloeckner HJ. Elastohydrodynamic lubrication of grease-lubricated rolling bearings. *ASLE Transactions*. 1980;23(1):45-52
- [58] Lugt PM, Velickov S, Tripp JH. On the chaotic behavior of grease lubrication in rolling bearings. *Tribology Transactions*. 2009;52(5):581-590
- [59] Van Zoelen MT, Venner CH, Lugt PM. Free surface thin layer flow on bearing raceways. *ASME Journal of Tribology*. 2008;130(2):021802
- [60] Gershuni L, Larson MG, Lugt PM. Lubricant replenishment in rolling bearing contacts. *Tribology Transactions*. 2008;51(5):643-651
- [61] Astrom H, Ostensen JO, Hoglund E. Lubricating grease replenishment in an elastohydrodynamic point contact. *ASME Journal of Tribology*. 1993;115(3):501-506
- [62] Jacod B, Pubilier F, Cann PM, Lubrecht AA. An analysis of track replenishment mechanisms in the starved regime. In: *Tribology Series*. Vol. 36. Amsterdam, The Netherlands: Elsevier; 1999. pp. 483-492
- [63] Cann PM, Lubrecht AA. The effect of transient loading on contact replenishment with lubricating greases. In: *Tribology Series*. Vol. 43. Amsterdam, The Netherlands: Elsevier; 2003. pp. 745-750
- [64] Westerberg LG, Höglund E, Lugt PM, Li J, Baart P. Free-surface grease flow: Influence of surface roughness and temperature. *Tribology Letters*. 2015;59(1):1-1
- [65] Baart P, van der Vorst B, Lugt PM, van Ostayen RA. Oil-bleeding model for lubricating grease based on viscous flow through a porous microstructure. *Tribology Transactions*. 2010;53(3):340-348
- [66] Zhang Q, Mugele F, van den Ende D, Lugt PM. A model configuration for studying stationary grease bleed in rolling bearings. *Tribology Transactions*. 2021:1-11. DOI: 10.1080/10402004.2021.1904071
- [67] Zhou Y, Bosman R, Lugt PM. A master curve for the shear degradation of lubricating greases with a fibrous structure. *Tribology Transactions*. 2019;62(1):78-87
- [68] Gonçalves DE, Campos AV, Seabra JH. An experimental study on starved grease lubricated contacts. *Lubricants*. 2018;6(3):82

- [69] Poon SY. An experimental study of grease in elastohydrodynamic lubrication. *Journal of Lubrication Technology*. 1972;**94**:27-34
- [70] Cann PM. Starved grease lubrication of rolling contacts. *Tribology Transactions*. 1999;**42**(4):867-873
- [71] Lewis SR, Lewis R, Evans G, Buckley-Johnstone LE. Assessment of railway curve lubricant performance using a twin-disc tester. *Wear*. 2014;**314**(1-2):205-212
- [72] Brandão JA, Meheux M, Ville F, Seabra JH, Castro J. Comparative overview of five gear oils in mixed and boundary film lubrication. *Tribology International*. 2012;**47**:50-61
- [73] Rieglert J, Kassfeldt E. Performance of environmentally adapted hydraulic fluids at boundary lubrication. In: *Tribology Series*. Vol. 32. Amsterdam, The Netherlands: Elsevier; 1997. pp. 467-473
- [74] Cousseau T, Björling M, Graça B, Campos A, Seabra J, Larsson R. Film thickness in a ball-on-disc contact lubricated with greases, bleed oils and base oils. *Tribology International*. 2012;**53**:53-60
- [75] Yokouchi A, Hokao M, Sugimura J. Effects of soap fiber structure on boundary lubrication of lithium soap greases. *Tribology Online*. 2011;**6**(4): 219-225
- [76] Costello MT. Study of surface films of amorphous and crystalline overbased calcium sulfonate by XPS and AES. *Tribology Transactions*. 2006;**49**(4): 592-597
- [77] Hu Y, Wang L, Politis DJ, Masen MA. Development of an interactive friction model for the prediction of lubricant breakdown behaviour during sliding wear. *Tribology International*. 2017;**110**: 370-377
- [78] Alp A, Erdemir A, Kumar S. Energy and wear analysis in lubricated sliding contact. *Wear*. 1996;**191**(1-2):261-264
- [79] Begelinger A, De Gee AW. Failure of thin film lubrication—A detailed study of the lubricant film breakdown mechanism. *Wear*. 1982;**77**(1):57-63
- [80] Lundberg J. Influence of surface roughness on normal-sliding lubrication. *Tribology International*. 1995;**28**(5):317-322
- [81] Lugt PM. Modern advancements in lubricating grease technology. *Tribology International*. 2016;**97**:467-477

A Review on the Contact Mechanics Modeling of Rough Surfaces in the Elastic Regime: Fundamentals, Theories, and Numerical Implementations

*Farouk Maaboudallah, Mohamed Najah
and Nouredine Atalla*

Abstract

This chapter reviews advanced models for solving the normal contact problem of two elastic bodies with rough boundaries. Starting from the fundamental formulation of Greenwood and Williamson, an extension is proposed with details on the possible algorithmic implementation to consider the interactions between asperities. A second multi-scale-based approach, considering the self-affine nature of the rough surface, also known as Persson's theory, is briefly discussed. As a third method, special attention is given to review the standard Boundary Element Method (BEM). Finally, all the mentioned methods are applied to a rough gold surface measured by Atomic Force Microscope (AFM) and the evolution of the real contact area with loading is analyzed. The aim of this contribution is to present the basic guidelines to tackle the problem of contacting rough surfaces, accounting for the real surface topography.

Keywords: contact mechanics, roughness, elastic contact, true contact area, atomic force microscopy

1. Introduction

Among the most complicated problems in mechanics, there is the contact modeling of rough surfaces where one seeks to predict the stresses, strains, and true contact area. These predictions play a very important role in studying many phenomena such as friction [1], wear [2], thermal [3] and electrical conductivity [4], sealing [5], squeal [6, 7], etc. Understanding the micromechanical characteristics of these phenomena leads to a robust design of mechanical systems by increasing their performances. For example, in micro-systems with brittle behavior such as (i) radio frequency micro-electro-mechanical-systems (RF MEMS) with silicon-to-Silicon (Si-to-Si) contacts [8], (ii) micro-turbines using Si or Polydimethylsiloxane (PDMS)-based micro-valve and [9] (iii) Si-to-Si wafer bonding [10–12], the performances and the reliability of the device rely on the quality of the contact [13–17]. An accurate prediction of the pressure and the true contact area leads to a good

dimensioning of the adhesion forces and thus, to an increase in the reliability of components.

As part of the design process of these systems, the contact problem is addressed by assuming that the contact interfaces are perfectly flat. This assumption neglects the notion of roughness, which often leads to an overestimation of the contact surface and an underestimation of the contact pressure. In reality, every surface, even mirror polished, still exhibits roughness at the micro- and nano-scales. A rough surface can be seen as the superposition of several wavelengths, forming hills (asperities or local maxima) and valleys (local minima), and it is fully described by two statistical functions: (i) the height probability density function (HPDF) and (ii) the power spectral density function (PSDF). The former describes the randomness of the rough surface, while the latter quantifies the contribution of the different wavelengths to the surface topography. Both HPDF and PSDF are widely used to characterize engineering surfaces [18–20] as well as to generate numerically artificial surfaces [21, 22].

When two rough surfaces come in contact, the mechanical load is borne by the top of the highest asperities. Thus, the real contact area is only a small fraction of the nominal area. The first and most popular theory that elucidated this point was made in the 1960s by the pioneers' Greenwood and Williamson (GW) [23]. In such theory, the rough surface is represented by a set of spherically shaped asperities, with the same radius of curvature and whose height varies randomly following a given probability density function. Then, the Hertz theory of one elastic sphere contacting a rigid flat plane is extended to the entire surface. In the same period, Bush et al. [24] proposed a refined model approximately equivalent to its counterpart (i.e. GW theory). The special point with respect to GW theory is that Bush et al. assumed that asperities have a paraboloidal shape. Then, they used the random process theory [25] to describe the statistics of the rough surface. Other models quite similar to those described above can be found in Refs. [26–28]. Using the above theories, it has been found that, at a low squeezing load, the predicted true contact area A increases linearly with the applied load.

The aforementioned contact models assume that all the contacting asperities behave independently. Thus, the interaction between the different contact region are neglected (i.e. each asperity is locally deformed without inducing a displacement of the neighboring asperity). This last assumption is not met for medium to high loading cases (i.e. nearly full contact case) since the contacting asperities become tighter and hence, the contribution of the surface deflections produced by each of them, at the level of the neighboring micro-contacts, becomes significant [29, 30]. On the other hand, O'Callaghan et al. [31] and Hendriks et al. [32] demonstrated experimentally that asperities can interact strongly and even coalesce at low loads questioning the reliability of the classic asperity-based models. To consider the interaction between asperities, authors in the literature have proposed several models based on GW theory. For instance, Paggi and Ciavarella [33, 34] included interaction between asperities by means of semi-analytical modeling to simulate the effect of the bulk. In the same context, Afferrante et al. [35] have introduced a multi-asperity model that takes into account the coalescence between two contacting asperities. Despite all these advanced models, the semi-analytical approach remains very approximate compared to numerical methods such as the finite or the boundary element method [36].

The original GW theory has also been criticized since it deals with special cases where the height distribution follows a Gaussian or exponential distribution. Especially, it is well admitted by the scientific community that the roughness can appear at many scales exactly like the fractal patterns, but down to a wavelength

that corresponds to, perhaps, some lattice constant. The use of GW theory with the “fractal” characteristic has been questioned by many authors, in particular Persson [37]. The latter comes out with an ingenious idea, completely different from the asperity-based model, to tackle the scaling effect on realistic rough surfaces [37–39]. In contrast to asperity-based models, Persson’s theory considers the stress probability distribution as a function of the surface resolution. The idea is to determine the evolution of the contact stress density function when the PSDF is extended to cover a wide frequency range. Initially, the problem is solved by assuming a full-contact assumption (i.e. smooth surfaces assumption) under initial uniform pressure p_0 . Then, step by step, the roughness is added according to the self-affine character carried by the PSDF which leads to the variations in the contact pressure [40]. According to Persson, the contact stress distribution satisfies a diffusion-like equation. Persson’s approach was also criticized by the leaders of the asperity-based models. They argued that Persson’s proof is not rigorous while deriving the diffusion equation [40]. Hence, the predicted contact area, using Persson’s theory, is smaller compared to the available results in the literature.

In parallel with analytical models, several research groups have proposed numerical simulations reproducing the behavior of rough surfaces in contact. Among these methods, there is the finite element method (FEM) introduced for the first time by Hyun et al. [41]. This category of method is free of any assumption. The only disadvantage it presents is the convergence which is related to (i) the numerical treatment (the penalty method for instance) and (ii) the discretization error. Indeed, to have significant results it is necessary that the size of the discretization is much smaller than the shortest wavelength of the rough surface [5]. However, the finest mesh leads to a prohibitive computational cost. The latest point was clearly demonstrated by Yastrebov et al. [36]. It was shown that the numerical error of the discretization depends on two ratios; (i) $\Delta x/\lambda_s$ and (ii) λ_l/L where Δx is the distance between the mesh points, λ_s and λ_l refer to the shortest and the longest wavelength of the surface PSDF, respectively. L is the length of the representative elementary volume (i.e. the simulation box). Authors in [36] argued that previous ratios should tend towards zero for an accurate prediction and a good representation of the mechanical behavior of each asperity. However, if these criteria are no longer met, in particular the second ratio criterion, it is necessary to conduct several stochastic simulations so that the average prediction is relevant. To overcome these drawbacks, authors developed more attractive numerical techniques allowing to discretize only the rough surface but not the bulk. These methods are based on the Green Functions (GF) (fundamental solution) and were able to refine the mesh in order to perform more accurate simulation and thus, predict a reliable contact area—pressure law [42–44]. The first development of efficient Boundary Element Method (BEM) solvers goes back to the 1990s when Brandt et al. [45] suggested the multi-level multi-summation (MLMS) scheme allowing to simulate realistic rough surface within a reasonable computational cost. In the same context, Venner et al. [46] combined the MLMS solver with the full multi-grid (FMG) iteration method to solve elasto-hydrodynamically lubricated contact problem. It should be noted that the coupled scheme MLMS-FMG solver failed to converge when solving the dry contact problem with roughness [47] since the corresponding convergence theorems do not handle problems with multiple inequality constraints. In order to enhance the efficiency of the numerical scheme and to optimize the CPU cost, Polonsky et al. [42] enhanced MLMS solver by using a iteration scheme based on the conjugate gradient (CG) method showing good convergence properties for a 3D rough surface with large numbers of nodes (approximately 10^6 nodes). Nogi et al. [48] and Polonsky et al. [49] have considered the Fast Fourier Transform (FFT) for

solving rough contact problems for both homogeneous and layered solids. They demonstrated that the FFT-based method can increase dramatically the computational speed. Recently, Bemporad et al. [44] introduced the Non-Negative Least Squares (NNLS) algorithm with a suitable warm start based on accelerated gradient projections (GPs). The results in [44] clearly prove that the NNLS-GPs solver is faster than the previously mentioned solvers. It should be noted that the standard BEM is based on the linear elasticity assumption for a homogeneous medium. Hence, it can not handle the contact problem of rough boundaries including geometrical, interfacial, and material nonlinearities such as large deformation, adhesion, or plasticity. Sometimes, BEM can be adjusted to tackle the above-mentioned nonlinearities [50–53] but for convenience in this type of problem, authors preferred FEM instead of BEM [54, 55].

This review paper provides a comprehensive comparison of the above-mentioned models with particular attention to the standard Boundary Element Method (BEM), which is based on the Green functions. The concern of the present study is limited to solve the frictionless rough contact problem of micro-systems with purely brittle behavior (i.e. in the elastic regime). Thus, the chapter is organized as follows. First, we start to recall and describe 4 theories, namely (i) the original GW model in its continuous and discrete form, (ii) the modified GW to take into account interaction between the contacting asperities, (iii) Persson theory, and (iv) the BEM. Then, the methods will be applied to a 1 μm -thick gold rough surfaces. The first one is measured by the atomic force microscopy (AFM) technique while the others are numerically generated using a suitable algorithm taking as an input the statistical functions of the measured Au rough surface (i.e. HDF and PSDF). Finally, the chapter will be closed with an analysis and discussion of the predicted contact area and pressure.

2. Theoretical methods of contact mechanics

2.1 The original Greenwood and Williamson theory

2.1.1 Continuous form

Consider a rigid perfectly smooth plane moving towards a rough surface of an elastic body with a motion δ (see **Figure 1**). In the GW theory, the rough surface is idealized by assuming that all summits (i.e. local maxima) are spherical with the same radius of curvature R . These are referred to as asperities. The height of each asperity is treated as a random variable which follows a given probability law denoted by $h(z)$. The idea of GW theory is to solve the frictionless contact between the rough surface and the rigid flat plan by using the Hertz theory. In fact, for a

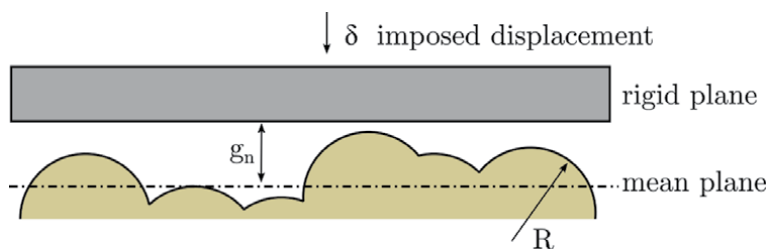


Figure 1. The Greenwood and Williamson theory. The rough surface is described by several spherical asperities of radius R . The function g_n is the normal gap between the rigid plane and the mean one for the rough surface.

spherical elastic body in contact with a rigid plan, Hertz theory gives the exact solution under the framework of the small strains. Let us denote E_1 and E_2 the Young modulus of the rough surface and the rigid plane, respectively. ν_1 and ν_2 are the corresponding Poisson coefficient. The contact area A and load F can be expressed in terms of the rigid body motion δ as,

$$A = \pi R\delta, \quad (1)$$

$$F = \frac{4}{3}E^* R^{1/2}\delta^{3/2}, \quad (2)$$

where E^* refers to the composite Young modulus. It's given by the following expression,

$$\frac{1}{E^*} = \frac{1 - \nu_1^2}{E_1} + \frac{1 - \nu_2^2}{E_2}. \quad (3)$$

For a rigid plan, E^* denotes the plan stress modulus.

Following the configuration in **Figure 1**, there will be contact between the rigid plane and the rough surface if and only if, the height z of any asperity is greater than the normal gap g_n . This event $\{z > g_n\}$ has its own probability that can be written as,

$$\mathcal{P}(\{z > g_n\}) = \int_{g_n}^{+\infty} h(z) dz. \quad (4)$$

Now, if the rough surface has N asperities, then the expected number of contacting asperities n will be,

$$n = N \int_{g_n}^{+\infty} h(z) dz. \quad (5)$$

The total number of asperities N can be expressed as: $A_0 D$, with A_0 is the nominal area of contact and D represents the density of summits.

If we define the displacement of the asperities as $\omega = z - g_n$, then the true contact area A and the expected total load F are given by,

$$A = \pi NR \int_{g_n}^{+\infty} (z - g_n) h(z) dz, \quad (6)$$

and

$$F = \frac{4}{3} NE^* R^{1/2} \int_{g_n}^{+\infty} (z - g_n)^{3/2} h(z) dz. \quad (7)$$

Note that one needs to know A_0 , D , R and the probability density of asperities h to accurately apply the original GW model. While A_0 is obtained from the sample size, the topography parameters (i.e. D , R and h) can not be directly measured. In the same framework, Nayak used the random process theory to statistically evaluate the topography parameters by the means of three spectral moments m_0 , m_2 and m_4 , also known as the mean square height, slope and curvature of the surface [25]. In the case of homogeneous, Gaussian and isotropic rough surfaces, the expression of the spectral moments is given by the following equation:

$$m_i = \int_{-\infty}^{+\infty} q^i \text{PSDF}(q) dq = \frac{1}{L} \int_0^L \left(\frac{d^i z}{dx^i} \right)^2 dx, \quad (8)$$

where L is the surface length, i is a positive integer referring to the order of the moment and q is the wavenumber (i.e. spacial frequency). Since data from measurement tools are discrete, McCool [56] proposed to use the finite difference approximations to evaluate the spectral moments. While m_0 is the variance,

$$m_0 = \frac{1}{N_p - 1} \sum_{i=1}^{N_p} (z_i - \bar{z})^2, \quad (9)$$

the second and fourth spectral moments can be calculated as,

$$m_2 = \frac{1}{N_p - 1} \sum_{i=1}^{N_p-1} \left(\frac{z_{i+1} - z_i}{\Delta} \right)^2, \quad (10)$$

$$m_4 = \frac{1}{N_p - 2} \sum_{i=1}^{N_p-2} \left(\frac{z_{i+2} - 2z_{i+1} + z_i}{\Delta} \right)^2, \quad (11)$$

with N_p the total sampling points and Δ the sampling length (i.e. $N\Delta = L$) and \bar{z} the mean surface height. Finally, the parameters D , R and h can be obtained using the random process theory as described by Nayak in [25].

2.1.2 Discrete form

GW theory can be rewritten in a discrete form. To do so, let us assume now that each asperity is characterized by its own radius R_i and height z_i . Then, the displacement of the i -th asperity can be expressed using Macaulay bracket as,

$$\omega_i = \langle \delta - (z_M - z_i) \rangle, \quad (12)$$

where z_M is the maximum height of the rough surface. We have $z_M = \max(z_i)$. The true contact area A as well as the expected total load F are given by,

$$A = \pi \sum_{i=1}^N R_i \omega_i, \quad (13)$$

$$F = \frac{4}{3} E^* \sum_{i=1}^N R_i^{1/2} \omega_i^{3/2}. \quad (14)$$

Note that, in the discrete GW formulation, the gap function is given by $g_n = (z_M - \bar{z}) - \delta$ where \bar{z} is the mean plane of the rough surface.

2.2 Greenwood and Williamson model with interaction

The original GW model has been criticized for various reasons. First, in terms of the shape of the asperities, several authors have argued that in reality the asperity has a shape that tends towards a sinusoidal curve. In fact, experimental investigations has clearly shown that a sinusoidal description is more realistic than a circular one [57]. Second, in terms of computational point of view, sinusoidal asperities have

interesting mathematical properties such as continuity and differentiability, which is not the case for the circular ones where stress concentrations occur and therefore, become problematic to tackle the plasticity behavior [58]. Third, with respect to asperities interaction, the GW theory assumes that each asperity deforms in an independent manner leading to an underestimation of the predicted contact pressure.

The main idea of this contribution is take into account the interaction between the asperities. All these developments will be with an asperity of sinusoidal form (see **Figure 2**).

2.2.1 Modified Hertz theory for a single sinusoidal asperity

First, let us recall some basic results within the Hertz theory framework of two contacting bodies: flat surface and a sinusoidal body. The Young and the Poisson ratio for the deformable sinusoidal body are denoted E_1 and ν_1 , respectively. Assuming that a far field displacement δ is applied to the rigid plan. When the contact is activated, the rigid body motion δ will be accommodated by the displacement of the asperity ω and the displacement of the substrate u_z . We write,

$$\delta = \omega + u_z. \quad (15)$$

In Eq. (15), the u_z term can be evaluated analytically [59] or numerically by approaching the displacement of the elastic half-space using curve fitting approach [58]. In this chapter, Boussinesq-like form will be used to compute u_z . It is given by:

$$u_z = \frac{1 - \nu_1^2}{\pi E_1 a} F, \quad (16)$$

where a is the radius of the contact spot and F is the contact load. Note that Eq. (16) is quite similar to the integral formulation of the Boundary Element Method.

Following Johnson work [60], the contact load, F , as well as the compression of the asperity, ω , can be given through,

$$F = \sum_{i=1}^n \frac{4A_i E^* i a^{2i+1} 2 \cdot 4 \dots 2i}{(2i+1) 1 \cdot 3 \dots (2i-1)}, \quad (17)$$

$$\omega = \sum_{i=1}^n \frac{2 \cdot 4 \dots 2i}{1 \cdot 3 \dots (2i-1)} A_i a^{2i}, \quad (18)$$

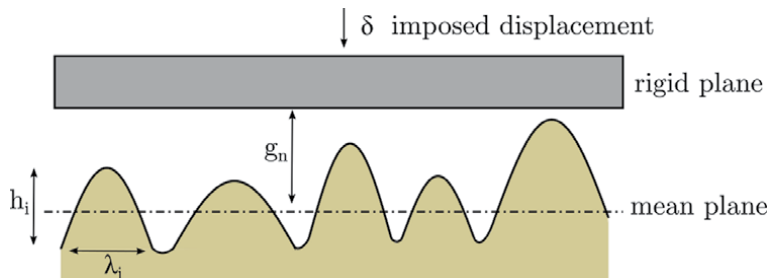


Figure 2. The modified Greenwood and Williamson theory. The rough surface is described by several sinusoidal asperities of a height h_i and and wavelength λ_i . The function g_n is the normal gap between the rigid plane and the mean one for the rough surface.

where E^* refers to the plan stress Young modulus and A_i represents the expansion coefficient of Taylor series at the vicinity of the contacting point. They depend closely on the height h_i and the wavelength λ_i of each asperity (see **Figure 2**).

If we confine ourselves to the second order, the contact load and the compression of the asperity will be written as follows,

$$F = \frac{8}{3}A_1E^*a^3 + \frac{64}{15}A_2E^*a^5, \quad (19)$$

$$\omega = 2A_1a^2 + \frac{8}{3}A_2a^4. \quad (20)$$

Note that when only the first order of the Taylor expansion is considered, Eq. (19) is simplified to Hertz formula given by Eq. (2).

2.2.2 Asperity interaction model

To account for the interactions, the Boussinesq solution will be added to Eq. (15). We write,

$$\delta_i = \omega_i + u_{z,i} + u_{z,i}^j. \quad (21)$$

The additional term, $u_{z,i}^j$, refers to the interaction between the i -th and j -th asperities. We have,

$$u_{z,i}^j = \sum_{\substack{j=1 \\ j \neq i}}^n \frac{1 - \nu_1^2}{\pi E_1 r_{ij}} F_j, \quad (22)$$

where r_{ij} refers to the euclidean norm between the i -th and j -th asperities. $u_{z,i}^j$ may read as the displacement of the i -th asperity caused by the j -th contacting asperity whose contact force is F_j . The latter can be computed using Eq. (19). In this case, the contact radius will stand for the asperity j .

Therefore, the resolution of the contact problem with interaction is to find a set of contact spots radii $a = (a_1, \dots, a_n)$, for each load increment δ_i , that minimizes the objective function $\Theta(a)$ such as:

$$\left\{ \begin{array}{l} \Theta(a) = \frac{1}{2} \sum_{i=1}^n (r_i)^2 = \frac{1}{2} \|r(a)\|_2^2 \\ r_i = \delta_i - 2A_1a_i^2 - \frac{8}{3}A_2a_i^4 - \frac{1 - \nu_1^2}{\pi E_1 a_i} F_i - \sum_{\substack{j=1 \\ j \neq i}}^n \frac{1 - \nu_1^2}{\pi E_1 r_{ij}} F_j \\ F_i = \frac{8}{3}A_1E^*a_i^3 + \frac{64}{15}A_2E^*a_i^5 \\ F_j = \frac{8}{3}A_1E^*a_j^3 + \frac{64}{15}A_2E^*a_j^5 \end{array} \right. \quad (23)$$

Since the problem in Eq. (23) is non linear, Levenberg-Marquardt (LM) algorithm is used to find the contact radii. In fact, the resolution of the contact problem consists in minimizing the objective function $\Theta(a)$ defined in Eq. (23) using an iterative scheme. The global procedure can be split in 7 phases summarized in the following flowchart:

For each contact step do,

1. **Contact detection:** detect all the contacting asperities;
2. **Initialization:** initialize the contact radii vector a_i . If $i = 0$, It can be initialized by 0. Otherwise, it can be warm-started by taking into account the loading history of the previous iteration $i - 1$;
3. **Jacobian and Hessian matrices construction:** compute the Jacobian, \mathbf{J} , and Hessian, \mathbf{H} , matrices such as the residual function at iteration $i + 1$ is defined as follows:

$$\Theta(a_{i+1}) = \Theta(a_i) + \nabla\Theta(a_i)^T \cdot \Delta a + \frac{1}{2} \Delta a^T \cdot \mathbf{H} \cdot \Delta a, \quad (24)$$

where Δa is the radii step.

Since the contact problem is formulated as a nonlinear least-squares (NLS) problem, the gradient of the objective function can be written as,

$$\nabla\Theta(a) = \mathbf{J}(a)^T r(a), \quad (25)$$

where J denotes the Jacobian matrix. It is given by,

$$\mathbf{J}(a) = \nabla r(a)^T = \begin{pmatrix} \nabla r_1^T \\ \nabla r_2^T \\ \vdots \\ \nabla r_n^T \end{pmatrix}. \quad (26)$$

The Hessian matrix is the square matrix of second-order partial derivatives of $r(a)$. We write,

$$\mathbf{H} = \begin{pmatrix} \frac{\partial^2 \Theta}{\partial a_1^2} & \frac{\partial^2 \Theta}{\partial a_1 \partial a_2} & \cdots & \frac{\partial^2 \Theta}{\partial a_1 \partial a_n} \\ \frac{\partial^2 \Theta}{\partial a_2 \partial a_1} & \frac{\partial^2 \Theta}{\partial a_2^2} & \cdots & \frac{\partial^2 \Theta}{\partial a_2 \partial a_n} \\ \vdots & \vdots & \ddots & \vdots \\ \frac{\partial^2 \Theta}{\partial a_n \partial a_1} & \frac{\partial^2 \Theta}{\partial a_n \partial a_2} & \cdots & \frac{\partial^2 \Theta}{\partial a_n^2} \end{pmatrix}. \quad (27)$$

For this case, the Hessian matrix can be rewritten as follows,

$$\mathbf{H}(a) = \mathbf{J}(a)^T \mathbf{J}(a) + \sum_{i=1}^n r_i \nabla^2 r_i. \quad (28)$$

LM algorithm differs from Newton's or Gauss-Newton's (GN) method by using a damped approximation of the Hessian matrix. In fact, in LM method GN approximation is damped using a suitable controlling strategy to avoid the weakness of the GN method when the Jacobian matrix is rank-deficient. We write,

$$\mathbf{H} \approx \mathbf{J}^T \mathbf{J} + \lambda \mathbf{I}, \quad (29)$$

where λ is the damping factor and I is the identity matrix.

4. **Compute the radii step:** the goal of this step is to find the direction Δa such as

$$(\mathbf{J}^T \mathbf{J} + \lambda \mathbf{I}) \Delta a = -2\mathbf{J}^T r_i. \quad (30)$$

Note that Eq. (30) is the normal equations for the following linear least-squares problem,

$$\min_{\Delta a} \frac{1}{2} \left\| \begin{bmatrix} \mathbf{J} \\ \lambda \mathbf{I} \end{bmatrix} \Delta a + \begin{bmatrix} r \\ 0 \end{bmatrix} \right\|_2^2. \quad (31)$$

Note also that the damping factor λ affect both the search direction and the step size Δa . In this research work, the trust-region (TR) method is used, after each iteration, to control and update the damping factor λ .

5. **Update the solution:** compute a_{i+1} such as

$$a_{i+1} = a_i + \Delta a. \quad (32)$$

6. **Evaluate the objective function:** compute the residuals r at the new solution a_{i+1} . Compute the new objective function $\Theta_{new} = \Theta(a_{i+1})$ at the new solution a_{i+1}

If $\Theta_{new} < \Theta(a_i)$, accept the new solution a_{i+1} . Otherwise, reject the radii step Δa , keep the old parameter (the guess, the residual and the objective function) and adjust the damping factor using TR algorithm.

7. **Convergence verification:** Compute the error. If the procedure has converged, return the contact radii a_{i+1} for the current contact step. If the procedure had not yet converged but the radii step Δa was accepted, compute the Jacobian matrix at the new solution a_{i+1} , then go to the step 4.

Overall, the resolution of the contact problem with interaction falls into two loops. The first one handles the contact steps defined for each far field displacement δ . Thus, for each step, the NLS problem is defined. The second loop solves the NLS problem by solving a sequence of linear least-squares sub-problem.

2.3 Persson scaling theory

In 2001, Persson [39] came out with an ingenious idea, completely different compared the asperity-based models, to tackle the micro-mechanic contact problem of rough surfaces. The Persson theory starts by considering the contact of the two rough bodies to be initially perfect (i.e. smooth contacting surfaces see **Figure 3**). For the full contact set up, the contact pressure p_0 is assumed uniform. Following the self-affine behavior carried by the PSDF, the roughness is progressively added which

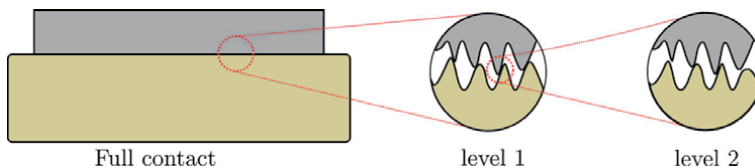


Figure 3. Two elastic bodies in contact. Illustration of the scaling theory. Both bodies has roughness on many different length scales.

lead to a variation of the contact pressure and the gap. It's important to note that when the PSDF covers a wide wavenumber range from the roll-off distance to the cut-off limit, Persson argued that the evolution of the pressure is given by its density function $P(p, \zeta)$, where ζ is the magnification factor which is related to the roll-off wavelength (or wavenumber). We have $\zeta = k/k_0 = \lambda_0/\lambda$. When the roughness is added, the function $P(p, \zeta)$ verifies the following diffusion equation,

$$\begin{cases} \frac{\partial P(p, \zeta)}{\partial \zeta} = f(\zeta) \frac{\partial^2 P(p, \zeta)}{\partial p^2} \\ P(p, 1) = \delta(p - p_0) \\ P(-\infty, \zeta) = 0 \\ P(+\infty, \zeta) = 0 \end{cases} \quad (33)$$

where,

$$f(\zeta) = G'(\zeta)p_0^2. \quad (34)$$

G' is a function of the magnification. We write,

$$G(\zeta) = \frac{\pi}{4} \left(\frac{E^*}{p_0} \right)^2 \int_{k_0}^{\zeta k_0} k^3 \text{PSDF}(k) dk, \quad (35)$$

from which it follows,

$$f(\zeta) = \frac{\pi}{4} E^{*2} k_0 k^3 \text{PSDF}(k). \quad (36)$$

k_0 is the wavenumber related to the roll-off distance and the quantity $\pi \int_{k_0}^{\zeta k_0} k^3 \text{PSDF}(k) dk$ is the second profile PSDF moment, m_2 , for an isotropic surface.

It is important to note that Eq. (33) is supposed to hold for the full contact condition (first configuration of the **Figure 3**). For the partial contact, the 3-rd boundary condition $P(-\infty, \zeta) = 0$ should be replaced by,

$$P(0, \zeta) = 0. \quad (37)$$

2.4 Boundary element method

The Boundary Element Method (BEM) belongs to the most efficient numerical methods for solving normal contact problems between two linear elastic bodies with rough boundaries. Unlike asperity-based models, the BEM is free of any kind of assumption. Its only restriction is in the discretization of the rough surface. Indeed, an adequate mesh is required to guarantee the convergence of the predicted results. However, with the development of computer tools, the restriction of discretization is easily overcome.

The relevance of BEM is based on the treatment of the problem of contact of rough surfaces without the need to discretize the bulk. The fundamental BEM formulation deals with the frictionless contact of homogeneous and linear elastic bodies with rough boundaries. Several developments have been proposed to extend the BEM to address the contact problem of heterogeneous bodies with rough boundaries [61] including severe nonlinearities such as adhesion [50, 51], friction [52] or plasticity [53]. The purpose of this section is to present the basic BEM formulation to solve frictionless contact problem of rough surfaces.

Let us assume a system defined in **Figure 4** which is equivalent of two bodies with two rough boundaries. The Young modulus E_i and the Poisson ratio ν_i refer to the i -th body with $i = 1$ or 2 . In the configuration presented in **Figure 4**, an elastic half plane comes in contact with a rigid rough surface when the far field displacement δ is imposed. The profile of the rough surface is characterized by the function $\zeta(x)$ measured with respect to the mean plane. The peak of the rough surface is the ζ_{\max} such as $\zeta_{\max} = \max_{x \in S}(\zeta(x))$. When the asperity comes in contact with the elastic half-plane, a displacement \bar{u} is defined. It characterizes the distance between the local peak of the contacting asperity and the position of the elastic half-plane of the undeformed configuration, which is also equal to $\zeta_{\max} - \zeta$ with ζ , in this case, denotes the local peak of the contacting asperity. Otherwise, a generic displacement of the elastic half-plane is simply denoted by $u(x)$.

In the fundamental BEM, the normal displacement field, $u(x)$, at the coordinate x is related to the contact pressure $p(y)$ at the coordinate y by the following integral form:

$$u(x) = \int_S G_r(x, y) p(y) dy, \quad (38)$$

where $G_r(x, y)$ is the Green-function which links the displacement $u(x)$ at x to the contact pressure $p(y)$ acting at y . It is given by the Boussinesq solution as follows:

$$G_r(x, y) = \frac{1}{\pi} \left(\frac{1 - \nu_1^2}{E_1} + \frac{1 - \nu_2^2}{E_2} \right) \frac{1}{r}, \quad (39)$$

where r is the distance between the points x and y . It refers to the standard Euclidean norm. We have, $r = \|x - y\|$.

Therefore, the frictionless contact problem of the rough surfaces is solved by the following optimization problem,

$$\begin{aligned} &\text{For} && \text{a given far field displacement } \delta \\ &\text{find} && u(x) \text{ and } p(x) \\ & && \text{on } x \in S \\ &\text{such as} && u(x) = \int_S \frac{1}{\pi} \left(\frac{1 - \nu_1^2}{E_1} + \frac{1 - \nu_2^2}{E_2} \right) \frac{1}{\|x - y\|} p(y) dy \\ &\text{with} && \begin{cases} u(x) - \bar{u}(x, \delta) \geq 0 \\ p(x) \geq 0 \\ (u(x) - \bar{u}(x, \delta)) p(x) = 0 \end{cases} \end{aligned} \quad (40)$$

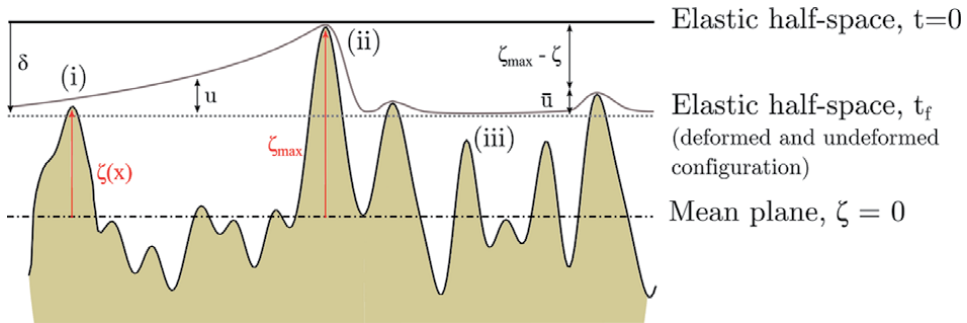


Figure 4. Contact problem configuration: rigid rough surface and an elastic half-plane. The latter moves normally towards the rigid rough surface according to a far field displacement δ .

The discretized form of the above formulation can be given if we consider the following set of the discretized parameters,

1. the barycentric coordinate: $x_{i,j} = \frac{1}{S_{ij}} \int_{x \in S_{ij}} x \, dA$;
2. the average height: $\zeta_{i,j} = \frac{1}{S_{ij}} \int_{x \in S_{ij}} \zeta(x) \, dA$;
3. the resultant contact load: $p_{i,j} = \int_{x \in S_{ij}} p(x) \, dA$;
4. the displacement: $u_{i,j} = \frac{1}{S_{ij}} \int_{x \in S_{ij}} u(x) \, dA$.

Note that S_{ij} refers to a cell of the surface S . The latter can be seen as a square grid spacing by Δ and containing $N \times N$ points. Therefore, the cell S_{ij} is a square surface of dimension Δ^2 .

Hence, the discretized form of Eq. (38) can be written as follows,

$$u_{i,j} = \sum_{k=1}^N \sum_{l=1}^N G_{r_{i-k,j-l}} p_{k,l}, \quad \forall (i,j) \in I_N = \{1, \dots, N\} \times \{1, \dots, N\} \quad (41)$$

where $G_{r_{i-k,j-l}}$ represents the averaged Green function over the cell S_{ij} . We write,

$$G_{r_{i-k,j-l}} = \frac{1}{\Delta^2} \int_{S_{ij}} \int_{S_{kl}} G_r(x,y) \, dydx. \quad (42)$$

and

$$p_{k,l} \geq 0, \quad \forall (k,l) \in I_N = \{1, \dots, N\} \times \{1, \dots, N\}. \quad (43)$$

To solve numerically the frictionless contact problem, it is convenient to recall some definitions introduced for the first time by Paggi et al. [44, 52]. First, let us define the set \bar{I}_c such as,

$$\bar{I}_c = \left\{ (i,j) \in I_N : \zeta_{i,j} < \zeta_{\max} - \delta \right\}, \quad (44)$$

which can be read as the set of the elements S_{ij} that are certainly not in contact (see the configuration (iii) in **Figure 4**). Therefore, the complementary set of \bar{I}_c is simply $I_c = I_N \setminus \bar{I}_c$ which represents the initial trial elements S_{ij} that are in contact. Secondly, we define the real contact set I_c^* which includes the actual contact elements S_{ij} . It should be noted that, due the interaction between the asperities (see the configuration (i) in **Figure 4**), I_c^* is a subset of I_c . We may have,

$$u_{i,j} > \bar{u}_{i,j}, \quad \text{where } \bar{u}_{i,j} = \delta - \zeta_{\max} + \zeta_{i,j}. \quad (45)$$

It should be noted that the condition,

$$(u_{i,j} - \bar{u}_{i,j}) p_{i,j} = 0, \quad \forall (i,j) \in I_c, \quad (46)$$

must hold in the last case implying non contact between the boundaries and thus, a zero contact pressure. In the opposite case, where the contact occurs, the contact pressure is strictly positive and hence, $u_{i,j} = \bar{u}_{i,j}$.

If we denote $u_{i,j} - \bar{u}_{i,j}$ by $\omega_{i,j}$, the complementary condition in Eq. (45) will read,

$$\omega_{i,j} p_{i,j} = 0, \quad \forall (i,j) \in I_c. \quad (47)$$

Thus, for all elements S_{ij} such as $(i,j) \in I_c$, the discretized form in Eq. (45) can be reduced to the set I_c as,

$$\omega_{i,j} + \bar{u}_{i,j} = \sum_{(k,l)} G_{r_{i-k,j-l}} p_{k,l}, \quad \forall (i,j) \in I_c. \quad (48)$$

Using the matrix form, the frictionless contact problem can be expressed following the classic Linear Complementarity Problem (LCP) as follows,

$$\begin{aligned} \text{For} & \quad \text{a given far field displacement } \delta \\ \text{find} & \quad \omega \text{ and } p \\ \text{such as} & \quad \omega = Ap - \bar{u} \\ \text{with} & \quad \omega \geq 0, p \geq 0, \omega^T p = 0. \end{aligned} \quad (49)$$

where ω , p and \bar{u} are vectors in \mathbb{R}^n , n is the number of elements of I_c . They represent, respectively, the unknown elastic correction, the unknown contact force and the compenetration which is related to the far field displacement δ and the distance $\zeta_{\max} - \zeta$. A is matrix obtained through the Green-functions. Note that problem (48) is equivalent to the following convex quadratic program (QP),

$$\begin{aligned} \min_p & \quad \frac{1}{2} p^T A p - \bar{u} p \\ \text{s.t.} & \quad p \geq 0, \end{aligned} \quad (50)$$

where its solution p and its dual ω solve the LCP defined in Eq. (48). The opposite remains true.

Solving the discretized form of LCP is not trivial since neither the contact pressure nor the displacement are known in priory. In the literature, authors developed several numerical schemes such as (i) pivoting methods (known also as Lemke's algorithm), (ii) Non-Negative Least Squares (NNLS) solver and (iii) the FFT-based algorithm to solve efficiently the contact problem. The pivoting-based method reaches the exact solution after a finite number of pivoting. However, when the matrix A is large, pivots number can be quite large and hence, we lost the efficiency [62]. Regarding NNLS, it takes advantage of the linear elasticity property to recast the LCP as a NNLS problem with a particular factorization. In other words, Eq. (49) will be rewritten as,

$$\begin{aligned} \min_p & \quad \frac{1}{2} \|Cp - C^{-T}\bar{u}\|_2^2 \\ \text{s.t.} & \quad p \geq 0, \end{aligned} \quad (51)$$

where C is the so-called Cholesky matrix derived through Cholesky factorization of the matrix A . We write $A = C^T C$. Note that, using the algorithm developed in [44], the QP in Eq. (50) is solved without an explicit computation of the matrix C or its inverse C^{-1} . This last point makes the NNLS solver optimal and efficient to solve the fictionless contact problem of rough surfaces. In addition to the above methods, the FFT-based scheme can be an alternative solution to solve the LCP while reducing the CPU time [49]. In fact, the matrix A in Eqs. (48) and (50) of size $N_x^2 \times N_y^2$,

with N_i denotes the number of the contacting nodes following i -th direction. Unlike the sparsity property within FEM, the resulted A matrix is symmetric completely full. Furthermore, performing operations with it to solve the contact problem, especially for rough surfaces with high resolution, will be heavy and will require a lot of memory and computational power. In the formulation of the FFT-based solver, the convolution theorem is applied to Eq. (38) in order to compute the displacement. First, the Discrete Fourier Transform (DFT) algorithm is used to expand the matrix A as well as the pressure p into Fourier's space. Then, the inverse DFT is applied to solve Eq. (38) following an optimization scheme to compute the displacement u . In this chapter, the NNLS and FFT-based solver will be considered to reveal how the true contact area and the distribution of local pressures vary with the applied load, the measured and generated surface roughness.

3. Experimental rough surface

In the previous section, several theories have been reviewed with details and comments on the possible algorithmic implementation to tackle the frictionless contact problem of two elastic bodies with rough boundaries. We have, however, not yet discussed the roughness from an experimental and numerical point of view. In this section, we thus present an AFM measurement of Au surface. Special attention will be given to the characterization of the Au measured surface following the PSDF in order to generate numerically rough surfaces similar to what has been observed experimentally. For this, we introduce first basic concepts to characterize the measured rough surface by the means of the PSDF. Then, a brief comment will be given on the comparison between the measured and the generated Au rough surface.

3.1 Theoretical background

Every surface exhibits roughness at the micro- or nano-scales. The surface variations can be fully characterized by their height probability density and power spectral density functions (i.e. HPDF and PSDF). The former holds the out-of-plane information while the latter describes the spatial arrangement. The HPDF can take various forms (i.e. exponential, Gaussian, Weibull ...) depending on the fabrication and the post-processing techniques. Surfaces fabricated using a random deposition process, such as evaporation and magnetron sputtering in the microelectronics industry, generally lead to surface heights with near-Gaussian distribution.

The relevant statistical quantities that characterize the HPDF are: (i) the mean \bar{z} , (ii) the variance σ^2 , (iii) the skew (S_k) and (iv) the kurtosis (K_u) of surface heights. They are defined by Eqs. (51), (52), (53) and (54), respectively.

$$\bar{z} = \frac{1}{N_p} \sum_{i=1}^{N_p} z_i \quad (52)$$

$$\sigma^2 = \frac{1}{N_p} \sum_{i=1}^{N_p} (z_i - \bar{z})^2 \quad (53)$$

$$S_k = \frac{1}{N_p \sigma^3} \sum_{i=1}^{N_p} (z_i - \bar{z})^3 \quad (54)$$

$$K_u = \frac{1}{N_p \sigma^4} \sum_{i=1}^{N_p} (z_i - \bar{z})^4 \quad (55)$$

On the other hand, the PSDF quantifies the contribution of the different wavelengths to the surface topography. It is directly calculated from the Fast Fourier Transform (FFT) of measurement data $z(x_k, y_l)$ using Eq. (55):

$$\text{PSDF}(k_{x_k}, k_{y_l}) = \frac{\Delta^2}{(2\pi)^2 N_p} |\text{FFT}(z(x_k, y_l))|^2, \quad (56)$$

where Δ refers to the sampling length, (x_k, y_l) are the discrete (x, y) coordinates and (k_{x_k}, k_{y_l}) represent the discrete spatial frequencies.

According to Persson's work on the nature of rough surfaces [63], the PSDF follows a power law for $k \in [k_r, k_s]$ and reaches a plateau C_0 for $k \in [k_l, k_r]$, where k_r is the roll off frequency, $k_s = 2\pi/\Delta$ is the highest measurable frequency and k_l represents the lowest measurable frequency and is related to the scan length L as $k_l = 2\pi/L$. The theoretical form of the PSDF is given as follows,

$$\text{PSDF}(k) = C_0 \times \begin{cases} 1 & \text{if } k_l < k \leq k_r \\ \left(\frac{k}{k_r}\right)^a & \text{if } k_r < k \leq k_s, \\ 0 & \text{else} \end{cases}, \quad (57)$$

where the exponent a can be expressed depending on the Hurst component as $a = -2(1 + H)$.

3.2 Rough surface topography measurement

This section presents the characterization of a real rough surface through its HPDF and PSDF. The surface of a 1 μm -thick Au film deposited on a silicon wafer using radio frequency magnetron sputtering technique is considered for the study of a real surface topography. The AFM measurements are performed under Veeco Dimension 3100 instrument using a super sharp silicon (SSS) probe from NANOSENSORS, the scanned area is $1.5 \times 1.5 \mu\text{m}^2$ with a resolution of 512 in both directions.

Figure 5a presents the 3D view of the measured surface. The standard deviation of surface heights σ is 2.7 nm and the mean height \bar{z} is 11 nm. The surface HPDF is presented in normalized form and compared to the normal distribution in **Figure 6**. It's characterized by a skewness of -0.08 and a kurtosis of 2.7.

The 2D PSDF computed from the AFM data using Eq. (55) shows that the surface is highly isotropic (see **Figure 7a**). It can be seen from **Figure 8** that the radially averaged 2D PSDF increases with the increase of λ ($\lambda = 2\pi/k$) up to a roll of wavelength λ_r and then it reaches a plateau. The linear region in the PSDF plot presents two slopes, the first one is proportional to $k^{-6.5}$ (i.e. $\text{PSDF} \propto k^{-6.5}$) for $k \in [k_r, k_c]$ while the second one is proportional to $k^{-4.6}$ (i.e. $\text{PSDF} \propto k^{-4.6}$) for $k > k_c$. The second slope is probably attributed to the effect of the finite AFM tip radius that filters out wavelengths smaller than a critical wavelength $\lambda_c = 2\pi/k_c$ [64]. Note that the PSDF becomes constant for high values of k indicating a reliability cutoff, where data close this constant tail region line are affected by instrumental noise and should be discarded [64]. The magnitude of the PSDF plateau C_0 , the roll-off

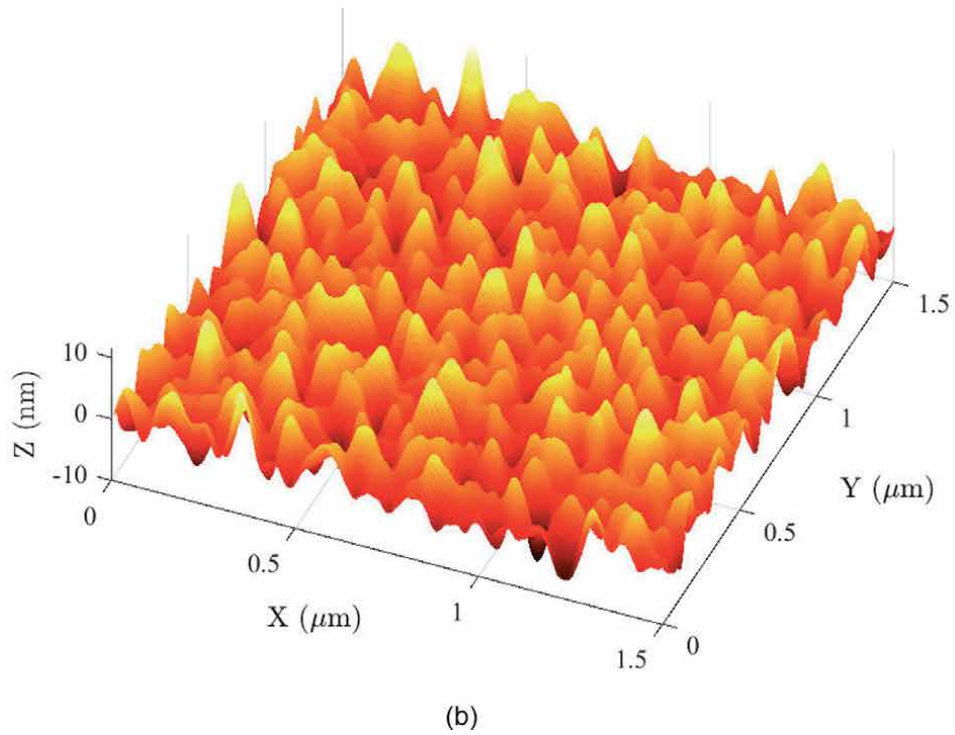
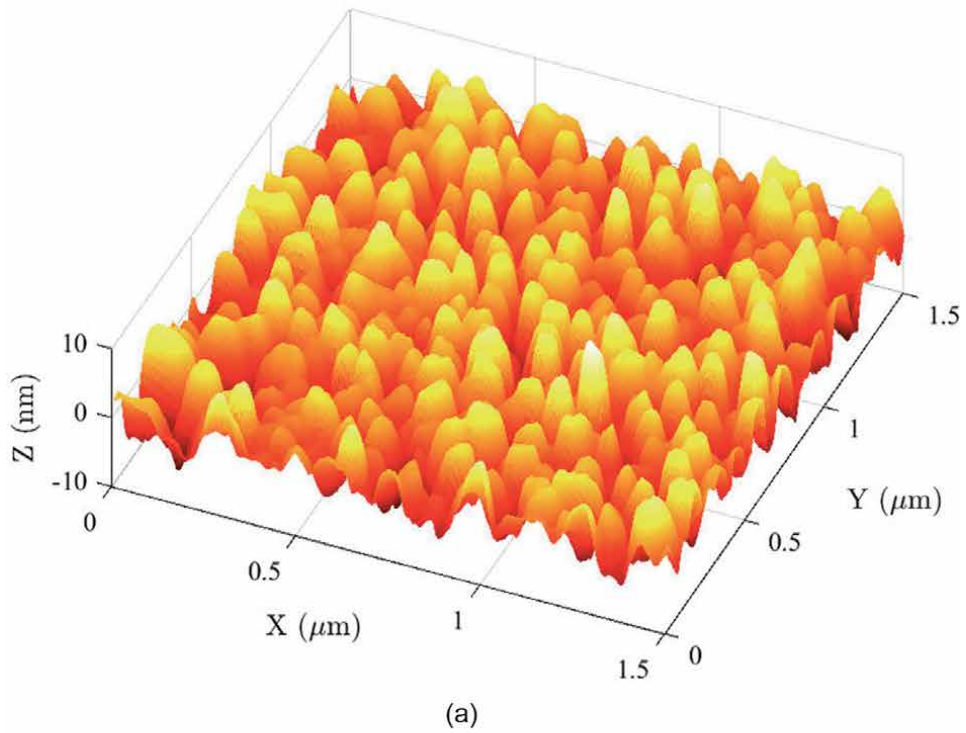


Figure 5. 3D view of (a) Au micro-surface measured using AFM and (b) numerically generated rough surface. The resolution of the real and artificial rough surface is 512 in both directions.

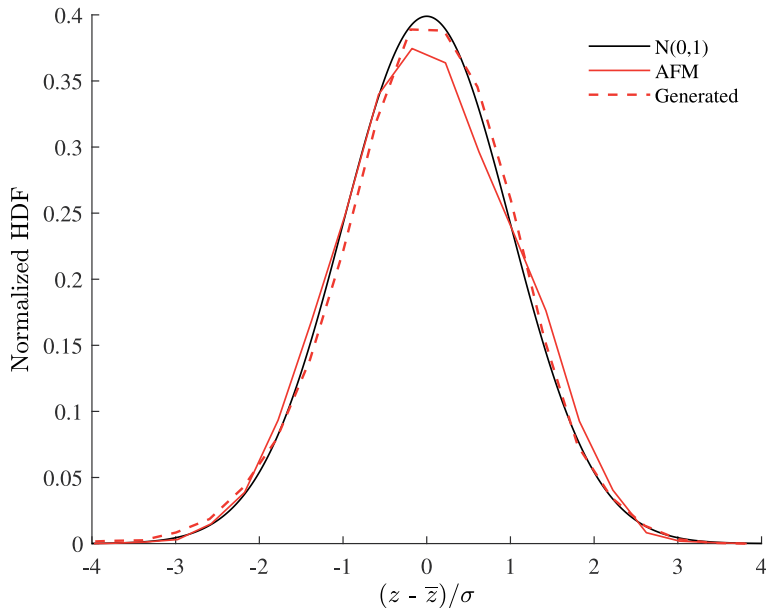


Figure 6.
Normalized HDFs of AFM and artificial surfaces.

wavelength λ_r and the critical wavelength λ_c are obtained by curve fitting of the different regions, their respective values are $3.8 \times 10^2 \text{ nm}^4$, 90 nm and 50 nm.

3.3 Rough surface generation

The artificial surface is aimed to mimic the behavior of Au surface. Thus, a Gaussian surface is generated using an implementation inspired by the Wu method [21] and based on the fitted PSDF of the measured Au surface (see **Figure 8**—red dashed line). The artificial surface is characterized by geometric and statistical quantities similar to those of Au surface, specifically (i) the standard deviation of surface heights $\sigma = 2.7 \text{ nm}$, (ii) the roll-off frequency $k_r = 2\pi/\lambda_r$ with $\lambda_r = 90 \text{ nm}$, (iii) the critical frequency $\lambda_c = 50 \text{ nm}$ (iv) the scanning length $L = 1.5 \mu\text{m}$, (v) the sampling length $\Delta = 2.93 \text{ nm}$ and (vi) the exponent a of the PSDF. The latter takes values of -6.5 for $k \in [k_r, k_c]$ and -4.6 for $k > k_c$. The plots of the 3D view, HDF and PSDF of the generated surface are presented respectively in **Figure 5b**, **6** and **7b** along with those from Au measured surface. Even if both surfaces are mathematically equivalent (i.e. similar HDF and PSDF), the small discrepancies on the HDF and PSDF lead to slightly different topographies, with Au surface having wider summits. However, as discussed in 4.3, the area-load mechanical behavior of both surface is similar with a maximum error of 9%.

4. Results and discussion

4.1 Convergence of the reference solution: BEM

The accuracy of the estimated contact area through the BEM is highly linked to the discretized rough surfaces and thus, strongly depends on the number of cells chosen to model the roughness. To highlight this problem, also known as the mesh-convergence in the literature, several computations were carried out on the 12

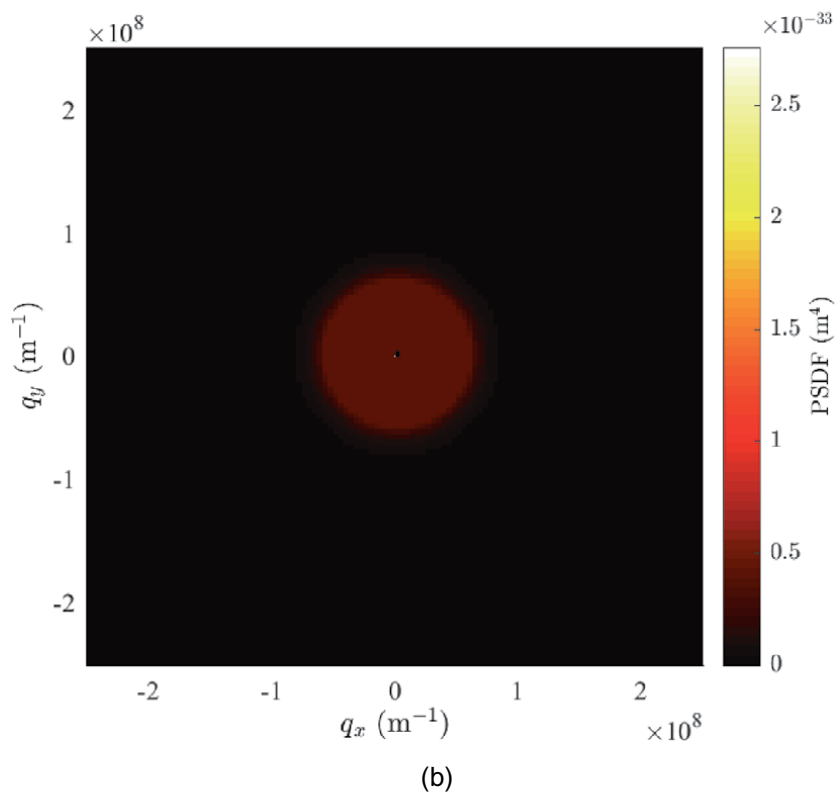
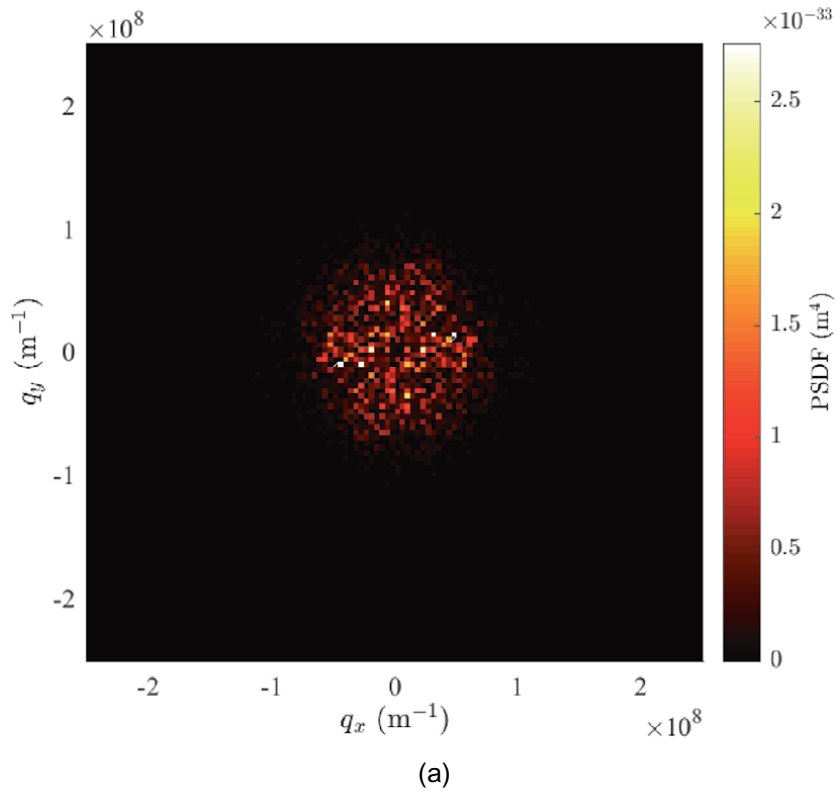


Figure 7. 2D PSDFs of (a) Au micro-surface measured using AFM and (b) numerically generated rough surface.

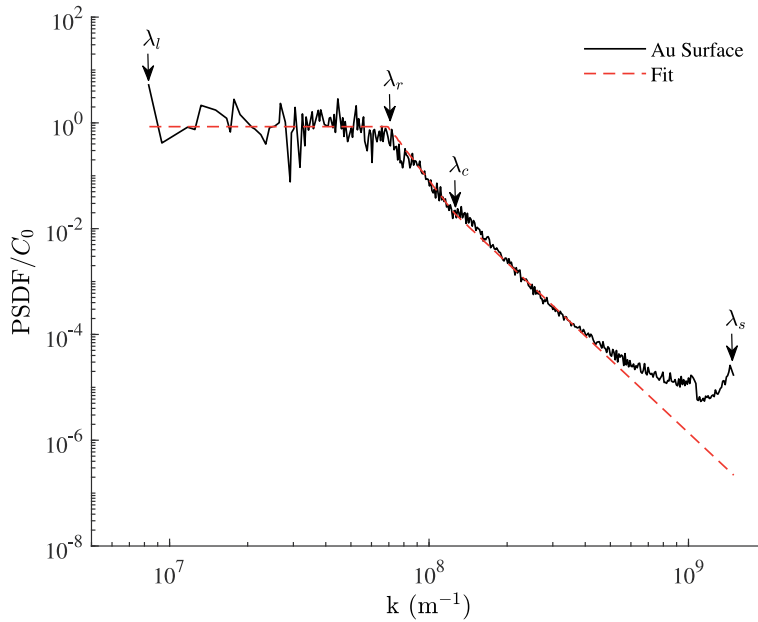


Figure 8.

Radially averaged PSDF of from AFM measurements on Au surface and the corresponding fit.

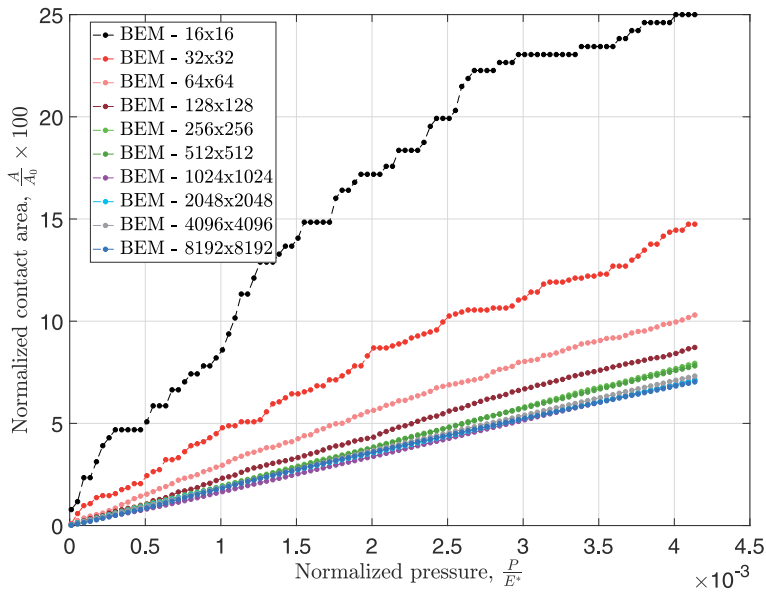
generated rough surfaces using Wu's procedure [21]. It should be noted that the artificial rough surfaces are generated using the fitted PSDF based on the AFM measurement of the real Au micro-surface (see **Figure 8**). The numerical discretization of the 12 generated rough surfaces varies from 4×4 to 8192×8192 pixels. For each case, the normalized contact area $A/A_0 \times 100$ is plotted as a function of the normalized contact pressure P/E^* , where A refers to the real contact area, A_0 denotes the nominal area, P represents the contact pressure and E^* is the composite Young modulus. The results are briefly summarized in **Figure 9** for both FFT and NNLS solvers.

One can observe from **Figure 9** that the contact law, $A/A_0 \times 100 = f(P/E^*)$, is clearly mesh sensitive for both FFT and NNLS solvers. In fact, the predicted results for a coarse mesh, i.e. 4×4 , 8×8 , 16×16 and 32×32 , are not consistent for the NNLS solver (see **Figure 9b**) and the resulting real contact area is overestimated. However, it can be seen clearly that, for the same solver, the convergence is reached with 64×64 pixels. On the other hand, the FFT solver has an identical behavior with a lower convergence rate. Indeed, the convergence of the FFT solver starts from a 256×256 pixel mesh which is finer than the converging mesh of the NNLS (i.e. 64×64). As regard to the CPU time, no comparison can be made as the two solvers have been implemented on two different codes. However, the FFT-based solver is sufficiently fast and requires less memory. For instance, on a computing station equipped with 32 GB RAM and 12 logical cores, the FFT-based solver manages to solve the frictionless contact problem of a generated rough surface of 512×512 pixels, while the NNLS solver ran out of memory.

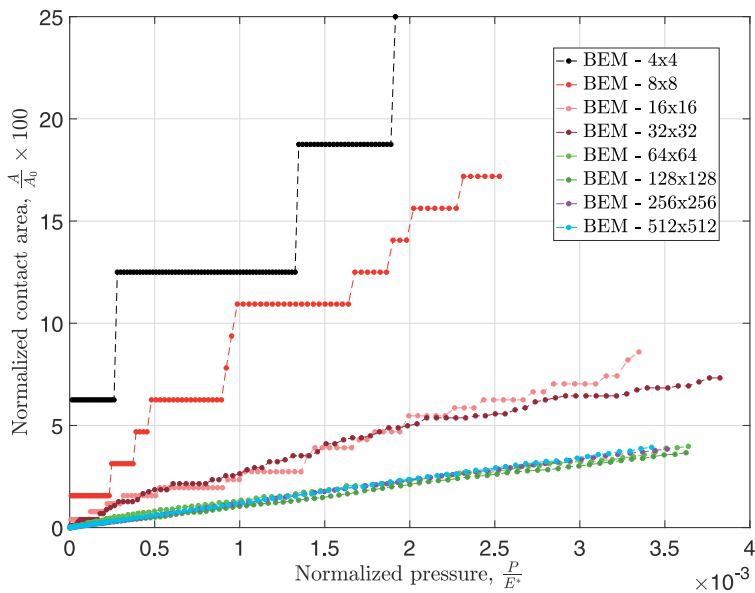
In the following, the predicted results using 512×512 pixels by means of the FFT-based solver is considered as a reference solution to study the above theories.

4.2 Linearity between the contact area and pressure

Let us consider a generated rough surface in **Figure 5b** which is in contact with a flat plane. The latter moves normally towards the rough surface according to a far



(a)



(b)

Figure 9. Effect of the mesh discretization on the true contact area—contact pressure law for a generated rough surface. (a) FFT solver. (b) NNLS solver.

field displacement δ . In this section, the predicted contact area using the above theories are compared and discussed in respect to the reference solution which is the BEM prediction on the finest discretization of the generated rough surface. The analysis mainly covers the evolution of the normalized true contact area as a function of the normalized contact pressure using five models,

1. The Boundary Element Method on the generated rough surface. The resolution is performed on the finest discretized rough surface which contains 512×512 pixels using three codes: the first is the NNLS and it is denoted by BEM-NNLS.

The second is based on the FFT. Thus, it is denoted by BEM-FFT. The third is Lars Pastewka's code available to the public on <http://contact.engineering/>. The later is denoted by BEM-L. Patewska.

2. The Discrete Greenwood and Williamson model using spherical asperities without interaction. It is denoted by GW theory;
3. The modified Greenwood and Williamson model using sinusoidal asperities with interaction. It is denoted by GW-interaction;
4. The analytic solution of Persson Theory which is denoted by Persson theory;
5. The Bush-Gibson-Thomas asperity contact theory, known as BGT theory.

The predicted results are presented in **Figure 10**. Overall, the above theories predict the same behavior for a small pressure margin. The normalized contact area—normalized contact pressure relationship is almost linear whether the interaction is taken into account or not. For an accurate modeling, the contact area vs. contact pressure may be approximated by a power law function rather than a linear function. This first results is well known in the literature [65]. However, the coefficient of the proportionality (i.e. the slop of **Figure 10**) varies from one theory to another. For instance, the BGT's slope is quite different from that predicted by the

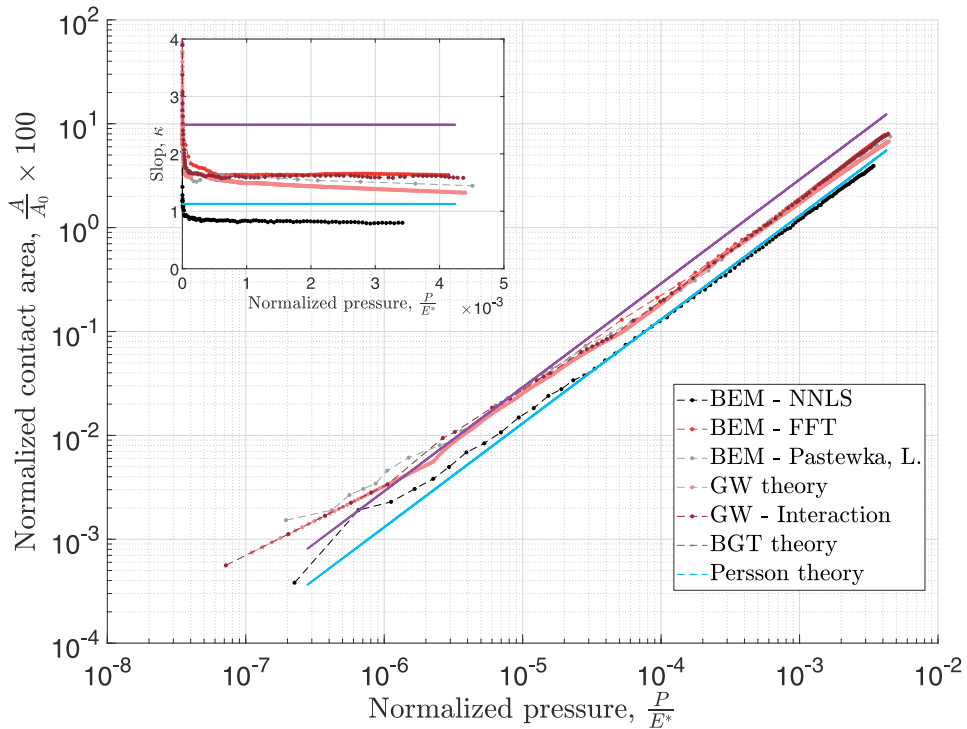


Figure 10. The comparison between the BGT, GW model with and without interaction, Persson theory and BEM. Observe that the predicted laws area-contact pressure are power law function except BGT prediction which involves linear approximation. The inset show the evolution of the slop, for each prediction, as a function of the dimensionless contact pressure.

reference solution and the Persson theory. With regards to the asperity based models, the coefficient of proportionality of GW theory with or without interaction are quite similar. They vary from 1.36 for the GW theory to 1.60 for GW-interaction model. In particular, the enhanced GW model gives similar results to those obtained by BEM using the FFT-based solver and Patewska application. Note, however, that these last coefficients are lower than the asymptotic BGT theory which predict a coefficient of 2.5. On the other hand, Persson theory prediction is lower than the asperity based models; for the same pressure, Persson's theory predicts a smaller contact area. The same observations can be made for the BEM solution using the NNLS solver, which is not the case in the studies available in the literature. This non-conventional result can be explained by the fact that the BEM - NNLS is performed on 1 randomly generated rough surface. For this type of problem, it is more convenient to run Monte-Carlo like simulation on several realization using the same PSDF. The last point will be addressed in Section 4.3.

Given that all contact models presented above, the pioneering theory of GW [23] gives an accurate results for a fraction of contact area lower than 20%. The predicted true contact area are very similar to the other enhanced models. With regards to the literature, the obtained results can be analyzed using Nayak's parameter α which is related to the i -th order moment m_i of the PSDF. For our case, the measured and generated surfaces have Nayak's parameter roughly equal to 2.2 which is close to the analysis conducted by Carbone et al. [65, 66]. For $\alpha = 2$, they showed that GW theory gives reasonable predictions for a low squeezing pressure. Under the same conditions, they showed that the linearity between true contact area and contact pressure holds only for small contact area fractions. However, when the squeezing load is higher, the prediction of the above theories deviates from linearity which is in line with the findings in this contribution.

4.3 Comment on the predicted contact area of measured and generated rough surfaces

In the previous sections, all the above methods were successfully applied on numerically generated rough surfaces. Recall that these were generated using Wu's algorithm [21]. It takes as input the fitted PSDF based on the measured one. Let us, however, consider the case of a measured Au rough surface. The objective of this section is to conduct a BEM simulation on the measured Au rough surface and compare the results with those obtained on randomly generated rough surfaces using Monte-Carlo simulation on 1000 realizations.

The results for the evolution of the real contact area in dimensionless form for Au measured rough surface are depicted in **Figure 11**. They are compared to BEM solution over 1000 equivalent rough surfaces in order to obtain statistical relevant results. The average prediction over 1000 realizations is also computed (see **Figure 11** red dashed line). The obtained predictions of Au measured rough surface are a little bit higher than the average BEM predictions on randomly generated rough surfaces. The maximum error does not exceed 9% for the considered contact pressure margin. Note that this difference is observed despite the fact that the PSDFs of the measured and generated rough surfaces are equivalent (see **Figures 6** and **8**). The observed discrepancy can be attributed to (i) the measured HDF of Au surface which not a perfect Gaussian (i.e the measured kurtosis is 2.7 instead of 3), (ii) the fluctuations on the Au PSDF due to local irregularities and (iii) the AFM white noise that causes the Au PSDF to flatten at high spatial frequencies k [64].

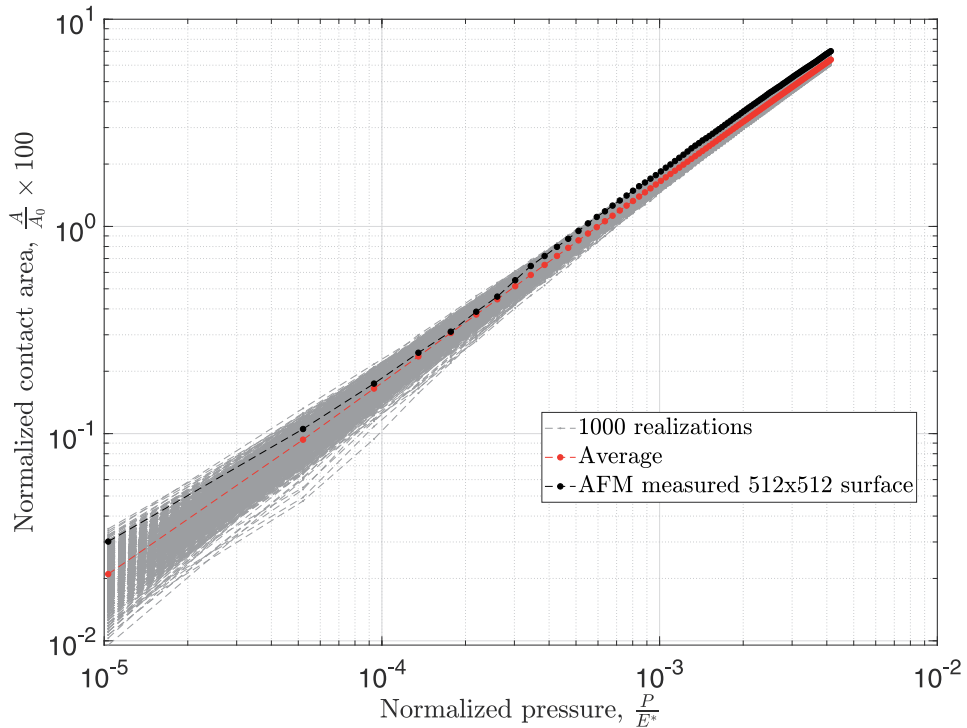


Figure 11. True contact area vs. contact pressure in dimensionless form: comparison between BEM solution on 1000 realizations (e.g. 1000 randomly generated rough surfaces—gray dashed lines), average curve over the 1000 realization (red dashed line) and BEM solution on the measured 512×512 Au rough surface using AFM technique (black dashed line).

5. Conclusion

The aim of this contribution is to present the basic guidelines to tackle the problem of contacting rough surfaces accounting for the real surface topography. For this purpose, the authors presented different theories of contact mechanics and introduced the procedure to characterize the surface topography from AFM measurements by the mean of the height distribution and power spectral density functions (HDF and PSDF).

First, a brief description has been devoted to synthesize the fundamentals of Greenwood's theory with and without interaction, Persson's theory and the Boundary Element Method. Next, a rough surface of length $1.5 \mu\text{m}$, which is comparable to the contact electrode surfaces for ohmic contact micro-switches, was fabricated by sputtering $1 \mu\text{m}$ thick gold over silicon wafer and measured by AFM technique with 512 heights per side.

The measured HDF and PSDF was approximated and then, used to generate several artificial surfaces to study the mesh effect of the BEM, considered as the reference solution, by means of two solvers (i.e. FFT and NNLS). The convergence study showed that the predicted results using NNLS solver converge from an approximation of 64×64 pixels, while 256×256 pixels are needed for the FFT-based solver to converge. However, the latter is fast and requires less computational power compared to the NNLS solver.

The Greenwood and Williamson's theory, with and without interaction, and Persson's theory were applied to the generated rough surface and compared to the BEM. All these models predict approximately a power-law evolution of the contact

surface as a function of dimensionless pressure. A notable difference was observed in the slope of each prediction, and the proportionality coefficients found are consistent with the literature. It is worth mentioning that the pioneering theory of GW gives accurate results for small contact area fraction and is in a good agreement with GW-interaction model and BEM-FFT predictions. However, GW results start to deviate when the pressure load increases since the interactions between asperities have a larger effect.

Finally, the Au rough surface was studied using the BEM and the results were successfully compared with intensive Monte-Carlo simulations on 1000 generated rough surface populations. The generation of artificial surfaces from the approximated HDF and PSDF succeed to catch the real surface topography and allows to estimate the mechanical behavior of contacting rough surfaces with a high level of confidence.

Acknowledgements

The first author would like to warmly thank Prof. Vladislav Yastrebov and Prof. Marco Paggi for their immense help and extremely relevant explanations during the workshops organized at Mines-Paristech France and IMT-Lucca Italy, respectively. This research work could not have been done without their help.

Conflict of interest

The authors declare no conflict of interest.

Author details

Farouk Maaboudallah^{1*†}, Mohamed Najah^{2†} and Nouredine Atalla¹

¹ Groupe d'Acoustique de l'Université de Sherbrooke (GAUS), Department of Mechanical Engineering, University of Sherbrooke, Quebec, Canada

² Institut Interdisciplinaire Dinnovation Technologique (3IT), Department of Electrical Engineering, University of Sherbrooke, Quebec, Canada

*Address all correspondence to: farouk.maaboudallah@usherbrooke.ca

† These authors contributed equally.

IntechOpen

© 2022 The Author(s). Licensee IntechOpen. This chapter is distributed under the terms of the Creative Commons Attribution License (<http://creativecommons.org/licenses/by/3.0>), which permits unrestricted use, distribution, and reproduction in any medium, provided the original work is properly cited. 

References

- [1] Panagouli OK, Mastrodimou K. Dependence of friction coefficient on the resolution of asperities in metallic rough surfaces under cyclic loading. *International Journal of Solids and Structures*. 2017;**108**:85-97
- [2] Wang H, Zhou C, Wang H, Hu B, Liu Z. A novel contact model for rough surfaces using piecewise linear interpolation and its application in gear wear. *Wear*. 15 July 2021;**476**:203685
- [3] Panagouli OK, Margaronis K, Tsotoulidou V. A multiscale model for thermal contact conductance of rough surfaces under low applied pressure. *International Journal of Solids and Structures*. 2020;**200-201**:106-118
- [4] Zhai C, Hanaor D, Proust G, Brassart L, Gan Y. Interfacial electro-mechanical behaviour at rough surfaces. *Extreme Mechanics Letters*. 2016;**9**:422-429
- [5] Yastrebov VA, Durand J, Proudhon H, Cailletaud G. Rough surface contact analysis by means of the finite element method and of a new reduced model. *Comptes Rendus Mcanique*. 2011;**339**:473-490
- [6] Magnier V, Brunel JF, Dufrenoy P. Impact of contact stiffness heterogeneities on friction-induced vibration. *International Journal of Solids and Structures*. 2014;**51**:1662-1669
- [7] Maaboudallah F, Atalla N. An efficient numerical strategy to predict the dynamic instabilities of a rubbing system: Application to an automobile disc brake system. *Computational Mechanics*. 31 March 2021;**67**:1465-1483
- [8] Rogozhin A, Miakonkikh A, Tatarintsev A, Lebedev K, Kalnov V, Rudenko K. Silicon Ohmic Lateral-Contact MEMS Switch for RF Applications. *Proceedings Vol. 10224*. Zvenigorod, Russian Federation: International Conference on Micro- and Nano-Electronics. 2016. pp. 1-7. DOI: 10.1117/12.2267093
- [9] Qian J-y, Hou C-w, Li X-j, Jin Z-j. Actuation mechanism of microvalves: A review. *Micromachines (Basel)* – MDPI. 2020;**172**(11):2. Available from: <https://www.ncbi.nlm.nih.gov/pmc/articles/PMC7074679/>
- [10] Schmidt MA. “Silicon Wafer Bonding for Micro mechanical Devices”. Hilton Head Island, South Carolina: Solid-State Sensors, Actuators, and Microsystems Workshop; 12-16 June 1994. pp. 127–131. DOI: 10.31438/trf.hh1994.30
- [11] Manneborg A, Nese M, Bhlickers P. “Silicon-to-silicon anodic bonding with a borosilicate glass layer.” *Journal of Micromechanics and Microengineering*. 1991;**1**:139
- [12] Gui C, Albers H, Gardeniers JGE, Elwenspoek M, and Lambeck PV. “Fusion bonding of rough surfaces with polishing technique for silicon micromachining”. *Microsystem Technologies*. 1997;**3**:122–128
- [13] Ma Q, Tran Q, Chou T-KA, Heck J, Bar H, Kant R, et al. Metal contact reliability of RF MEMS switches. In: *Reliability, Packaging, Testing, and Characterization of MEMS/MOEMS VI*. Proceedings. Vol. 6463. San Jose, California, United States: MOEMS-MEMS 2007 Micro and Nanofabrication. 2007. p. 646305. DOI: 10.1117/12.702177
- [14] Zhao Y-P, Wang L, Yu T. Mechanics of adhesion in MEMS—a review. *Journal of Adhesion Science and Technology*. 2003;**17**(4):519-546. Cited by 366
- [15] Nguyen N, Schubert S, Richter S, Dtzel W. Hybrid-assembled micro dosing system using silicon-based micropump/valve and mass flow sensor.

- Sensors and Actuators A: Physical. 1998; **69**(1):85-91
- [16] Hayamizu S, Higashino K, Fujii Y, Sando Y, Yamamoto K. Development of a bi-directional valve-less silicon micro pump controlled by driving waveform. Sensors and Actuators A: Physical. 2003; **103**(1):83-87
- [17] Sensortech uk. Silicon micro valve technology. Vacuum. 1994;**45**(12):1
- [18] Gong Y, Misture ST, Gao P, Mellott NP. Surface roughness measurements using power spectrum density analysis with enhanced spatial correlation length. Journal of Physical Chemistry C. 2016;**120**(39):22358-22364
- [19] Panda S, Panzade A, Sarangi M, Roy Chowdhury SK. Spectral approach on multiscale roughness characterization of nominally rough surfaces. Journal of Tribology. 2017;**139**(3):1-10
- [20] Chen JQ, Huang QS, Qi RZ, Feng YF, Feng JT, Zhang Z, et al. Effects of sputtering power and annealing temperature on surface roughness of gold films for high-reflectivity synchrotron radiation mirrors. Nuclear Science and Techniques. 2019;**30**(7):1-6
- [21] Wu JJ. Simulation of rough surfaces with FFT. Tribology International. 2000;**33**(1):47-58
- [22] Pérez-Ràfols F, Almqvist A. Generating randomly rough surfaces with given height probability distribution and power spectrum. Tribology International. 2019;**131** (October 2018):591-604
- [23] Greenwood JA, Williamson JBP. Contact of nominally flat surfaces. Proceedings of the Royal Society A: Mathematical, Physical and Engineering Sciences. 1966;**295**(1442):300-319
- [24] Bush AW, Gibson RD, Thomas TR. The elastic contact of a rough surface. Wear. 1975;**35**:87-111
- [25] Nayak PR. Random process model of rough surfaces. Journal of Lubrication Technology. 1971;**93**:398-407
- [26] Miki BB. Thermal contact conductance; theoretical considerations. International Journal of Heat and Mass Transfer. 1974;**17**:205-214
- [27] Cooper MG, Mikic BB, Yovanovich MM. Thermal contact conductance. International Journal of Heat and Mass Transfer. 1969;**12**: 279-300
- [28] Sridhar MR, Yovanovich MM. Review of elastic and plastic contact conductance models—Comparison with experiment. Journal of Thermophysics and Heat Transfer. 1994;**8**(4):633-640
- [29] Berthe D, Vergne P. An elastic approach to rough contact with asperity interactions. Wear. 1987;**117**:211-222
- [30] Yongsheng L, Guiping Y, Yan H, Linqing Z. The characteristics of elastically contacting ideal rough surfaces. Journal of Tribology. 1996;**118**: 90-97
- [31] O'Callaghan PW, Probert SD. Real area of contact between a rough surface and a softer optically flat surface. Journal of Mechanical Engineering Science. 1970;**12**:259-267
- [32] Hendriks CP, Visscher M. Accurate real area of contact measurements on polyurethane. Journal of Tribology. 1995;**117**:607-611
- [33] Paggi M, Ciavarella M. The coefficient of proportionality k between real contact area and load, with new asperity models. Wear. March 2010;**268** (7):1020-1029
- [34] Ciavarella M, Greenwood JA, Paggi M. Inclusion of interaction in the Greenwood and Williamson contact theory;**265**(5):729-734

- [35] Afferrante L, Carbone G, Demelio G. Interacting and coalescing hertzian asperities: A new multiasperity contact model. *278-279*:28-33
- [36] Yastrebov VA, Anciaux G, Molinari J-F. From infinitesimal to full contact between rough surfaces: Evolution of the contact area. *International Journal of Solids and Structures*. 1 January 2015;*52*:83-102
- [37] Persson BNJ. Relation between interfacial separation and load: A general theory of contact mechanics. *Physical Review Letters*. 2007;*99*(12):1-4
- [38] Persson BNJ, Albohr O, Tartaglino U, Volokitin AI, Tosatti E. On the nature of surface roughness with application to contact mechanics, sealing, rubber friction and adhesion. *Journal of Physics: Condensed Matter*. 2004;*17*:R1-R62
- [39] Persson BNJ. Contact mechanics for randomly rough surfaces. *Surface Science Reports*. 2006;*61*:201-227
- [40] Manners W, Greenwood JA. Some observations on Persson's diffusion theory of elastic contact. *Wear*. 2006;*261*:600-610
- [41] Hyun S, Pei L, Molinari J-F, Robbins MO. Finite-element analysis of contact between elastic self-affine surfaces. *Physical Review E*. 2004;*70*:026117
- [42] Polonsky IA, Keer LM. A numerical method for solving rough contact problems based on the multi-level multi-summation and conjugate gradient techniques. *Wear*. July 1999;*231*(2):206-219
- [43] Stanley HM, Kato T. An FFT-based method for rough surface contact. *Journal of Tribology*. 1997;*119*:481-485
- [44] Bemporad A, Paggi M. Optimization algorithms for the solution of the frictionless normal contact between rough surfaces. *International Journal of Solids and Structures*. 2015;*69-70*:94-105
- [45] Brandt A, Lubrecht AA. Multilevel matrix multiplication and fast solution of integral equations. *Journal of Computational Physics*. 1990;*90*:348-370
- [46] Venner CH, Lubrecht AA. Numerical analysis of the influence of waviness on the film thickness of a circular EHL contact. *Journal of Tribology*. 1996;*118*:153-161
- [47] Lubrecht AA, Ioannides E. A fast solution of the dry contact problem and the associated sub-surface stress field, using multilevel techniques. *Journal of Tribology*. 1991;*113*:128-133
- [48] Nogi T, Kato T. Influence of a hard surface layer on the limit of elastic contact part I: Analysis using a real surface model. *Journal of Tribology*. 1997;*119*:493-500
- [49] Polonsky IA, Keer LM. A fast and accurate method for numerical analysis of elastic layered contacts. *Journal of Tribology*. 1999;*122*:30-35
- [50] Popov VL, Pohrt R, Li Q. Strength of adhesive contacts: Influence of contact geometry and material gradients. *Friction*. 2017;*5*:308-325
- [51] Li Q, Argatov I, Popov VL. Onset of detachment in adhesive contact of an elastic half-space and flat-ended punches with non-circular shape: Analytic estimates and comparison with numeric analysis. *Journal of Physics D: Applied Physics*. 2018;*51*:145601
- [52] Paggi M, Bemporad A, Reinoso J. Computational methods for contact problems with roughness. In: Paggi M, Hills D, editors. *Modeling and Simulation of Tribological Problems in Technology* CISM International Centre for Mechanical

Sciences. Cham: Springer International Publishing; 2020. pp. 131-178

Press; June 2021, 1985. ISBN: 9781139171731. DOI: 10.1017/CBO9781139171731

[53] Frrot L, Bonnet M, Molinari J-F, Anciaux G. A Fourier-accelerated volume integral method for elastoplastic contact. *Computer Methods in Applied Mechanics and Engineering*. 2019;**351**: 951-976

[61] Leroux J, Fulleringer B, Nlias D. Contact analysis in presence of spherical inhomogeneities within a half-space. *International Journal of Solids and Structures*. 2010;**47**:3034-3049

[54] Seitz A, Wall WA, Popp A. Nitsches method for finite deformation thermomechanical contact problems. *Computational Mechanics*. 2019;**63**: 1091-1110

[62] Cottle RW, Pang J-S, Stone RE. *The Linear Complementarity Problem*. Society for Industrial and Applied Mathematics. Classics in Applied Mathematics 2009. ISBN:978-0-89871-686-3. eISBN:978-0-89871-900-0. DOI: 10.1137/1.9780898719000

[55] Seitz A, Wall WA, Popp A. A computational approach for thermo-elasto-plastic frictional contact based on a monolithic formulation using non-smooth nonlinear complementarity functions. *Advanced Modeling and Simulation in Engineering Sciences*. 2018;**5**:5

[63] Persson BN, Albohr O, Tartaglino U, Volokitin AI, Tosatti E. On the nature of surface roughness with application to contact mechanics, sealing, rubber friction and adhesion. *Journal of Physics: Condensed Matter*. 2005;**17**(1):R1. Available from: <https://iopscience.iop.org/article/10.1088/0953-8984/17/1/R01>

[56] McCool JJ. Finite difference spectral moment estimation for profiles the effect of sample spacing and quantization error. *Precision Engineering*. 1982;**4**(4):181-184

[64] Jacobs TD, Junge T, Pastewka L. Quantitative characterization of surface topography using spectral analysis. *Surface Topography: Metrology and Properties*. 2017;**5**(5):013001. Available from: <https://iopscience.iop.org/article/10.1088/2051-672X/aa51f8/meta>

[57] Poon CY, Bhushan B. Comparison of surface roughness measurements by stylus profiler, AFM and non-contact optical profiler. *Wear*. 1995;**190**:76-88

[58] Zhang S, Song H, Sandfeld S, Liu X, Wei YG. Discrete Greenwood Williamson modeling of rough surface contact accounting for three-dimensional sinusoidal asperities and asperity interaction. *Journal of Tribology*. 2019;**141**(12):121401 (11 pages). DOI: 10.1115/1.4044635

[65] Carbone G, Bottiglione F. Asperity contact theories: Do they predict linearity between contact area and load? *Journal of the Mechanics and Physics of Solids*. 2008;**56**:2555-2572

[59] Ciavarella M, Delfine V, Demelio G. A "re-vitalized" Greenwood and Williamson model of elastic contact between fractal surfaces. *Journal of the Mechanics and Physics of Solids*. 2006; **54**(12):2569-2591

[66] Carbone G, Bottiglione F. Contact mechanics of rough surfaces: A comparison between theories. *Meccanica*. 2011;**46**:557-565

[60] Johnson K. *Contact Mechanics*. Cambridge: Cambridge University

Remote Nondestructive Thermal Control of Elastic Abrasive Cutting

Anna Stoyanova, Irina Aleksandrova and Anatoliy Aleksandrov

Abstract

High temperatures during abrasive cutting lead to increased harmful gas emissions released into the environment, intensified cut-off wheel wear, microstructural changes in the machined material, and occurrence of thermal flaws. Temperature measurement in abrasive cutting is difficult due to the small size of the heated area (only tenths of mm^2), high temperatures (above 1000°C), continuous change of the conditions within one cut-off cycle, large temperature gradient (more than 200°C), high cutting speed (above 50 m/s) and high mechanical load. The infrared thermography (IRT) application for thermal control of elastic abrasive cutting have been studied. The performed thermal measurements have been verified with the results obtained from the temperature models of workpiece, cut-off wheel, and cut piece depending on the conditions in elastic abrasive cutting of two structural steels C45 and 42Cr4. The parameters of effective abrasive cutting have been determined by applying multi-objective optimization.

Keywords: abrasive technology, elastic abrasive cutting, nondestructive thermal control, multi-objective optimization

1. Introduction

Abrasive cutting is widely used in industry due to its high production rate (machining is performed at a speed of $100\text{--}200\text{ mm}^2/\text{s}$) and low labor costs. It is characterized by high temperatures (above 1000°C) in the cutting zone, intensive wear and deterioration of the abrasive tool cutting ability, spark generation, increased emissions of environmentally harmful gases, high noise level, risk of accidents, changes in the microstructure of surface materials and occurrence of thermal flaws [1–7]. Those disadvantages are related to the high cutting speed (above 50 m/s), constant changes in cutting conditions within a cut-off cycle, and unfavorable geometry of abrasive grains (negative rake angles).

Almost all mechanical work (over 97%) converts into thermal energy and only a small part of it transforms into hidden energy to change the crystal lattice of the material being machined [8, 9].

As a result of the conversion of the mechanical energy used in the cutting process into thermal energy, various heat sources emerge and the process of generating that heat depends on cutting conditions.

As far as every physical phenomenon has two sides—quantitative and qualitative, then, as a rule, the control of the energy transfer in a specific physical phenomenon involves the measurement of two quantities. When controlling heat

exchange processes, the two quantities to be measured are temperature and thermal flux. Measuring the thermal parameters of thermal non-stationary processes, in particular, a rapidly changing thermal flux remains relevant today. Among the techniques for measuring unstable thermal fluxes, those using infrared cameras are preferred [10–12]. Infrared thermography provides remote and wireless real-time measurements of temperature fields of high-speed moving objects. However, to obtain accurate measurements, all emerging noises and interferences need to be compensated or minimized, which is a kind of a “payoff” for the universality of the thermographic thermal control.

By changing the abrasive cutting conditions, which directly define the thickness of the layer of material being cut, and, as a result, the temperatures of the tool, chip, workpiece, and cut piece, the thermal fluxes are controlled and conditions for increasing the tool life, the intensity of the cutting process and the quality of the machined surfaces are provided. Therefore, to improve the effectiveness and applicability of abrasive cutting, it is necessary to study and model the parameters of the process and to optimize the conditions for its implementation. This allows us to apply thermographic monitoring for preventive detection of unexpected changes in the parameters of the elastic abrasive cutting process and for ensuring a high-quality process.

To study the thermal phenomena in elastic abrasive cutting, an innovative approach has been used. It involves a wireless thermal control provided by infrared thermography and the application of the methodology of planned experiments and multi-objective optimization. An original thermographic procedure for increasing the precision of the thermal control during abrasive cutting is offered.

2. Abrasive cutting as a subject of thermal investigation, modeling, and optimization

The manufacture of workpieces by cutting is implemented on various machines and installations (automatic lathes, band cutting machines, mechanical hacksaws, band saws circular saws, abrasive cut-off machines, presses, electric spark, and electrochemical installations) depending on the dimensions, profile, type and physico-mechanical properties of the input material and the admissible deviation from nominal dimensions. When comparing cutting methods by technological criteria, the most important criteria are cutting intensity (production rate), tool life, and material loss in the form of chips related to the cut width. Choosing an optimal variant for workpiece cutting is a technical and economic task, which has a considerable impact on the cost of the machine-building production.

Abrasive cutting is a universal method that is applied to manufacturing workpieces of metal and non-metal materials of different hardness by means of high-speed reinforced abrasive (cut-off) wheels of a diameter d_s ranging from 115 to 400 mm and a width ranging from 2 to 3.5 mm. Abrasive cut-off wheels are highly effective self-sharpening tools that perform cutting by means of thousands of miniature “cutting tools”—abrasive grains of aluminum oxide or silicon carbide.

Reinforced cut-off wheels whose grain size is in compliance with ISO 8486—grain numbers from 24 (coarse) to 60 (fine); medium-hard (*P*), hard (*R* or *S*), and very hard (*T*), with a BF bond—fiber-reinforced resinoid bond or an AGE bond—glass-fiber-reinforced resinoid bond providing higher safety against breakage, are used [13, 14].

Abrasive cutting is a complex and varied process performed under different kinematic schema (**Figure 1**) where the cut-off wheel performs the main rotary motion (at a rotational frequency n_c) and a radial feed (at a speed V_{fr}) (**Figure 1a**).

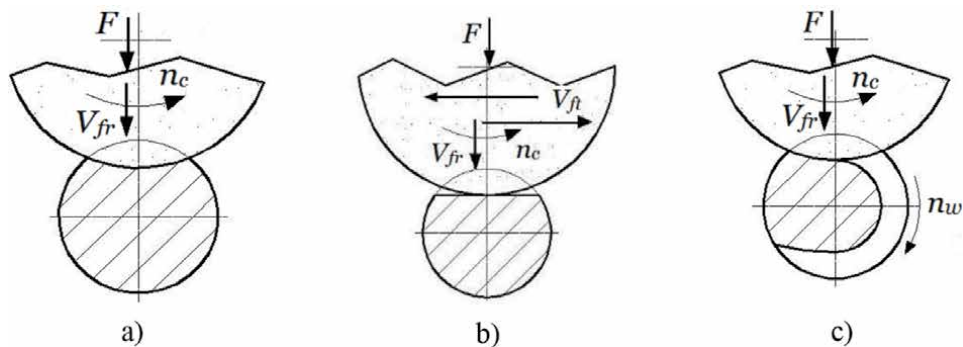


Figure 1.
 Schemas of abrasive cutting.

To facilitate the cutting process, an oscillatory motion (at a speed V_{ft}) of the cut-off wheel in a direction perpendicular to the basic feed (**Figure 1b**) or a rotary motion of the workpiece (at a rotational frequency n_w) (**Figure 1c**) is introduced [1, 2, 4, 15–17].

The oscillatory motion facilitates the cutting process and helps to reduce the cost of the abrasive wheels. However, some shocks occur at both ends of the oscillatory motion, which leads to overloading the cut-off wheel, occurrence of vibrations, and an increase in wear. The implementation of such a motion makes the machine complex and costly. Those disadvantages are avoided when using the schema including a rotary motion of the workpiece (**Figure 1c**). If we compare abrasive cutting schemas, it can be seen that when performing a cut-off cycle (cutting one workpiece), the cut-off wheel working stroke upon cutting a rotating workpiece (**Figure 1c**) is approximately twice as short as that for the schemas in **Figure 1a** and **b**. It results in reducing the cut-off time and the friction forces between the lateral surfaces of the cut-off wheel and workpiece thus, on one hand, decreasing the temperature in the cutting zone and cut-off wheel wear and, on the other hand, increasing process production rate. When cutting a rotating workpiece, the lower cut-off wheel wear and the higher production rate is also due to the shorter length L of the contact arc between the cut-off wheel and the workpiece in comparison to the one used when cutting a fixed workpiece. In cutting a fixed workpiece, the chips produced in the process of cutting do not fit in the cut-off wheel pores, which results from the higher values of the contact arc L regardless of the thinner layer being cut. Therefore, the process production rate decreases, and tool wear increases.

The cut-off wheel can be fed into the workpiece at a constant speed of radial feed ($V_{fr} = \text{const}$) provided in a kinematic way by the cutting machine (rigid abrasive cutting) or can be pressed onto the workpiece with a constant force F ($V_{fr} \neq \text{const}$)—elastic abrasive cutting [3].

The kinematic schemas of rigid abrasive cutting are similar to those in external cylindrical grinding, where dependencies for defining the tool-workpiece contact area, contact arc length, and thickness of layer being cut, pointed in [14, 18–20], are required. The principal disadvantage of this method is the change in the power and heat loads of the cut-off wheel within one cut-off cycle, which is related to the change in the instantaneous cross-sectional area of the layer is cut. This results from the fact that with the cut-off wheel feed from the periphery to the center of the workpiece being cut the contact arc length between the cut-off wheel and the piece changes as the instantaneous thickness of the layer being cut h remains constant (with a fixed workpiece) or changes according to a particular law (with a rotating workpiece).

Within one cycle of elastic abrasive cutting, the length of the contact arc L and the thickness h of the layer being cut change, while the instantaneous cross-sectional area of this layer remains constant [8, 15, 21–23]. This ensures stabilization of the dynamic and thermal phenomena accompanying cutting and appears a precondition for more effective use of the cut-off wheel, as well as for enhancing the quality of the machined surface. Simultaneously, the contact arc length L , the thickness h of the layer being cut and the cutting depth a depend on the process operating conditions, which determines the effect of the compression force F , workpiece rotational frequency n_w and cut-off wheel diameter d_s , on the process parameters—tool wear, tool life, production rate, cutting forces and power, temperatures of the cut-off wheel, workpiece, and cut piece.

1. The increase of the compression force F results in an increase in the contact arc length L and cutting depth a . It is, on one hand, a precondition for increasing the process production rate and, on the other hand, for increasing the temperature of the cut-off wheel, workpiece, and cut piece, as well as the wear of the cut-off wheel since its pores are filled with chips very fast.
2. The increase in the workpiece rotational frequency n_w results in an equivalent increase of the tangential feed rate thus increasing the thickness of the chip being cut by a single abrasive grain and faster filling the cut-off wheel pores, i.e. more intensive tool wear and longer time per cut. On the other hand, the increase of n_w leads to an increase in the contact zone between the cut-off wheel and workpiece as a result of the increase of contact arc. This, coupled with the fact that in the course of cutting the workpiece appears a tool coolant absorbing part of the released heat, which subsequently is transferred to the chip, determines the increase of the workpiece temperature and the decrease of the cut-off wheel temperature. The increase of the workpiece rotational frequency implies a decrease of the cut piece temperature on account of an increase in the thickness of the layer is cut and the cross-section of the chip being cut by one abrasive grain, as well as enhanced heat removal resulting from the longer time per cut.
3. As the cut-off wheel diameter d_s decreases, the number of abrasive grains cutting a layer per one revolution of the cut-off wheel also decreases. This causes an increase in the thickness of the chip being cut by one abrasive grain. In addition, when the cut-off wheel rotational frequency is constant, the decrease of the wheel diameter results in a decrease of speed, which further deteriorates the cutting abilities of the abrasive grains. All this is a precondition for increasing the dimension and rate of cut-off wheel wear, the time per cut, and the workpiece temperature and, on the other hand, for decreasing the temperature of the cut piece and cut-off wheel because of enhanced heat removal.

The analysis has been carried out shows that elastic abrasive cutting is a sophisticated multi-parameter and multi-factor subject of study, modeling, and optimization [24]. It is characterized by a number of target parameters—economic (productivity and cost), dynamic (cutting forces and power) and technological (cut-off wheel wear and tool life, cutting temperature, noise, roughness and precision of machined surfaces, physico-mechanical properties of the surface layer—structure, microhardness, surface residual stresses, flaws, etc.). Each of the above parameters has a specific meaning in relation to abrasive cutting yet is insufficient for its optimum control.

The parameters of elastic abrasive cutting are determined by numerous control factors—physico-mechanical properties of the materials being machined, methods and components of the cutting mode, cut-off wheel type and characteristics, type and way of supplying cooling fluids, etc.

In the course of abrasive cutting, a number of interrelated, yet of a different type, nature, and intensity, phenomena occur and various materials, cut-off wheels, and cutting modes are used. Each abrasive cutting process is unique and could be studied from different perspectives: technological, energetic, informational, organizational, etc. When it is investigated, new experimental data and models are obtained, which differ from those of the preceding processes. Therefore, its investigation, modeling, analyzing, control, and optimization are always specific.

3. Thermal phenomena in abrasive cutting

3.1 Heat generation and heat removal in abrasive cutting

The mechanical work done in cutting involves deformation (elastic and plastic) of the material being machined, action of friction forces on the face and flank of cutting abrasive grains, and formation of new surfaces (dispersion). The amount of heat generated in cutting per unit of time, expressed by the work done in cutting and the mechanical equivalent of heat ($I = 427 \text{ kgm/kcal}$), is as follows:

$$Q = \frac{F_c V_c}{I} = 9.8 F_c V_c \quad (1)$$

where: F_c —main cutting force; V_c —cutting velocity; $V_c = V_s$ (V_s —velocity of the main rotary motion of the cut-off wheel).

Intensive thermal fluxes flow through the tool, chip, and material being machined in high-speed abrasive cutting. The large amount of heat generated in the course of abrasive cutting is transferred to the workpiece (Q_w), cut-off wheel (Q_s), and chip (Q_{ch}) and it is released into the environment (Q_p) [4, 7, 8, 21, 22, 25]. The transfer of heat in those directions is implemented by heat conduction, convection, and radiation.

A wide range of changes in the thermal flux components depending on the selected schema for process implementation (rigid or elastic abrasive cutting), the characteristic of the cut-off wheel, the physico-mechanical properties of the material being machined and the cutting mode has been established.

$Q_w = (10\% \div 85\%)Q$; $Q_w = (10\% \div 85\%)Q$; $Q_{ch} = (30\% \div 75\%)Q$; $Q_p \approx 10\%Q$ [4, 7, 8, 22, 25, 26]. This implies different temperatures of the working and lateral surfaces of the cut-off wheel, as well as different temperatures of the workpiece and chip.

Actually, the whole action of the friction forces in the contact zone below the neutral line AF (**Figure 2**) is transformed into heat (Q_f) and enters the workpiece.

During the initial contact between the abrasive grain and the workpiece, taking into account the comma-shaped cross-section of the layer being cut when $h < h_k$ (h_k —thickness of the layer being cut, where micro-cutting starts, and which depends on the radius of curvature of the edge of the abrasive grain), chipless plastic ejection of the material being machined occurs before the abrasive grain. There is also some heat dissipation [14, 17, 19]. Heat transfer is implemented by heat conduction and radiation.

When the values of the layer being cut are $h > h_k$, a cutting process where chips are formed starts. The heat Q_d generated as a result of deformation and used for

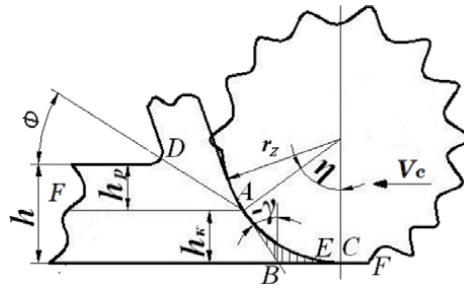


Figure 2.
Schema of chip formation in abrasive cutting.

shear along the shear surface within chip formation depends on the thickness of the material being cut h_z and the cross-section A_z of the material being cut by one abrasive grain. It is distributed as the heat transferred to the chip and heat transferred to the workpiece. It is assumed that the part of heat Q_d transferred to the workpiece is $Q_w = 0.7Q_d$ [14, 17, 19]. In fact, the heat resulting from chip formation and transferred to the chip is less due to convection losses.

The part of heat transferred to the workpiece is reduced when increasing the cutting speed because of the change in the ratio between the cutting speed and the heat dissipation rate in the deformation zone [14, 17, 19]. The dissipation rate of generated heat depends on the gradient of the temperatures along the shear surface and the heat conductivity of the material being machined. When the cutting speed, i.e. the speed at which the abrasive grain crosses the thermal flux, is low, the heat from the shear surface is transferred unobstructed to the workpiece. As the cutting speed increases, the cutting abrasive grain crosses the thermal flux faster and faster. As a result, a smaller amount of heat is transferred to the workpiece and a larger amount of heat remains in the chip:

$$Q_w = 0.7\chi Q_d \quad (2)$$

where χ is a coefficient of a decrease of the heat transferred to the workpiece caused by the change in the ratio between the cutting speed and heat dissipation rate [19, 27] $\chi = 0.3 + (80.1 - V_c)10^{-3}$.

Since a large part of heat (almost all the heat generated by plastic deformation and part of the heat generated by friction) is generated in the chip, the largest part of process heat remains there. Heat in the abrasive grain occurs externally as a result of friction and heat transfer from the hot chip to the colder abrasive grain, from plastic deformation, from the shear of the material under the neutral line, as well as from friction along the grain flank. As a consequence of conduction, the heat generated on the surface AB (**Figure 2**) is transferred to the abrasive grain and workpiece. The better the heat transfer from the surfaces being heated, the lower the temperature of those surfaces, i.e. the properties of heat conductivity and heat resistance influence the performance of cut-off wheels and the quality of machined surfaces.

The temperature of the cut-off wheel work surfaces (above 100°C) depends on the thermal flux density $\phi = dQ/dA$ (A —contact surface area of the abrasive cut-off wheel and workpiece) and tool thermal characteristics. In the course of cutting heat enters the material being machined through the contact area between the cut-off wheel and workpiece. The size of that area and, respectively, the dimensions and power of the heat source depend on the parameters of the cutting mode. The shape and dimensions of the heat source are mainly determined by the cut-off wheel thickness b_s , the wheel characteristics, and the length of the contact arc L between the tool and workpiece. In the course of cutting the workpiece appears a coolant of

the tool, absorbing part of the released heat, which is consequently transferred to the chip. In this respect, it would be better to expand the contact zone (b_sL), which would result in an increase of the workpiece temperature and a decrease in the cut-off wheel temperature. Simultaneously, the temperature in the cutting zone is also affected by load of abrasive grains and the volume of the machined material removed by one abrasive grain, which are directly dependent on the wheel characteristics.

The cutting process in abrasive cutting is accompanied by melting of chips and plenty of sparking, which result from a large amount of heat generated in the cutting zone by friction forces, deformation of the material being machined, and reaction during burning. During burning every material has a specific point at which it ignites. When reaching the ignition temperature under the influence of oxygen, the physically and chemically clean surfaces of the steel workpieces being machined are oxidized to form iron oxide and slag. During oxidation, a considerable amount of heat is released, which provides additional heating of the very small volumes of metal of the chips removed by the abrasive grains up to the melting temperature. The presence of carbon in the material being machined increases burning and the temperature in the cutting zone, which is the reason for the different colors of the formed sparks in abrasive machining. Under the influence of the high speed of the abrasive cut-off wheel grains, the slag and iron oxide been formed are removed as glowing sparks [17]. The oxidation of the chip and the material being machined is useful since the oxide crust is fragile and facilitates chip removal. In accordance with the foregoing, the melting of the chip can be viewed as a positive factor because after melting the chip decreases its dimensions, which contributes to its easier removal by the cut-off wheel and to avoiding the filling of the tool pores with chips.

The burning of materials in abrasive cutting does not allow us to directly measure the temperature of the removed chip since it ignites when it forms or immediately after that. The brightness and type of sparks formed during abrasive machining (a product of burning) are defined solely by the content of the chemical elements in the material being machined. The density and length of the spark flow depend on the components of the cutting mode.

The increase of the heat entering the cut-off wheel intensifies tool wear and decreases tool reliability and cutting intensity as a result of a decrease in the relative pressure of the abrasive grains on the surface being machined (because of the softening of the cut-off wheel bond). Heating up the workpiece in the cutting zone leads to changes in the microstructure of the surface material and the occurrence of thermal flaws. Structural changes in the cross-section of the cut, which require further machining, also occur as a result of smearing and chipping parts of the cut-off wheel, as well as of friction between its lateral surfaces and workpiece face [6, 7]. All the above mentioned demonstrates the decisive role of temperature in abrasive cutting regarding cut-off wheel performance and quality of machined surfaces. It also shows that the heat released in the course of abrasive cutting is an important informative factor for optimizing the operating conditions in abrasive cutting and enhancing the effectiveness of the process and the quality of machined surfaces. Therefore, it needs to be studied, modeled, and optimized. The investigation and measurement of temperature distribution in abrasive cutting play a key role in machine building.

A great number of studies [4, 7, 15, 21, 22, 28] show that by controlling the thermal fluxes in the cutting zone, possibilities for improving the cut-off thermal mode are provided thus ensuring longer tool life, higher intensity of the cutting process and higher quality of machined surfaces. This could be achieved not only by changing abrasive cutting conditions (cutting schema and parameters of cutting

mode), which directly determine the thickness of the layer being cut, and respectively the temperatures of the tool, chip, workpiece, and cut piece, but also by choosing the cut-off wheel characteristic.

3.2 Methods and tools for investigating temperature in abrasive cutting

Depending on the specific nature of cutting processes, various methods for investigating temperature are applied [27]:

1. Analytical and numerical methods (heat source method; finite difference method; finite element method)—They are based on the heat balance equation and the differential equation of heat conduction [27]:

$$\lambda \left(\frac{\partial^2 \theta}{\partial x^2} + \frac{\partial^2 \theta}{\partial y^2} \right) - \rho C_p \left(V_c \frac{\partial \theta}{\partial x} + V_f \frac{\partial \theta}{\partial y} \right) + \dot{Q} = 0 \quad (3)$$

where: λ —thermal conductivity coefficient; C_p —specific heat capacity of the chip material; ρ —material density; θ —temperature of a point with coordinates x, y ; $\dot{Q} = \tau_s \dot{\epsilon}$ —heat exchange rate per unit of volume (τ_s —stress of cutting; $\dot{\epsilon}$ —speed of plastic deformation).

2. Experimental methods—They are used to measure the average and local temperatures, determine the zone of temperature distribution, and to visualize the temperature field. According to the way of measurement they are as follows:

- Contact methods—Indirect (calorimetric technique, microstructural analysis technique, method of chip coloring, thermal pain technique, and electrical modeling) and direct—thermocouple technique (artificial, semi-artificial, natural, and running). With those methods, the energy exchange between the environment and thermometric substance is based on heat conduction [29].
- Wireless measurement methods—They are based on the laws of thermal radiation of bodies. The wireless temperature measurement devices used in practice are as follows: optical pyrometers, spectral ratio pyrometers, radiation pyrometers, infrared thermometers, thermal imaging cameras [29, 30]. Choosing a proper device depends on a number of factors—temperature range, material, object dimensions, distance, ambient temperature. It should also be taken into account that the devices record the total energy in their range of vision. When measuring, they also include additional energy sources, including reflected energy, if they are in the range of vision.

Measuring temperature in abrasive cutting is difficult because of the small dimensions of the zone being heated (only tenths of mm^2), high temperatures (hundreds of degrees Celsius), high-temperature gradient (more than $200^\circ\text{C}/\text{mm}^2$), high mechanical load, and high heating speed. This predetermines the preferential use of analytical and numeric methods, as well as wireless methods, for investigating the thermal phenomena in that process.

The thermal phenomena in rigid abrasive cutting are well studied unlike those in elastic abrasive cutting. Numeric, analytical, and finite-element models were

developed to define and analyze temperature distribution [3, 13, 18, 20, 31]. Thermal fluxes were investigated under different cutting conditions and strategies for optimizing the parameters of rigid abrasive cutting with regard to decreasing the temperature in the cutting zone were proposed [32–41]. In addition, a high-accuracy simulation model for forecasting temperature was proposed. It can be used for forecasting and preventing thermal flaws [33].

Analytical models for determining the temperature in elastic abrasive cutting were also proposed. On the basis of the analysis of thermal phenomena, the inability to directly measure chip temperature was justified and a methodology and an analytical dependency for the theoretic definition of chip temperature, reflecting the effect of the cutting speed and the workpiece rotational frequency, were proposed [42]. A model of the chip temperature, proving the decisive influence of the thickness of the layer being cut by one abrasive grain on it, was developed. An approach to the theoretical and experimental definition of the amount of heat released for one cut-off cycle and transferred to the workpiece being machined, as well as of the cut piece temperature, was proposed [43].

By applying the calorimetric technique for measuring temperature and the methodology of the planned experiment, a theoretical and experimental model for the temperature of the cut piece made of C45 steel depending on the cut-off wheel speed and workpiece rotational frequency was built. It was established that cut piece temperature decreases as cutting speed decreases and workpiece rotational frequency increases. This effect is related to the enhanced heat removal resulting from an increase in the thickness of the layer being cut, the cross-section of the chip being cut by one abrasive grain, and time per cut.

The possibilities for wireless temperature measurement and monitoring by applying infrared thermography are studied in [4, 7, 25, 44]. It was found that the cut-off wheel compression force on the workpiece had the greatest effect on the maximum cut-off wheel temperature, respectively on the tool life [4, 7]. It was also found that temperature increased as the workpiece diameter increased. Furthermore, when cutting fixed workpieces, the combination of larger cut-off wheel diameter and a greater compression force results in generating higher temperatures and obtaining lower values of G-ratio. Studies were done with a focus on the possibilities of using infrared thermography as a tool for wireless and non-invasive thermal investigation of the process and tools of elastic abrasive cutting of rotating workpieces [25, 44]. Experimental data from thermographic measurements done by an infrared camera regarding the effect of workpiece rotational frequency, compression workforce, and cut-off wheel diameter when machining various materials on the temperature distribution on workpiece surface, cut-off wheel, and cut piece were presented.

The analysis of the methods and approaches used for investigating and monitoring temperature in abrasive cutting shows the advantages of wireless measurement methods such as infrared thermography (IRT). This method is increasingly recognized and widely used as a reliable and effective tool for thermal wireless non-destructive testing under real conditions of dynamic processes such as abrasive cutting [4, 7, 12, 25, 29, 44]. Its application allows us to enhance the effectiveness of abrasive cutting. However, the use of IRT has some disadvantages.

The availability of metal parts in equipment leads to a number of reflections that impede temperature measurements on the surfaces under study and vary depending on their orientation, temperature, and wavelength. Temperature measurements by using thermography do not provide us with absolute temperature values. To obtain such values, we should use modeling and look for a correlation with the change in surface temperature. IRT measurements are indirect with regard to temperature measurements in the cutting zone. Although the cut-off zone can be observed from

the side at a specific position of the camera, the infrared radiation from the cut-off wheel, workpiece, and produced chips affect the results from the temperature measurement of the surface being observed. Therefore, a thorough study of the possibilities for applying infrared thermography in abrasive cutting is required.

4. Infrared thermal control of elastic abrasive cutting

There is a qualitative and quantitative non-contact thermographic temperature control. Qualitative control does not require obtaining an accurate surface temperature, but it is sufficient to obtain thermal signatures, which are characteristic models of relative temperature phenomena at different combinations of the abrasive cutting process control factors values. The relative temperature values of the objects in the cutting area to the temperatures of the other equipment objects with similar conditions are used. Quality visual inspection is appropriate for collecting a large number of detailed data and transmitting them for easy interpretation. It is suitable for controlling the efficiency of the process by monitoring the temperatures of the cut-off wheel, workpiece, cut piece, and chip under certain conditions of the abrasive cutting process.

In quantitative thermographic measurement, the ambient temperature is the reference. The observation of the abrasive cutting is established by measuring the absolute temperature of the studied object, under the same environmental conditions. As the reference temperature must be measured, this requires even better knowledge of the variables affecting the radiometric measurement, as well as taking into account the limitations.

The transition from qualitative to quantitative thermographic control is associated with the need to solve four tasks:

- Methodical provision of the procedure for determining the surface temperature of the objects participating in the cutting process with the respective metrological analyses;
- Obtaining information about the spectral normal emissivity of the object and its surrounding background for the entire spectral range of the optoelectronic system;
- Taking into account the influence of the layers covering the surface of the controlled objects, partially transparent to the heat radiation, on the accuracy of determining the surface temperature by non-contact methods;
- Measurement of temperatures comparable to the temperature background, taking into account the influence of the background heat radiation on the experimental results.

The aim of the study is first to develop a methodology for monitoring the evolution of surface temperature to identify the process of elastic abrasive cutting by IRT. For this purpose, a modular thermographic measuring system is proposed to monitor the process from different positions.

The illustrated in **Figure 3a** and **b** setup is a part of the more complex experimental framework, which is not the object of the present study [13, 25, 31, 44, 45].

Special attachment is developed, which is fixed to the main carriage of a combined lathe, having a device for step-less adjustment of rotational frequency workpiece to perform the elastic abrasive cutting process [46, 47]. In this way, a constant rotational frequency of the cut-off wheel can be provided and adjust the amount of

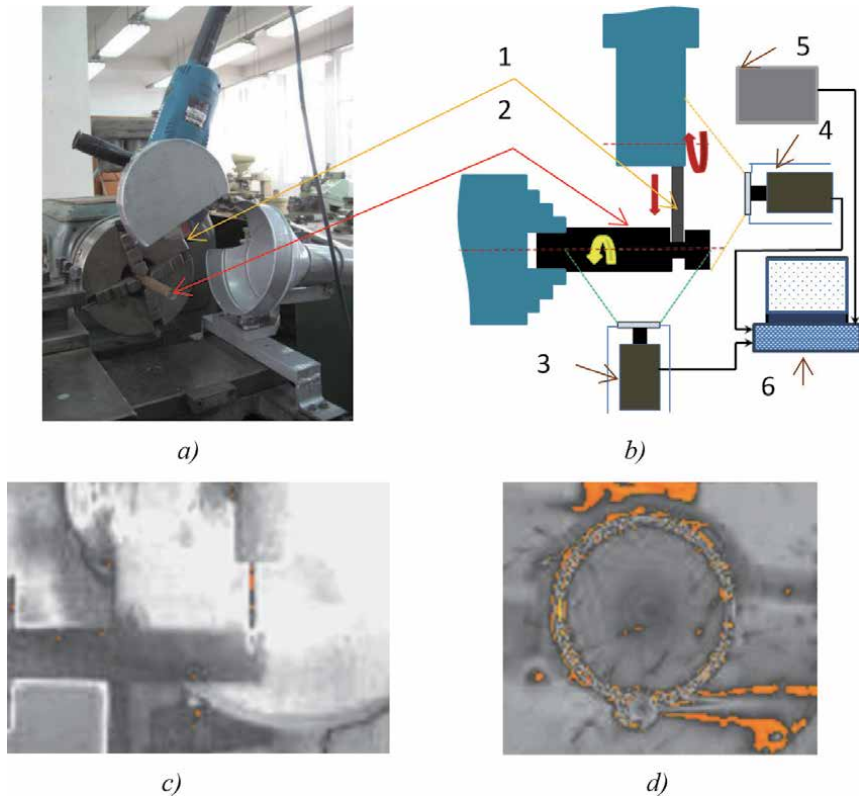


Figure 3. Elements of workstand for elastic abrasive cutting, (a); setup for remote thermal control of cutting process, (b); a thermogram of the abrasive cutting made from the direction to profile of the cut-off wheel, (c); a thermogram of the abrasive cutting made from the direction to full-face of the cut-off wheel, (d).

compression power F of the cut-off wheel (2) on the workpiece (1). High-speed reinforced cut-off wheels 41–180 × 22.2 × 3.0 A30RBF have been used during counter-directional cutting. Steel cylindrical rods with a diameter of 30 mm of C45 (1.0503) and 42CR4 (1.7045) were processed. **Figure 3c** and **d** shows the raw thermograms and the regions of interest (ROI) for the IRT control.

- a. Cut-off area of the workstand for elastic abrasive cutting
- b. Setup of abrasive cutting's remote non-destructive thermal control
- c. Raw thermogram from the camera (3) Raw thermogram from the camera (4)

Unlike previous studies, thermographic measurement of the surface temperatures is performed simultaneously with two factory-calibrated FLIR SC660 infrared cameras (3) and (4), which work synchronously with the same or different frame rates and are located orthogonally. The cameras have a temperature range from -40°C to $+2000^{\circ}\text{C}$, temperature sensitivity (NETD) $<0.045^{\circ}\text{C}$ and IP-link using FireWire. Matlab, FLIR ResearchIR Max and SDK softwares are used for thermal analysis and supporting cameras communication with the computer (6). The PASCO PS-3209 wireless sensor (5) is used in data collection mode for ambient temperature and relative humidity during thermographic measurements.

LabIR @ thermographic high-temperature applications paint, with high mechanical resistance for long-term uses and high emissivity is sprayed to cover the entire

work surface of the workpiece, the cut-off wheel, and exposed metal parts of the equipment. The layer paint thickness is measured by TROTEC BB20. Infrared cameras are located in isolating boxes with IR windows (shown in **Figure 3**). The outside of the boxes is also coated with paint to minimize the reflections from cameras.

A problem in the quantitative thermographic control of elastic abrasive cutting is the identification and suppression of thermal reflections in thermograms. The approach for thermal measurements of the process at an angle from 40 to 60°C was applied. Cold image subtraction and/or background subtraction is used as image processing methods for reflection reduction in thermograms.

After conducting the experiments for thermographic measurement to verify the calculated maximum temperatures of the cut-off wheel, workpiece, and cut piece and derive the corresponding correlation dependencies, the need to use a second infrared camera was eliminated. For the needs of elastic abrasive cutting online thermographic quality monitoring, only one camera is sufficient (camera (3) in **Figure 3b**).

Thermographic measurements were also performed with other approaches, which is not part of the present study. These relate to quantity thermography, such as the use of IR polarizing filters and deep learning to assess the condition of the elastic abrasive cutting process.

IRT used to detect the cut-off wheel wear can help abrasive cutting process automation and dynamically control.

The introduction of an online thermographic inspection system allows continuous monitoring of temperature evolution and thus prevents damage to the workpiece or machine. The following are illustrated possible information criteria for use in such a system.

Figure 4 illustrates the possibility of the IRT system to measure and record the surface temperatures (optional maximum, minimum, average values) in the camera field of vision. Areas (regions of interest—ROI, lines, polygons, etc.) can be selected to identify the temperature distribution and evolution in the process of abrasive cutting in the form of graphs. Such a local inspection of the change in surface temperature significantly increases the visual resolution of the selected area. This visualizes the momentary disturbances from the spark's temperatures. **Figure 4a** shows the temperature curves for the marked lines on the workpiece and the cut piece in a direction transverse to the workpiece axis and close to the cutting area. The temperature profile longitudinally on the axis of the workpiece in the area of the marked line is shown in **Figure 4c**. The temperature profiles for different lines passing through the axis of the cut-off wheel show the change in surface temperature near the cutting area and at the farthest end from this area. **Figure 4d** shows the regions of interest (ROI) for the workpiece, the cut-off wheel, and the cut piece whose maximum temperatures are measured.

Due to the lack of a standardized format for reading IR images, software for processing and computer analysis of thermographic images has been developed. So thermal images can be processed regardless of what type of camera they were shot. The wear of the cut-off wheels has been checked. For this purpose, they are divided into four categories: standard (new cut-off wheel, as a reference), slightly worn, critically worn, and worn, which can no longer be used. One or another classification can be prepared on the basis of different criteria for different applications of elastic abrasive cutting. During data processing, areas with elevated temperatures and possible causes of wear are identified. Thus, on the basis of the initial thermal histograms, criteria for diagnosing and evaluating the resources of the cut-off wheels are formed.

The thermal histogram family (according to the camera view of vision) of the entire thermogram or the thermal histogram family of a selected ROI can be used to account for deviations in the quality of the elastic abrasive cutting process relative to a pre-selected optimal process.

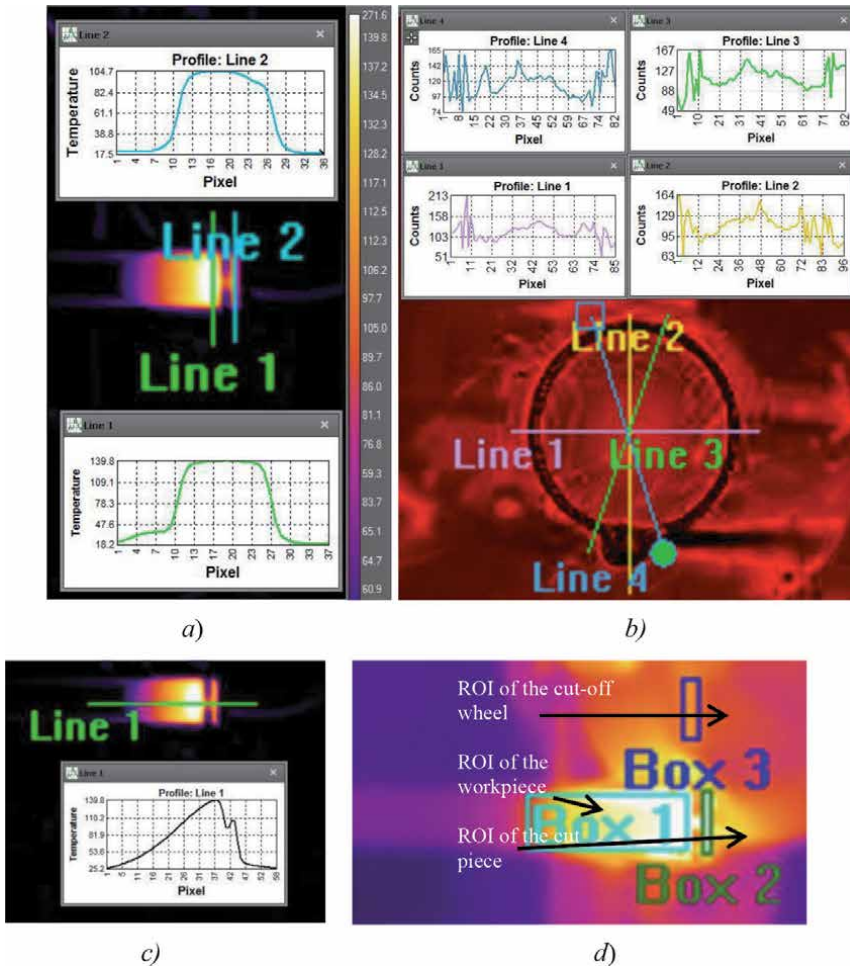


Figure 4. Thermograms image with chosen regions and temperature distribution along with selections. (a) Thermogram from camera (3) (b) thermogram from camera (4). (c) Thermogram from camera (3) (d) thermogram with chosen ROIs.

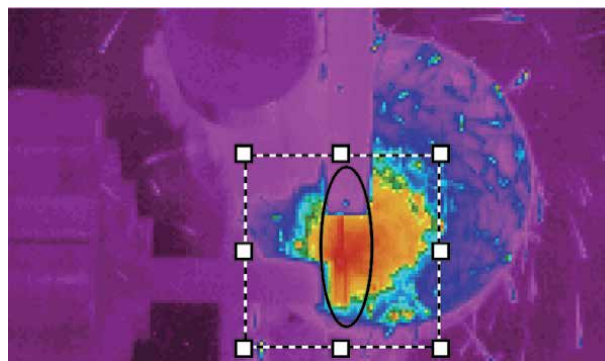


Figure 5. Infrared image captured with a standard thermal camera.

Figure 5 shows (according to the camera's view) a raw thermogram with selected ROI (rectangular area), and the area of the cut-off wheel marked with a black outline. **Figure 6** shows a raw 3D thermogram of the selected ROI. **Figure 7** shows the family of thermal histograms for the same ROI.

There are three density modes of temperature calculation in the histograms:

- High: per each pixel;
- Medium: average temperature using aperture size 3×3 ;
- Low: average temperature using aperture size 5×5 .

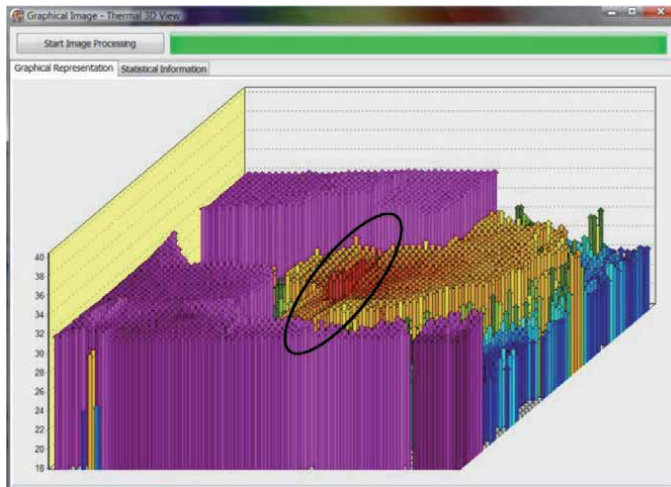


Figure 6.
3D thermogram of the selected ROI in Figure 5.

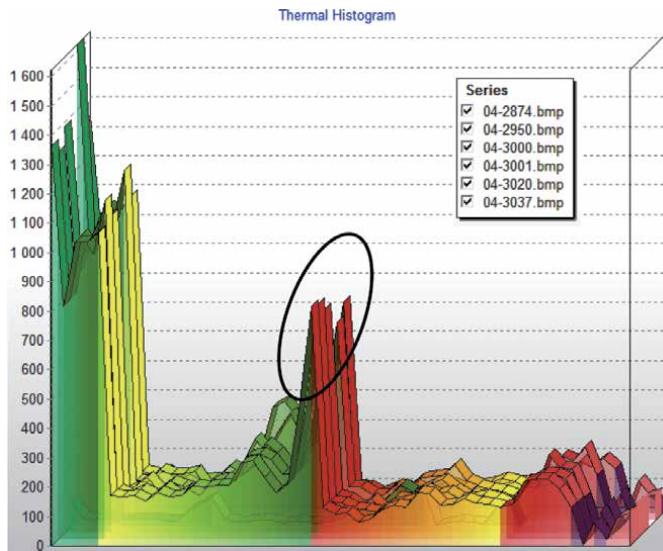


Figure 7.
3D layered thermal histograms (a family) for IR image sequence of the selected ROI with the workpiece, cut-off wheel, and cut piece.

Medium and Low approximations automatically exclude any garbage colors detected inside the camera apertures.

5. Thermal modeling and optimization of elastic abrasive cutting of structural steels

The general form of the models describes the dependency between the workpiece temperature T_w , cut-off wheel temperature T_s and cut piece temperature T_d in elastic abrasive cutting of C45 and 42Cr4 steels, and the operating conditions of the process (cut-off wheel diameter d_s , cut-off wheel compression force F exerted on the workpiece, and workpiece rotational frequency n_w), is as follows:

$$y_g = b_0 + \sum_{i=1}^3 b_i X_i + \sum_{i=1}^3 b_{ii} X_i^2 + \sum_{i < j} b_{ij} X_i X_j \quad (4)$$

where: y_g —studied response variables ($g = 1 - 6$): $y_1 = T_{w,C45}$, $y_2 = T_{s,C45}$, $y_3 = T_{d,C45}$, $y_4 = T_{w,42Cr4}$, $y_5 = T_{s,42Cr4}$, $y_6 = T_{d,42Cr4}$; $X_1 = d_s$, $X_2 = F$, $X_3 = n_w$ —control factors (**Table 1**).

To build the models (4), multi-factor experiments were conducted using an orthogonal central-composite design with a number of trials $N = 2^n + 2n + 1 = 15$ ($n = 3$ is the number of control factors). Three observations were made for each experiment. The variation levels of the factors, were chosen on the basis of preliminary conducted experimental studies on the cut-off wheel performance [13, 31] and thermal flux distribution in the workpiece, chip, cut-off wheel, and cut piece in elastic abrasive cutting [25, 44], are presented in **Table 1**.

The models (4) were built using the measured values of the workpiece maximum instantaneous temperature, cut-off wheel maximum contact temperature, and cut piece temperature at the end of the cut-off cycle.

After statistical analysis of the experimental results by applying the multi-factor regression analysis method and QstatLab software [48], the following regression models for the workpiece temperature, cut-off wheel temperature, and cut piece temperature were built:

- when machining C45 steels:

$$\begin{aligned} T_{s,42Cr4} &= 89.928 + 3.887d_s + 5F - 0.394n_w - 0.011d_s^2 \\ T_{s,C45} &= 103.865 + 0.447d_s + 8F - 0.201n_w \\ T_{d,C45} &= -88.426 + 3.69d_s + 4.667F - 0.359n_w - 0.011d_s^2 \end{aligned} \quad (5)$$

Factors		Factor levels		
		-1	0	+1
X_1	d_s (mm)	120	150	180
X_2	F (daN)	1	2	3
X_3	n_w (min^{-1})	22	91	160

Table 1.
 Factor levels in the experimental design.

- when machining 42Cr4 steels:

$$T_{w,42Cr4} = 2965.024 - 21.143d_s - 140.028F + 0.063d_s^2 + 37.403F^2 + 0.006n_w^2;$$

$$T_{s,42Cr4} = -89.928 + 3.887d_s + 5F - 0.394n_w - 0.011d_s^2$$

$$T_{d,42Cr4} = -89.928 + 3.887d_s + 5F - 0.394n_w - 0.011d_s^2$$

(6)

The models built extremely accurately describe the dependency between the variables and control factors. The values of the determination coefficients are $\hat{R}_g^2 = 0.849 - 0.965$ and they were determined at a significance level of $\alpha = 0.05$.

In **Figures 8** and **9** the bar diagrams of measured and calculated maximum temperatures are presented, at different parameters of the abrasive cutting process

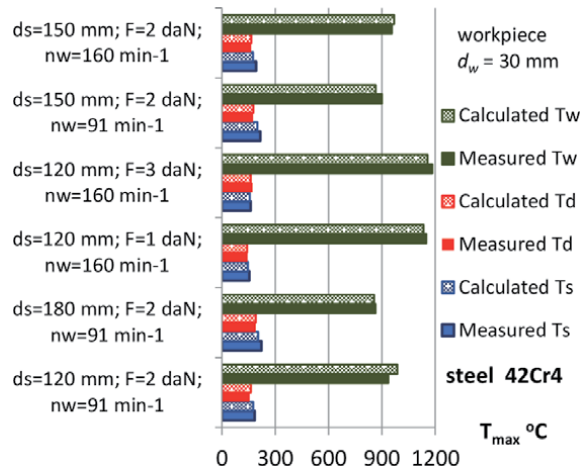


Figure 8. Temperature bar diagrams for different parameters of the elastic abrasive cutting of 42Cr4.

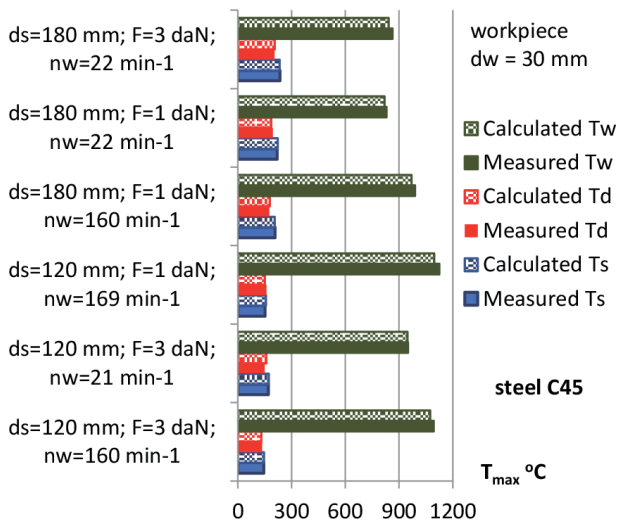


Figure 9. Temperature bar diagrams for different parameters of the elastic abrasive cutting of C45.

for both materials with the same workpiece diameter. The maximum temperatures are the averages of five measurements for the cut-off wheel, the workpiece, and the cut piece. The error of the calculated values does not exceed 2% (under 20°C) in the worst case.

The analysis of the models built makes possible the evaluation of the effect of the operating conditions on the temperatures of the workpiece, cut-off wheel, and cut piece:

- Among all factors under study, the workpiece rotational frequency has the highest effect on temperature in elastic abrasive cutting. As n_w increases within the range being studied, cut piece temperature and cut-off wheel temperature decrease (respectively by up to 29% and 19%) whereas workpiece temperature increases by up to 12%. The nature of this change is linked to the enhanced heat removal as a result of: the thicker layer being cut, the increased cross-section of the chip being cut off by one abrasive grain, the increased time per cut, and the increased contact zone between the cut-off wheel and workpiece resulting from the longer contact arc.
- As the cut-off wheel diameter d_s decreases within the range under study, cut piece temperature and cut-off wheel temperature decrease whereas the workpiece temperature increases as the change is within the range from 11 to 17%. That is related to the thicker layer being cut and the increased cross-section of the chip being cut off by one abrasive grain, which enhances heat removal as abrasive cut-off time increases and cutting speed decreases.
- The compression force has the least effect on temperature. As it increases, the temperatures of the cut piece, cut-off wheel, and workpiece increase by 5–11%. The minimum effect of the compression force is related to the fact that when F increases, the elastic abrasive time per cut decreases, and on the other hand, the length of contact arc and the depth of cut increase.
- The nature of influence of workpiece rotational frequency, cut-off wheel diameter and compression force on the temperature in elastic abrasive cutting are equal for the two materials under study (C45 and 42Cr4 steels). Nevertheless, the temperatures of cut-off wheel, workpiece, and cut piece are higher when machining 42Cr4 steel (by 4–7%), which is related to the higher hardness and strength of this material.

Each studied temperature parameter of the elastic abrasive cutting process has a specific meaning yet is insufficient for its optimum control. The optimum values of the temperatures of the cut piece, cut-off wheel, and workpiece for each material being machined will be obtained at different combinations of values of control factors (cut-off wheel diameter, compression force, and workpiece rotational frequency). Therefore, optimization by one parameter is irrelevant. Multi-objective optimization provides much more information so as to make a justified decision on the selection of optimum elastic abrasive cutting conditions. There are various algorithms for its implementation, which differ in the type and number of target parameters, as well as in the method for determining the optimal solution [45, 49]. To determine the optimum elastic abrasive cutting conditions, multi-purpose optimization was implemented as the area where the temperature parameters under study obtain minimum values were determined. The optimization problem is reduced to solving the following system of inequalities:

Steel, type	Optimization method	Control factors			Response variables		
		d_s (mm)	F (daN)	n_w (min ⁻¹)	T_w (°C)	T_s (°C)	T_d (°C)
C45	Genetic algorithm	150	2	91	863.15	168.53	199.2
	Random search method with increasing density	120	0.96	159.48	1057.03	133.02	133.02
42Cr4	Genetic algorithm	150	2	91	864.56	176.67	212.20
	Random search method with increasing density	120	0.8	159.99	1034.02	140.97	146.35

Table 2. Optimum conditions of elastic abrasive cutting.

$$\begin{cases}
 d_{s,l} \leq d_s \leq d_{s,u} \\
 F_l \leq F \leq F_u \\
 n_{w,l} \leq n_w \leq n_{w,u} \\
 T_d = f(d_s, F, n_w) \rightarrow \min \\
 T_s = f(d_s, F, n_w) \rightarrow \min \\
 T_w = f(d_s, F, n_w) \rightarrow \min
 \end{cases} \quad (7)$$

where $d_{s,l}$, $d_{s,u}$, F_l , F_u , $n_{w,l}$, $n_{w,u}$ are respectively the top and bottom levels of the control factors of the elastic abrasive cutting process (cut-off wheel diameter d_s , compression force F and workpiece rotational frequency n_w)—**Table 1**.

Functions $T_d = f(d_s, F, n_w)$, $T_s = f(d_s, F, n_w)$ and $T_w = f(d_s, F, n_w)$ reflecting the correlation dependencies of the temperatures of workpiece, cut-off wheel, and cut piece on the control factors of elastic abrasive cutting process are described by Eqs. (5) and (6) for the two materials being machined—C45 and 42Cr4 steels.

The optimum conditions of elastic abrasive cutting, providing the best combination of minimum values of the temperatures of workpiece, cut-off wheel, and cut piece, were determined by applying two methods—genetic algorithm and random search method with increasing density. The optimization problem was solved upon machining of C45 and 42Cr4 steels by using QStatLab software [48].

The defined optimum conditions of the elastic abrasive cutting process are presented in **Table 2**.

6. Conclusions

This chapter considers the specifics of implementing the process of elastic abrasive cutting and analyzes the conditions for stabilizing the dynamic thermal phenomena accompanying it. The processes of heat generation and heat removal in abrasive cutting are generally analyzed, as well as the methods and tools applied to investigate temperature and thermal fluxes. An innovative approach to non-destructive thermal measurement and control of elastic abrasive cutting experimented for two types of structural steels by applying the methodology of planned experiment and multi-objective optimization has been proposed.

Latest trends show that there is a need to apply an automatic smart system for controlling thermal fluxes in the cutting zone so as to ensure a higher quality of machined surfaces and longer cutting tool life. This is also linked to the design of a new approach to non-destructive thermal control of abrasive cutting when developing a smart thermographic system.

Acknowledgements

The authors would like to thank for the financial support from National Science Fund under which Project No. DN 17/16 the present work was conducted.

Nomenclature

a	cutting depth, mm
b_s	thickness of the cut-off wheel, mm
d_s	diameter of the cut-off wheel, mm
d_w	diameter of the workpiece, mm
F	cut-off wheel compression force, N
h	thickness of the layer being cut, mm
L	length of the contact arc, mm
n_s	rotational frequency of the cut-off wheel, min^{-1}
n_w	rotational frequency of the workpiece, min^{-1}
T_d	temperature of the cut piece, °C
Q	heat generated in cutting per unit time
Q_{ch}	heat transferred to the chip
Q_d	heat generated as a result of deformation
Q_f	heat transformed from friction force
Q_p	heat transferred into environment
Q_s	heat transferred to the cut-off wheel
Q_w	heat transferred to the workpiece

Author details


Anna Stoynova^{1*}, Irina Aleksandrova² and Anatoliy Aleksandrov²

1 Technical University of Sofia, Sofia, Bulgaria

2 Technical University of Gabrovo, Gabrovo, Bulgaria

*Address all correspondence to: ava@ecad.tu-sofia.bg

IntechOpen

© 2022 The Author(s). Licensee IntechOpen. This chapter is distributed under the terms of the Creative Commons Attribution License (<http://creativecommons.org/licenses/by/3.0>), which permits unrestricted use, distribution, and reproduction in any medium, provided the original work is properly cited. 

References

- [1] Ganev G. Elastic abrasive cutting of rotational workpieces in mechanical engineering [thesis]. Gabrovo: Technical University of Gabrovo; 2013 (in Bulgarian)
- [2] Neugebauer R, Hess K-U, Gleich S, Pop S. Reducing tool wear in abrasive cutting. *International Journal of Machine Tools and Manufacture*. 2005; **45**(10):1120-1123. DOI: 10.1016/j.ijmachtools.2005.01.002
- [3] Nenkov N, Aleksandrova I, Ganev G. Methods of abrasive cutting of workpieces. *Mashinostroene*. 1999;5-6: 38-40 (in Bulgarian)
- [4] Kaczmarek J. Using a thermovision method for measuring temperatures of a workpiece during abrasive cut-off operation. *Advance in Manufacturing science and Technology*. 2011;35(4): 85-95
- [5] Levchenko E, Pokintelitsa N. Investigation of thermal processes in abrasive pipe sampling. *MATEC Web of Conferences*. 2017;129:01082. DOI: 10.1051/mateconf/201712901082
- [6] Riga A, Scott C. Failure analysis of an abrasive cut-off wheel. *Engineering Failure Analysis*. 2001;8(3):237-243. DOI: 10.1016/S1350-6307(00)00014-5
- [7] Kaczmarek J. The effect of abrasive cutting on the temperature of grinding wheel and its relative efficiency. *Archives of Civil and Mechanical Engineering*. 2008;8(2):81-91. DOI: 10.1016/S1644-9665(12)60195-2
- [8] Malkin S, Guo C. Thermal analysis of grinding. *CIRP Annals*. 2007;56(2): 760-782. DOI: 10.1016/j.cirp.2007.10.005
- [9] Jamuła B. Temperature measurement analysis in the cutting zone during surface grinding. *Journal of Measurements in Engineering*. 2021; **9**(2):106-116. DOI: 10.21595/jme.2021.21894
- [10] Abukhshim N, Mativenga P, Sheikh M. Heat generation and temperature prediction in metal cutting: A review and implications for high speed machining. *International Journal of Machine Tools and Manufacture*. 2006;46(7/8):782-800. DOI: 10.1016/j.ijmachtools.2005.07.024
- [11] Davies M, Ueda T, M'Saoubi R, Mullany B, Cooke A. On the measurement of temperature in material removal processes. *CIRP Annals*. 2007;56(2):581-604. DOI: 10.1016/j.cirp.2007.10.009
- [12] Artozoul J, Lescalier C, Bomont O, Dudzinski D. Extended infrared thermography applied to orthogonal cutting. *Applied Thermal Engineering*. 2014;64(1-2):441-452. DOI: 10.1016/j.applthermaleng.2013.12.057
- [13] Catalogue of the Abrasive Tools Factory—Berkovitsa [Internet]. 2020. Available from: <https://zai-bg.com/wp-content/uploads/2020/01/ZAI-2020.pdf> [Accessed: 16 October, 2021]
- [14] Stoev Z, Popov K, Todorov N. *Abrasive Machining of Metals*. Tehnika: Gabrovo; 1979. p. 290. (in Bulgarian)
- [15] Putz M, Cardonea M, Dixa M. Cut-off grinding of hardened steel wires - modelling of heat distribution. *Procedia CIRP*. 2017;58:67-72. DOI: 10.1016/j.procir.2017.03.198
- [16] Ojolo S, Orisaleye J, Adelaja A. Development of a high speed abrasive cutting machine. *Journal of Engineering Research*. 2010;15:1-8
- [17] Aleksandrova I, Hristov H, Ganev G. Dynamic and technological characteristics of the process elastic

- abrasive cutting of rotating workpieces. *Journal of the Technical University Sofia, Branch Plovdiv: Fundamental Sciences and Applications*. 2011;**16**: 123-128
- [18] Aleksandrova I. *Finishing Technologies*. Gabrovo: University Publishing House Vasil Aprilov; 2013. p. 226. (in Bulgarian)
- [19] Reznikov A. *Abrasive and Diamond Machining of Materials*. Reference Book. Moscow: Mashinostroenie; 1977. p. 392. (in Russian)
- [20] Mishra K, Salonitis K. Empirical estimation of grinding specific forces and energy based on a modified Werner grinding model. *Procedia CIRP*. 2013;**8**: 287-292. DOI: 10.1016/j.procir.2013.06.104
- [21] Wang Z, Li Y, Yu T, Zhao J, Wen H. Prediction of 3D grinding temperature field based on meshless method considering infinite element. *The International Journal of Advanced Manufacturing Technology*. 2018;**100**: 3067-3084. DOI: 10.1007/s00170-018-2801-4
- [22] Hou H, Komanduri R. On the mechanics of the grinding process, part III – Thermal analysis of the abrasive cut-off operation. *International Journal of Machine Tools and Manufacture*. 2004;**44**(2-3):271-289. DOI: 10.1016/j.ijmachtools.2003.09.009
- [23] Putz M, Cardone M, Dix M, Wertheim R. Analysis of workpiece thermal behaviour in cut-off grinding of high-strength steel bars to control quality and efficiency. *CIRP Annals*. 2019;**68**(1):325-328. DOI: 10.1016/j.cirp.2019. 04.023
- [24] Aleksandrova I, Stoyanova A, Aleksandrov A. Modelling and multi-objective optimization of elastic abrasive cutting of C45 and 42Cr4 steels. *Journal of Mechanical Engineering*. 2021;**67**(12):635-648. DOI: 10.5545/sv-jme.2021.7327
- [25] Stoyanova A, Aleksandrova I, Aleksandrov A, Ganev G. Infrared thermography for elastic abrasive cutting process monitoring. *MATEC Web of Conferences*. 2018;**210**. DOI: 10.1051/mateconf/ 201821002018
- [26] Neslušán M, Mrkvica I, Čep R, Raos P. Heat distribution when nickel alloy grinding. *Tehnički vjesnik/ Technical Gazette*. 2012;**19**(4):947-951
- [27] Yascheritsyn I, Feldstein E, Kornievich M. *Theory of Cutting*. Moscow: New knowledge; 2007. p. 512 (in Russian)
- [28] Eshghy S. Thermal aspects of the abrasive cut off operation. Part 2 – Partition functions and optimum cut off. *Journal of Engineering for Industry*. 1968;**90**(2):360-364. DOI: 10.1115/1.3604641
- [29] Kus A, Isik Y, Cakir M, Coşkun S, Özdemir K. Thermocouple and infrared sensor-based measurement of temperature distribution in metal cutting. *Sensors*. 2015;**15**:1274-1291. DOI: 10.3390/s150101274
- [30] Saez-de-Buruaga M, Soler D, Aristimuño P, Esnaola J, Arrazola P. Determining tool/chip temperatures from thermography measurements in metal cutting. *Applied Thermal Engineering*. 2018;**145**(25):305-314. DOI: 10.1016/j.applthermaleng.2018.09.051
- [31] Aleksandrova I, Ganev G, Hristov H. Performance of cut-off wheels during elastic abrasive cutting of rotating workpieces. *Tehnički vjesnik/ Technical Gazette*. 2019;**26**(3):577-583. DOI: 10.17559/TV-20151223184850
- [32] Sahu P, Sagar R. Development of abrasive cut-off wheel having side grooves. *The International Journal of*

Advanced Manufacturing Technology. 2006;**31**:37-40. DOI: 10.1007/s00170-005-0138-2

[33] Lopes J, Ribeiro F, Javaroni R, Garcia M, Ventura C, Scalón V, et al. Mechanical and thermal effects of abrasive cut-off applied in low and medium carbon steels using aluminum oxide cutting disc. *The International Journal of Advanced Manufacturing Technology*. 2020;**109**:1319-1331. DOI: 10.1007/s00170-020-05753-5

[34] Luo S, Tsai Y, Chen C. Studies on cut-off grinding of BK7 optical glass using thin diamond wheels. *Journal of Materials Processing Technology*. 2006; **173**(3):321-329. DOI: 10.1016/j.jmatprotec. 2005.11.036

[35] Ortega N, Martynenko V, Perez D, Krahmer D, López de Lacalle L, Ukar E. Abrasive disc performance in dry-cutting of medium-carbon steel. *Metals*. 2020; **10**(4):538. DOI: 10.3390/met10040538

[36] Ni J, Yang Y, Wu C. Assessment of water-based fluids with additives in grinding disc cutting process. *Journal of Cleaner Production*. 2019;**212**:593-601. DOI: 10.1016/j.jclepro.2018. 12.066

[37] Braz C, Ventura C, De Oliveira M, Antonialli A, Ishikawa T. Investigating the application of customized abrasive cutoff wheels with respect to tool wear and subsurface integrity in metallographic cutting of pure titanium. *Metallography, Microstructure, and Analysis*. 2019;**8**:826-832. DOI: 10.1007/s13632-019-00587-4

[38] Ortega N, Bravo H, Pombo I, Sánchez J, Vidal G. Thermal analysis of creep feed grinding. *Procedia Engineering*. 2015;**132**:1061-1068. DOI: 10.1016/j.proeng.2015.12.596

[39] Shaw M. The rating of abrasive cutoff wheels. *Journal of Engineering for Industry*. 1975;**97**(1):138-146. DOI: 10.1115/1.3438526

[40] Vologin K. Selection of rational conditions for cutting workpieces of difficult to machine material with abrasive wheels [thesis]. Moscow: Moscow State University of Technology Stankin; 2002 (in Russian)

[41] Nguwen T, Zhang C. Performance of new segmented grinding wheel system. *International Journal of Machine Tools and Manufacture*. 2009; **49**(3-4):291-296. DOI: 10.1016/j.ijmachtools.2008.10.015

[42] Alexandrova I, Ganev G, Hristov H. Thermal phenomena in elastic abrasive cutting of rotating workpieces - part one. *Mechanical and Electrical Engineering*. 2014;**12**:38-42 (in Bulgarian)

[43] Alexandrova I, Ganev G, Hristov H, Alexandrov A. Thermal phenomena in elastic abrasive cutting of rotating workpieces - part two. *Mechanical and Electrical Engineering*. 2015;**1**:42-45 (in Bulgarian)

[44] Stoynova A, Aleksandrova I, Aleksandrov A, Goranov G. Non-contact measurement and monitoring of cut-off wheel wear. In: *Proceedings of the IEEE XXVIII International Scientific Conference Electronics (ET)*; 12-14 September. Sozopol. Bulgaria: IEEE; 2019. DOI: 10.1109/ET.2019.8878321

[45] Mukherjee I, Ray P. A review of optimization techniques in metal cutting processes. *Computers & Industrial Engineering*. 2006;**50**(1-2): 15-34. DOI: 10.1016/j.cie. 2005.10.001

[46] Ganev G, Aleksandrova I, Hristov H. Wear and lifetime of abrasive tools during elastic abrasive cutting. *Machine Building and Electrical Engineering*. 2012;**10-11**:20-25 (in Bulgarian)

[47] Ganev G, Aleksandrova I, Hristov H. Study and modelling of time for elastic abrasive cutting of rotating

workpieces. *Machine Building and Electrical Engineering*. 2012;**12**:26-31 (in Bulgarian)

[48] QStatLab v.6[Internet]. 2021. Available from: <http://www.qstatlab.co.uk/bg/> [Accessed: 11 October, 2021]

[49] Ogedengbe T, Okediji A, Yussouf A, Aderoba O, Abiola O, Alabi I, et al. The effects of heat generation on cutting tool and machined workpiece. *Journal of Physics: Conference Series*. 2019;**1378**: 022012. DOI: 10.1088/1742-6596/1378/2/022012

Analysis of the Tribological Evolution of Nitride-Based Coatings

*Christian Ortiz Ortiz, Erick Hernandez-Rengifo
and Julio Cesar Caicedo*

Abstract

This chapter describes the fundamental and technological role of nitride-based hard coatings as protective coatings in some applications within the metalworking industry. For this, this chapter will present a critical review of previous research and recent developments on nitride-based coatings in different systems such as (multi-layers, quaternaries, among others), where it will be possible to demonstrate their main properties and advantages that they can grant when they are implemented on conventional steels, such as greater hardness, surface control, electrochemical resistance, resistance against wear, among others. These results will determine that this type of coatings are suitable candidates to be implemented as protective coatings on cutting tools, which suffer from high wear in machining processes in the metalworking industry.

Keywords: tribology behavior, wear mechanisms, multilayer coatings, adhesive properties, surfaces analysis

1. Introduction

Through constant development within the metalworking industry, current processes consist of designing and producing new structures at a higher speed, cheaper with more efficient processes that present a low rate of wear on the equipment and devices used during said processes. Therefore, hard wear-resistant coatings have been incorporated as protective coatings on cutting tools in recent decades with the purpose of giving a longer useful life to this type of device, which suffers from high wear during the machining processes [1–3]. This type of coatings currently has a wide range of investigations, which have been able to generate different configurations such as binary, ternary or quaternary systems, single or multilayer systems, as well as a great combination of different elements that have conferred characteristics. Special to this type of coatings, such as high hardness, high biocompatibility, high resistance to wear, high resistance to corrosion, among other specific characteristics required depending on their use and application. A specific type of coatings such as those based on nitrides, which have generated great interest within various and novel coating systems, these coatings were implemented approximately since 1970 [4], being one of the first anti-wear coatings used in the industry. This type of coatings have great hardness, high resistance to wear and high resistance to

corrosion among other interesting properties, such as TiN [4], TiCrN [5], [Al₂O₃/Si₃N₄] [6], TiCN [7], BCN [8] among other configurations.

Nitride-based coatings are constituted by the incorporation of nitrogen atoms (N) within the crystalline structure of transition metals such as Ti, Al, Cr, V among others, which generates a distortion within their structure, causing internal stresses, with changing specific properties of the material. In addition, the inclusion of N atoms interstitially within the structures generates a physicochemical change in the material, giving it changes in its behavior based on a new metal-ceramic structure that it now presents. Therefore, properties such as hardness and corrosion resistance increase considerably in relation to simpler coatings based on transition metals. On the other hand, the distortion within their structures due to the inclusion of N atoms generating stresses within their structure as mentioned above, causes physical changes in the coating, such as an increase in the density of these coatings, which influences characteristics. Surface surfaces such as roughness and the presence of these residual stresses within the structure, causes an increase in the mechanical properties of the coating, among other changes in material properties.

2. Methodology and experimental details

The deposition of the coatings was performed using a multi-target sputtering magnetron. This specific type of system allows to perform the multilayer deposition process in situ. This equipment uses four (4) magnetrons (Torus - 4 “, 10 cm Kurt J. Lesker) with diameters of 10 cm, three (3) radio frequency sources (13.56 MHz, RFX 600A), and three (3) direct current sources (MDX 500, Advanced Energy). In addition, the pressure during the deposition process is monitored by a control and measurement system (Baraton, MKS), which has four (4) gas flow controllers, a radiation heating system (Athena 500), which has a maximum temperature of 400°C, and a planetary type rotary sampling system. For TiN, TiCrN, TiCN, BCN and CrAlN coatings, titanium (Ti), titanium carbide (TiC) and Chromium-Aluminum (Cr-Al) targets were used, respectively; each cathode with an approximate purity of 99.99%. Two (2) different type of substrate were used, silicon with preferential crystallographic orientation (100) and AISI 1045 and H13 steel substrates respectively. The silicon substrates were subjected to a surface cleaning process in an ultrasonic system and the steel substrates were prepared superficially using sandpaper (SiC) and finally polished in a metallographic polisher. Before starting the deposition process, a vacuum with a pressure of 1.4×10^{-4} mbar was applied. The TiCN coating was deposited using a working pressure of 1.4×10^{-2} mbar in a gas mixture of 50 sccm (Ar) and 16 sccm (N₂) at 250°C, and a r.f power density of 5 W/cm² was applied on the TiC target. For BCN coating, it was deposited by a pressure of 7.4×10^{-3} mbar in a gas mixture of 44 sccm (Ar) and 6 sccm (N₂) at 250°C, and a r.f power density of 7 W/cm² was applied on the BC target. For the CrAlN coating was deposited using a working pressure of 6.4×10^{-3} mbar was used a gas mixture of 50 sccm (Ar) and 5.5 sccm (N₂) at 250°C, and the r.f power density applied to the Cr target and Al target was 2.5 W/cm² and 4.5 W/cm² respectively [8]. The deposition of the Si₃N₄ based coatings was performed by magnetron sputtering with an r.f source (13.56 MHz) on silicon (100) and AISI 316 stainless steel substrates. A cathode (Si₃N₄) with a purity of 99.9% approximately. During the deposition a power of 550 W was used and a bias voltage of -20 V was applied, the distance between substrates-targets was approximately 7 cm, and the deposition process was carried out at a temperature of 200°C inside the chamber. In addition, the substrate holder rotated at a

speed of 60 RPM during the entire deposition process with a working pressure of 5.1×10^3 mbar. The coating obtained a thickness of approximately 2.5 μm .

The structural analysis of TiCN, BCN and CrAlN coatings was analyzed by X-ray diffraction (PANalytical X'pert proTM), using a Cu K α radiation source with a wavelength of $\lambda = 1.5405 \text{ \AA}$. By X-ray photo-electron spectroscopy (XPS) using a SAGE HR100 (SPECSTM) equipment with a monochromatic source (Mg K α 1253.6 eV), CasaXPS V2.3.15 software was used to determine the chemical composition of the obtained coatings. The morphological study of the coatings was carried out by atomic force microscopy (AFM) with an Asylum Research MFP-3D® device and with a scanning probe image processor (SPIP®), the grain size and roughness of the coatings obtained were calculated. The mechanical study was carried out by nanoindentation using an Ubi1-HysitronTM device, which uses a Berkovich diamond tip at variable loads. From this test, load–displacement curves were obtained as a function of penetration for the coatings. Based on these curves, hardness and elastic modulus were determined using the Oliver-Phar method.

2.1 Tribological experimental details

The tribological characterization of the coatings was performed under ASTM G99-17 standard, using a Microtest MT 4001-98 tribometer. This equipment consists of a rotating platform, with controlled speed on which the test sample is adjusted in an environment with or without lubricant. On this surface, a mechanical arm which contains a counterpart (100Cr6 or Steel 440) with a spherical shape of 6 mm in diameter in direct contact with the surface under study is adjusted. A load applied to the counterpart (5 N) is adjusted on this mechanical arm; with an angular velocity of 160 rpm and linear velocity of 0.1 m/s and other parameters of each tribological test are presented in **Table 1**. In addition, a JEOL model JSM-6490LVTM scanning electron microscopy (SEM) was used to observe the wear track. The adhesive characterization of the coatings was performed under ASTM G171-03 standard, using a Microtest MTR2 equipment, the parameter used in the test were; a sliding distance of 6 mm, variable load from 0 to 90 N and a sliding velocity of of 1.97 mm/min using a Rockwell C indenter. In addition, the identification of cohesive failure (Lc1) and adhesive failure (Lc2) was performed using the NANOVEA SCRATCH TESTER software, which analyzes the change of the friction coefficient versus load or distance, and the results were corroborated by optical micrographs and SEM micrographs of the scratch tracks. The coatings thickness and the wear scratch images were obtained by using a KLA Tencor D-120 profilometer; the thickness of all the coatings was 3 μm [6, 9].

	TiN, TiCrN	TiCN, CrAlN, BCN	Si ₃ N ₄
Load (N)	5	5	5
Counterpart	440	100Cr6	100Cr6
Environments	dry	Dry and lubricated	Dry and lubricated
Substrate	Steel H13	Steel 1045	Steel 316
Distance (m)	100	1000	300
Lubricant		20 W50	20 W50
Angular Velocity (rpm)	160	160	160
Linear Velocity (m/seg)	0.1	0.1	0.1

Table 1.
Tribological parameters.

3. Comparison between nitride coatings

3.1 Structural study for TiN and TiCrN nitride coatings

Figure 1 shows the diffraction patterns for the initial coating based on (TiN), where diffraction peaks located in the crystallographic planes (111) (200, 220), (311), (222) and (400) were obtained. In addition, the incorporation of Cr atoms within its structure for the formation of the coating (TiCrN), which still shows the same characteristics peaks. On the other hand, the displacement of the characteristics peaks of the multilayer system formed by [TiN/TiCrN] can be evidenced as a function of the increase in the bilayers number deposited on Si substrates (100). Determining that the increase in the number of interfaces causes a distortion of the crystalline structure due to residual stresses within this multilayers system, which will influence the mechanical and tribological properties of this type of coatings. From these results it was possible to infer that all coatings have a face-centered cubic crystal structure (FCC) [5, 10].

3.1.1 Structural study for TiCN, BCN and CrAlN coatings nitride coatings

Figure 2 shows the X-ray diffraction patterns for more complex coatings such as TiCN, BCN and CrAlN coatings. From these results, 2θ diffraction sequences were evident for face-centered cubic (FCC), NaCl type structures with and $Fm\bar{3}m$ space group [11]. The conformation of this type of coatings (TiCN, BCN and CrAlN) is associated by the substitution mechanism, in which, the carbon atoms (C) substitute the nitrogen atoms (N), giving rise the ordered CN systems in Ti, B and unordered for TiCN and BCN coatings. On the other hand, the CrAlN coating is the result of the coupling the two FCC phases of AlN and CrN, which generated a conjugated complex, where Al and Cr atoms are located in reticular positions and aluminum atoms (Al) are substituted by atoms of (Cr) while nitrogen atoms are located in the interstitial position of the CrAlN crystal [12–14]. Through these results, a NaCl-type FCC structure was determined for the three coatings, in which Ti, B, Cr and Al atoms would be located at the Wyckoff 4a site and the Wyckoff 4b site is randomly occupied by C and N atoms. Thus, titanium carbon-nitride as well as boron carbo-nitride are agreement with the international indexing files JCPDF 00-042-1488 and JCPDF

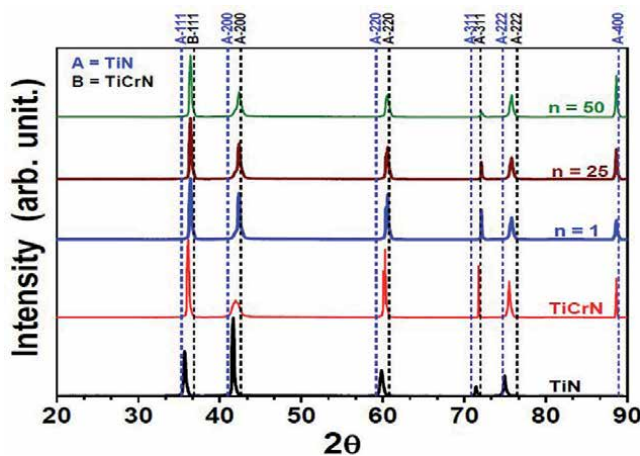


Figure 1. X-ray diffraction patterns for monolayers [TiN and TiCrN] and multilayers [TiN/TiCrN] n as a function of the number of bilayers 1, 25, and 50.

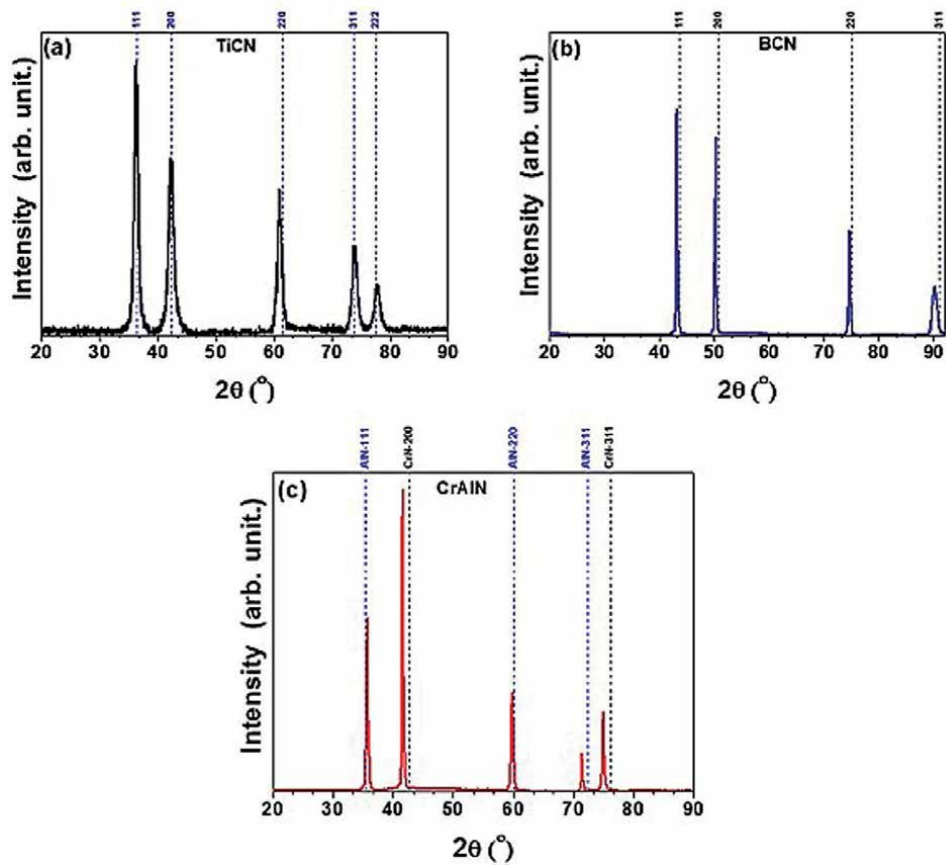


Figure 2. Diffraction patterns for all coatings: (a) TiCN, (b) BCN and (c) CrAlN. Dotted lines indicate the peaks position obtained from the international indexing files (JCPDF) of TiCN, BCN and CrN–AlN respectively.

00-035-1293, while for aluminum chromium nitride two indexing are performed, taking into account the structure of chromium nitride (CrN) JCPDF 00-003-1157 and aluminum nitride (AlN) JCPD 00-025-1495 [15]. In addition, it can be observed that the CrAlN coating is constituted by CrN and AlN, which present the same NaCl-type FCC crystal structure and a 225-Fm3m space group. These results established that the higher intensity peak (111) located at the for angles $2\theta = 36.342^\circ$ and 43.228° for TiCN and BCN coatings respectively. Otherwise, for the CrAlN coating, where the peak of higher intensity (200) was located at angle $2\theta = 41.646^\circ$. Finally, shifts towards smaller 2θ angles relative to the positions where the material is stress-free (dotted line). These shifts of the diffraction peaks suggest a variation of the lattice parameter of the crystal structures of the coatings. Considering that TiCN, CrAlN and BCN coatings present cubic structures, it can be observed that when the value of the theta angle (θ) decreases, the lattice parameter increases, evidencing an increase of the internal stresses (compression type) within the crystalline structure of the coatings.

3.1.2 Structural study for Si_3N_4 nitride coatings

Figure 3 shows the XRD diffraction patterns for Si_3N_4 coating deposited on silicon (100), where diffraction peaks located in the (111), (220), (311), (400), (511), (440) and (533) crystallographic planes characteristics of a face-centered cubic structure FCC were obtained. In addition, a preferential texturization is observed in the (311)

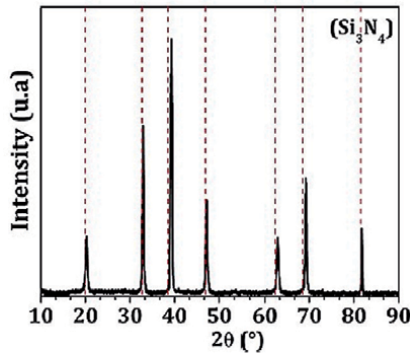


Figure 3.
Diffraction patterns of the Si_3N_4 single layers coating deposited on silicon.

plane, it was also observed that the peaks presented horizontal displacements at 2θ with respect to those reported in the JCPDC 00-051-1334 file (dotted line), were caused by internal stresses generated during the deposition process, which caused a deformation in the crystallographic planes of the structure of the coatings.

3.2 Chemical comparison between nitride coatings

3.2.1 Chemical study for TiCN, BCN and CrAlN coatings nitride coatings

Figure 4 shows the survey spectra for the TiCN, BCN and CrAlN coatings. These spectra presented high intensity peaks where their location with their

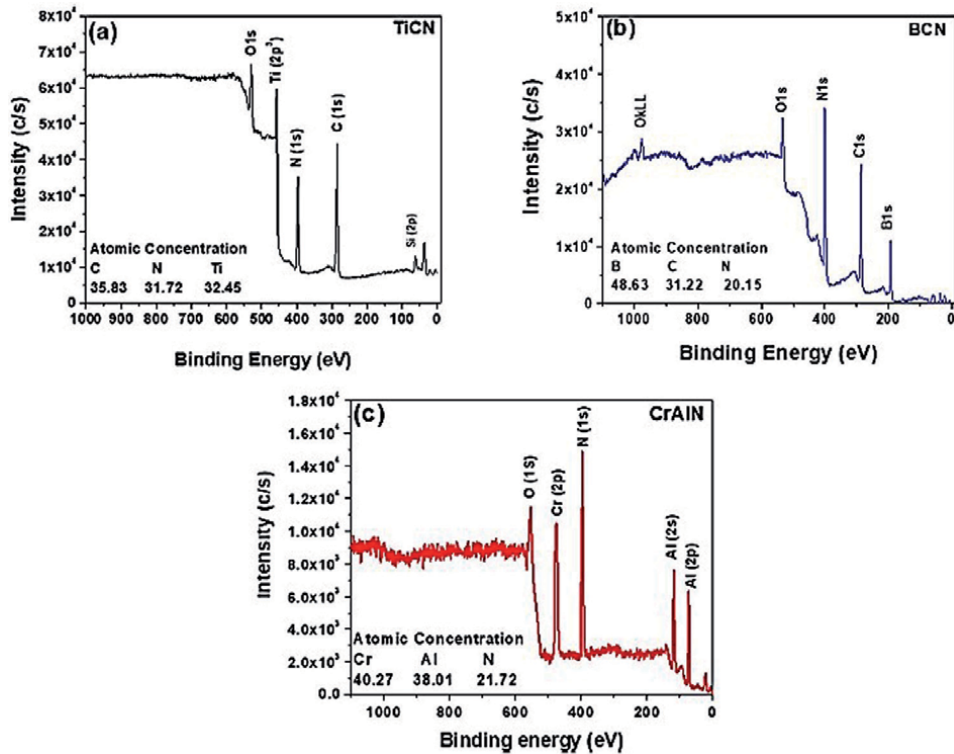


Figure 4.
XPS survey results for the three coatings used: (a) TiCN, (b) BCN and (c) CrAlN.

respective binding energies were determined. For the TiCN coating, Ti (2p₃), C (1s) and Si (2p) peaks located at the binding energy 458.4 eV; 284.8 eV and 61.6 eV respectively were obtained; for the BCN coating, N (1s), C (1s) and B (1s) peaks located at the binding energy 400 eV; 285.6 eV and 192.8 eV respectively were obtained; and for the CrAlN coating Cr (2p), N(1s), Al (2s) and Al (2p) peaks located at the binding energy 475.99 eV; 396.97 eV; 119 eV and 74 eV respectively were obtained. Previous studies indicated that the signals of C (1s) and N (1s) are associated with C-N and Ti-N bonds, these results are agreement with the literature [16]. Analysis of the XPS spectra for the BCN coating showed the binding energies corresponding to the N (1s), C (1s) and B (1s) signals were consistent to the formation of the BCN ternary compound as corroborated in the literature [17]. For the ternary CrAlN coating, Cr (2p_{3/2}), Al (2p) and N (1s) signals associated with Cr-Al bonds were presented, binding energies for Cr-N and Al-N were also evidenced, confirming the formation of the ternary CrAlN compound [18]. Finally, the stoichiometry was determined for all the coatings ($Ti_{32.45}-C_{35.83}-N_{31.72}$, $B_{48.63}-C_{31.22}-N_{20.15}$ and $Cr_{40.27}-Al_{38.01}-N_{21.72}$).

3.2.2 Chemical study for Si₃N₄ nitride coatings

Figure 5a show the depth spectra for the Si₃N₄ coating, showing the spectral lines of the elements present in the coating by X-ray photoelectron spectroscopy (XPS) technique. From this result, elements such as Si and N, and elements in low quantity such as Oxygen were found. In order to know the detailed surface stoichiometry of the coating, the high resolution XPS spectra of Si-2p and N-1s species are also presented in the **Figure 5b** and **c** respectively. The Si₃N₄ coating has an atomic N/Si ratio of 1.32 (stoichiometry $Si_{57}N_{43}$). The Si₃N₄ has an ideal stoichiometry ratio of 1.33 which is in agreement with what is found in the literature. In addition, the

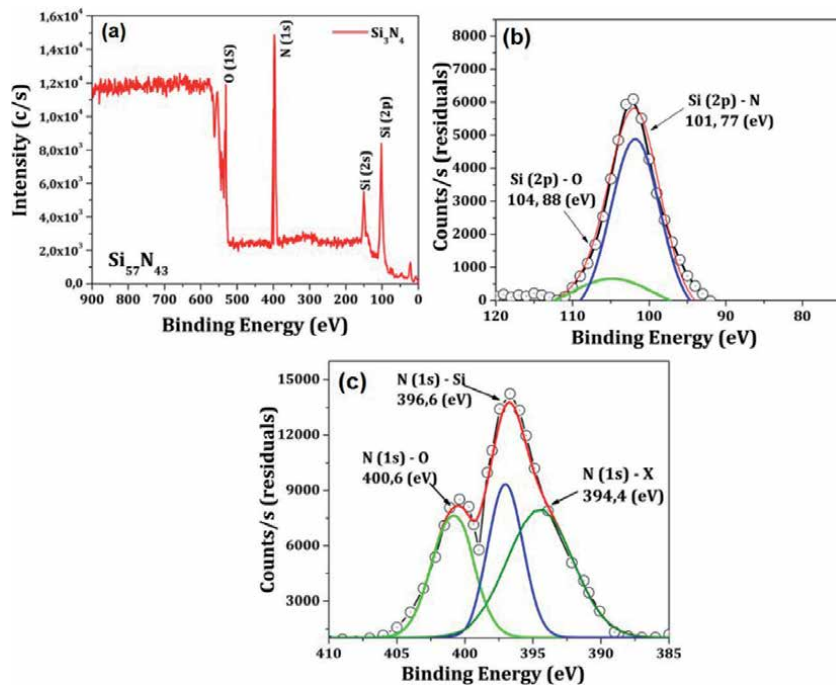


Figure 5. Depth spectra obtained by the XPS technique for the Si₃N₄ nitride coatings and high resolution XPS spectra for the Si₃N₄ coating: (a) Si-2p signal; (b) N-1s signal.

high-resolution Si-2p spectrum (**Figure 5b**) presented two peaks located at a binding energy of 101.77 eV and 104.88 eV, respectively. These two peaks are attributed to the Si-O and Si-N bonds of the Si_3N_4 [19]. On the other hand, **Figure 5c** shows the high-resolution spectrum for the N-1s peak, which is fitted by three peaks. The first peak, corresponding to (N-O) bond, located at a binding energy of 400.51 eV [20]; the second peak, corresponding to the (N-Si) bond, located at a binding energy of 396.96 eV, and the third peak, can be attributed to a different chemical state of N due to its different bonding configurations with neighboring atoms such as H and C located at a binding energy of 394.4 eV [21].

3.3 Morphological comparison between nitride coatings

3.3.1 Morphological study for TiN and TiCrN nitride coatings

To quantitatively study the surface morphology of the samples, the atomic force microscopy (AFM) technique was used. **Figure 6a** and **b** present the images corresponding to titanium nitride (TiN) and titanium chromium nitride (TiCrN) respectively. From these results, it was evident that the TiCrN surface has a more regular surface compared to TiN. This surface change is attributed to the incorporation of chromium (Cr) into its crystalline structure, which causes a compressive deformation, making a much denser and compact structure with a more orderly growth.

Figure 4c and **d** show the roughness and grain size for the TiN and TiCrN layers and the [TiN/TiCrN] based multilayer system as a function of the bilayers number $n = 1, 25$ and 50 respectively. These results indicated that the TiCrN layer presented better surface properties (roughness and grain size) compared to the TiN layer. In addition, by means of the multilayer system, it was evidenced that by increasing the bilayers number or interfaces, the surfaces presented a lower number of imperfections due to the fact that the system becomes much denser generating a more regular surface, because an increase in the density of the system is promoted due to a higher number of interfaces. Authors such as J.C. Caicedo et al. [22] also showed this behavior in multilayer systems. In addition, the roughness is a factor that influenced the tribological properties, influencing the formation of asperities, the type of contact and the wear generated at the beginning of the tribological test [23, 24].

3.3.2 Morphological study for TiCN, BCN and CrAlN coatings nitride coatings

Using SPIP® statical analysis software, AFM images were obtained in contact mode (**Figure 7a-c**). From these images, the surface roughness and grain size values of each coating were obtained (**Figure 8a** and **b**). From these images it can be clearly observed the change in surface morphology as the nature of the coating changes, taking into account that the three materials have a similar thickness.

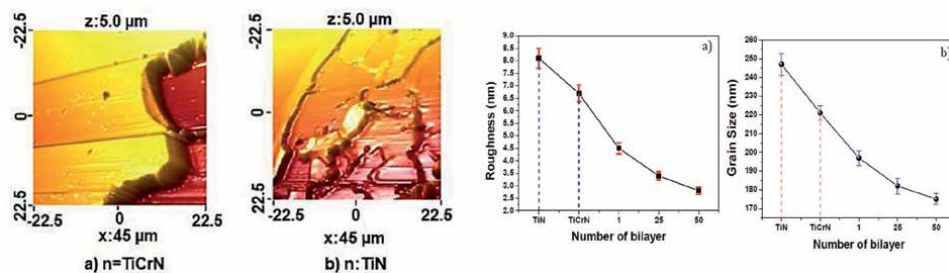


Figure 6. Atomic force microscopy for single layer coatings: (a) TiCrN and (b) TiN.

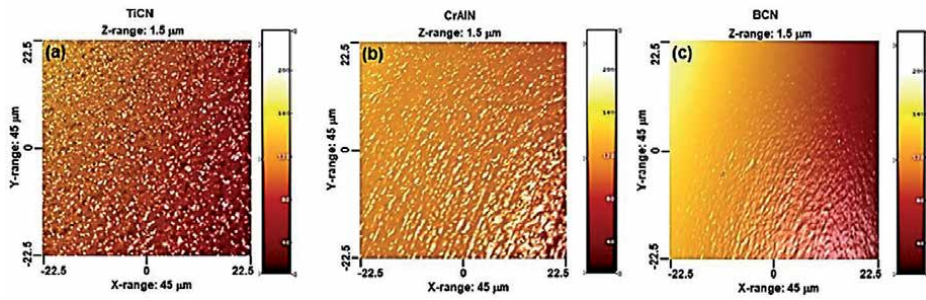


Figure 7.
 AFM images for all coatings: (a) TiCN, (b) CrAlN and (c) BCN.

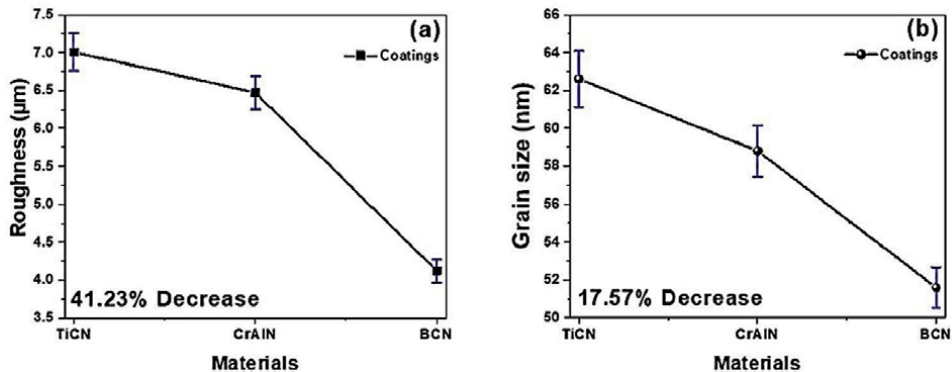


Figure 8.
 Influence of TiCN, BCN and CrAlN coatings' nature on morphological surface: (a) roughness as a function of coating materials, (b) grain size as a function of coating materials.

Figure 8 shows the relationship between surface roughness and grain size. These results indicated that the TiCN coating presented the higher values for roughness = 7.01 µm and grain size = 62.6 µm; followed by the CrAlN coating, which presented roughness = 6.47 µm and grain size = 58.8 µm. Finally, the BCN coating presented the best characteristics (lowest values) of roughness = 4.12 µm and grain size = 51.6 µm. Thus, there was a decrease of 41.23% and 17.57% for roughness and grain size respectively. From the results obtained by AFM, it was observed that the BCN coating presented the best results, which is due to the susceptibility of BCN to grow with low roughness on the substrate with respect to the other coatings, also producing the reduction of the grain size (which is directly proportional to the reduction of the roughness), causing a more compact coating to be generated.

3.3.3 Morphological study for Si₃N₄ coatings nitride coatings

Figure 9 presents the AFM images of the Si₃N₄ coating, where it was determined that the coating presented a grain morphology with circular geometry with a low grain size and a homogeneous surface. This surface characteristic is attributed to a high ionic bombardment of Ar⁺ atoms generated during the deposition process, which modifies the surface morphology of the coating. Thus, ion bombardment causes an increase in the energy of the atoms adsorbed on the substrate surface, generating an increase in the nucleation sites. This results in a reduction of grain size, roughness and columnar growth, as well as an increase in the density of the coatings [5, 25]. **Figure 9b** shows the values of the roughness and grain size for

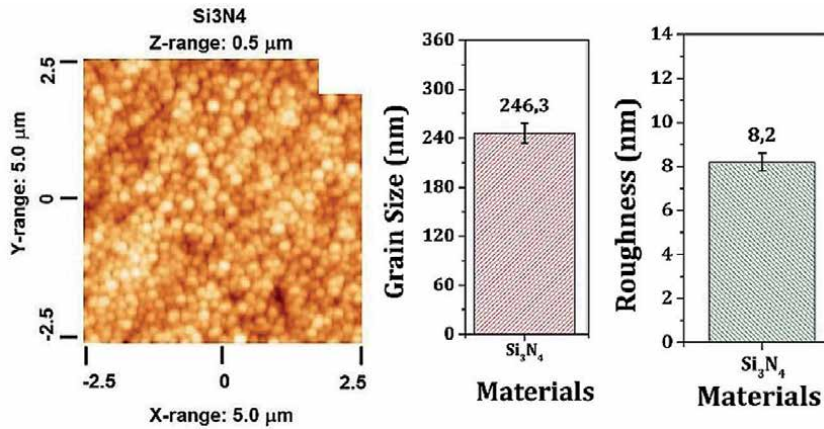


Figure 9. Atomic force microscopy (AFM) images for the single layer Si₃N₄ coatings, showing the morphological analysis of the Si₃N₄ coatings: roughness and grain size.

the coating, where it was determined that the Si₃N₄ surface presented optimal results, so these morphological characteristics will greatly affect the mechanical and tribological properties of this coating.

3.4 Mechanical properties comparison between nitride coatings

3.4.1 Mechanical properties for TiN and TiCrN nitride coatings

Figure 10 shows the load-depth curves obtained during the nanoindentation test for the TiN and TiCrN single layer coating and the TiN/TiCrN multilayer system as a function of the bilayers number. These results showed a higher penetration for the substrate (steel H13). In addition, the TiCrN layer showed a lower penetration compared to the TiN layer and for the multilayer system, there was a decrease in penetration as the bilayers number increased. This behavior is due to the surface properties of each coating as corroborated in the **Figure 10b** and **c**. Thus, **Figure 10b** and **c** shows the values of hardness (H) and elastic modulus (E) for the individual coating and multilayers system (TiN, TiCrN and [TiN/TiCrN]) where it was determined that both presented hardness higher than 10 Gpa, which serves as a parameter to qualify them as hard coatings, which allows to have a longer life time and lower wear rates in cutting tools that implement this type of coatings [26]. Finally, these results show a hardness of 18.5 Gpa and an elastic modulus 284.17 Mpa, as well as a hardness of 20.35 Gpa and elastic modulus 314.2 Mpa for the TiN and TiCrN single layers, respectively.

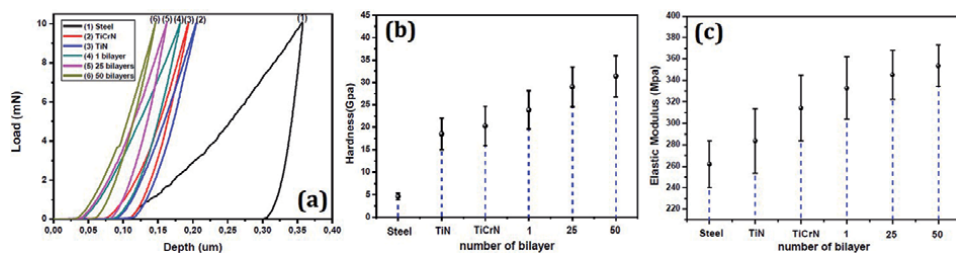


Figure 10. Nanoindentation results (a) Load-displacement curves for the TiN and TiCrN single layers; (b) Hardness and (c) Elastic modulus values.

The TiCrN single layer showed better properties due to the higher compressive stresses generated in the coating during the sputtering of the deposition process [22].

3.4.2 Mechanical properties for TiCN, BCN and CrAlN coatings nitride coatings

After the structural and morphological studies presented above, the mechanical properties of TiCN, CrAlN and BCN coatings deposited on AISI 1045 steel substrates presented in the **Figure 11a** were analyzed by means of load-displacement curves. **Figure 11b** and **c** show the hardness and elastic modulus of the coatings, where values were obtained for TiCN (H = 28 GPa, E=224 GPa), followed by CrAlN (H=30 GPa, E=251 GPa) and then BCN (H=33 GPa, E=335 GPa). These results obtained are attributed to surface factors such as those presented by AFM (**Figure 7**), where a direct relationship between the roughness and grain size is shown. Thus, having a smaller grain size results in a higher grain edge density and these grain edges act as impediments to the movement of dislocations. Thus, higher shear stresses are required for the dislocations to pass through these obstacles, so these coatings will have better mechanical properties [27–30]. On the other hand, the elastic modulus (E) of coatings is related to the type of material, but not to its microstructure; in this sense the elastic modulus (E) depends on its crystalline structure and microstructural factors such as the lattice parameter.

3.4.3 Mechanical properties for Si₃N₄ coatings nitride coatings

Figure 12 shows the results of hardness (H) and reduced elastic modulus (Er) of the Si₃N₄ coating deposited on an AISI 316 steel. Through these results it was possible to determine that this coating presented a higher resistance to being indented in comparison to the Al₂O₃ coating. This behavior is attributed to surface factors such as a smaller grain size, which means an increase in the amount of grain boundaries, which act as impediments to the displacement of dislocations. On the other hand, the presence of compressive stresses generated during the deposition process contributed to the increase in the hardness of this coating. Thus, the Si₃N₄ coating obtained the best mechanical properties such as hardness (H) and reduction elastic modulus (Er).

3.5 Tribological properties comparison between nitride coatings

3.5.1 Tribological properties for TiN and TiCrN nitride coatings

Figure 13 shows the tribological behavior of individual TiN and TiCrN coatings as well as the [TiN/TiCrN] multilayer system as a function of the bilayers number.

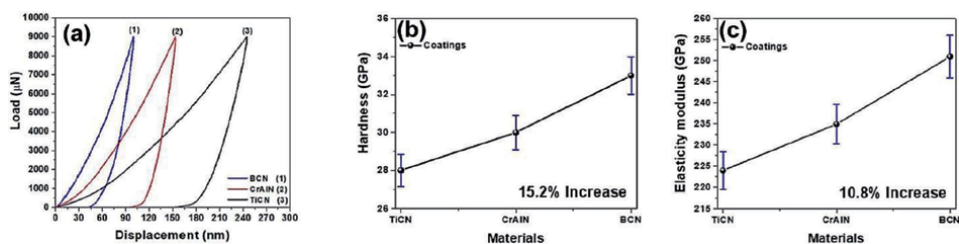


Figure 11. Nanoindentation results: (a) Load-displacement curves for the TiCN, CrAlN and BCN single layers, (b) Hardness and (c) Elastic modulus values.

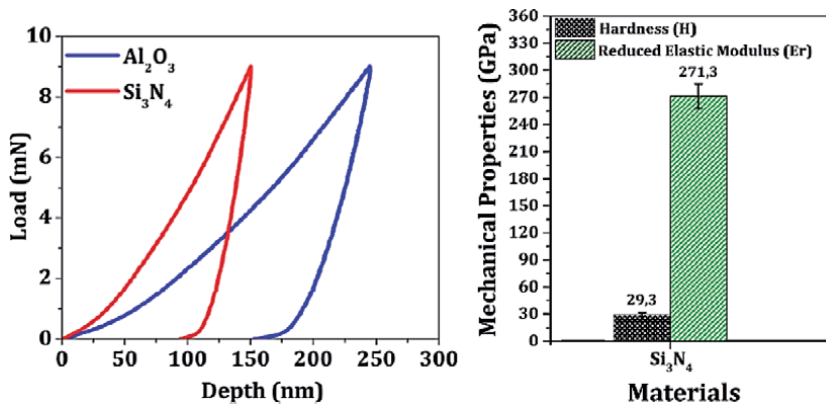


Figure 12. Load-depth curves for the Si_3N_4 coatings and mechanical properties as a function of the material: hardness and reduced modulus of elasticity Si_3N_4 coatings.

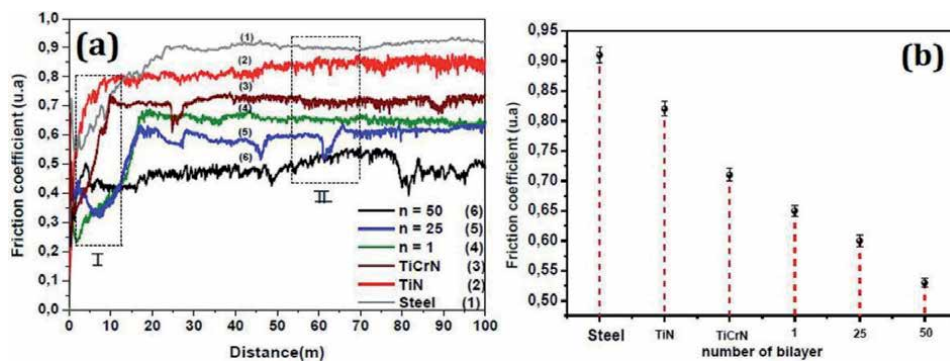


Figure 13. Tribological study of single layer coatings [TiN and TiCrN] and multilayer system [TiN/TiCrN] n as a function of the bilayers number (a) Friction coefficient versus distance and (b) Friction coefficient values for single layer [TiN and TiCrN] and multilayer system [TiN/TiCrN] n .

Through this behavior, two characteristics stages were identified. Stage I, known as the starting period, where there is a rapid increase in the friction coefficient due to the direct contact between the asperities and the counterpart (Steel 440), in this way, these asperities are eliminated and deformed. Stage II, known as running-in, in which the deformation of the asperities is maintained together with the appearance of defects of the coating, leading to the formation of wear particles or debris [24].

Figure 13b show the value of the friction coefficient in the stabilization stage. From this result, it is evident that the TiCrN coating showed a decrease compared to the TiN coating, this decrease in the coefficient is attributed to the deformation of the crystalline structure by the incorporation of chromium atoms, which modifies its surface and mechanical properties, as show above (**Figures 6** and **10**). Furthermore, this tribological behavior can be related to the mechanical friction model proposed by Archad, where the friction coefficient of each coating depends on surface factors such as roughness $R(s,a)$, and elastic-plastic properties (hardness H , or elastic modulus E_r). By means of this model, it is established that when the surface of the coating has a low roughness (**Figure 6**) and a high hardness (**Figure 10**) the friction coefficient will be lower since there will be less wear on the surface [31].

The study of the adhesion of coatings was carried out by means of the scratch teste. For this, **Figure 14a** and **b** show the behavior of TiN and TiCrN coatings

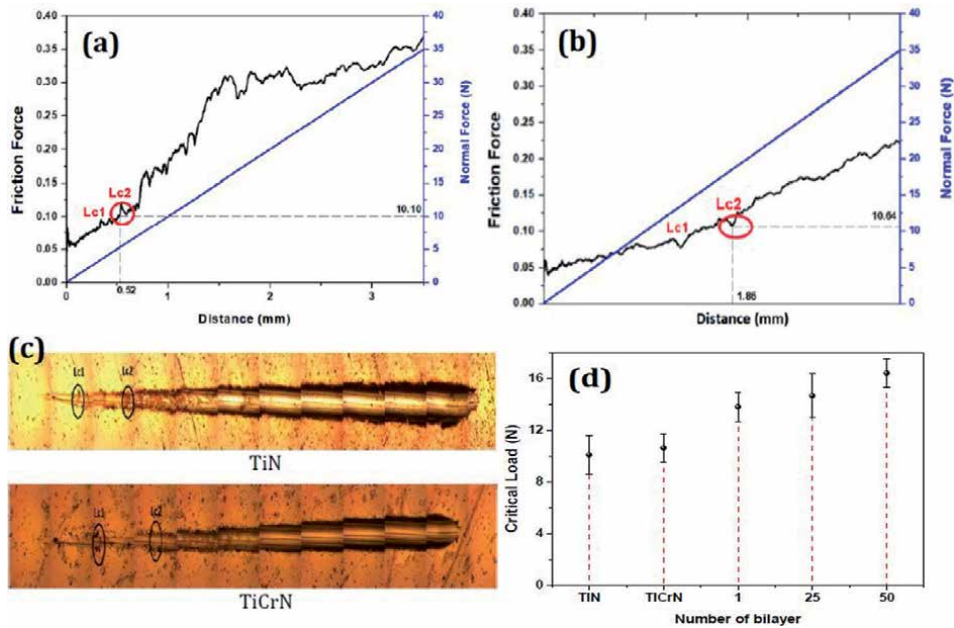


Figure 14. Friction coefficient and normal strength versus distance and critical load Lc_2 for single layers (TiN and TiCrN) and optical micrographs of the wear track of the dynamic scratch test at a resolution of $\times 10$.

respectively, where two characteristics stages known as (Lc_1 and Lc_2) could be characterized. Lc_1 , is known as the cohesive failure where the first cracks or first failure in the coating start to occur and Lc_2 known as the adhesive type failure where delamination occurs at the edge of the scratch track presented in **Figure 14c**. In addition, **Figure 14a** and **b** show the adhesion strength for the single layer coatings as a function of Lc_1 and Lc_2 failures, where the change in slope corresponding to the adhesive and cohesive failure are observed. Thus, these results were corroborated with the micrographs of the wear tracks of each test where the morphological changes suffered by the surface due to the cohesive and adhesive failure can be appreciated [32].

Finally, **Figure 14d** show the value of the critical load (Lc_2) for the TiN and TiCrN single layer coatings as well as the multilayer system [TiN/TiCrN] as a function of the bilayers number. From these results it was possible to show that the TiCrN coating presented a higher resistance to be delaminated, this increase of the Lc_2 load in comparison to the TiN coating is attributed to physical factors, such as the change produced within its crystalline structure by the incorporation of chromium atoms in its structure as corroborated in **Figure 1**. This change in the crystalline structure due to the increase of compressive stresses generated that a higher amount of external energy is required to cause a delamination of the coating. In addition, for the multilayer system, it was determined that the increase in the number of interfaces directly affects the delamination resistance of the coatings, because the interfaces restrict movement of the cracks through the coating.

3.5.2 Tribological properties for TiCN, BCN and CrAlN coatings nitride coatings

Figure 15 show the tribological behavior of TiCN, BCN and CrAlN coatings deposited on AISI 1045 steel substrate when in direct contact with a 100Cr6 steel counterpart in lubricated and non-lubricated environments. These results showed two characteristic stages, stage I, known as the starting period, which is related to the

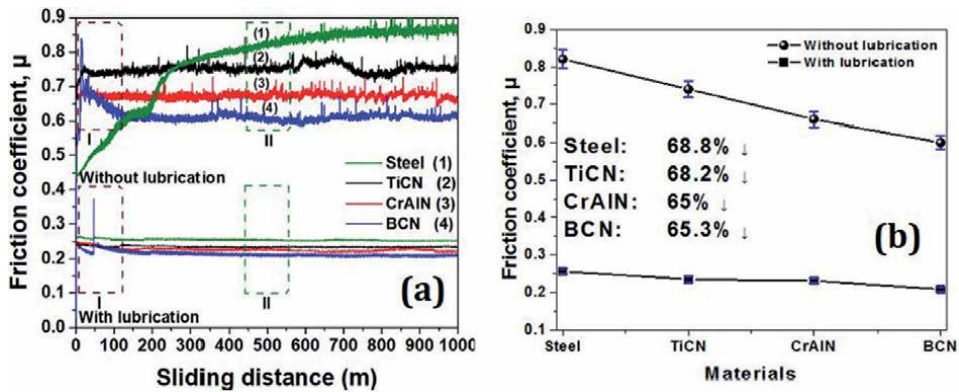


Figure 15. Tribological results of the AISI 1045 steel substrates with TiCN, BCN and CrAlN single layer coatings with and without lubrication: friction coefficient as a function of the sliding distance and friction coefficient for different coatings (TiCN, CrAlN and BCN): without lubrication and with lubrication.

interference of the friction mechanism due to the initial surface contact associated with the surface and counterpart; therefore; this contact generated a rapid increase in the friction coefficient and stage II is characterized by the friction coefficient presents a settlement period, where a deformation and elimination of the asperities takes place, causing a stabilization of the friction coefficient. Thus, at the settling distance there is an equilibrium of the friction coefficient in relation to the adhesive and interferential friction mechanisms. Therefore, the value of the friction coefficient will depend on the predominant effect related to the adhesive and interferential mechanisms. Finally, **Figure 13b** shows the value of the friction coefficient for all coatings and substrate (AISI 1045) in the non-lubricated environment, where they were obtained for Substrate = 0.82; TiCN = 0.74; CrAlN = 0.66 and BCN = 0.6. On the other hand, the values of the friction coefficient obtained in a lubricated environment were Substrate = 0.26; TiCN = 0.24; CrAlN = 0.23 and BCN = 0.21. Taking into account the last result, it was established that the BCN coating presented the best tribological behavior for both environments (dry and lubricated), this good behavior is attributed to its surface and mechanical properties presented above.

Through the results obtained by the scratch test presented in **Figure 16**, it was possible to evidence an increase of the critical load (L_{c2}) as a function of the nature of the coating (TiCN, CrAlN and BCN). Moreover, the change of the critical load is related to the increase of the mechanical properties of the coatings (**Figure 11**), the reduction of the surface roughness (**Figures 7 and 8**) and the reduction of the friction coefficient (**Figure 15**). In addition, factor such as resistance to plastic

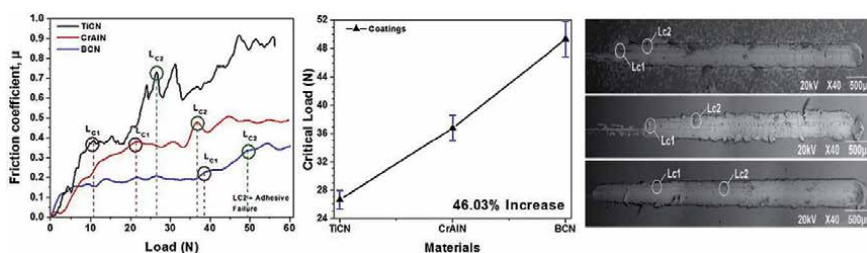


Figure 16. Friction coefficient as a function of the applied load for all TiCN, BCN and CrAlN coatings showing the cohesive failure (L_{c1}) and adhesive failure (L_{c2}) and critical load as a function of the coating's nature (TiCN, BCN and CrAlN).

deformation and elastic recovery prevent the propagation and displacement of cracks through the coating, thus requiring a higher applied external load to cause failure between the coating and the substrate (adhesive failure). Therefore, an increase in the critical adhesive load (Lc2) of 46.03% was found for the boron carbide nitride (BCN) coating relative to the coating with lower mechanical properties (TiCN).

3.5.3 Tribological properties for Si₃N₄ coatings nitride coatings

Figure 17a shows the friction coefficient of Si₃N₄ based coating deposited on AISI 316 steel substrates in a lubricated and dry environment. The results of the tribological study in dry environment evidenced two characteristic stages during the test. Stage I, known as the starting period, is associated with the interferential friction mechanism due to the direct contact between the surface roughness of the coating and the counterpart (100Cr6 steel), whereby, which, the roughness decreases and generates wear particles on the surface [5]. These particles cause a rapid increase in the friction coefficient followed by a slight decrease until it stabilizes. Subsequently, in stage II, the reduction of these roughness is maintained along with the appearance of new defects in the coating, leading to a stabilization of the friction coefficient [33].

In the lubricated environment, the curves show a different behavior in relation to the tribological study in dry environment (not lubricated), since the incorporate of the lubricant inside the tribological contact generated a large decrease in the friction coefficient. Therefore, the decrease in the friction coefficient is attributed to the fact that the lubricant supports the applied external load, decreasing the roughness reduction and caused a lower amount of wear particles (debris) on the tribo-system surface. **Figure 17b** shows the value of the friction coefficient as a function of the material, in dry and lubricated environment. This behavior is related to the friction model proposed by Archad [31]. This model correlates the mechanical (H, Er) and morphological (roughness) properties of the coating, where surface with better mechanical properties and lower roughness will present a lower friction coefficient, as was the case for the Si₃N₄ coating. This is due to the fact that the Si₃N₄ coating is able to withstand the continuous passage of the counterpart in relation to the uncoated steel substrate, thus producing a lower wear rate on its surface.

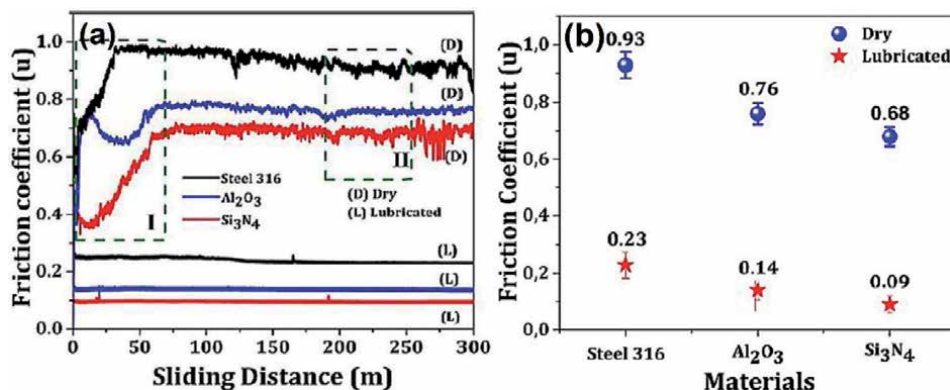


Figure 17. Friction coefficient for Si₃N₄ coatings in lubricated and non-lubricated environment: (a) friction coefficient versus sliding distance (b) friction coefficient as a function of the material evaluated.

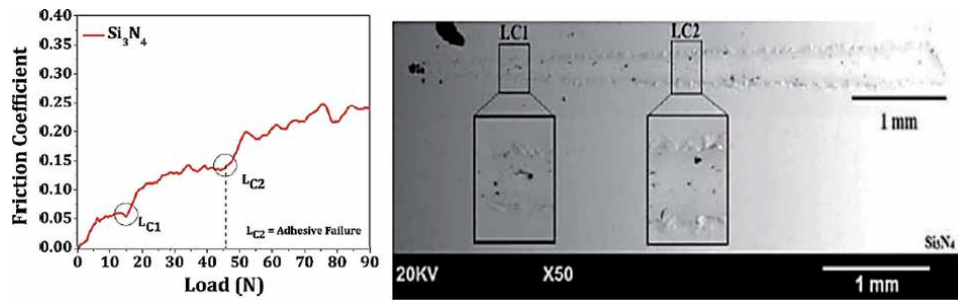


Figure 18. SEM micrographs of the wear tracks generated in the scratch test for Si_3N_4 coatings deposited on 316 stainless steel substrates.

Figure 18 shows the friction coefficient as a function of critical load for Si_3N_4 coating, in addition to the SEM micrograph of the scratch track where the types of failures, cohesive failure (L_{C1}) and adhesive failure (L_{C2}), were determined. In the cohesive failure (L_{C1}) the first cracks are produced by the applied external load, and in the adhesive failure (L_{C2}) a delamination is generated at the edge of the scratch track. These tribological characteristics are due to the mechanical and surface properties of the coating.

4. Conclusions

From the study of the mechanical and tribological behavior of TiN and TiCrN coating. It was determined that the TiCrN coating presented the best set of properties, these better properties were attributed to the incorporation of chromium (Cr) atoms within the crystalline structure of TiN. Therefore, structural, morphological and mechanical changes were produced, which influenced its behavior under applied load states.

The above results determined that the boron nitride (BCN) coating had the lowest friction coefficient (0.208) in a lubricated environment and had a friction coefficient of 0.6 in a non-lubricated environment. This tribological behavior is associated with its low roughness and high mechanical properties with respect to the coatings (TiCN and CrAlN). In this research, a decrease in the friction coefficient was obtained comparing non-lubricated and lubricated environments by 68.2%, 65% and 65.3% for TiCN, CrAlN and BCN coatings, respectively. On the other hand, cohesive failure (L_{C1}) and adhesive failure (L_{C2}) were obtained for BCN coating with 38.41 N and 49.32 N, respectively.

The tribological properties analyzed by Pin On Disk in dry and lubricated environment for the Si_3N_4 coating presented the lowest friction coefficient in relation to uncoated steel. This behavior is attributed to its structural, mechanical and morphological properties, so the Si_3N_4 coating proved to be a suitable candidate to be implemented in the food and pharmaceutical industry.

Acknowledgements

This research was supported by Universidad Militar Nueva Granada, Bogotá, Colombia; CIC biomaGUNE, San Sebastian, Spain; Centro de Desarrollo Tecnológico y Asistencia Técnica a la Industria del Servicio Nacional de Aprendizaje (CDT-ASTIN-SENA), Cali, Colombia; Universidad Autónoma de Occidente, Cali, Colombia.

Author details

Christian Ortiz Ortiz*, Erick Hernandez-Rengifo and Julio Cesar Caicedo
Universidad del Valle, Cali, Colombia

*Address all correspondence to: christian.ortiz.ortiz@correounivalle.edu.co

IntechOpen

© 2021 The Author(s). Licensee IntechOpen. This chapter is distributed under the terms of the Creative Commons Attribution License (<http://creativecommons.org/licenses/by/3.0>), which permits unrestricted use, distribution, and reproduction in any medium, provided the original work is properly cited. 

References

- [1] Grigoriev S, Vereschaka A, Milovich F, Tabakov V, Sitnikov N, Andreev N, et al. Investigation of multicomponent nanolayer coatings based on nitrides of Cr, Mo, Zr, Nb, and Al. *Surf. Coatings Technol.* 2020;**401**:126258 <https://doi.org/10.1016/j.surfcoat.2020.126258>
- [2] Hacisalihoglu I, Yildiz F, Alsaran A. Wear performance of different nitride-based coatings on plasma nitrided AISI M2 tool steel in dry and lubricated conditions. *Wear.* 2017;**384-385**:159-168 <https://doi.org/10.1016/j.wear.2017.01.117>
- [3] Chauhan KV, Rawal SK. A Review Paper on Tribological and Mechanical Properties of Ternary Nitride based Coatings. *Procedia Technol.* 2014;**14**:430-437 <https://doi.org/10.1016/j.protcy.2014.08.055>
- [4] Kumar S, Maity SR, Patnaik L. Effect of heat treatment and TiN coating on AISI O1 cold work tool steel. *Mater. Today Proc.* 2019;**26**:685-688 <https://doi.org/10.1016/j.matpr.2019.12.367>
- [5] Ortiz CH, Colorado HD, Aperador W, Jurado A. Influence of the number of bilayers on the mechanical and tribological properties in [TiN/TiCrN]_n multilayer coatings deposited by magnetron sputtering. *Tribol. Ind.* 2019;**41**:330-343 <https://doi.org/10.24874/ti.2019.41.03.03>
- [6] Ortiz CH, Hernandez-Rengifo E, Guerrero A, Aperador W, Caicedo JC. Mechanical and tribological properties evolution of [si₃n₄/al₂o₃]_n multilayer coatings. *Tribol. Ind.* 2021;**43**:23-39 <https://doi.org/10.24874/ti.952.08.20.01>
- [7] Chen R, Tu JP, Liu DG, Mai YJ, Gu CD. Microstructure, mechanical and tribological properties of TiCN nanocomposite films deposited by DC magnetron sputtering. *Surf. Coatings Technol.* 2011;**205**:5228-5234 <https://doi.org/10.1016/j.surfcoat.2011.05.034>
- [8] Correa JF, Aperador W, Caicedo JC, Alba NC, Amaya C. Structural, mechanical and tribological behavior of TiCN, CrAlN and BCN coatings in lubricated and non-lubricated environments in manufactured devices. *Mater. Chem. Phys.* 2020;**252**:123164 <https://doi.org/10.1016/j.matchemphys.2020.123164>
- [9] Hernandez-Rengifo EH-R, Ortiz CH, Hidalgo CH, Ballesteros JA, Caicedo JC. Comparative Study of Tribological and Mechanical Properties Between Single Layers of Al₂O₃ and Si₃N₄ Deposited on AISI 316 Stainless Steel. *Tribol. Ind.* 2021;**43**:259-273 <https://doi.org/10.24874/ti.956.09.20.01>
- [10] Paksunchai C, Denchitcharoen S, Chaiyakun S, Limsuwan P. Growth and Characterization of Nanostructured TiCrN Films Prepared by DC Magnetron Cosputtering. *J. Nanomater.* 2014;**2014**:1-9 <https://doi.org/10.1155/2014/609482>
- [11] Hovsepian PE, Ehiasarian AP, Petrov I. Structure evolution and properties of TiAlCN/VCN coatings deposited by reactive HIPIMS. *Surf. Coatings Technol.* 2014;**257**:38-47 <https://doi.org/10.1016/j.surfcoat.2014.07.065>
- [12] Correa JF, Aperador W, Caicedo JC, Alba NC, Amaya C. Structural, mechanical and tribological behavior of TiCN, CrAlN and BCN coatings in lubricated and non-lubricated environments in manufactured devices. *Mater. Chem. Phys.* 2020;**252**:123164 <https://doi.org/10.1016/j.matchemphys.2020.123164>
- [13] Wu Z, Li S, Xu Z, Wang Q, Zhou F. Tribological properties of boron carbonitride coatings sliding against

different wood (acerbic, beech, and lauan) balls. *Adv. Compos. Lett.* 2019;**28**:1-10 <https://doi.org/10.1177/0963693519875737>

[14] Falsafein M, Ashrafizadeh F, Kheirandish A. Influence of thickness on adhesion of nanostructured multilayer CrN/CrAlN coatings to stainless steel substrate. *Surfaces and Interfaces.* 2018;**13**:178-185 <https://doi.org/10.1016/j.surfin.2018.09.009>

[15] Caicedo JC, Aperador W, Mozafari M, Tirado L. Evidence of Electrochemical Resistance on Ternary V-C-N Layers. *Silicon.* 2018;**10**:2499-2507 <https://doi.org/10.1007/s12633-018-9782-7>

[16] Vyas A, Li KY, Zhou ZF, Shen YG. Synthesis and characterization of CN_x/TiN multilayers on Si(100) substrates. *Surf. Coatings Technol.* 2005;**200**:2293-2300 <https://doi.org/10.1016/j.surfcoat.2004.10.015>

[17] Nocua JE, Morell G, Piazza F, Weiner BR. Synthesis and characterization of stoichiometric boron nitride nanostructures | Síntesis y caracterización de nanoestructuras estequiométricas de nitruro de boro. *Superf. y Vacío.* 2012;**25**:194-198

[18] L. Ipaz, W. Aperador, J. Caicedo, J. Esteve, G. Zambrano, A Practical Application of X-Ray Spectroscopy in Ti-Al-N and Cr-Al-N Thin Films, in: *X-Ray Spectrosc., InTech*, 2012. <https://doi.org/10.5772/29640>.

[19] Hu H, Carim AH. Determination of attenuation lengths and electron escape depths in silicon nitride thin films. *J. Electrochem. Soc.* 1993;**140**:3203

[20] Kishi K, Roberts MW. Adsorption of nitrogen and ammonia by polycrystalline iron surfaces in the temperature range 80-290 K studied by electron spectroscopy. *Surf. Sci.* 1977;**62**:252-266 <https://doi.org/>

[https://doi.org/10.1016/0039-6028\(77\)90441-1](https://doi.org/10.1016/0039-6028(77)90441-1)

[21] Shin SH, Cho JW, Kim SH. Structural investigations of CaO-CaF₂-SiO₂-Si₃N₄ based glasses by Raman spectroscopy and XPS considering its application to continuous casting of steels. *Mater. Des.* 2015;**76**:1-8 <https://doi.org/10.1016/j.matdes.2015.03.035>

[22] Caicedo JC, Cabrera G, Caicedo HH, Amaya C, Aperador W. Nature in corrosion-erosion surface for [TiN/TiAlN]_n nanometric multilayers growth on AISI 1045 steel. *Thin Solid Films.* 2012;**520**:4350-4361 <https://doi.org/10.1016/j.tsf.2012.02.061>

[23] Navarro-Devia JH, Amaya C, Caicedo JC, Aperador W. Performance evaluation of HSS cutting tool coated with hafnium and vanadium nitride multilayers, by temperature measurement and surface inspection, on machining AISI 1020 steel. *Surf. Coatings Technol.* 2017;**332**:484-493 <https://doi.org/10.1016/j.surfcoat.2017.08.074>

[24] Piedrahita WF, Aperador W, Caicedo JC, Prieto P. Evolution of physical properties in hafnium carbonitride thin films. *J. Alloys Compd.* 2017;**690**:485-496

[25] Ipaz L, Caicedo JC, Esteve J, Espinoza-Beltran FJ, Zambrano G. Improvement of mechanical and tribological properties in steel surfaces by using titanium-aluminum/titanium-aluminum nitride multilayered system. *Appl. Surf. Sci.* 2012;**258**:3805-3814 <https://doi.org/10.1016/j.apsusc.2011.12.033>

[26] Donnet C, Erdemir A. Historical developments and new trends in tribological and solid lubricant coatings. *Surf. Coatings Technol.* 2004;**180-181**:76-84 <https://doi.org/10.1016/j.surfcoat.2003.10.022>

[27] Choi EY, Jang CS, Kang MC, Kim KH. Synthesis and Characterization of

Ti-C_x-N_{1-x} Coatings Prepared by Arc Ion Plating. *Solid State Phenom.* 2006;**118**:311-316 <https://doi.org/10.4028/www.scientific.net/SSP.118.311>

[28] Caicedo JC, Amaya C, Yate L, Gómez ME, Zambrano G, Alvarado-Rivera J, et al. TiCN/TiNbCN multilayer coatings with enhanced mechanical properties. *Appl. Surf. Sci.* 2010;**256**:5898-5904 <https://doi.org/10.1016/j.apsusc.2010.03.071>

[29] J.E. Sánchez, O.M. Sánchez, L. Ipaz, W. Aperador, J. Caicedo, C. Amaya, M.A. Landaverde, F.J. Espinoza-Beltrán, J. Muñoz-Saldaña, G. Zambrano, Mechanical, tribological, and electrochemical behavior of Cr_{1-x}Al_xN coatings deposited by r.f. reactive magnetron co-sputtering method, *Appl. Surf. Sci.* 256 (2010) 2380-2387. <https://doi.org/10.1016/j.apsusc.2009.10.071>.

[30] Barshilia HC, Deepthi B, Rajam KS. Deposition and characterization of CrN/Si₃N₄ and CrAlN/Si₃N₄ nanocomposite coatings prepared using reactive DC unbalanced magnetron sputtering. *Surf. Coatings Technol.* 2007;**201**:9468-9475 <https://doi.org/10.1016/j.surfcoat.2007.04.002>

[31] Archard JF. Contact and Rubbing of Flat Surfaces. *J. Appl. Phys.* 1953;**24**:981-988. <https://doi.org/10.1063/1.1721448>.

[32] Caicedo JC, Aperador W, Amaya C. Determination of physical characteristic in vanadium carbon nitride coatings on machining tools. *Int. J. Adv. Manuf. Technol.* 2017;**91**:1227-1241 <https://doi.org/10.1007/s00170-016-9835-2>

[33] Piedrahita WF, Aperador W, Caicedo JC, Prieto P. Evolution of physical properties in hafnium carbonitride thin films. *J. Alloys Compd.* 2017;**690**:485-496 <https://doi.org/10.1016/j.jallcom.2016.08.109>

Wear Life of Bonded MoS₂ Film Lubricant

Naofumi Hiraoka

Abstract

Bonded MoS₂ film lubricants are widely used in industry as solid lubricants. It has excellent lubrication properties, but it also has characteristics that require careful consideration. As is well known, its friction and wear are greatly affected by the environmental atmosphere and its wear life depends on the pre-treatment of the substrate. It was found that in many cases the wear life could not be correctly estimated by a specific wear rate and could be explained by the fatigue life, especially under high loading conditions. The atmosphere dependent wear life can also be explained by the fatigue life.

Keywords: solid lubricant, coating, friction, wear, atmosphere, fatigue, space use

1. Introduction

Molybdenum disulfide (MoS₂), along with graphite or PTFE, is a commonly used solid lubricant. One of the most commonly used forms of MoS₂ is a bonded film lubricant. Its application process is relatively simple and stable performance can be obtained, compared to other coatings such as sputtering. They are often used in automobiles and OA equipment, especially in aerospace applications.

Lubrication properties of MoS₂ are known to be greatly affected by environmental atmosphere, and the same is true for bonded MoS₂ film lubricants. They generally perform well in dry air, inert gas environments and in vacuum, compared to moist air environment. Because of this, they often used in space applications.

However, the performance in the atmosphere is often important even for space applications, which may be used in the atmosphere before the launching for the tests etc., and for devices that moves in and out of vacuum and the atmosphere.

The lubrication properties of bonded MoS₂ film lubricant in vacuum and in air were investigated, and it was found that specific wear rate is often not effective in estimating the wear life. Fatigue at the interface between the film and the substrate is found to be the main factor that determines wear life of bonded MoS₂ film lubricant, and short life in the atmosphere could be attributed to the fatigue.

2. Overview of bonded MoS₂ film lubricant

Figure 1 shows the typical application process of the bonded MoS₂ film lubricant. It can apply to various forms of products, including inner side of the holes.

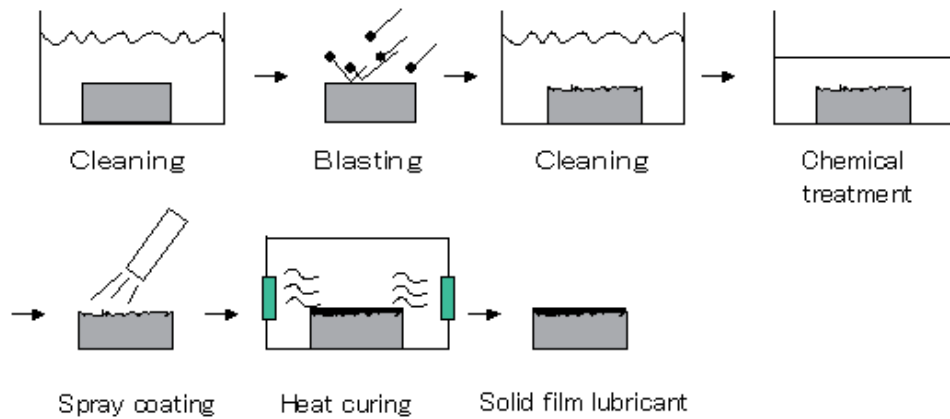


Figure 1.
Typical application process of bonded MoS₂ film lubricant.

The thickness of the film is typically about 10 micro-meters. Sometimes this is too large for some mechanical parts, e.g. precious ball bearings, but usually small enough to realize smooth engagement of the parts.

Figure 2 [1] shows the cross-section of the bonded MoS₂ film lubricant including substrate and film. The cross-section is enlarged vertically because it was cut diagonally. It can be seen that an intricately shaped substrate anchors the film. Such substrate surface morphology is produced by pretreatment of the substrate such as blasting. Chemical pretreatment passivates the surface of the substrate, some of which gives the surface a fine mesh-like structure. It has been reported that the final texture of the substrate surface is determined by blasting and that phosphate treatment, a type of chemical treatment, promotes significant changes in surface roughness [2]. Substrate pretreatment is an important process for providing a strong adhesion between the film and the substrate, resulting in a longer wear life of the bonded film lubricant [3].

As the lubrication performance in vacuum is excellent, the bonded MoS₂ film lubricants are often used in space applications [4–6]. **Figure 3** [4] shows the joint mechanism of the robot arm of the space station: ISS. Bonded MoS₂ film lubricant is applied to gears and sliding bearings in it. In general it seems to be often used for pure-sliding or rolling-sliding surfaces rather than pure-rolling surfaces.

Bonded MoS₂ film lubricants are used at a variety of sliding speeds and loading conditions, but naturally their limiting PV values are smaller than oil lubrication.

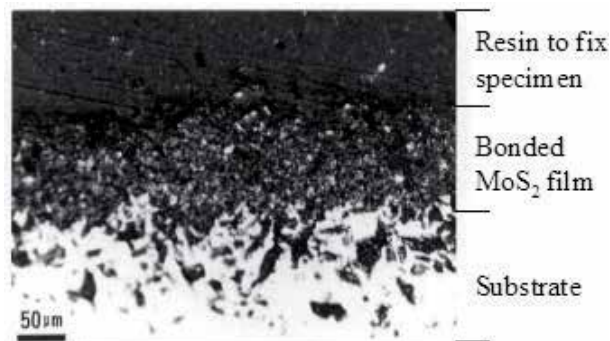


Figure 2.
Cross-section of bonded MoS₂ film lubricant [1].

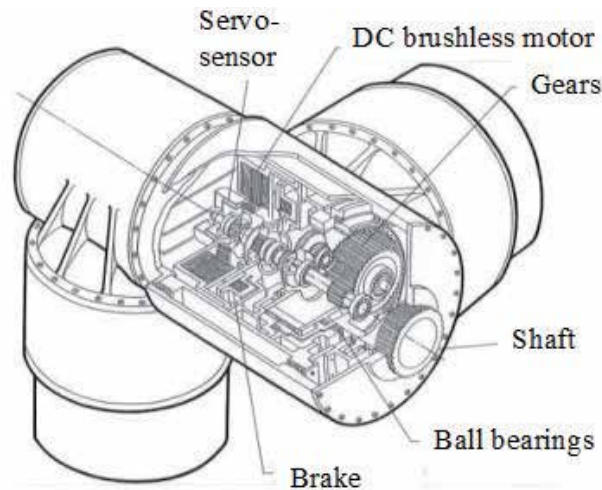


Figure 3.
Joint mechanism of robot arm of space station: ISS [3].

The working conditions under which they perform well seem to be high load and low speed conditions [7] where oil lubrication does not perform well. In this chapter, we will mainly discuss the friction and wear of bonded MoS₂ film lubricants under relatively high load and low speed conditions.

3. Wear life of bonded MoS₂ film lubricant

3.1 Effect of substrate

3.1.1 Experiment

The friction and wear life of journal bearings with bonded MoS₂ film lubricant applied to some substrates were investigated in vacuum using the test equipment shown in **Figure 4** [8]. **Figure 5** illustrates the friction measurement part of the equipment set in the vacuum chamber. The shaft was oscillated by AC servo motor through reduction gear and feedthrough. The radial load was applied by an air cylinder outside the vacuum chamber through a bellows. The bore and width of the bearing were 10 mm and 7 mm, respectively. The lubricant was applied both to the bearing and the shaft. The frictional torque was measured by the load cell above the test bearing.

The commercially available bonded MoS₂ film lubricant, including about 25 wt. % MoS₂ and phenolic resin binder, was spray coated and heat cured at 150°C for 1 h. The film thickness was about 10 micro-meters and the diameter clearance between the bearing and the shaft with lubricant film was 10-20 micrometers.

Table 1 [1] shows the substrate materials and pretreatment for the bearings and the shafts. **Table 2** [1] indicates the bearing and the shaft combinations. The circled numbers in the table correspond to those in **Table 1**. **Table 3** [1] shows the test conditions.

3.1.2 Experimental results

Figure 6 [1] illustrated the typical measured friction evolution. The measured friction drew the rectangular wave due to the oscillation motion and half of the total

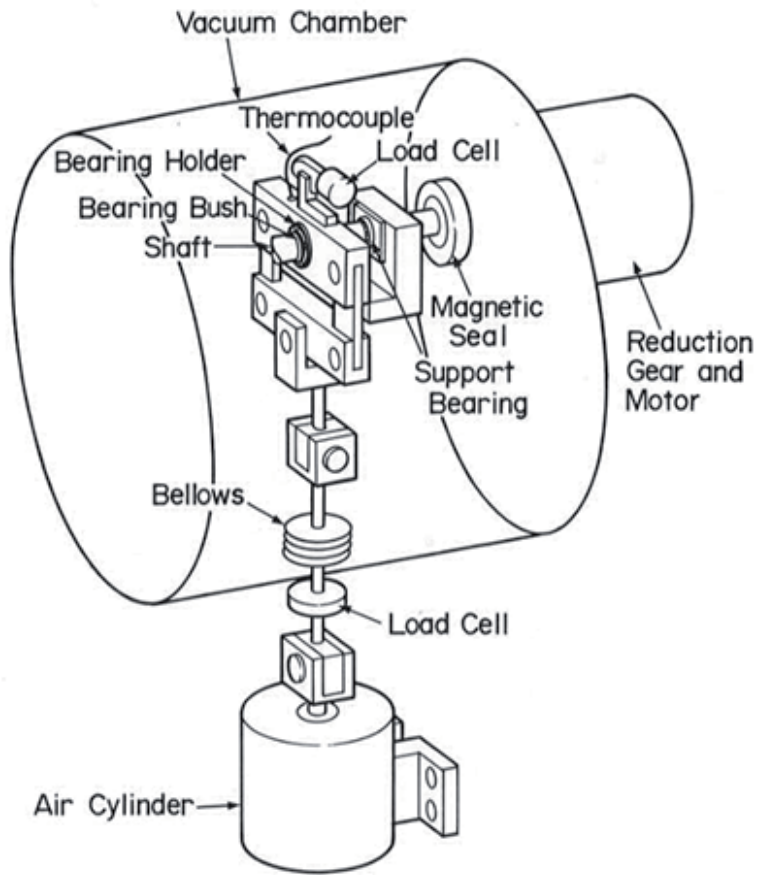


Figure 4.
In-vacuum journal bearing test equipment [7].

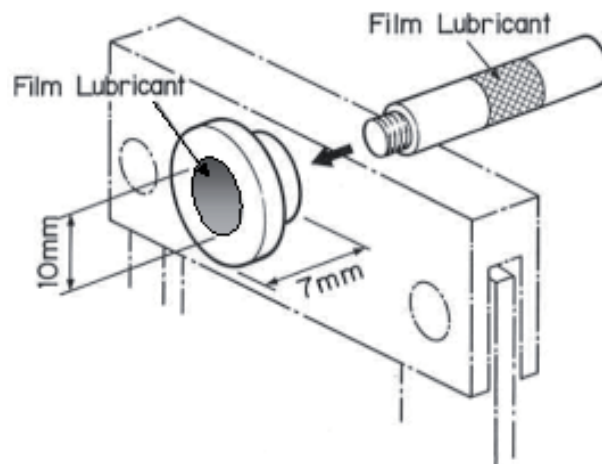


Figure 5.
Friction measurement part of the in-vacuum journal bearing test equipment.

No.	Substrate material	Heat-treatment	Hardness Hv.	Pretreatment
①	JIS 2017 aluminum alloy	JIS T4	120-130	Sand-blasting
②	JIS 440C stainless steel (martensitic stainless steel)	Quench hardening and tempering	570-590	Sand-blasting and passivating
③	JIS 304 stainless steel (austenitic stainless steel)	—	220-250	Sand-blasting and passivating

Table 1.
 Substrate materials and pretreatment for bearings and shafts [1].

Set No.	Substrate material	
	bearing	Shaft
1	①	②
2	②	②
3	③	③

Table 2.
 Bearing and shaft combinations [1].

Motion	Oscillation
Atmosphere	10 ⁻⁵ Pa vacuum
Load	1470 N
Angular velocity	10 deg./s
Oscillational angle	50 deg

Table 3.
 Test conditions [1].

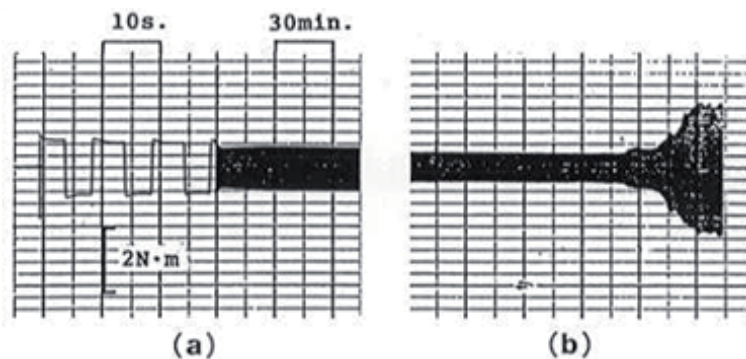


Figure 6.
 Typical measured friction evolution [1].

amplitude was used as the frictional force. The friction gradually decreased with the number of oscillations and suddenly increased. This sudden increase point was used as the wear life of the lubricant.

Figure 7 [1] shows the appearance of the tested shaft. A part of the film lubricant was removed and the metal substrate was exposed and scratched. **Figure 8** [1] shows

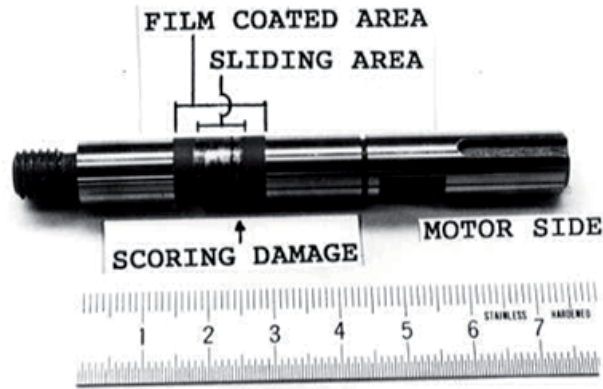


Figure 7. Appearance of the tested shaft [1].

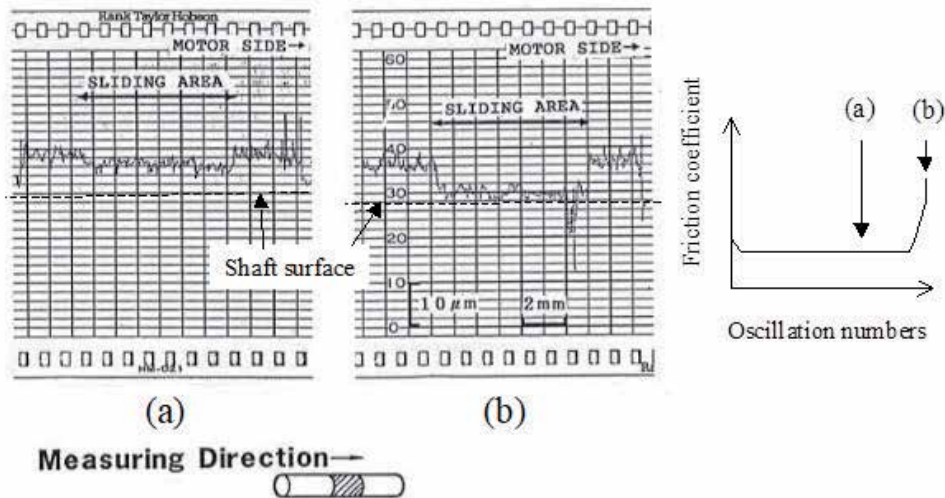


Figure 8. Lubricant film profiles: (a) about 60% of wear life, (b) after the friction increase [1].

the lubricant film profiles of Set No.3 specimen in **Table 2** at the points (a) and (b) in the wear life shown in the right diagram. Most of the film thickness remained near the end of the wear life, and the scratched part was observed at the end of the test.

Figure 9 [1] indicated the wear life and friction coefficient of the tested combinations. There was no significant difference in the friction coefficients, but the wear life of the SUS304 was much longer than the others.

3.1.3 Discussion

It was observed that the film thickness of the lubricant gradually decreased, but it seems that the wear life suddenly came with most of the film thickness remaining. This form of wear has been observed in several previous studies [9, 10]. This means that specific wear rates cannot be used to predict wear life. In some studies, specific wear rates has been proposed for the wear life estimation of the bonded MoS₂ film lubricant [9, 11]. It may be used for relatively large sliding speed and low load conditions, but cannot be used for small sliding speed and high load conditions like this case.

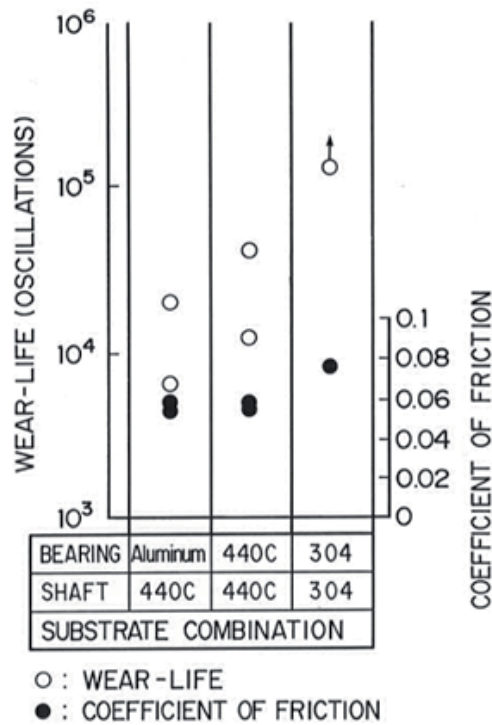


Figure 9.
 Wear life and friction coefficient of the tested combinations [1].

The sudden decrease of the film is probably due to the de-bonding of the film from the substrate, possibly due to fatigue. The adhesion strength between the substrate and the film must affect the fatigue strength, that is, the wear life, and is strongly dependent on the anchoring effect by the surface morphology of the pretreated substrate.

The surface morphology of the pretreated substrate was investigated using “pretreated surface specimen” shown in **Figure 10** [1]. A portion of one side of a

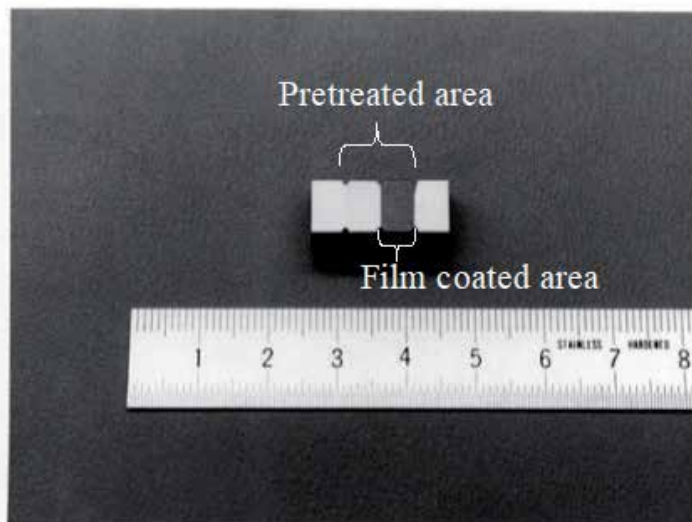


Figure 10.
 Pretreated surface specimen [1].

rectangular metal specimen was pretreated and the bonded MoS₂ film lubricant was applied to half of the pretreated area. **Figure 11** [1] shows the surface profiles of the specimens. As shown in (a) and (c), the pretreated areas of the aluminum alloy substrate and the SUS304 stainless steel substrate had a roughness that went up and down across the original surface, while that of the SUS440C stainless steel substrate

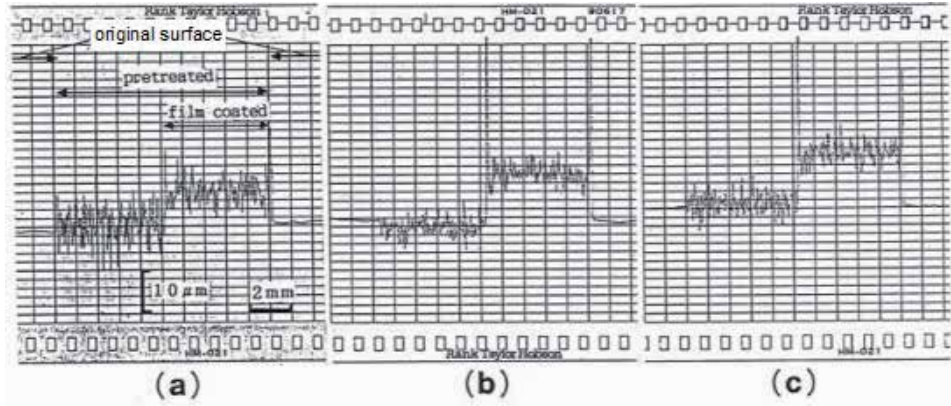


Figure 11. Surface profiles of the pretreated surface specimens, (a) aluminum alloy, (b) SUS440C, (c) SUS 304 [1].

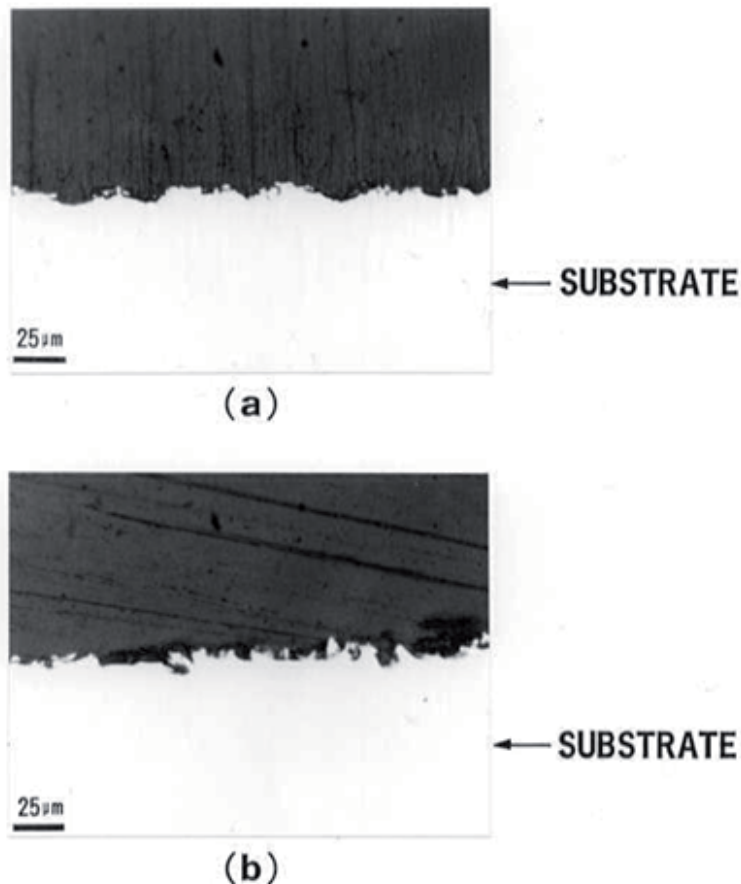


Figure 12. Cross-sections of the pretreated surface specimens: (a) SUS440C substrate, (b) SUS304 substrate [1].

was below the original surface. This means that ductile metal surfaces such as aluminum alloy and SUS304 stainless steel (austenitic stainless steel) were deformed plastically by the blasting and that of brittle metal such as SUS440C (martensitic stainless steel) seems to have had its surface layer taken away by the blasting. This resulted in a characteristic surface morphology.

Figure 12 [1] shows the cross- sections of the pretreated surface specimens. The SUS304 specimen indicated the intricate surface morphology, while the SUS440C specimen had a monotonous wavy surface morphology. Probably these morphologies brought the strong adhesion between the substrate and the film, that is, the long wear life, to the SUS304 substrate and short wear life to the 440C substrate. The work hardening would also have contributed to the long wear life of the SUS304 substrate. The short wear life of aluminum alloy substrate could be attributable to the deformation of surface morphology by the load due to the lack of the hardness.

3.2 Effects of atmosphere

3.2.1 Experiment and results

Friction and wear life characteristics were investigated under various loads, sliding speeds in air and vacuum atmospheres using the test equipment used in Section 3.1. Test materials and test conditions are shown in **Table 4** [8] and **Table 5** [8], respectively. SUS630 is a precipitation hardened stainless steel with high strength, and was chosen for the shaft specimen in consideration of actual applications.

Figure 13 [8] shows a typical change in the friction coefficient with the number of oscillations in air and in vacuum. The friction coefficient was several times larger and the wear life was several ten times shorter in air than in vacuum. The relationship between the friction coefficient and the load is shown in **Figure 14** [8]. Friction coefficient used was in the steady state as shown in **Figure 13**. Friction coefficient was about 0.2 in air and about 0.05 in vacuum regardless of test conditions.

Figure 15 [8] shows the relationship between the bearing pressure and the wear life. The wear life refers to the number of oscillations when friction increased sharply. There are two groups, one in vacuum and one in air, with differences in wear life of hundreds of thousands of oscillations. It seems that there is no relationship between the groups.

3.2.2 Discussion

Figure 16 [8] shows the lubricant film profile at about 70% wear life in air, obtained under the same test conditions as No. 5 in **Table 5**. Most of the film thickness remained, as in the in-vacuum test shown in **Figure 8**. This suggests that the wear life in air, as well as in vacuum, is due to the de-bonding of the film from the substrate, and that the fatigue strength of the film-substrate interface may determine the wear life.

Fatigue strength of some metals are known to be affected by atmosphere and be larger in vacuum than in air (e.g. [12]). However, it has been shown that the propagation rate of fatigue cracks in epoxy resins is almost the same in both

Shaft material	JIS 630 stainless steel (precipitation hardened stainless steel)
Bearing bush material	JIS 304 stainless steel
Bearing bore, mm × length, mm	10 × 7, 5 × 7, 10 × 3.5
Bearing clearance, μm	~20

Table 4.
Test materials [7].

No.	Bearing bore × width (mm)	Load (N)	Bearing pressure (MPa)	Oscillational angle (deg.)	Angular velocity (deg./s)	Atmosphere
1	10 × 7	5880	84	50	50	vacuum
2	10 × 7	1960	28	50	50	vacuum
3	10 × 7	980	14	50	50	vacuum
4	10 × 7	5880	84	50	50	air
5	10 × 7	1960	28	50	50	air
6	10 × 7	980	14	50	50	air
7	10 × 7	5880	84	50	5	vacuum
8	10 × 7	5880	84	50	5	air
9	10 × 7	1960	28	300	50	vacuum
10	10 × 7	1960	28	300	50	air
11	5 × 7	980	28	50	50	air
12	10 × 3.5	980	28	50	50	air

Table 5.
Test conditions [7].

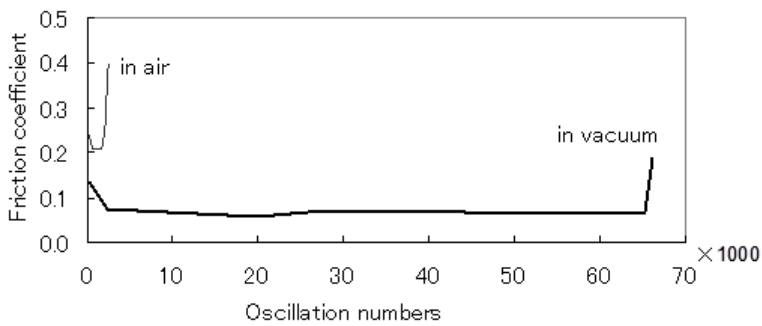


Figure 13.
Typical change in friction coefficient in air and in vacuum [7].

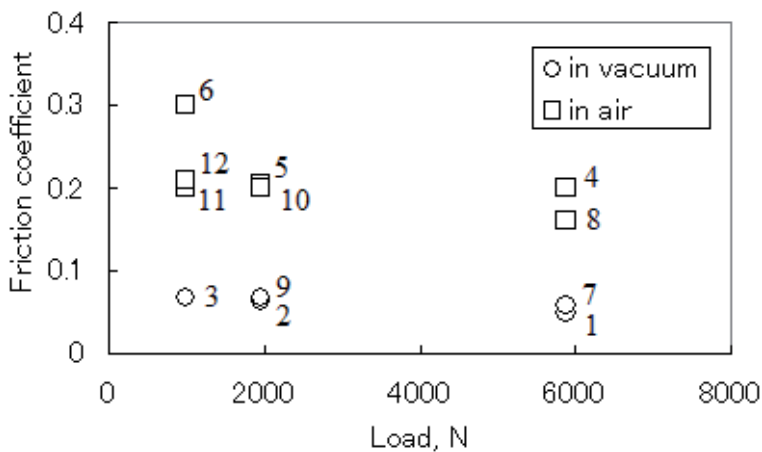


Figure 14.
Relationship between the friction coefficient and load [7]. The numbers correspond to those in Table 5.

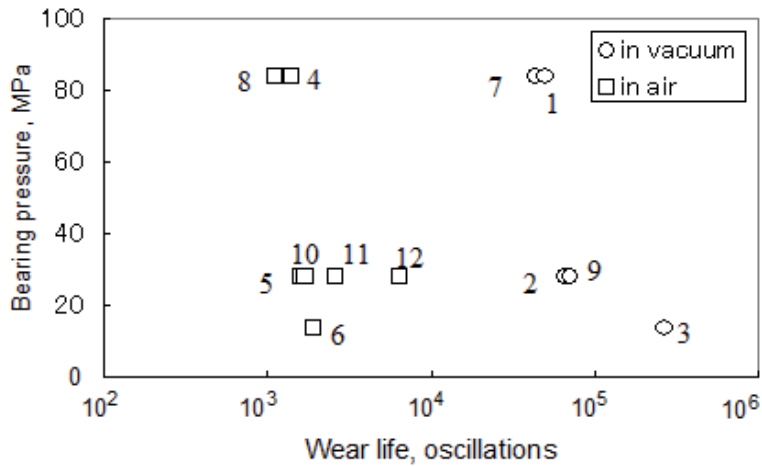


Figure 15.
 Relationship between bearing pressure and wear life [7]. The numbers correspond to those in Table 5.

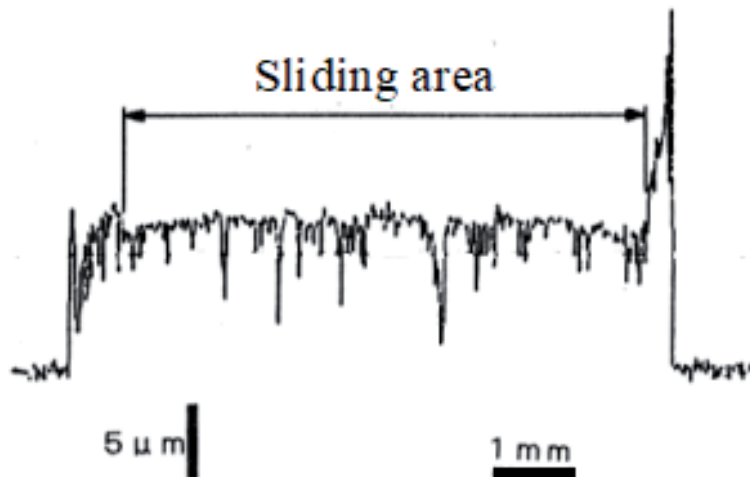


Figure 16.
 Lubricant film profile at about 70% wear life in air [7].

vacuum and air [13], and in general, the fatigue of resins, which are the binders of the films, is considered to be less affected by the atmosphere. Therefore, the short wear life due to fatigue of film lubricants in air is not considered to be due to their reaction to the environmental atmosphere. The factor that differs between vacuum and air and is considered to affect fatigue is the friction coefficient.

Stress analysis was performed to investigate the effects of the friction coefficient on the stress in the film [8]. The analysis was performed as a plane strain perfect elasticity problem. Young's modulus of the film was measured in dry air to be about 10 GPa. Calculation conditions are shown in Table 6 [8].

Figure 17 [8] shows examples of the calculated stresses in the film. Since the film thickness is small compared to the contact length, the stress is almost constant in the depth direction of the film.

Figure 18 [8] shows the relationship between the maximum shear stress at the interface between the film and the substrate in the direction parallel to the interface and wear life. All points are on a straight line, whether they are in vacuum

	Film thickness (μm)	Young's modulus of film (GPa)	Poisson's ratio of film	Young's modulus of substrate (GPa)	Poisson's ratio of substrate
	10	10	0.3	197	0.3
No.	Bearing bore (mm)	Shaft diameter (mm)	Line load (N/mm)	Friction coefficient	Corresponding test numbers
1	10.02	10	840	0.05	1, 7
2	10.02	10	280	0.05	2, 9
3	10.02	10	140	0.05	3
4	10.02	10	840	0.2	4, 8
5	10.02	10	280	0.2	5, 10, 12
6	10.02	10	140	0.3	6
7	5.02	5	140	0.2	11

Table 6.
Calculation conditions [7].

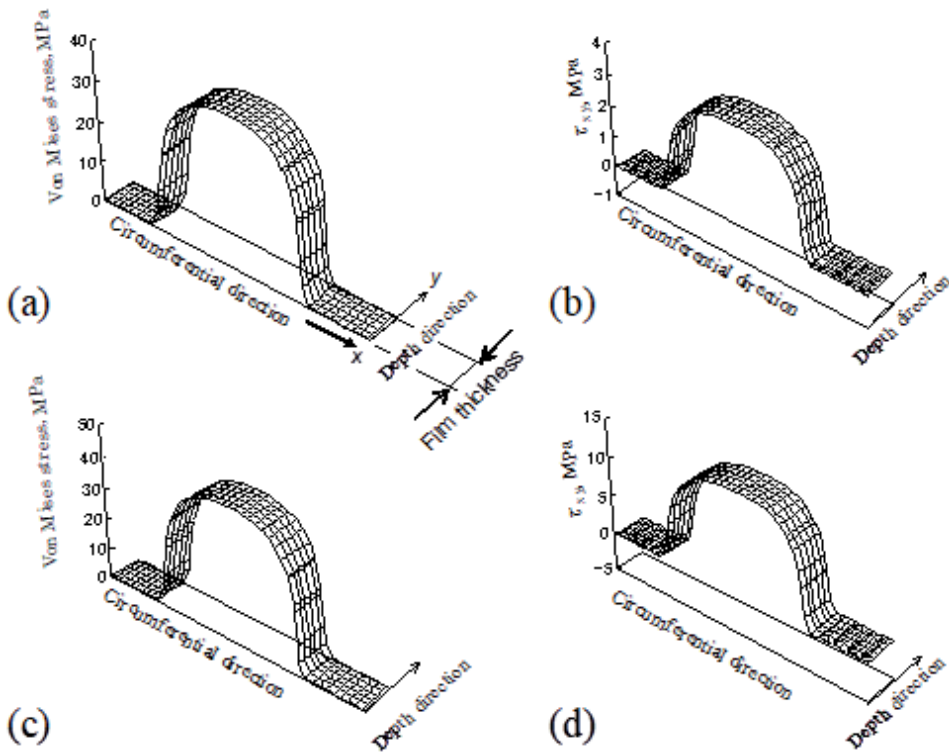


Figure 17.
Examples of calculated stresses in the film [7].

or in air. This is a typical S-N curve for fatigue phenomenon. Therefore, the wear life of the bonded MoS_2 film lubricant can be attributed to fatigue due to shear stress at the interface. Since the contact width is much larger than the film thickness, the shear stress at the interface is almost the same as the shear stress at the film surface, i.e., the product of the friction coefficient and the contact pressure,

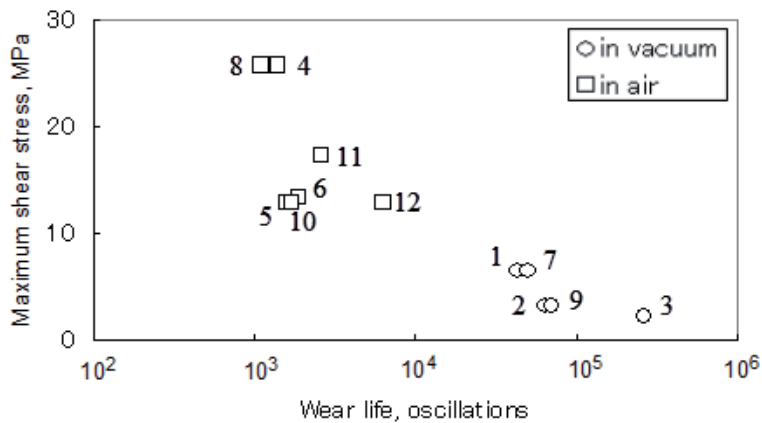


Figure 18. Relationship between the maximum shear stress at the interface between the film and the substrate and wear life [7].

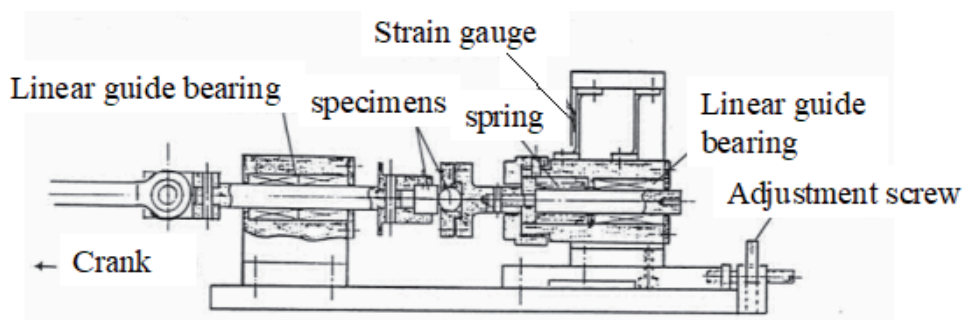


Figure 19. Repeated vertical loading machine [13].

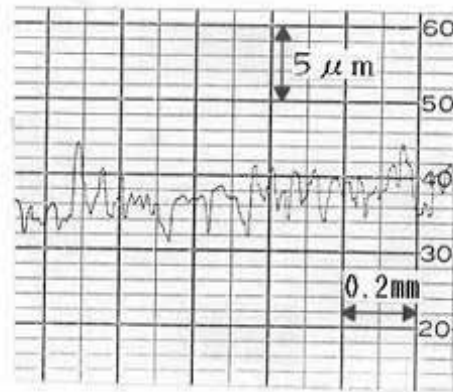
as shown in **Figure 17(b)** and **(d)**. Since the maximum von Mises stress, which contains a large component of vertical loading, did not show the same relationship as the shear stress, damage inside the film is not considered to be the cause of wear life in this case. Thus, the difference in wear life between vacuum and air is due to the friction coefficient between vacuum and air.

The effect of repeated vertical loading was investigated separately. **Figure 19** shows the “repeated vertical loading machine” [14], in which the bonded MoS₂ film lubricant on the flat surface was subjected to the repeated vertical pressure by a steel ball with 5/16 in. (~7.9 mm) diameter. A sinusoidal load of 0.98 N to 4.4 N was applied at a frequency of 1000 cpm.

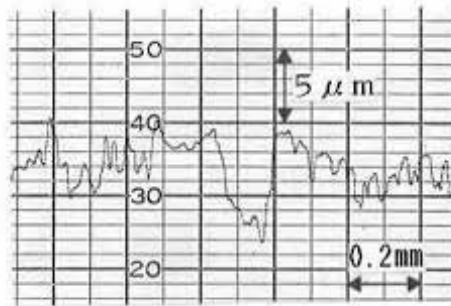
Only dents with a few micrometer depth were observed on the tested lubricant films after more than 10⁷ times loading, as shown in **Figure 20** [14], and no de-bonding was observed. Hence, the repeated shear stress, i.e. the friction, rather than the repeated vertical load causes the de-bonding of the film lubricant.

4. Conclusions

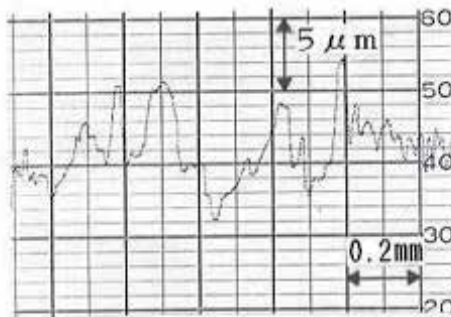
Wear life of bonded MoS₂ film lubricants was found to be caused by de-bonding of the film from the substrate due to fatigue under relatively high load and low speed condition. In order to improve wear life, it is important to select substrate materials with appropriate surface morphology through pretreatment to provide



(a)



(b)



(c)

Figure 20. Surface profiles of the film after the tests: (a) static loading, (b) 1×10^7 loadings, (c) 4.4×10^7 loadings [13].

strong adhesion to the film. The specific wear rate, which assumes that the amount of wear of the material is constant according to the load and sliding distance, is not suitable for estimating the wear life of bonded MoS₂ film lubricants under these conditions.

When the thickness of the film is much smaller than the contact length, as in the case treated here, the frictional force directly becomes the shear force at the interface, which determines the fatigue life of the film-substrate adhesion. In other words, the friction coefficient has a direct effect on the wear life of the film lubricants. It was shown that the wear life of bonded MoS₂ film lubricant in vacuum is much longer than in air. This is because the friction coefficient in vacuum is much smaller than in the air.


In order to improve the wear life in air, it is effective to reduce the friction coefficient in air. It is the moisture in air that increases the friction of MoS₂ in air. Attempts to reduce the friction in air, such as adsorbing a surfactant on MoS₂ to prevent the adsorption of water molecules and thus imparting hydrophobicity to MoS₂ [15], are expected to expand the application fields of bonded MoS₂ film lubricants.

Author details

Naofumi Hiraoka
Institute of Technologists, Gyoda, Saitama, Japan

*Address all correspondence to: hiraoka@iot.ac.jp

IntechOpen

© 2021 The Author(s). Licensee IntechOpen. This chapter is distributed under the terms of the Creative Commons Attribution License (<http://creativecommons.org/licenses/by/3.0>), which permits unrestricted use, distribution, and reproduction in any medium, provided the original work is properly cited. 

References

- [1] Hiraoka N, Sasaki A, Kawashima N, Honda T. Wear characteristics of bonded solid film lubricant under high load condition. IN: Proceedings of 25th Aerospace Mechanisms Symposium; 1991; Pasadena; 179-193.
- [2] Rovani A C, Kouketsu F, da Silva C H, Pintaude G: Surface characterization of three-layer organic coating applied on AISI 4130 steel. *Advances in Material Science and Engineering*. 2018. DOI: 10.1155/2018/6767245
- [3] Kawamura M. Solid lubrication. Kimura Y., editor. IN: *Tribology data book*. Tokyo: Technosystem; 1991, p. 147-184.
- [4] Kawashima N, Hiraoka N, Yoshii Y.: Space Tribology in Japan, IN: *Proceedings of Institution of Mechanical Engineers*. 1996: 210:173-178. DOI: 10.1243/pime_proc_1996_210_496_02.
- [5] Hiraoka N, Yoshii Y, Kawashima N: Bonded MoS₂ film lubricants in space application. *Journal of Japanese Society of Tribologists*. 1994: 39: 2: 87-92
- [6] Hiraoka N, Yoshii Y, Sasaki A: Solid lubrication Technology in JEMRMS, *Toshiba Review*. 1998:53:9:51-53.
- [7] Ito K: Typical properties of bonded lubricants. *Journal of Japanese Society of Tribologists*. 1991:36: 2:126-129.
- [8] Hiraoka N: Wear life mechanism of journal bearings with bonded MoS₂ film lubricants in air and vacuum. *Wear*. 2001:249:1014-1020. DOI: 10.1016/S0043-1648(01)00845-6.
- [9] Martin J T, Balster C H, Abdulhadi F: Measurement of shear modulus for solid lubricants: wear life coefficients for MoS₂ in epoxy resin. *Lubrication Engineering*. 1972:28:43-47.
- [10] Kishi K, Arita M, Yasud Y, Nameki T: Effects of substrate pretreatment on life of bonded MoS₂ film lubricants. IN: *Proceedings of JAST Tribology Conference*; 1992-10; Morioka; 125-128.
- [11] Finkin E F: A wear equation for bonded solid lubricant films: estimating film wear life. *Transactions of ASME. Journal of Lubrication Technology*. 1970:4:274-280. DOI: 10.1115/1.3451385.
- [12] JSME editor. IN: *Design material for metal material fatigue strength (III)*: JSME: 1994:p21-25. DOI: 10.11501/2519119.
- [13] Wakashima H, Kurobe T, Miyazaki T, Onishi T: Fatigue Crack Propagation in Epoxy Resin Containing Plasticizer. *Journal of the Society of Materials Science, Japan*. 1976:25:271:48-52. DOI: 10.2472/jsms.25.370.
- [14] Hiraoka N, Kawashima N, Honda T: Deformation characteristics of bonded solid film lubricant. IN: *Proceedings of the Space Sciences and Technology Conference*, 1989; Nagoya; 852-853.
- [15] Hiraoka N, Kato T: Lubrication properties of cationic surfactant-adsorbed molybdenum disulfide as a bonded film lubricant, *STLE Transactions*. 2003: 46: 2:211-216. DOI: 10.1080/10402000308982619.

Section 2

Applications

Tribology in Marine Diesel Engines

Sung-Ho Hong

Abstract

This chapter deals with the tribology of marine diesel engines. Several types of diesel engines have been installed and used in the engine room of marine ships. Some of them, used for propulsion, operate at low-speed in a two-stroke combustion process in conjunction with propellers. Four-stroke engines are used for power generation and operates at medium-speed. In general, two or more four-stroke engines, including spares, are installed in the large ships. Tribological problems are important issue in the respect of reliability in the marine diesel engines, and there are many tribological engine components including bearings, pistons, fuel injection pumps and rollers. Moreover, the marine engines have lubricant problems such as lacquering. Improvements to the tribological performance of marine engine components, and lubricants can provide reduced oil and fuel consumption, improved durability, increased engines power outputs and maintenance. Therefore, this chapter shows better designs and methods in order to improve the tribological problem in the marine diesel engines.

Keywords: marine diesel engine, medium-speed diesel engine, low-speed diesel engine; fuel injection pump, lacquering; bearing, condition monitoring

1. Introduction

The marine diesel engine was first installed in the *Selandia*, which is oceangoing vessel, in 1912. According to statistics, diesel engines used as a power source more than 95% in the ships of 2,000 tons or more [1]. Various types of engine used in the ship according to fuels such as diesel engine, gas engine and dual fuel engine. Among those marine engines, diesel engines have a large portion in marine engine market from the past to the present. Marine diesel engines burn refined but mostly residual fuels with a legislated maximum sulfur content between 0.0005% and 4.5% w/w sulfur. The intention is to reduce SO_x exhaust gas emissions for environmental reasons [2]. There has been a steady decline in NO_x emissions at an acceptable level due to the increasing number of rigorous exhaust legislations for marine diesel engines to minimize NO_x emissions. Reduced NO_x emission can also be achieved by selective catalyst reduction (SCR), which is the most widely used and established technology [3]. Although ship pollution rules of IMO (international maritime organization) strengthened like IMO Tier III, the demand for engine performance improvement is also increasing.

Marine diesel engine types are two-stroke cycle and four-stroke cycle. The two-stroke engines are engine that complete a power cycle with two strokes of the piston during only one crankshaft revolution, and operate with about 100 rpm.

On the other hand, the four-stroke engines are internal combustion engines in which the piston complete four separate strokes during two crankshaft revolutions, and work in the speeds of 250 to 850 rpm. In case of large ships such as container ship, the two-stroke engines commonly installed as propulsion and the four-stroke engines operated as generators. This is because the two-stroke engines have higher torque and superior power-to-weight ratio than the four-stroke engines. However, the four-stroke engines used as propulsion in relatively small ship such as passenger boats and ferries.

Distillate oil and residual oil are the two most common types of marine fuels. “Intermediate oil” is the third type of marine fuel that combines the first two main types. In a refinery, petroleum fractions of crude oil from distillate fuel are separated by a boiling process. Residual fuel, also called ‘tar’ or ‘petroleum pitch’, is a fraction of the fuel that does not boil. Unwanted substances, such as chemical waste, are found in this type of fuel. Fuel system components, fuel injection equipment, pistons, piston rings, and cylinder liners can be damaged by these undesirable materials [4].

Various problems arise in the process of increasing the size of an engines or improving its performance. The solution and improvement of tribological problems related to friction wear and lubrication is very important in terms of reliability in marine diesel engines. This chapter present researches on machine components of marine diesel engines, which have tribological problems such as wear, sticking and oil consumption.

2. Tribological improvement of machine components in marine diesel engines

Many ship owners demanded from marine engine manufacturers to execute various technological modifications to increase the engine efficiency and to extend the life time of machine components. One of methods to accomplish these demands is to improve the tribological characteristics of machine components in the marine engines. In the Section 2, tribological improvement of machine components such as cylinder liners, fuel injection pumps, and bearings are explained. In addition, it includes the contents of lacquering that causes the tribological problems and the contents of machine condition diagnosis using the lubricant analysis.

2.1 Cylinder liner

The cylinder liners are a hollow cylinder shell which acts as the enclosure in which the combustion takes place. They have enough strength under the fluid pressure due to combustion and high-level stress induced in them. The cylinder liners are a cylindrical part to be fitted into an engine block to form a cylinder, and they are called “cylinder sleeve” in some countries.

They have main functions such as formation of sliding surface, heat transfer and compression gas sealing. The cylinder liners are served as the inner wall of a cylinder, and forms a sliding surface for the piston rings in order to reduce wear of piston, piston ring and oil consumption while supplying the lubricant in the clearance. The cylinder liners receive combustion heat through the piston and piston rings, and transmit the heat to the coolant. The cylinder liners are responsible to tolerate the combustion pressure, the contact with piston and piston rings while guiding the piston [5]. When the lubrication characteristics between the cylinder liner and the piston are poor, wear occurs on the lubricating surfaces, and scuffing phenomena also appear in severe cases.

Since there are few failure dates, it is difficult to estimate the reliability of the cylinder liners and ad hoc reliability tests are prohibitively expensive. Therefore, the liners are subjected to rigorous maintenance in order to reduce the frequency of failures while in operation. Both wear degradation and thermal cracking are the leading causes of failure of cylinder liners [6]. The significant number of abrasive particles on the piston surface generated by intensive combustion of fuel and lubricant deterioration is the primary wear process in this location [6]. A fatigue process caused by repetitive thermal shocks results in thermal cracking of the liner. As a result of insufficient chemical treatment, a thermal shock is generated by a fast temperature shift of the cooling fluid that laps the liner's exterior surface. Furthermore, this shock is typically exacerbated by scale and corrosion in the cooling water spaces [6].

The cylinder liner-piston ring system is one of the major contributors for the mechanical losses in marine diesel engines [7]. Lubrication of cylinder liner is very important for any marine diesel engines because it controls the wear and enhance the life of the engine. In general, lubrication performs three purposes. First, it prevents metal-to-metal contact between the cylinder liner and piston rings by creating an oil layer. Second, it neutralizes sulfuric acid and controls corrosion caused by detergent. Third, it cleans the cylinder liner, especially the piston ring pack, and prevents failures and corrosion due to neutralization residues and fuel combustion. So, several researches related to lubricant of cylinder liners are performed. Measurement of iron ppm in the cylinder drain oil was used to assess the degree of cylinder wear. Moreover, the role of alkaline additive in protecting surface of the metal from the acid was estimated in cylinder liner. That is, linear wear rates were estimated as a function of sulfur contents in fuel, feed rate and alkalinity of lubricant [8].

Surface texture of the cylinder liner identified as one of the significant factors that improve the tribological properties of marine diesel engine with regard to wear, oil consumption, fuel efficiency, lubrication oil (wear particle concentration). Surface texture is one of technical methods which alter a material's surface by modifying its texture and roughness. Various surface texturing methods employed such as laser surface texturing (LST), pulsed air arc treatment, electropolishing, reactive ion etching (RIE), photochemical machining, maskless electro chemical texturing, micro-computer numerical control (CNC) texturing. Among the different surface texturing techniques, LST is one of the most widely used non-contact type method and **Figure 1** show the cylinder liner with surface texturing. The effect of partially LST is evaluated through testing of marine diesel engines. The ellipse patterns oriented at the sliding direction contributed the most to reduce the friction coefficient [7].



Figure 1.
Surface textured cylinder liner.

Generally, the honing applied to inner wall of the cylinder liners as shown in **Figure 2**. The function of the honing to hold a satisfactory amount of lubricant oil and reduce friction. The honing process is applied to get surfaces with good functions for the ring or liner contact. The honing tool is comprised of a number of honing stones, which are similar to grinding wheel [9]. The surface of honed cylinder liner is characterized by a negative skewness, R_{sk} (S_{sk}) and kurtosis, R_{ku} (S_{ku}) values higher than 3. The honing is comprised of smooth wear resistant plateaus with deep valley, which have the effect of oil reservoirs and traps for wear particles [10]. Moreover, the selection of honing machine depends on the honing process (vertical or horizontal honing), honing angle, depth of honing, bore diameter, stroke length. The processing condition of honing should be selected according to engine's output, engine type, and engine manufacturer recommendation.

2.2 Fuel injection pump

Fuel injection pump is one of the main components of the marine diesel engines. The fuel pump is device that supplies compressed fuel into the cylinders of the diesel engines, and controls the amount of fuel oil needed to gain the desired power. Moreover, it operates with a timing that keeps the engine running smoothly. The mechanical reciprocating fuel pump which used in marine engines is referred to as a "Bosch type pump," and it consists of a barrel and a helical plunger as shown in **Figure 3** [11, 12].

Various factors, such as lacquer, foreign debris, and insufficient clearance, can block the plunger inside the barrel and cause a 'stick' problem in most fuel pumps. **Figure 4** shows how the development of the lacquer in the pump limits the space between the plunger and the barrel [11]. Several researches tried to solve and improve the stick problem as follows:

- Optimal design of clearance between the plunger and the barrel
- Application of taper shape and grooves
- Design of cross-sectional shape in groove.



Figure 2.
Honing in cylinder liner.

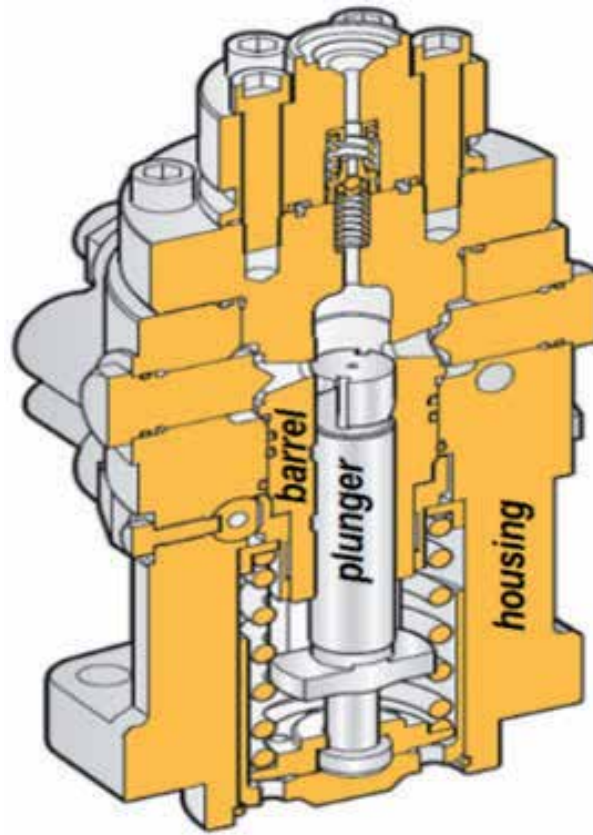


Figure 3.
Fuel injection pump [11].

- Prevention of lacquering

In this section, researches on optimal design of clearance, and application of taper shape and grooves focused among several methods. Grooves applied various machine components have several functions such as reduction of friction loss, oil reservoir and trapping of wear particles [13]. Trap effect of groove investigated with

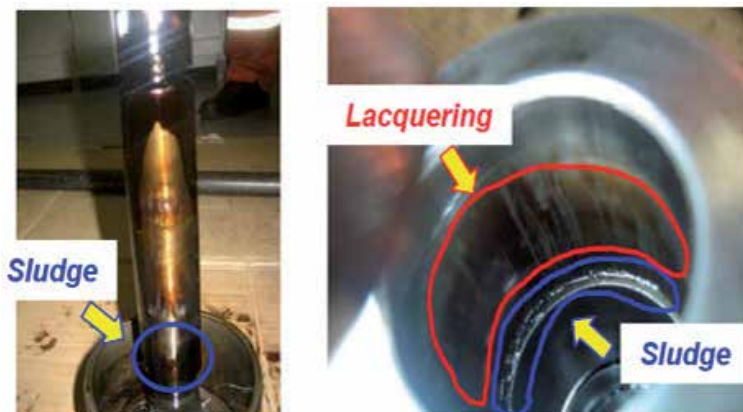


Figure 4.
Lacquer formation in fuel pump [15].

variation in cross-sectional shape and Reynolds number. The effect of groove is evaluated using computational fluid dynamics (CFD) analysis. The simulation based on the standard $k-\epsilon$ turbulence model and the discrete phase model (DPM). The simulation results are also capable of showing the particle trajectories in flow field. Various cross-sectional shapes of groove such as rectangular, triangle, U shaped, trapezoid, elliptical shape evaluated. Through the CFD analysis, it found that the cross-sectional shapes favorable to the creation of vortex and small eddy current are effective in terms of particle trapping effect [13]. In particular, the residual fuel used in marine diesel engines contain relatively many foreign materials or impurities, so the design of groove which have a good trap effect needed to prevent the three body abrasive wear and sticking. Prevention of lacquering explained in Section 2.3.

2.2.1 Optimal design of clearance

Regarding the lubrication characteristics of lubricating system, the influence of the clearance is significant, and many studies have been performed on the effect and design of clearance in terms of varieties of bearing and joints. The clearance between the plunger and barrel in fuel injection pump is also important to keep stable operation for marine diesel engines. In marine diesel engines, high viscosity fuel oils such as heavy fuel oil (HFO) and low viscosity fuel oils such as light diesel oil (LDO) have been used, and several lubrication techniques have been used depending on the fuel oil viscosity. The supplied fuel and lubricant oil lubricate the system when low-viscosity fuel oil is used, while only the fuel oil lubricates the system when high-viscosity fuel oil is used. Therefore, it is necessary to test the pump's lubrication characteristics at different viscosity levels. Furthermore, since the pump may work at high pressures of up to 1,500 bar, deformation should be taken into account. Due to the substantial effect of restriction circumstances on pump deformation, structural analysis is adequate for clearance design when maximum fuel oil supply pressure is applied. In addition, the highest reduction in clearance is used solely as a design limit.

The clearance in the fuel injection pump is estimated by structural and hydrodynamic lubrication studies. A structural study looks at structural changes in the plunger and barrel when they are subjected to maximum supply pressure due to fuel oil compression. Furthermore, the structural study also evaluates the maximum reduction in clearance caused by deformation. As viscosities and clearances vary, the hydrodynamic study of lubrication analyzes the lubrication properties. The clearance between the plunger and the barrel is divided into two sections, head and stem as shown in **Figure 5**. The lubrication characteristics are then compared by calculating the film parameters from the minimum film thickness and surface roughness, as shown in Eq. (1). The surface roughness is determined from the surface roughness of the plunger and barrel, as shown in Eq. (2).

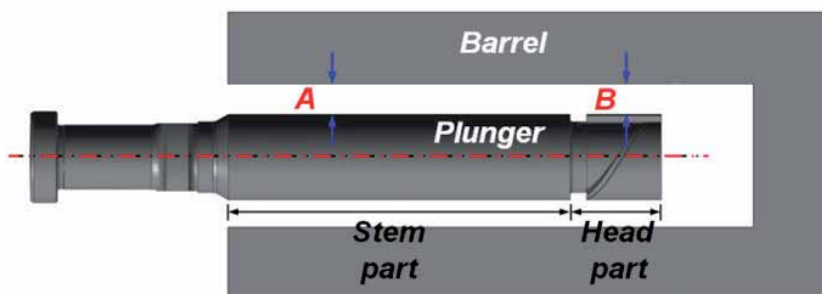


Figure 5. Dimensionless clearance of stem part (A) and head part (B) [11].

$$\text{Film parameter}(\lambda) = \frac{\text{Minimum film thickness}(h_m)}{\text{Surface roughness}(R_q)} \quad (1)$$

$$R_q = \sqrt{R_{q1}^2 + R_{q2}^2} \quad (2)$$

Figure 6(a) shows the positions of three sections where the deformations of the barrel and plunger have been evaluated. The deformation (enlarged 300 times) in the top, middle, and bottom sections is illustrated in **Figure 6(b)–(d)**. The ratio of displacement to clearance of the stem in the plunger is represented by a dimensionless displacement, which is a dimensionless value. Since the study is conducted in the absence of a clearance condition, overlapping regions indicate a decline in clearance. This is because the primary orientations for the barrel and the plunger are virtually perpendicular, and the spill port of a barrel has a significant impact on deformation. The clearance reduction is assessed in two parts. In the head, the barrel's and the plunger's deformations are studied. However, deformation of the plunger is investigated only in the stem as a low film pressure does not distort the plunger barrel. As shown in **Figure 7**, the deformation of the pump is studied quantitatively to determine the highest reduction in clearance. This figure also shows that the plunger's centerline and the barrel's line have a dimensionless displacement. The dashed line represents the displacement of the barrel, and the solid line represents that of the plunger. When deformation of the plunger is larger than that of the barrel, a reduction in clearance at the head occurs. **Figure 8** shows the dimensionless displacement at the red line of the plunger. In **Figure 8**, the region to the left of the pink dashed line is the area in which the plunger is inside the barrel during reciprocating motion. The maximum reduction in the clearance is the maximum displacement in the stem part. The structural analysis found that the clearance should be higher than the maximum clearance decrease to avoid metal-to-metal contact between the barrel and the plunger due to deformation.

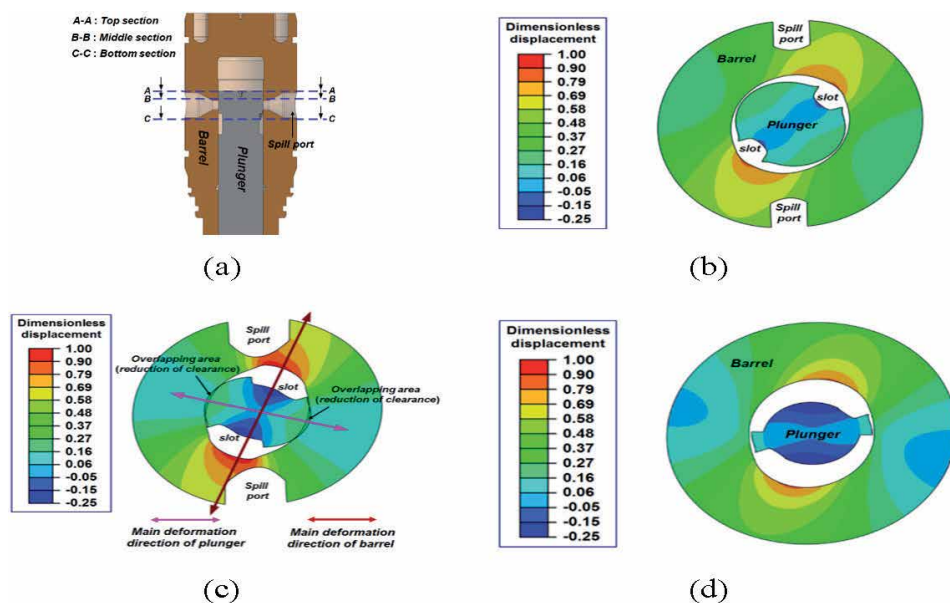


Figure 6. Dimensionless displacement on the three sections [11]. (a) Position of three sections in the axial direction (b) displacement of top section (c) displacement of middle section (d) displacement of bottom section.

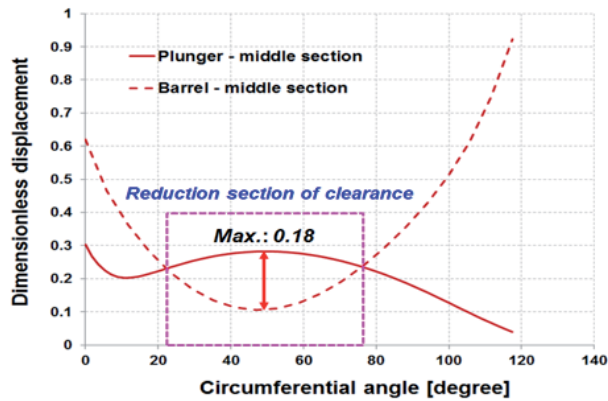


Figure 7.
Dimensionless displacement of barrel and plunger in the middle section [11].

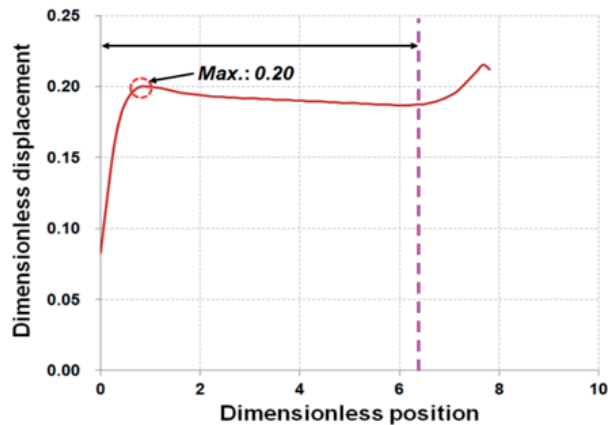


Figure 8.
Dimensionless displacement of plunger in stem part [11].

In hydrodynamic lubrication analysis, an unsteady-state two-dimensional Reynolds equation is used to model the fluid film between the barrel and the plunger, and the Reynolds boundary condition is applied. Moreover, the equilibrium equation of the moment at fixed point and the equilibrium of the forces in the vertical and horizontal directions are used. The lubrication characteristics of the pump with variation of clearance are investigated in two parts, head and stem. When the dimensionless viscosity is 0.57, **Figure 9(a)** shows the dimensionless minimum film thickness with a change in the dimensionless clearance of the head. Furthermore, when the clearance in the stem is constant, the film parameters do not change to be more than a specific clearance in the head. The film parameters obtained according to the results of the minimum film thickness are shown in **Figure 9(b)**. **Figure 10** shows the changes in dimensionless viscosity and dimensionless clearance of the film parameter. Increments in the dimensionless viscosity raise the film parameter. If a film parameter of 3 or higher shows good lubrication properties, the pump's lubrication qualities are satisfactory throughout a wide range of viscosities. While in a low viscosity state, the film parameter is less than 3 when the dimensionless clearance of the stem is 0.25, 0.32 and 0.37. This means that, at low viscosity, metal-to-metal contact between the plunger and the barrel is possible. However, a low viscosity situation results in a parameter of 4.25 for a dimensionless

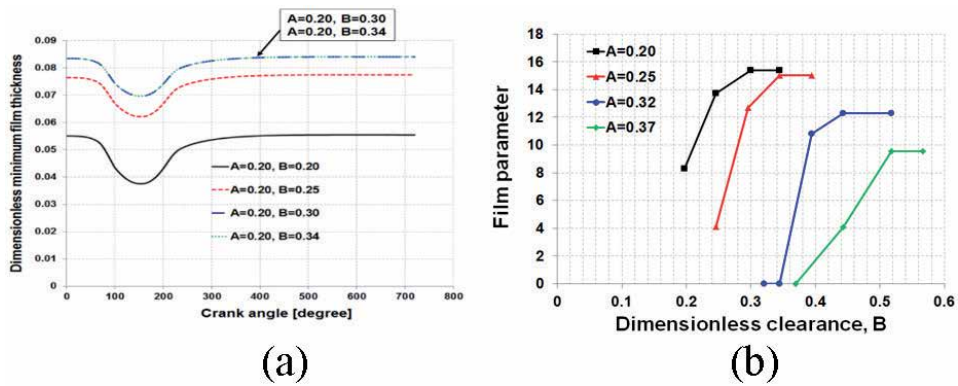


Figure 9. Dimensionless minimum film thickness and film parameter with dimensionless clearance (B) [11] (a) dimensionless minimum film thickness (b) film parameter.

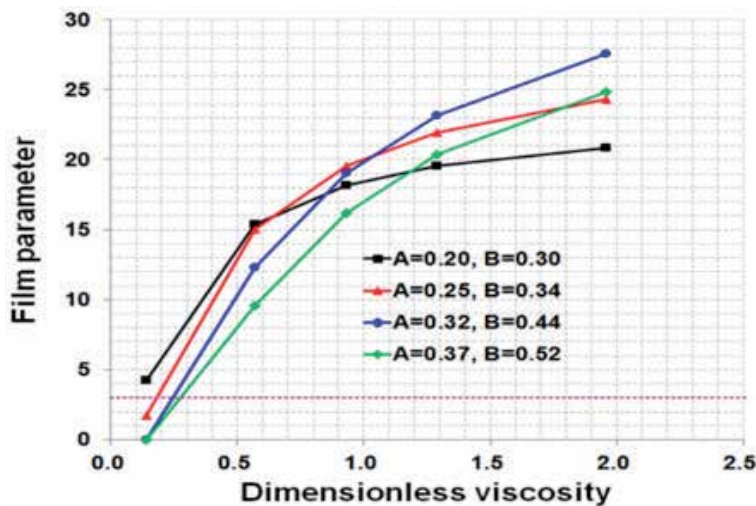


Figure 10. Film parameter with dimension viscosity and clearance (A, B) [11].

clearance of 0.20. Since the stem of the reciprocating fuel pump system has a relatively large lubrication area, the dimensionless clearance of the stem must be small, and the clearance in the stem had a significant impact on the lubrication properties of the system. According to the hydrodynamic lubrication study of marine diesel engines, metal-to-metal contact does not occur when the stem clearance is modest and the head clearance is more than a specific clearance.

The tolerance and machining limit of the clearance are also required to establish the pump clearance. Since the tolerance of the clearance must be caused by the machining process, and the clearance is decided by two surfaces, the clearance in a genuine mechanical system is not a single number but rather a range of values. Furthermore, the manufacturer’s processing capability is also taken into account while determining the clearance. Therefore, in this chapter, this concept is referred to as the “machining limit of the clearance”.

In the scenario where the dimensionless clearance machining limit is 0.17 and the dimensionless tolerance maximum is 0.05, the dimensionless clearance of the pump is determined. To prevent metal-to-metal contact, the ideal dimensionless clearance in the stem and head should be greater than 0.18 and 0.20, respectively.

Assuming that the hydrodynamic lubrication analysis shows that the hydrodynamic lubrication characteristics are good when $A = 0.20$ and $A = 0.30$, the dimensionless clearance of the stem ($A = 0.20$) will be inadequate because the maximum dimensionless reduction in clearance induced by deformation is greater than the dimensionless clearance. Therefore, to prevent metal-to-metal contact despite having good lubrication characteristics of the pump for the hydrodynamic lubrication analysis, the dimensionless clearance must be greater than 0.20 for the stem part. However, since the dimensionless clearance is larger than the maximum dimensionless reduction in the clearance, the dimensionless of the head ($B = 30$) is correct. Therefore, the dimensionless clearance is determined while considering the maximum dimensionless tolerance, as shown in **Table 1**. However, there are a few limitations to this method. The disturbance generated by the cam was not taken into account when calculating the reciprocating motion. Moreover, a variety of fuel oils are used in marine diesel engines, and changing fuel oil causes a stick in the fuel pump. In this approach, the changes in fuel oil were not taken into account. Furthermore, this method is more accurate than the fluid–structure interaction (FSI) method even though structural and hydrodynamic lubrication analyses are used to estimate the proper pump clearance. Although this design method of clearance has some significant drawbacks, it improved the fuel pump durability and made it feasible to create engines with a 20% increase in power [11].

2.2.2 Application of taper shape and grooves

The grooves were used to improve the lubrication performances and heat transfer in various mechanical components. In addition, profiles (taper shape) were applied to cylindrical roller bearings to release the stress concentration at the both ends of the rollers. Previous study has suggested application of partial grooving, circumferential grooving, taper shape, and the design of optimal clearance to improve the lubrication characteristics of the fuel pump in marine diesel engines. The hydrodynamic lubrication analysis of the fuel pump performed by using two-dimensional Reynolds equation and Reynolds boundary condition to compare lubrication characteristics of the pump with variation of taper shape, groove condition, and viscosity.

Figure 11(a) shows a tapered plunger, with tapered applied to the plunger stem. In the axial and radial directions, the dimensionless taper lengths of the upper section of the plunger stem are A_1 and B_1 , respectively. C_1 and D_1 are the dimensionless taper lengths of the lower section of the plunger stem, respectively. A grooved plunger is shown in **Figure 11(b)**. L_1 is the dimensionless distance between the stem's edge and the first groove. Dimensionless groove width and depth are represented by L_2 and H_2 , respectively. L_3 is dimensionless distance between grooves, and N is number of grooves. The depth of groove is considered in film thickness equation in case shallow groove. On the other hand, the pressure in the deep groove calculated using the continuity of flow rate.

Dimensionless maximum reduction of clearance	Head part	0.18
	Stem part	0.20
Dimensionless machining limit of clearance		0.17
Dimensionless clearance of the pump	Head part	$0.30 \leq C \leq 0.34$
	Stem part	$0.21 \leq C \leq 0.25$

Table 1.
Determination of optimal clearance [10].

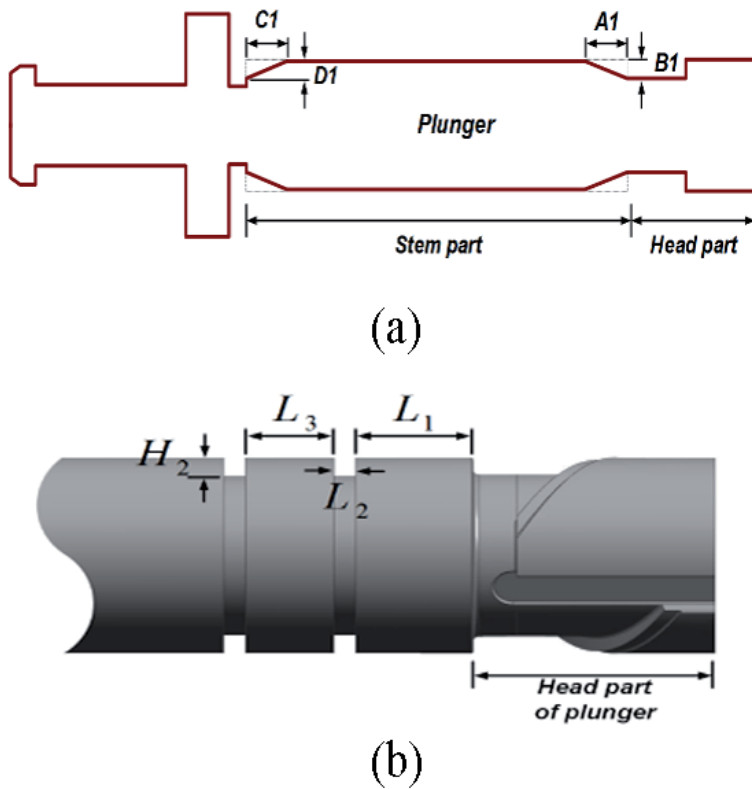


Figure 11. Geometries of plunger with taper and groove [12]. (a) Taper shape (b) circumferential groove.

The taper to the stem part of the plunger applied to improve lubrication characteristics of the pump by using a pressure generation by the wedge effect. The generated pressure helps to restore the plunger to the barrel center during reciprocating motion. **Figure 12(a)** and **(b)** show the effect of tapering the upper part of stem. The dimensionless minimum film thickness in the tapered plunger is greater than that of an untapered plunger. When A_2 increased from 0.312 to 0.938, the dimensionless minimum film thickness increases by roughly 15%. However, the minimum film thickness does not change when the A_1 increases beyond 0.938. Furthermore, the change in dimensionless minimum film thickness differs by less than 50% compared to the variation of B_1 . According to **Figure 12(c)**, tapering the bottom section of the stem does not affect lubricating properties. During reciprocating action, the lower section of the stem pops out of the barrel for a short period due to reduced fluid film pressure in the bottom part of the stem.

The imbalance in pressure can be alleviated by applying a circumferential groove, which allows passage in the circumferential direction. These grooves equalize these pressures and restore the plunger to the center of the barrel by facilitating flow around the periphery of the plunger from the high-pressure zone to the low-pressure zone. **Figure 13** shows the film parameter with dimensionless viscosity and groove type (shallow groove, deep groove). The film parameter in the case of shallow grooving is greater than that of deep grooving. The percentage of increase in the film parameter calculated based on the film parameter of no groove condition. A plunger with a shallow groove improves the lubrication properties more effectively in low-viscosity circumstances, since deep grooves are less efficient in high-viscosity conditions because of increased viscous friction. However, it is difficult to

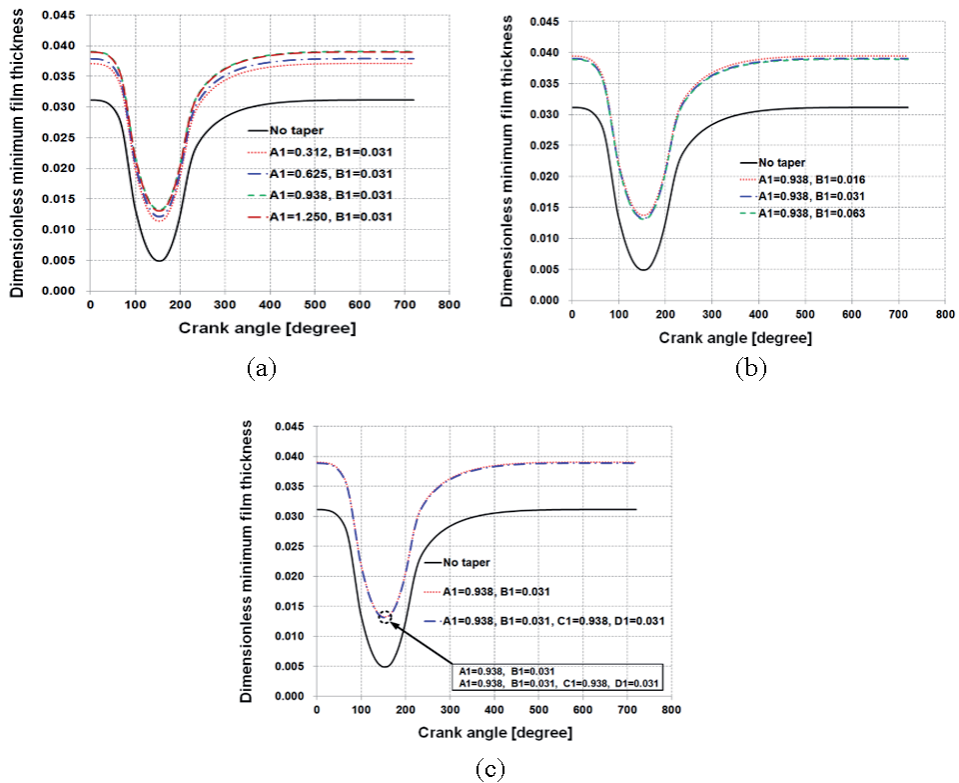


Figure 12. Dimensionless minimum film thickness with taper geometries and crank angle [12] (a) variation of A_1 , (b) variation of B_1 , (c) effect of C_1 and D_1 .

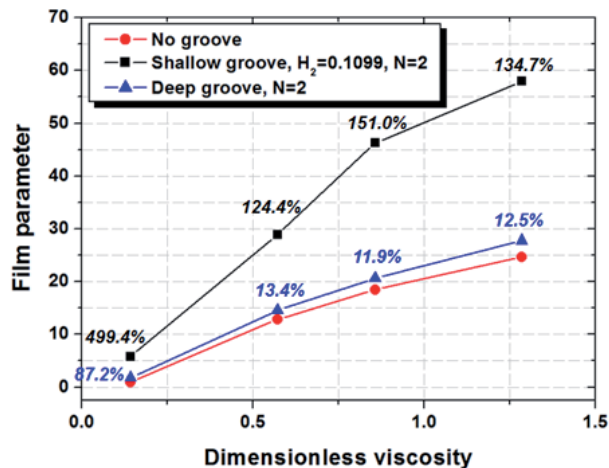


Figure 13. Film parameter with groove types and dimensionless viscosity [12].

apply circumferential grooves with shallow depth because of the economics of the product for processing, and the reduction in ability to trap wear particles.

The effect of application both circumferential groove and taper shaper to the plunger investigated. **Figure 14** shows various types of plunger. **Figure 15(a)** compared the lubrication characteristics of the plunger applied both taper and grooves with those cases where either are applied singly. A pump's film parameter is highest



Figure 14.
 Types of plunger [12].

when both taper and groove are used. In the low viscosity condition, the absence of groove and taper increases film parameters by about 390%. Furthermore, the use of a taper is more successful than the use of grooves in improving lubricating qualities. As shown in **Figure 15(b)**, the film parameter varies when the number of grooves is changed in the case of taper + groove. The difference in film parameters is less than 4% between $N = 2$ and $N = 3$. However, the lubricating properties of a pump with three or more grooves are not improved as the pressure imbalance occurs mainly in the head and upper part of the stem [12].

Besides, research on fuel pump with spiral grooves has performed in order to improve the durability of the fuel pump in marine engines. The application of spiral grooves is quite effective in the design of fuel pumps requiring high pressure for high power of the engines. This is because a spiral groove is one continuous groove and can effectively release uneven pressure distribution surrounding the plunger. In addition, spiral grooves are not machined to the both ends of the stem part because the grooves cause a pressure drop of compressed fuel [14].

2.3 Lacquering

Environmental restrictions affect the composition of marine fuel oil and the design of marine diesel engines. To significantly limit the sulfur content of fuel oil and emission, there is a requirement to strengthen environmental laws. Low-sulfur fuel oil is used in most marine engines to meet international environmental requirements. However, the use of such fuel oils can cause unexpected concerns. These concerns include higher lubricant consumption due to lacquer build-up on the cylinder lining, as seen in **Figure 16**.

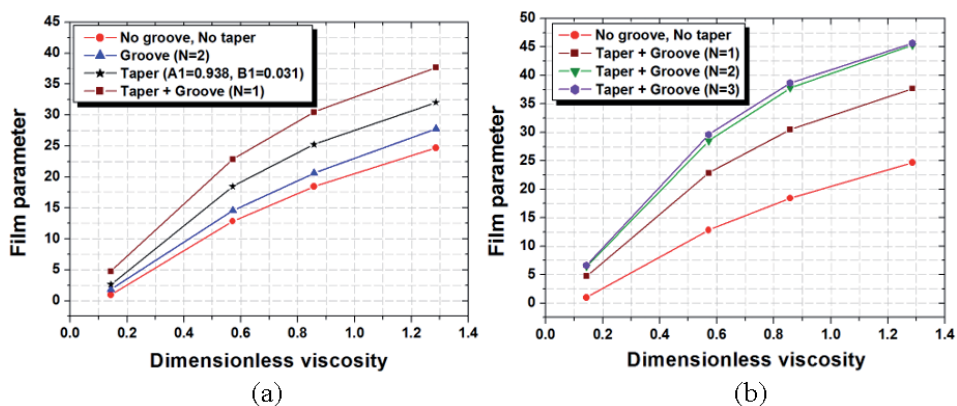


Figure 15.
 Film parameter with dimensionless viscosity (a) variation of type (b) variation of N [12].

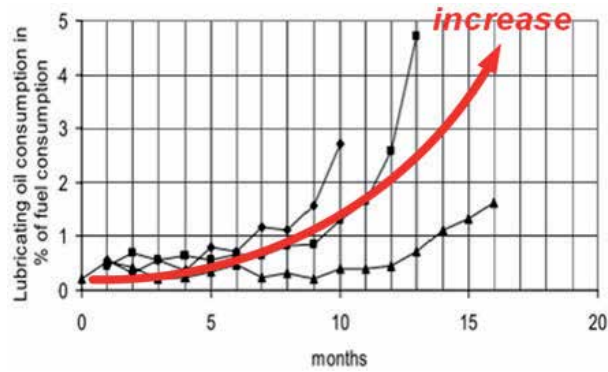


Figure 16.
Oil consumption increase in engines [15].

Lacquer forming (lacquering) in the cylinder liners of marine diesel engines has been a matter of concern for at least 20 years. Lacquer development increases lubricating oil consumption, sticks the injection pump, and causes scuffing in the cylinder liner. Cylinder liners are the most essential engine components when it comes to oil consumption and friction losses. According to studies, friction between the cylinder liner and the piston ring is responsible for up to 40% of engine friction losses. The surface of the cylinder liner consists of a mixture of deep enough valleys and smooth plateaus, which is called honing, in order for the liner to hold a satisfactory amount of lubricant oil and to reduce friction. **Figure 17** shows that cylinder liner lacquer results in deposits in the grooves. Such deposits reduce clearance to the point of contact between plunger and barrel. Sticking can occur due to reduced clearance, the lubrication characteristics of the pump are deteriorated [15, 17].

Previous studies have speculated on lacquer producing methods. Shell [18] and Alberola [19] have presented two proposals.

According to Alberola, lubricant oils are liquid polymers with low molecular weight; therefore, deposit formation due to thermal and oxidative degradation of these oils can be considered a thermosetting process. In this process, a polymeric liquid undergoes two macroscopic phase transformations, gelation and vitrification, which turn the liquid into a solid. Gelation is the production of branched molecules with a potentially infinite molecular structure that occur at a critical point in a chemical reaction. First, a paste-like gel-like coating is initially formed from the lubricating oils. Then, a vitrified or glassy solid is formed from thermosetting

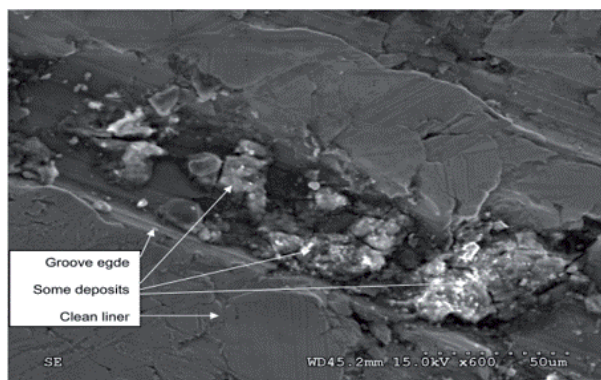


Figure 17.
Deposits in the groove of cylinder liner [15, 16].

polymers in the thermosets. During this phase, the polymeric network becomes tighter due to the chemical cross-linking processes that continue to take place. Because the thermoset structure has transformed to a vitrified glassy state, molecular segment motions are no longer feasible. Finally, the pasty properties are lost in the glassy deposit, which is commonly referred to as a lacquer or varnish [18].

According to Shell, condensation of partially combusted and cracked fuel components on the surface forms lacquer (**Figure 3**). To form the layer, these components oxidize and polymerize before mixing with the calcium and zinc salts of lubricant oil. These metal components act as catalysts in the oxidation of the surface. The layer turns into a hard glaze under high temperatures. This process results in the formation of hard and glassy layers on the surface [19].

However, the two proposals have yet to be confirmed by detained chemical analysis of the lacquer [15, 17].

There are a variety of reasons for the formation of lacquer. Lacquer can be formed due to the use of only fuel oil, or a mixture of fuel oil and lubricant oil. The boiling point and aromatic content of fuel oils also affect the formation of lacquer. Compared to fuel oils that do not form lacquer, lacquer-forming fuel oils have higher aromatics and paraffinic contents [20, 21]. A higher than normal final boiling point may indicate higher than normal content of polycyclic aromatic hydrocarbons (PAHs) in the fuel oils. Past work has also suggested that distillate fuels containing heavier ends are more prone to form lacquer [22]. The base number (BN) level of lubricant oils and sulfur content of fuel oils are directly related to lacquer formation [21]. The marine diesel engines are normally designed to burn residual fuel oils containing high-level sulfurs, and need lubricant oils with an appropriate level of BN to neutralize the corrosive combustion acids. However, higher BN and sulphated ash indicated a higher deposit risk. In addition, engine tests that the lacquer increases when either the liner temperatures or inlet air temperature are too low. This is because the low temperatures favor conditions for condensation of partially combusted and/or heavier fuel ends on the surface. Operation with a lot of idle, part-load, or combined full load (or over load) operation seems to be the most lacquer-prone.

There are many variations in the appearance of the lacquer under different conditions. Normally, amber and brown, lacquer appears darker when viewed from an angle, probably because more light is reflected from the surface where most of the deposit is located. Moreover, the term “glazing” is used to describe the appearance of lacquer. The lacquer has a strong bonding force with the surface, so it is not easily physically removed. The degree of bonding force has been evaluated through pull-off test. The allowable criteria of marine paints specified in ISO 4624 is about 3 ~ 4 MPa. The pull-off pressure of lacquer were over 9 MPa, and the values are two or more times larger than the allowable criteria of marine paints.

Anthraquinone and other quinones are also insoluble in most solvents, but they are soluble in acids, such as sulfuric acid and acetic acid as shown in **Figure 18**. The presence of quinones in the lacquer would explain why the lacquer dissolves readily in a weak organic acid. Through this phenomenon, acids are effective in removing the lacquer.

The lacquer can form due to a variety of causes, so there are various measures that can be taken to prevent or minimize the problem. The maintenances of fuel injectors, turbocharger and cooling around the liners are effective factors in preventing incomplete combustion, and also influence the prevention of lacquer formation. To prevent lacquer formation in the fuel pump, systematic control of the lubricant oil flow and periodic inspection of the pump were suggested, in order to ensure replacement of the sealing ring, and oil sediment removal. Other counter-measures are use of alternative lubricants, and of multifunctional fuel additives.



Figure 18.
Liner lacquer after partial cleaning with acetic acid [17].

Several companies have proposed an “advised range” for the BN depending on the sulfur content of fuel oil to prevent lacquer formation [17].

2.4 Bearings

The development of marine diesel engine was high-power, compact structure, and hence the bearings were required to work normally under smaller size, high load, and thinner oil film conditions. **Figure 19** shows big end bearings of connecting rod. In recent years, coupling simulations between elasto-hydrodynamic lubrication (EHL) and nonlinear multi-body dynamics (MBD) are carried out to dynamically-loaded bearings of marine diesel engines, and the coupling analysis is an effective method to investigate the lubrication characteristics of marine bearings [23].

In a marine engine, the connecting rod bearing is a key friction component. It converts the reciprocating action to rotary motion by connecting the crankshaft and pistons, as well as the cross-head slide. The bearing of the connecting rod significantly affects engine performance by improving its reliability, durability, and strength. To analyze the EHL for the large end connecting rod bearing of a low-speed two-stroke marine diesel engine, AVL Excite Power Unit software was used.



Figure 19.
Big end bearing of medium-speed diesel engine.

This software considers nonlinear multibody dynamics. Bearing lubrication can be calculated more accurately if the following factors are taken into account: friction surface roughness, elastic deformation of the bearing and journal, oil supplying qualities, and the influence of the cavity on the oil film lubricant [24].

The wear caused by insufficient lubrication is the most general cause of endurance life issues. An absence of lubrication in the journal-bearing system leads to bearing seizure, and normally, to total destruction of the part. Insufficient lubrication caused by factors such as a machining error in the manufacture of the crank pin and the bearing leads to metal-to-metal contact between the crank pin and the bearing, which results in adhesional wear. The crank pin bearing which connects the connecting rod and crank arm, converting a reciprocating motion into a rotary motion plays an important role in a marine diesel engine. Through the motion analysis of the piston-connecting rod-crank arm system, the bearing loads and lubricant velocity were calculated. The numerical algorithm for the hydrodynamic lubrication analysis coupled with the motion analysis of the piston-connecting rod-crank arm system developed to investigate lubrication characteristics. The maximum film pressure decreased with decreasing clearance and lubricant temperature, and that film thickness increased with decreasing clearance and lubricant temperature. The lubricant temperature had a higher effect on the film thickness than the clearance [25].

Fretting is phenomenon that concerns mechanical components in contact that are designed to be fixed but undergo small relative displacement due to fluctuation loads. The fretting is one of main issues of connecting rod bearing in marine diesel engines. **Figure 20** shows fretting fatigue fracture between bearing bush and small end. The fretting damage begins with local adhesion between mating surfaces and processed when adhered particles are removed from the surface, they may react with air or other corrosive environments. Surface crack can be initiated by fretting, and led to catastrophic failure after crack propagation. The fretting influenced by contact pressure, friction coefficient and relative slip motion. **Figure 21** shows numerical results about contact pressure, tangential stress and slip amplitude at certain crank angle. The fretting severity on mating surface is evaluated as fretting damage parameter (FDP). The FDP is defines in Eq. (3). The τ is the frictional shear stress at the interface and δ is the absolute slip amplitude in the tangential stress direction in Eq. (3). The potential for fretting initiated fatigue fracture on the mating surface is also evaluated using the Ruiz criterion and defined as fretting fatigue damage parameter (FFDP) in Eq. (4). The σ is the tensile tangential stress on the contact surface in Eq. (4). The greater slip amplitude and tangential stress can increase the possibility of fretting fatigue damage. Moreover, the contact pressure at the mating surface is not an effective parameter to predict the fretting damage because the areas where contact pressure is high, the FDP and FFDP are close to zero.

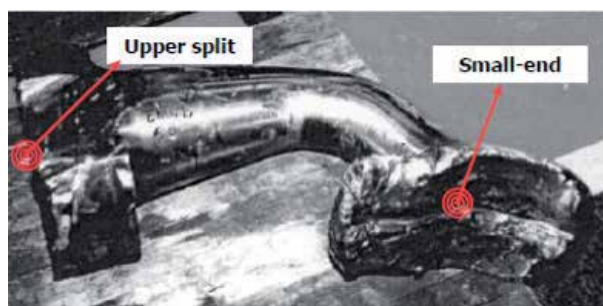


Figure 20.
Fretting fatigue failure of connecting rod [26].

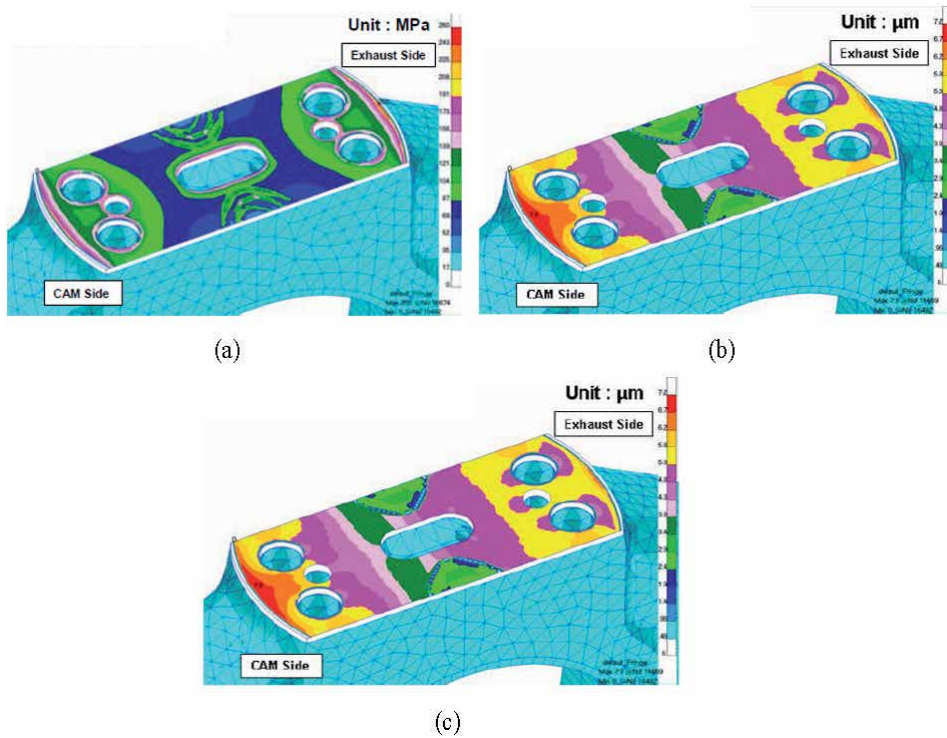


Figure 21. Numerical results with AVL software [26]. (a) Contact pressure distribution at crank angle 490° (b) tangential stress distribution at crank angle 110° (c) slip amplitude distribution at crank angle 310° .

Therefore, the possibility of fretting damage at the upper split in connecting rod bearing was investigated using the Excite software from AVL and Ruiz criterion [26]. The Ruiz criteria is an effective empirical approach for evaluation of fretting fatigue damage parameter and has been demonstrated in two dimensional fretting studies of a typical dovetail interface problem. Moreover, this criterion is suitable for predicting the fretting damage of the connection rod bearing in marine diesel engines.

$$FDP = \tau \cdot \delta \quad (3)$$

$$FFDP = \sigma \cdot \tau \cdot \delta \quad (4)$$

Aside from crank pin bearings and connecting rod bearings, various bearings are used in marine diesel engines. Since the size of most bearings are large, it is difficult to carry out experimental studies due to cost and volume, so most researches on bearings are focusing on analytical studies. However, in order to improve practically lubrication characteristics of bearings in marine diesel engines, more experimental studies should be conducted simultaneously.

2.5 Condition monitoring with oil analysis

Maintenance strategies play a crucial role in reducing the cost of down time and improving system reliability. Consequently, machine condition monitoring plays an important role in maintaining operation stability and extending the period of usage for various machines. Machine condition monitoring through oil analysis is an effective method for assessing machine's condition and providing early warnings regarding a machine's breakdown or failure as shown in **Figure 22**.

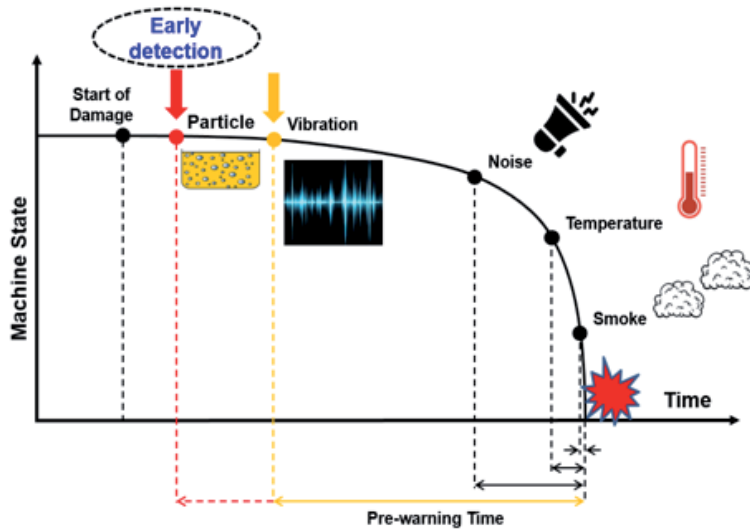


Figure 22.
Advantage of machine condition monitoring with oil analysis.

The three main methods of oil analysis are off-line, in-line, and on-line techniques as shown in **Figure 23**. The method of analyzing lubricants through oil sampling is an off-line and has been mainly utilized in the past. The in-line is the method to analyze directly where the main flow of lubricant oil occurs, and the on-line is the method to analyze the lubricant oil in the by-pass. The in-line can interfere with the flow of lubricant during the measurement process and can be difficult to measure under conditions such as high temperature and high pressure. On-line analysis is the most effective method of the three methods used for analyzing lubricant oils. This is because it can monitor the machine condition effectively using oil sensors in real time without requiring excellent analysis skills and eliminates human errors. Determining the oil quality usually requires complex laboratory equipment for measuring factors such as density, viscosity, base number (BN), acid number (AN), water content, additive and wear debris. Real-time monitoring with oil analysis is also utilized in various industries, such as manufacturing, aerospace, power plants, construction equipment, wind-turbine and marine diesel engines.

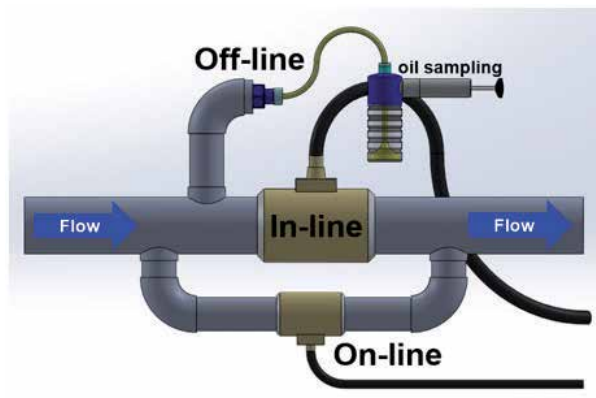


Figure 23.
Methods of oil analysis.

It is well known that faults and failures in marine diesel engines are always caused by wear in the tribo-systems. Vibration source complexity, multiphasic interference, and lower frequencies are the factors that make wear monitoring challenging. This has led to the use of oil analysis as a primary means of monitoring the status of marine diesel engines [27]. Even if the oil analysis has been applied in condition monitoring for marine diesel engines until now, there are some dissatisfactory circumstances in the oil analysis for them. This is because oil analysis takes in off-line mode, and it is not real-time. However, the on-line monitoring system with lubricant sensors is efficient to diagnose condition of marine diesel engines. Among oil properties, wear particle, viscosity, capacitance, base number, dielectric constant, water contents (relative humidity) are commonly measured [27]. The viscosity of the lubricant is its resistance to flow, and the condition of marine engines are normally diagnosed by monitoring the increment or decrement of it. However, if other lubricants with different viscosity or a large amount of fuel are not mixed, a sudden change in the viscosity of the lubricant does not occur easily in a short time.

The moisture is easily observed in lubricant oil contamination and it causes to increase the acid number, multiply microorganism and deteriorate the lubricant quality. The contamination of moisture is caused by water leakage during the operation of mechanical system. Water is a typical polar substance, and the presence of water in the lubricant oil increases the permittivity. The permittivity is a measure of the electric polarizability of a dielectric. The relative permittivity is called the dielectric constant. The dielectric constant of water is almost 80, whereas lubricant oil is about 2. A small increase in water contents of the lubricant oil caused as a sharp increase in permittivity. Therefore, it is possible to measure the amount of moisture in the lubricant oil by the dielectric constant. The Karl Fischer is a representative method for measuring moisture, but it requires a complex experimental device and skilled skill for the analyzer. Therefore, the measurement of water contents with moisture sensor or dielectric constant sensor is effective in the lubricant oil analysis [28, 29]. The oil analysis method with dielectric constant sensor is applied in marine diesel engines [27].

The base number (BN) is a property that is more associated with engine oils than industrial oils. It can be defined as the lubricant's ability to neutralize acids that are produced during use. The lubricant with proper BN should be used according to sulfur contents of marine fuels to prevent deposit and corrosion in shown in **Figure 24**.

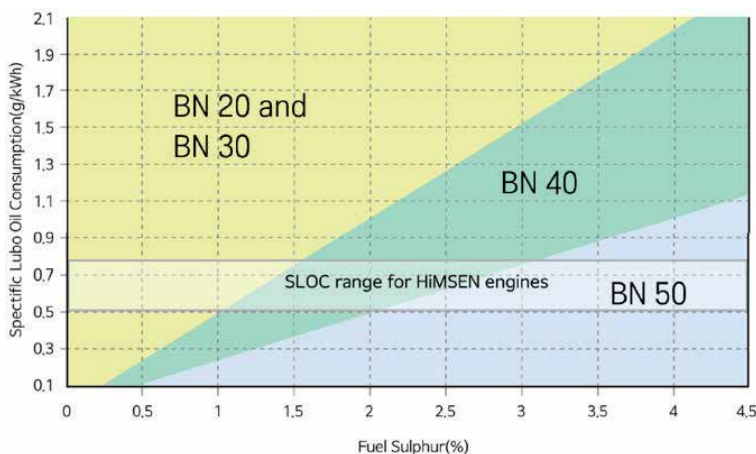


Figure 24. BN guideline according to fuel sulphur in marine diesel engines.



Figure 25.
CaCO₃ deposits on the piston top.

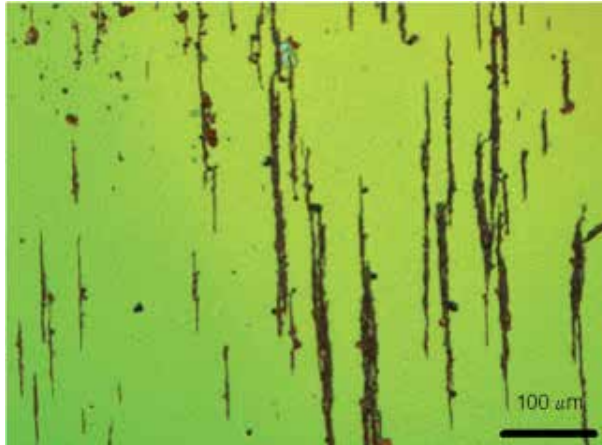


Figure 26.
Ferrogram photomicrograph of marine engine oil [30].

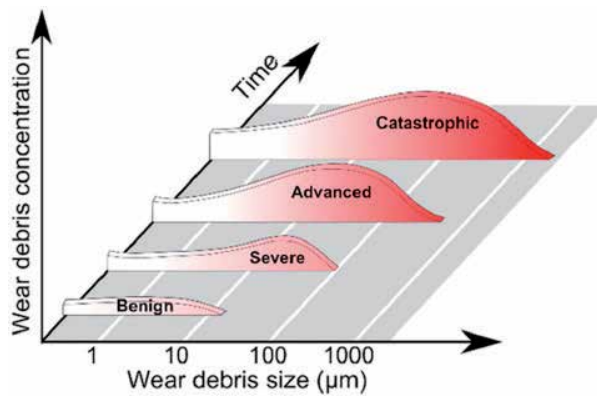


Figure 27.
Relationships of wear debris size, concentration, and machine conditions [31].

When a fuel with a high sulfur content is used and a lubricant oil with a low BN is used, there is a risk of corrosion. Conversely, when a fuel with a low sulfur content is used and a lubricant oil with a high BN is applied, deposit problem occur as shown in **Figure 25**. This is because the lubricant oil with a high BN partially neutralized sulfuric acid, and the remaining additive such as detergent react chemically, resulting in deposits. The tracking the BN of engine oil can determine how much life is remaining. The most reasons for a drop in the BN are related to low quality fuel such as residual fuels and oil oxidation. Therefore, the BN of lubricant in the marine diesel engines must be measured in order to monitor the condition of them.

Condition monitoring of machinery through analysis of wear debris is now an extensively applied as a tool in diagnostic technology. Wear debris analysis or analytical ferrography is a method of predicting the health of equipment in a non-intrusive manner by studying wear particles in lubricant oils. **Figure 26** show the ferrogram photomicrographs of marine engine oil. The shape and length of ferrous wear particles in engine oil evaluated by ferrography as shown in **Figure 26**. The correlation between wear debris, time and wear particles concentration is shown in **Figure 27**. During initial or normal operation of new engines, the wear size is normally between 1 μm and 10 μm . However, in abnormal condition, larger wear particles between 20 μm and 100 μm are detected. Thus, wear particles larger than 20 μm should be monitored in order to provide an early warning of the machine condition [28, 29]. The analysis of wear debris is important to detect critical stages of accelerated wear that precedes costly and dangerous components failures. Therefore, application of wear particle analysis and ferrography by oil sensors is essential means to keep good maintenance in marine diesel engines [32].

3. Conclusions

This chapter explained the tribology of marine diesel engines, which are the heart of a marine system. Modern marine diesel engines must satisfy stringent reliability requirement. Various researches on tribological issues in the marine diesel engines were performed, the lubrication characteristics of machine components such as bearings, cylinder liners, fuel injection pump were improved. Besides, the phenomenon of lacquer is explained in terms of generating mechanism, causes, physical and chemical properties, and prevention or removal methods. Furthermore, condition monitoring with oil analysis is introduced to keep maintenance and to reduce the downtime cost of the marine diesel engines. A variety of tribological researches are needed in the future in order to improve the reliability of the marine diesel engines.

Acknowledgements

This work supported by Korea Institute of Energy Technology Evaluation and Planning (KETEP) grant funded by the Korea government (MOTIE) (No. 20214000000010).

Appendices and nomenclature

A	Dimensionless clearance of stem part
A1	Dimensionless taper length of upper part in the axial direction
B	Dimensionless clearance of head part
B1	Dimensionless taper length of upper part in the radial diction


C	Dimensionless clearance
C1	Dimensionless taper length of lower part in the axial direction
D1	Dimensionless taper length of lower part in the radial direction
H ₂	Dimensionless groove depth
h _m	Minimum film thickness
L ₁	Dimensionless distance from edge of stem part to the first groove
L ₂	Dimensionless width of groove
L ₃	Dimensionless distance between grooves
N	Number of circumferential grooves
R _p	Maximum peak height roughness
R _q	Root mean square roughness
R _{q1}	Root mean square roughness of plunger
R _{q2}	Root mean square roughness of barrel
R _v	Maximum valley depth roughness
δ	Absolute slip amplitude in the tangential stress direction
λ	Film parameter
σ	Tensile tangential stress on the contact surface
τ	Frictional shear stress at the interface

Author details

Sung-Ho Hong
Dongguk University-Gyeongju, Gyeongju, South Korea

*Address all correspondence to: hongsh@dongguk.ac.kr

IntechOpen

© 2021 The Author(s). Licensee IntechOpen. This chapter is distributed under the terms of the Creative Commons Attribution License (<http://creativecommons.org/licenses/by/3.0>), which permits unrestricted use, distribution, and reproduction in any medium, provided the original work is properly cited. 

References

- [1] Sciencing. Types of marine diesel engines [Internet]. 2021. Available form: <https://sciencing.com/types-marine-diesel-engines-7241726.html> [Accessed: 2021-07-05]
- [2] Sautermeister FA, Priest M, Lee PM, Fox MF. Mint: Impact of sulphuric acid on cylinder lubrication for large 2-stroke marine diesel engines: Contact angle, interfacial tension and chemical interaction. *Tribology International*. 2013;59:47-56. DOI: 10.1016/j.triboint.2012.06.002
- [3] Mehdi G, Zhou S, Zhu Y, Shah AH, Chand K. Mint: Numerical investigation of SCR mixer design optimization for improved performance. *Processes*. 2019;7:168. DOI: 10.3390/pr7030168
- [4] EPA. In-used Marine Diesel Fuel [Internet]. 2021. Available form: http://widit.knu.ac.kr/epa/ebtpages/Air/Mobile_Sources/Marine_Engines/siteout/s2out34.pdf [Accessed: 2021-07-05]
- [5] TPR. Products and Technology [Internet]. 2021. Available form: https://www.tpr.co.jp/tp_e/products/cylinderliners/about.html [Accessed: 2021-07-05]
- [6] Bocchetti D, Giorgio M, Guida M, Pulcini G. Mint: A competing risk model for reliability of cylinder liners in marine diesel engines. *Reliability Engineering and System Safety*. 2009;94:1299-1307. DOI: 10.1016/j.res.2009.10.010
- [7] Guo ZW, Yuan CQ, Bai XQ, Yan XP. Mint: Experimental study on wear performance and oil film characteristics of surface textured cylinder liner in marine diesel engine. *Chinese Journal of Mechanical Engineering*. 2018;31:52. DOI: 10.1186/s10033-018-0252-3
- [8] Jayakumar N, Mohanamurugan S, Rajavel R. Mint: Study of wear in chrome plated cylinder liner in two stroke marine diesel engine lubricated by Hans Jensen swirl injection principle. *Materialstoday*. 2017;4:1535-1541
- [9] Cabanettes F, Dimkovski Z, Rosen BG. Mint: Roughness variations in cylinder liners induced by honing tool's wear. *Precision Engineering*. 2015;41:40-46. DOI: 10.1016/j.precisioneng.2015.01.004
- [10] Pawlus P, Reizer R, Wieczorowski M. Mint: Analysis of surface texture of plateau-honed cylinder liner – A review. *Precision Engineering*. 2021;72:807-822. DOI: 10.1016/j.precisioneng.2021.08.001
- [11] Hong SH. Mint: A new clearance design method for reciprocating fuel pump of medium-speed diesel engines. *Tribology Transactions*. 2018;61:773-783. DOI: 10.1080/10402004.2017.1414909
- [12] Hong SH, Lee BR, Cho YJ. Mint: Improvement of lubrication characteristics in the reciprocating fuel pump of marine diesel engines. *Journal of Mechanical Science and Technology*. 2016;30:5225-5232. DOI: 10.1007/s12206-016-1057-x
- [13] Hong SH. Mint: CFD analysis of trap effect of groove in lubricating systems: Part I –variation in cross-sectional shape of groove. *Tribology and Lubricants*. 2016;3:101-105. DOI: 10.9725/kstle.2016.32.3.101
- [14] Hong SH. Mint: Application of spiral grooves in fuel pump for medium-speed diesel engines. *Tribology Transactions*. 2018;61:532-538. DOI:10.1080/10402004.2017.1365989
- [15] Hong SH. Mint: A literature review of lacquer formation in medium-speed and low-speed engines. *Journal of Mechanical Science and Technology*.

2016:30:5651-5657. DOI: 10.1007/s12206-016-1134-1

[16] Buhaug O. Investigation of cylinder liner lacquers in the North Sea and Norwegian Sea regions. In: Proceedings of CIMAC congress; 21-24 May 2007; Vienna: 2007. p. 1-10

[17] Hong SH, Ju SW. Mint: Effective test of lacquer in marine diesel engines. International Journal of Naval Architecture and Ocean Engineering. 2017;9:199-208. DOI: 10.1016/j.ijnaoe.2016.10.002

[18] Barnes J, Berentsen P. Cylinder liner lacquering in distillate-fueled medium speed engines and development of an advanced anti-lacquer lubricant. In: Proceedings of CIMAC congress; 7-14 June 2004; Kyoto: 2004. p. 1-12

[19] Alberola N, Vassel A, Bourgognon H, Rodes C. Mint: The microcoking ELF/ECL test a new lubricant thermos-oxidation test based on original design. Lubrication Engineering. 1990;47:480-484

[20] Zhu L. Design optimization in the solution of piston ring sticking and carbon deposit. In: Proceedings of CIMAC congress; 13-17 May 2013; Shanghai: 2013. p. 1-5

[21] Chandel RS, Bala SR. Effect of welding parameters and groove angle on the solution of root beads deposited by the SAW process. In: Proceeding of Trends in Welding Research; 18-22 May 1986; Tennessee: 1986. p. 379-385

[22] Allen RW. Mint: The influence of marine fuel quality on lubrication oil performance. CIMAC Lubricants Working Group. 1993:D53

[23] Xing H, Wu Q, Wu Z, Duan S. Mint: Elastohydrodynamic lubrication analysis of marine stern tube bearing based on multi-body dynamics: Energy

Procedia. 2012;16:1046-1051. DOI: 10.1016/j.egypro.2012.01.167

[24] Wu Q, Duan S, Wu Z, Xing H. Mint: Lubrication study on a connecting rod big end bearing of two-stroke marine diesel engine: In: Proceedings of 2010 International Conference on Computer Application and System Modeling (ICCASM 2010); 22-24 October 2010; Shanxi: 2010. P. 184-188

[25] Moon SM, Cho YJ, Kim TW. Mint: Evaluation of lubrication performance of crank pin bearing in a marine diesel engine. Friction. 2018;6:464-471. DOI: 10.1007/s40544-017-0196-0

[26] Son JH, Ahn SC, Bae JG, Ha MY. Mint: Fretting damage prediction of connecting rod of marine diesel engine. Journal of Mechanical Science and Technology. 2011;25:441-447. DOI: 10.1007/s12206-010-1206-6

[27] Liu Y, Liu Z, Xie Y, Yao Z. Mint: Research on on-line wear condition monitoring system for marine diesel engine. Tribology International. 2000;33:829-835

[28] Liu H, Tang X, Lu H, Xie W, Hu Y, Xue Q. Mint: An interdigitated impedance microsensor for detection of moisture content in engine oil. Nanotechnology and Precision Engineering. 2020;3:75-80. DOI: 10.1016/j.npe.2020.04.001

[29] Meshkatoddini MR, Abbospour S. Mint: Aging study and lifetime estimation of transformer mineral oil. American Journal of Engineering and Applied Science. 2008;1:384-388. DOI: 10.3844/ajeassp.2008.384.388

[30] Zhu X, Zhong C, Zhe J. Mint: Lubricant oil condition sensors for online machine health monitoring – A review. Tribology International. 2017;109:473-484. DOI: 10.1016/j.triboint.2017.01.015

[31] Flanagan IM, Jordan JR, Whittington HW. Wear-debris detection and analysis techniques for lubricant-based condition monitoring. *J Phys E Sci Instrum.* 1988;21:1011-1016.

[32] Isa MC, Yusoff NHN, Nain H, Yati MSD, Muhammad MM, Nor IM. Mint: Ferrographic analysis of wear particles of various machinery systems of a commercial marine ship. *Procedia Engineering.* 2013;68:345-351. DOI: 10.1016/j.proeng.2013.12.190

The Role of Friction on Metal Forming Processes

*Luis Fernando Folle, Bruno Caetano dos Santos Silva,
Gilmar Ferreira Batalha and Rodrigo Santiago Coelho*

Abstract

The friction that occurs in forming processes plays a fundamental role in the industry as it can be responsible for both manufacturing failure and its success. Scientific research has been done to try to understand this phenomenon as well as simulation software has been implemented aiming to predict the tribological behavior of the metallic pair in contact. Thus, this chapter is dedicated to the analysis of the main parameters that can influence the coefficient of friction, especially for metal manufacturing processes. Some simulation models that try to predict the behavior of friction under certain conditions of process speed, contact pressure and operating temperature will also be presented.

Keywords: metal forming process, friction coefficient, shear friction factor, Tribological Modeling and simulation, friction test, Tribological parameters

1. Introduction

The plastic deformation manufacturing area can be divided into two large sets, massive forming (which includes the processes of rolling, forging, extrusion, and wire drawing) and sheet forming (which includes bending, cup drawing, shearing and miscellaneous processes). This can be seen schematically in **Figure 1**. The main difference between these two sets lies in the dimensions of the final part after it is processed. In terms of dimensions in the Cartesian plane, a sheet has two dimensions much larger than the third and in massive forming there is no definable difference between the dimensions in the Cartesian plane. For each of these large groups, friction has a characteristic behavior due to both applied force levels and strain levels. Generally, when talking about sheet processes, considering the same material, both the strains and the applied forces are smaller because there is not much material in the thickness to generate a great resistance against the load application.

For all these processes illustrated above, friction will occur, since there will always be contact between two or more surfaces and eventually a lubricant between them. Friction occurs when there is contact between a (forming) tool and the material being deformed.

In general, friction is associated with a negative aspect of forming processes (energy consumption, tool wear, increased forming force, increased tool temperature, etc.). However, this is not always the case. In some processes such as rolling, friction is fundamental for the material to be “holding” by the cylinders. Even in sheet forming, friction plays a fundamental role in preventing defects such as wrinkling.

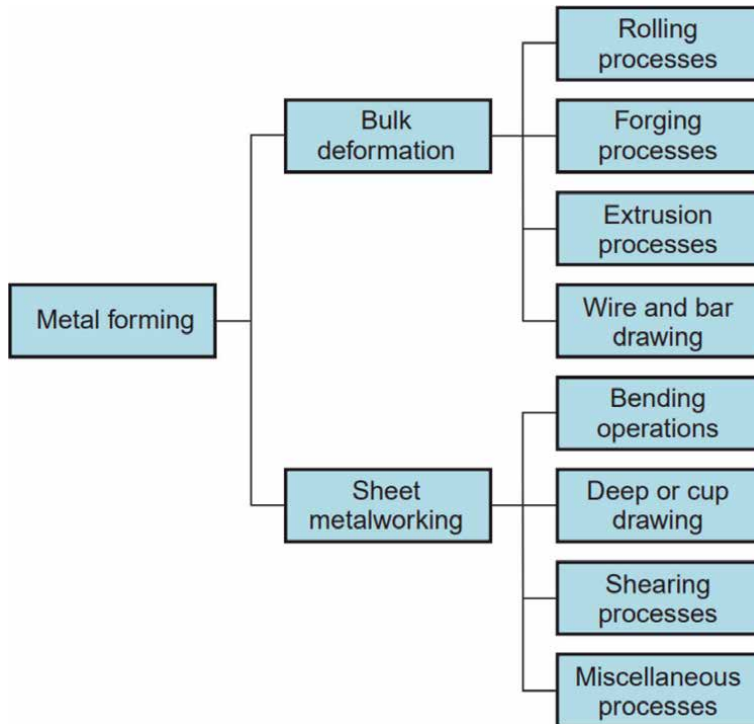


Figure 1.
 Classification of metal forming operations. Source: Groover [1].

So that excessive friction is not the agent causing defects, a lubricating film is used between the contact surfaces. In industrial processes, it is normal to use excess lubricating oils to avoid problems such as die wear. However, with the demand for cleaner manufacturing processes so as not to harm the environment, the use of lubricating oils must be reduced or replaced with another one with non-harmful components or even eliminated. In this way, there are studies which focuses on the lubricant free forming using tools with structured or textured surfaces (**Figure 2**), as can be understood in more detail in the studies carried out by [2–4].

In the case of cold forming, liquid lubricants are generally used. In the past, the use of animal fats and natural oils was common, nowadays the use is concentrated in mineral oils. The exact physical principle that governs the behavior of these lubricants is not yet fully known, but their application always brings improvements to the process, such as:

- Decrease in the total forces needed for the forming operation; friction force is less on lubricated surfaces than on dry ones;
- Better flow of workpiece material within the dies that improves the distribution of strains and facilitates the fabrication of more complex parts;
- Prevention of die wear caused by adhesion or abrasion of surfaces;
- Quality assurance of products where surfaces are better preserved, free from “scratches”.

Consequently, the control of friction levels plays an important role in the distribution of stresses and strains. A very low friction coefficient can generate fixing

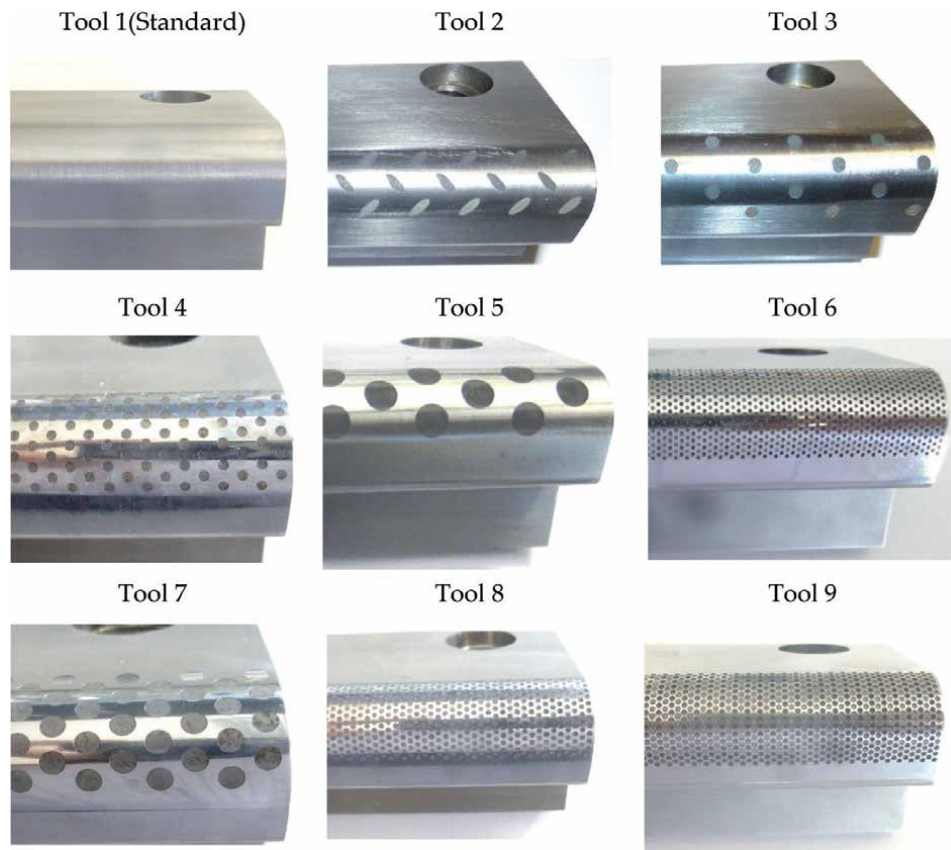


Figure 2.
Conceptual model of different structured test tool surfaces [2].

problems, promoting the appearance of geometric defects such as shape distortions. In sheet forming, for example, the friction force between the sheet press and the die must be high enough to obtain the desired plastic deformations, avoiding the wrinkling of the sheet. On the other hand, a very high friction force will promote wear of the surfaces in contact, which can lead to the appearance of cracks in the final product. Therefore, it is very important to control the friction levels in forming operations.

In the forming processes, it is well known that the success to obtain a part depends on three main factors: the geometry of the tools, the material properties of the piece and the interaction between the contact surface of these two materials. It is also known that the costs associated with the third factor represent around 5% of the final production value of the part. As such, any friction-related improvement in sheet forming can generate immediate payback for manufacturers. Decreasing the friction on the forming process can contribute to a lesser wear on the tools, thus increasing their useful lives, as well as representing a reduction in the required presses forces and, consequently, an increase in the energy efficiency of the forming process.

With the emergence of stricter environmental laws and the tendency to manufacture parts with zero waste, it will be necessary to create more efficient manufacturing methods that operate with highly reduced wastes. In this aspect, numerical simulation can contribute considerably, offering fast solutions that are very close to reality, that is, they can predict failures in the manufacture of parts without these being physically created. Within this context, a critical area is the measurement of

friction in forming, where the methods created so far sometimes fail to adapt to what happens in practice.

2. Types of lubrication conditions

In 1902, Stribeck was the first to report the dependence of the coefficient of friction on the shaft speed in bearings. In his work he presented a curve with three different lubrication regimes. This curve was named “Stribeck Curve”. Subsequently, the coefficient of friction was presented as a function of the combination of the following parameters: lubricant viscosity, number of bearing shaft revolutions and normal shaft pressure. **Figure 3** schematically illustrates the Stribeck curve where the initiation of various types of lubrication mechanisms as a function of lubricant viscosity, η , slide velocity, v , and normal pressure, p .

Friction effects are always related to energy dissipation, so they are sometimes considered undesirable in manufacturing processes. In the case of metal forming, metal flow is limited by the contact pressure between die and part. Thus, friction can generate internal and surface defects, in addition to influencing the tensions in the tools, load and energy required. The purpose of the lubricant is to separate the tool and workpiece surfaces, thus shifting the friction conditions from the boundary friction area in the direction of hydrodynamic friction as shown in **Figure 3**.

There are four distinct lubrication conditions that determine the influence of friction on metal forming:

- Dry Friction, where there is no lubricant present, and the friction coefficient is governed by the contact between the surface roughness peaks of each part. Condition used, for example, in hot rolling of sheets, V-bending of sheets and extrusion of aluminum alloys.
- Boundary Lubrification, is a condition very similar to dry friction with the difference that the surfaces in contact may eventually have the presence of oxides that act as an intermediary element between the parts. This is the case with aluminum and carbon steel, which will always have an oxidized layer when in contact with air. Another situation in this condition would be a thin layer of lubricant that acts as an interface between the parts along with air pockets between them.
- Mixed lubrication is the condition in which a film of lubricant surrounds all the material to be formed. This situation results in an intermediate lubrication between the Boundary Lubrification and Hydrodynamic conditions. It is the situation most widely found in metal forming where the presence of the lubricant generates an efficient friction in the production of pieces.
- Hydrodynamic Lubrification, which exists when a thick layer of lubricant is present between the die and the component. This subject is dealt with in fluid mechanics, where the stresses generated are related to the fluid's viscosity.

Figure 3 also shows the separation between the contact surfaces, as friction approaches Hydrodynamic Lubrification, there will be an increasing separation between work material and tools. This is not only in macroscopic conditions but can also occur in microscopic level where the lubricant will be retained in the roughness valleys and will be able to act when the pressure is greater. This will be explained further in the next item.

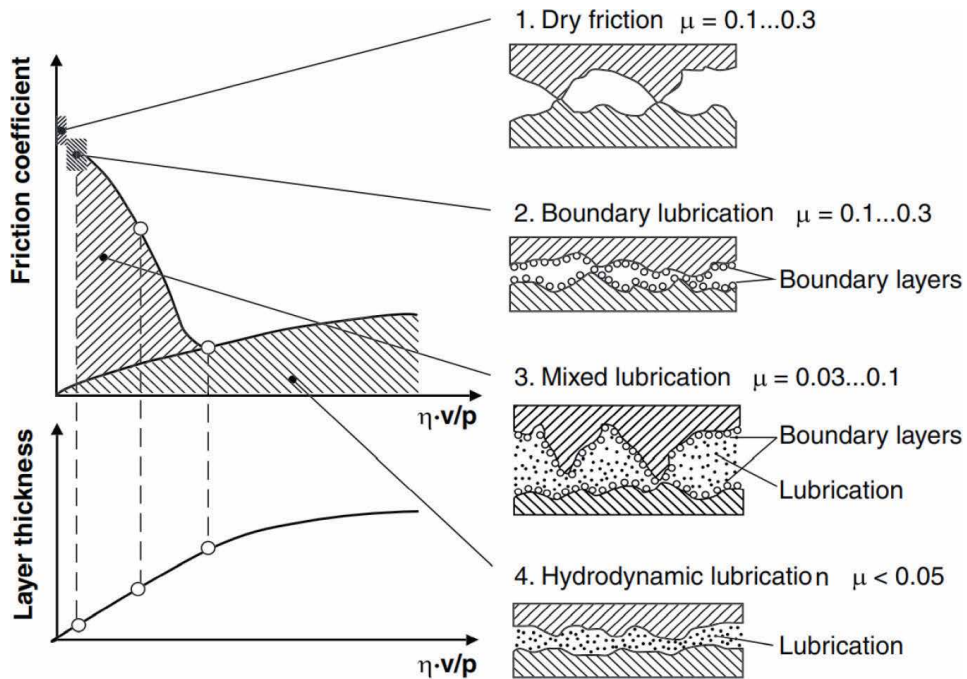


Figure 3. Stribeck diagram for different states of lubrication, with η dynamic viscosity, v sliding speed, p pressure/surface pressure. Source: Klocke [5].

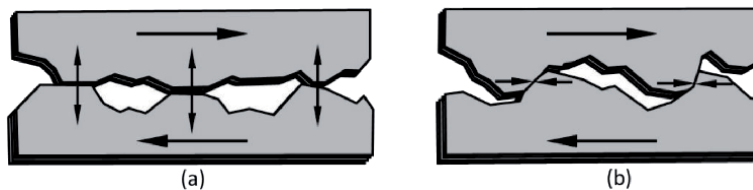


Figure 4. Schematic illustration of the components of the coefficient of friction present in metal/metal contact. Source: Folle and Schaeffer [6].

In addition to the conditions described above, two main factors can occur in the contact between two surfaces, the first is a friction by material adhesion that is caused by micro-welding at the contact interfaces and the second is a penetration friction. In the first case (**Figure 4a**), there is usually the pullout of the material with a lower hardness (workpiece) and this material ends up working as an interface material that promotes scratching of the shaped parts. In the second case (**Figure 4b**), there is a very large approximation between the parts that the roughness ends up being interpenetrated. In this case, it is very likely that material will be pulled out of the workpiece, promoting abrasive wear on the pieces and tools. In either case, a good lubrication condition can resolve.

3. Models used to describe friction

To describe the friction phenomenon in forming, it is important to use a model that reasonably describes the reality, especially when the analysis surface is large. For this case, the friction force makes a relevant contribution to the total force

required in the operation. Despite the great development in models that describe the behavior of materials, conventional computational numerical simulations generally do not provide correct results regarding friction. This is due to the use of very simplified friction models.

Two models are generally used to describe friction at the interface between tool and work material depending on the process being considered. The first is the Amontons-Coulomb model shown in Eq. (1), where there is a linear relationship between normal pressure and shear stress.

$$\tau = \mu \cdot p \tag{1}$$

where μ is the coefficient of friction (COF), p is the normal pressure and τ is the frictional shear stress.

Eq. (1) is valid only for relatively small shear stresses, because when τ exceeds the shear strength, k , of the workpiece material, the second model must be used. This second model was proposed by Orowan [7] and is shown in Eq. (2).

$$\tau = m \cdot k \tag{2}$$

where m is the shear factor, where its value ranges from 0 to 1 and k is the maximum shear strength of the work material.

Figure 5 represents the combination of the Amontons-Coulomb model and the limit shear stress model proposed by Orowan [7]. Shear stress is shown as a function of normal pressure. The first part of the figure is considered to be the Coulomb part. The relationship between the frictional force and the normal force, defined as the friction coefficient μ , is constant in this part of the curve.

When the normal pressure increases, the lubricant pockets start to leak and promote a decrease in friction visualized by the decrease in the slope of the curve, until reaching a constant value that is given by the maximum shear stress of the material. At this point, the friction coefficient no longer makes sense, and the concept of friction factor appears. This phenomenon is represented by the horizontal part of the curve (**Figure 5**).

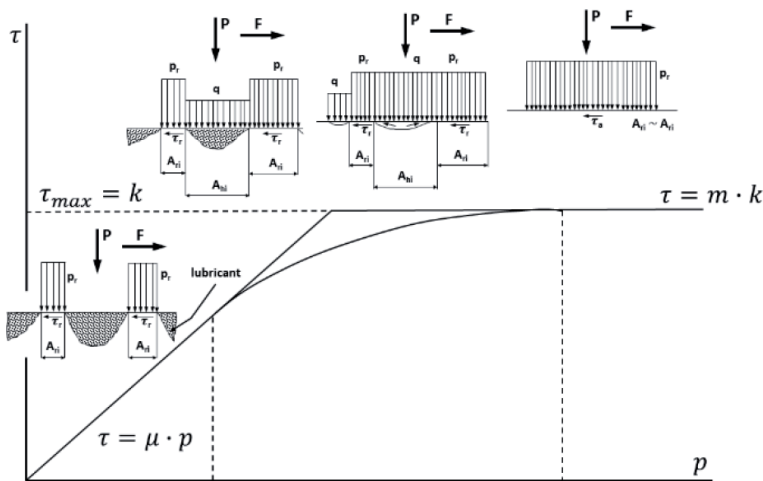


Figure 5. Relationship between contact pressure and frictional shear stress. Source: Based on Rodrigues and Martins [8] and Altan and Tekkaya [9].

In terms of metal forming processes, the coulombian friction coefficient is more used in sheet metal fabrication since the pressures cannot be so great as there is not enough material in the thickness to be deformed. As for the forming processes in bulk deformation, the shear friction factor must be used because in this case the pressures are always close to the maximum shear stresses of the work material.

4. Friction measurement tests for forming processes

There are several tests that were developed to measure the friction coefficient and friction factor in order to both understand how each process variable influences it and also to be loaded in finite element software for simulation of part manufacturing. The most common test still used today is the pin-to-disk test. **Figure 6** schematically shows how these tests work. This test consists of placing a specimen in the form of a ring or disc in a testing machine and forcing a pin against the specimen, making a rotary movement along the axis of the specimen. During the test, the tangential force and the normal force are measured in the contact area. The test can be done with a flat or spherical pin, depending on the condition being analyzed. The analysis is quite versatile, as friction can be determined for different sliding speeds, lubrication conditions, pressure forces and even working temperatures, depending on the complexity of the machine. Another advantage of this test is that some machines are marketed solely and are already adapted according to the most used standards. However, there are some disadvantages of this test that are related to the working pressures, which cannot be very large and in relation to the manufacturing processes, not being applied to some cases such as forging and sheet bending.

In processes where the contact pressure reaches values high enough to get close to the maximum shear stress of the work material, there is another test called the ring upsetting test, shown in **Figure 7**. This test has good applicability, reproducibility, and reduced cost. Therefore, it is often cited in the literature to determine both the friction coefficient and the friction factor for different lubrication states, both hot and cold. The sample is produced in a cylindrical ring shape with a hole in

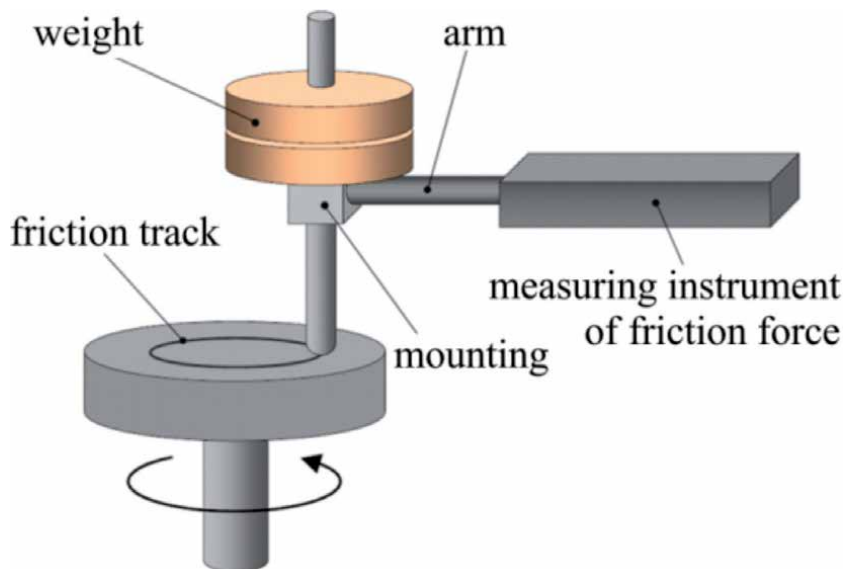


Figure 6. Schematic illustration of pin-on-disc test. Source: Trzepieciński and Lemu [10].

the center (**Figure 7** in the upper left corner). The sample is pressed axially between two parallel plane dies and after a specific strain, the geometry is measured and compared to the initial geometry. Thus, depending on the relationship between the start and end diameters, there will be a different friction on the part. If there is too much friction, the inside diameter gets smaller and the outside diameter larger. In case of little friction, the internal diameter becomes larger. To determine the friction values in this test, calibration curves are needed (**Figure 7** on the right), which can be obtained in different ways, but the most common is with the help of numerical simulations. The graph in **Figure 7** on the right shows the results of the ring upsetting test with different lubrication states. It should be noted that the friction coefficients determined are not absolute values, but average values over the entire contact surface between the specimen and the tool that were also determined along the entire path traveled.

For sheet metal forming process, the most used test in the literature today is the Strip Drawing Test or Bending Under Tension (BUT) Test shown in **Figure 8**. The test consists of bending a sheet metal strip through a pin of predetermined radius and on this pin to make the sheet slide. For this, a force is applied at one of the sheet ends so that there is relative movement between the sheet and the pin. At the other end, a force is applied against the movement in order to tension the sheet and to be able to vary the contact pressure incident on the pin. The force that generates the movement is F_1 and the force that is applied in the opposite direction is F_2 . The radius pin r has the function of simulating the friction in the passage of the stamping die radius, since it is in this region that the tensions are greater.

In this test, there are two forces required to make the sheet slide on the pin, one is the friction force between the contact surfaces and the other is the force required to bend and unbend the sheet. As the purpose of the test is to know the friction force between the contact surfaces, it is carried out in two steps. In the first one, the pin through which the sheet passes can freely rotate through its axis, so that there is no relative movement in the pin/sheet interface. This creates a condition of minimal friction, as the force required to make the sheet move is due solely to the sheet's bending and unbending force. In the second step, this same pin is fixed on its axis,

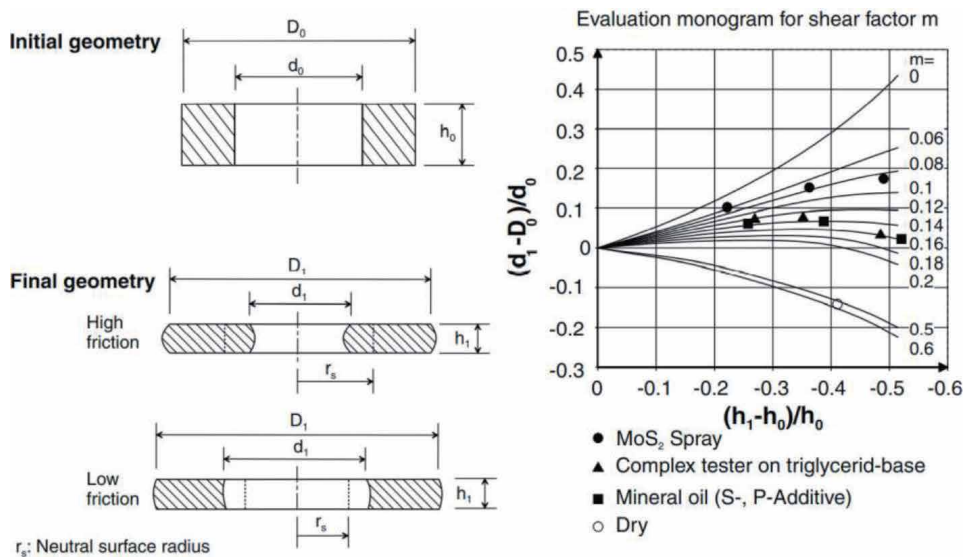


Figure 7. Specimen geometry in ring upsetting and a graphic calculated via FEM simulation for the evaluation of ring upsetting tests. Source: Klocke [5].

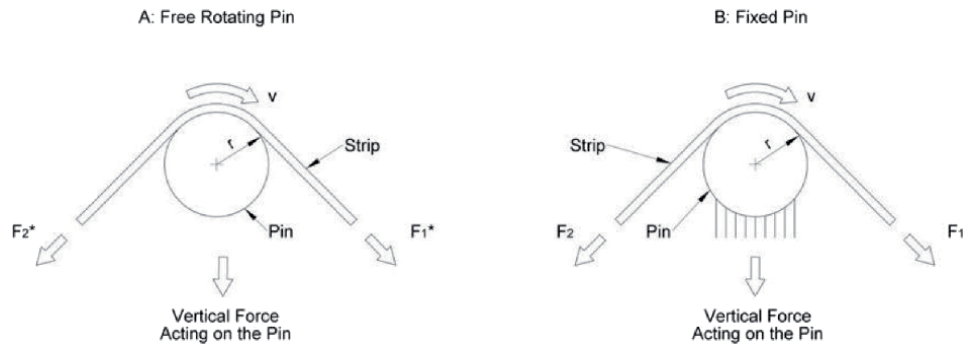


Figure 8.
Bending under tension test. Source: Folle and Schaeffer [11].

preventing any movement. The force required to make the sheet move is then made up of the bending force plus the friction force. Thus, the bending force, measured in the first step, can be deducted from the second, and only the friction force is obtained as a result.

The BUT test described above was conceived from the idea of knowing the friction in the passage of the die radius and is the traditional way of performing this test. However, some authors [12–15] have proposed some variations on this test in order to facilitate its construction or generate results closer to the deep drawing process. This is primarily due to the fact that to run the BUT test, it is necessary to build specific equipment for this, which is often difficult to perform. Thus, authors [13–16] have proposed some systems in which it is possible to adapt to a universal testing machine. In other works [17, 18], a measurement is proposed in which a torque is obtained on the pin through which the sheet passes. The idea of this variant of the BUT test aims to eliminate the test carried out with the free pin (which can rotate on its axis), since the torque measured on the pin is generated solely by the friction force, which is the purpose of the test. This test has the advantage of being able to represent the most critical region of sheet metal forming processes, which is in the die radius, however, it is only valid for sheet metal, not applying to bulk forming. Another disadvantage is that there is still no marketable machine that can be purchased for this purpose, all available models were built in research institutes, requiring a project for their implementation.

5. Parameters that influence friction in forming process

Friction depends on several parameters such as lubrication, normal pressure, workpiece and tool surface roughness, type of contact pair materials, slip speed and temperature. In forming at high temperatures, the coefficient of friction is generally higher than in cold forming. This is because strain at high temperatures can increase adhesion at the contact interface and because the best lubricants cannot withstand high temperatures, causing performance to suffer. There are other factors that strongly influence friction, such as the oxide layers that form debris that promote wear on the tools. Researchers already know that friction is more influenced by factors such as temperature, contact pressure and lubrication, but other factors can also be listed and have been summarized in **Figure 9**.

The first factor to be considered in metal forming processes is the shape and finish of the surfaces. **Figure 10** shows work done by Tillmann et al. [19] where the surface type and hardness were varied in a pin-in-disk test. The idea of modifying

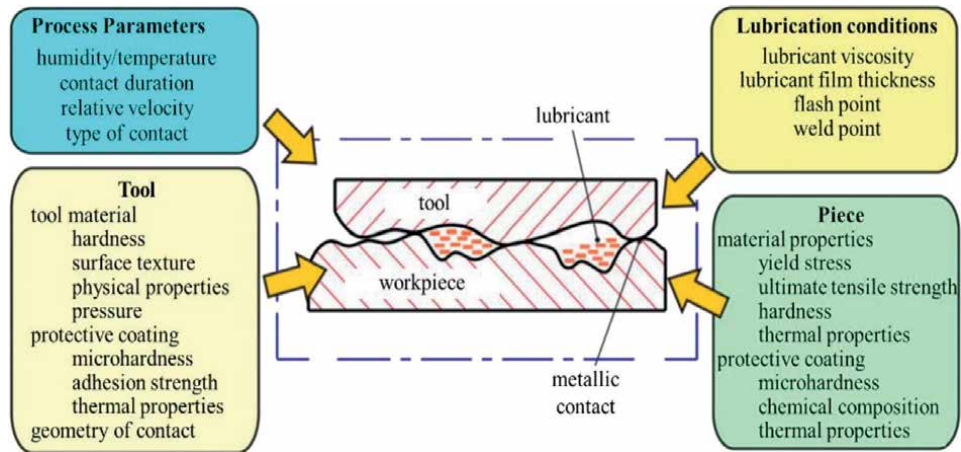


Figure 9. Parameters that can influence the friction in metal forming. Source: Trzepiecincki and Lemu [10].

the surface of tools is commonly used to generate lubricant entrapment pockets that when surface pressure increases, lubricant is released from these pockets, thus decreasing friction. This effect is also desired for large displacements between the tools and the workpiece to avoid wear.

The friction results from **Figure 10** are shown in **Figure 11** where you can see that the surfaces that generate the least friction are those with lubricant storage cavities as in **Figure 11(a)** and **(b)**. **Figure 11(c)** does not give good results as the surface peaks are too high causing there to be very punctual contact between the dies and the sheet and the lubricant not even being reached by the opposite surface.

As previously mentioned, lubrication is one of the main factors influencing friction as it can act as an efficient separation element between the parts in contact. It is already known that Teflon represents one of the lubricants that generates less friction at work interfaces, since it acts almost as a hydrodynamic lubrication, taking the friction coefficient to values below 0.05. **Figure 12** shows a comparison

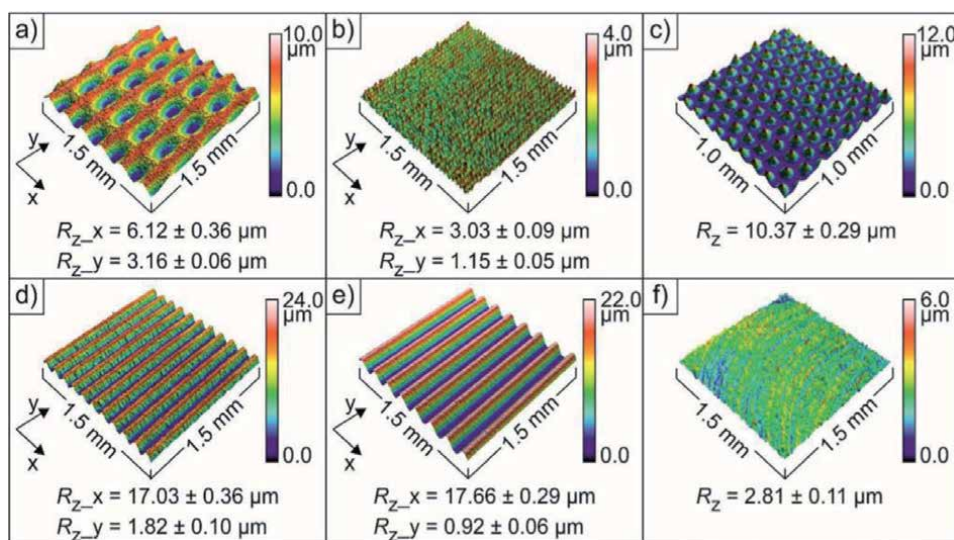


Figure 10. 3D images and mean roughness R_z values of the bionic structures a) St_1 , b) St_2 , c) St_3 , d) St_4 e) St_5 , and f) flat reference surface. Source: Tillmann et al. [19].

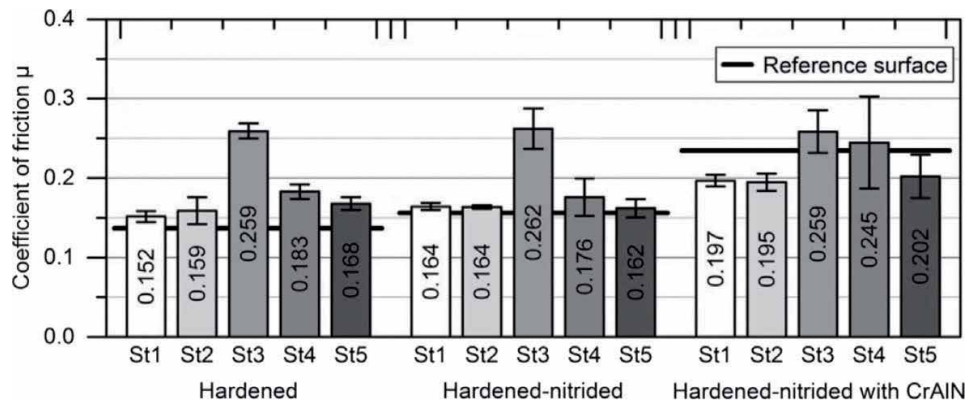


Figure 11. Friction coefficient results obtained by Tillmann et al. [19].

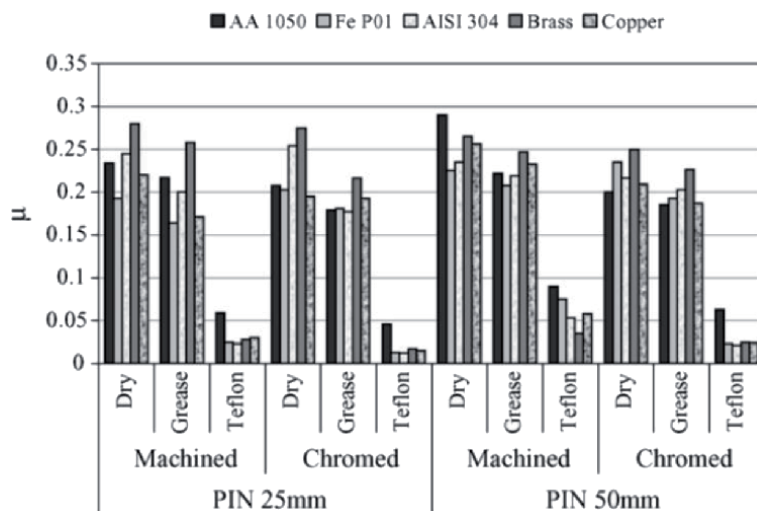


Figure 12. Friction coefficient for different finishes, lubricants, and materials. Source: Fratini et al. [20].

made through the BUT test with 3 lubrication conditions, dry, with grease and with Teflon, with 2 surface conditions, only machined and chromed, with 2 pin sizes and for 5 different working materials. In this study, it is possible to see that the friction conditions were lower when Teflon was applied. For the other conditions, friction changes around an average of about 0.2.

A very low friction condition is sometimes not the best option for the forming process, as the flow of the working material must be controlled so that the piece is free from defects. **Figure 13** shows two pieces made by sheet forming with different lubricants and the figure on the right was made with a Teflon sheet. It is possible to see that a very low friction promoted a freedom of strains in the material that caused the appearance of wrinkles on the edges, and this is considered a process defect.

In terms of numerical simulation, there are several efforts to adapt the friction variables in software. In the work of [21] a Pin-on-Disk System was used to evaluate the contact pressure in relation to friction, where a decreasing variation curve was constructed as shown in **Figure 14**. This curve was loaded into the software to evaluate the spring back, and the error with respect to the real piece was 7.4% while the error with constant friction was 31.1%.



Figure 13. Pieces stamped with different lubricants under the same conditions. Left figure: Liquid lubricant. Right figure: Teflon sheet. Source: Folle and Schaeffer [6].

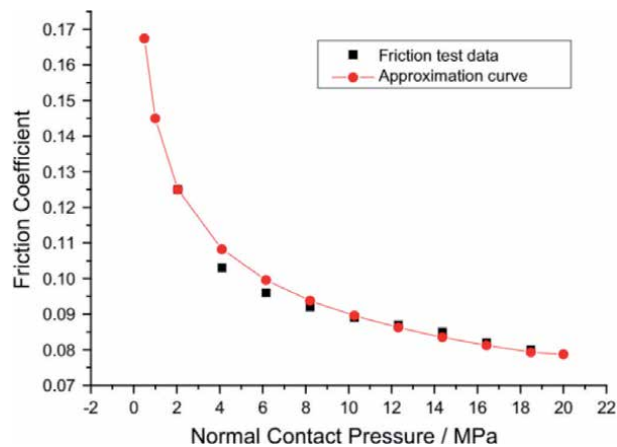


Figure 14. Variation curve used in the work of [21].

In the work of [22], a friction model was developed that considers the change in surface texture at the microscale and its influence on the friction behavior at the macroscale. This friction model was implemented in finite element code and applied to a full-scale sheet metal forming simulation. The results in **Figure 15**, showed a higher friction coefficient distribution compared to the constant friction model, however, this work was not compared with a real part, but the friction values were within acceptable levels.

Efforts to develop more efficient friction models are still current. In the work of [23], a model was also developed that considers the measured surface topographies of the sheet metal and the tool to determine the pressure distribution of the lubricant. Lubricant pressure distribution is used to estimate the load carried by solid-to-solid roughness contacts and the lubricant to calculate the overall coefficient of friction. The new mixed lubrication friction model is used in the FE code to make simulations of the real part shown in **Figure 16**. The results of the simulated and real major and minor deformations were very close for the presented model (**Figure 17**), although the friction was not simulated constant to check the differences between the 2 models.

In the work of [24], the researchers made the evaluation of friction in relation to the sliding speed and the contact pressure for an aluminum alloy and obtained the curve in **Figure 18**. With these results, they performed a numerical simulation of a profile U-shaped and evaluated both sheet thickness (**Figure 19**) and spring back.

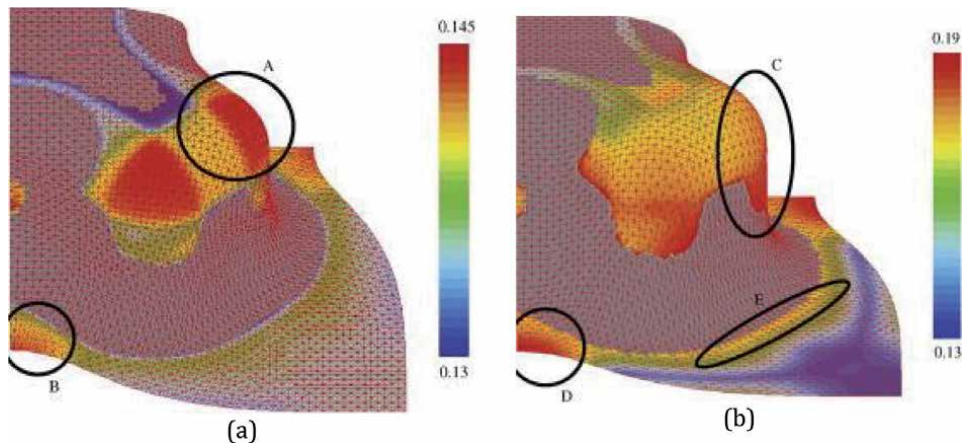


Figure 15. Simulation result with constant friction model (a) and texture change model (b). Source: Hol et al. [22].



Figure 16. Part geometry that was simulated by Shisode et al. [23].

For the thickness of the sheet, the variable friction model was perfectly suited to the real result. As for the spring back, there was a noticeable reduction in the error level, from 25–8% in one of the sheet's inclination angles.

Recent advances in friction measurement research have supported the development of software that is able to simulate the variation of the friction coefficient based on properties such as surface roughness and calibration tests. **Figure 20** shows two surfaces that were scanned and loaded into the TriboForm® software to estimate friction and **Figure 21** shows the result that the software generated from the data provided. From **Figure 21**, it is possible to see that the behavior of the friction coefficient in relation to the sliding speed, the contact pressure and the level of deformation agree with the literature. This generates more precision in predicting the material's behavior against these variables and, consequently, also generates a better scenario for decisions of those involved in the fabrication of the piece.

To illustrate these improvements being applied in software, **Figure 22** shows two simulations made under different friction conditions, the first with constant friction and the second with variable friction. In this case, the simulation with a friction coefficient more faithful to reality proved to be more efficient in predicting process problems and this has been gaining strength in simulation software.

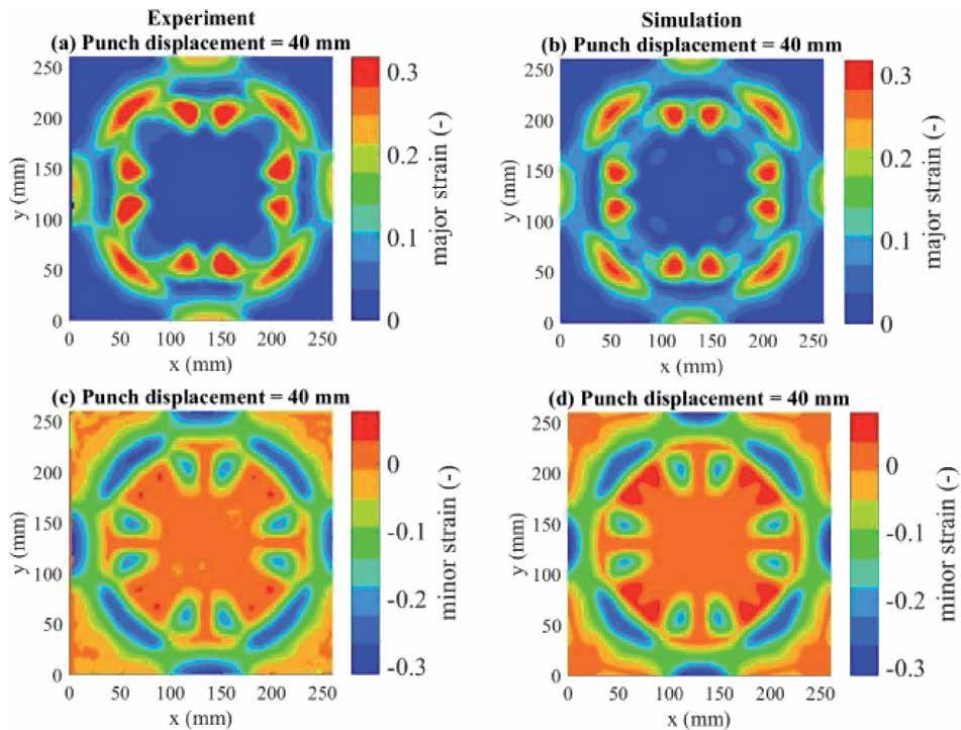


Figure 17. Comparison of major and minor strain distributions between experiments and simulations. Source: Shisode et al. [23].

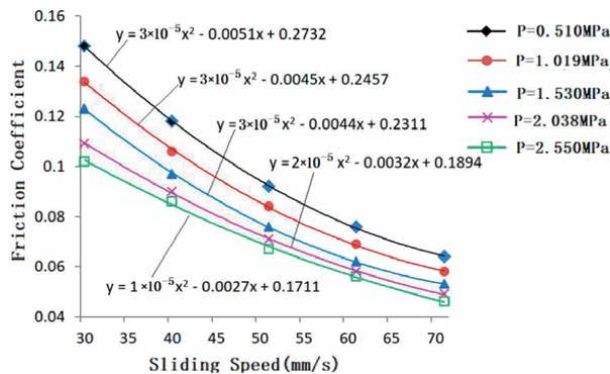


Figure 18. Friction coefficient curve with different sliding speeds, with five loads. Source: Dou and Xia [24].

It can be seen in the **Figure 22**, the results of the finite element modeling and simulation with constant friction and variable friction compared to a real production sheet metal part. The figure shows that a simulation with constant friction masked a problem that appeared in the real part and with the use of variable friction (TriboForm), the simulation can predict the defect circled in green in the photo on the right. Thus, it is important that friction is well characterized so that production defects can be avoided.

Other studies are being conducted to further improve the understanding of the characteristics of the tribological system in relation to the forming process, especially for sheet metal, also using dedicated software such as TriboForm and TriboZone. The work of [26], for example, aimed to identify the influence of the

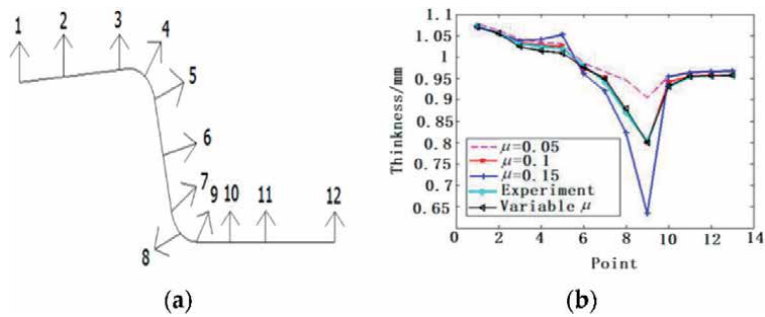


Figure 19. (a) Thickness measurement points; (b) thickness comparison between numerical result and actual measurements. Source: Dou and Xia [24].

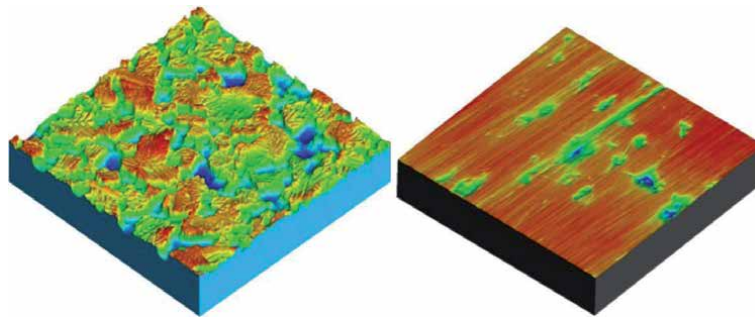


Figure 20. Impression 3D surface texture sheet (left) and tooling (right). Source: Sigvant et al. [25].

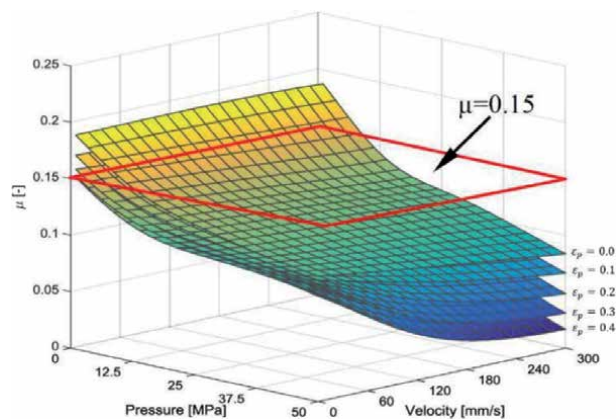


Figure 21. Simulated friction behavior for different strain levels in the sheet material. Source: Sigvant et al. [25].

heterogeneity of roughness along the tool in the material forming process using TriboZone software. In **Figure 23**, it is possible to see that a roughness heterogeneity model adds more reliability to the results, however, there was a great similarity in relation to the TriboForm variable friction model, which makes this model equally effective. On the other hand, models that only depend on pressure and constant models can generate more dispersed deformation data, which should not correspond to reality.

Another work using the same simulation platform, but with the objective of testing the influence of the amount of lubricant on the piece's deformations was



Figure 22. Simulation with constant friction and variable friction compared to a real piece. Source: Sigvant et al. [25].

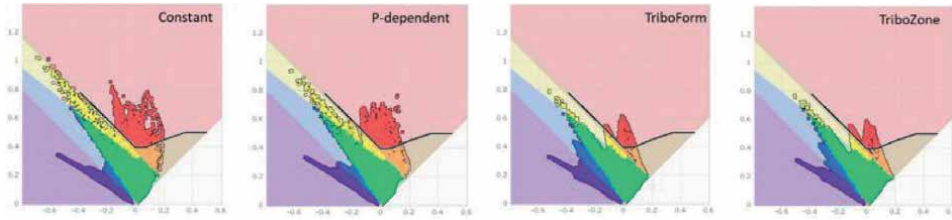


Figure 23. FLD of the part considering the different types of friction model. Source: Sigvant et al. [26].

done by Tatipala et al. [27]. In this study, an automotive door side was chosen, and the amounts of lubricant applied in each zone were measured. **Figure 24** shows the variation in lubricant amounts in relation to the part's blank position.

The information on the variation of lubrication amounts in each region of the part was loaded into the software and the strains were evaluated. **Figure 25** shows that with a variable amount of lubricant, there will also be a different strain on the sheet, which makes the result of strains on the sheet more accurate.

As shown so far, friction in the forming process is a major contributor to the deformation performance of a piece. Research has indicated that it is important to have an adequate surface, both for the work material and for the tools, so that there is a correct lubrication system. It is equally important to know the main mathematical models that can be applied to each manufacturing situation by the forming process, predicting with more precision the results for the manufacturing of a piece or product. These friction models have been studied more intensively to be loaded in numerical simulations and thus predict possible manufacturing defects. The main results of the studies showed that there is a considerable improvement in predictability with respect to spring back, wrinkle defects, strains in the workpiece and final sheet thickness.

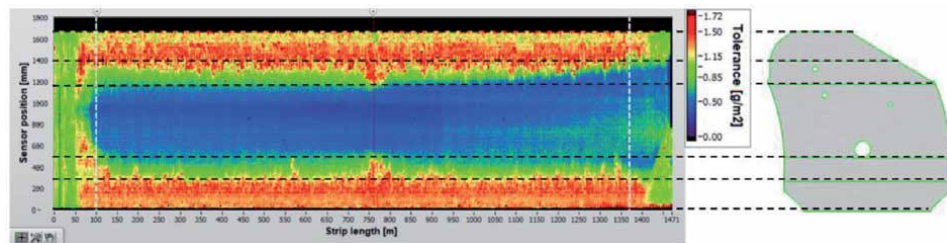


Figure 24. Variation of the amount of lubricant measured in each region of the blank. Source: Tatipala et al. [27].

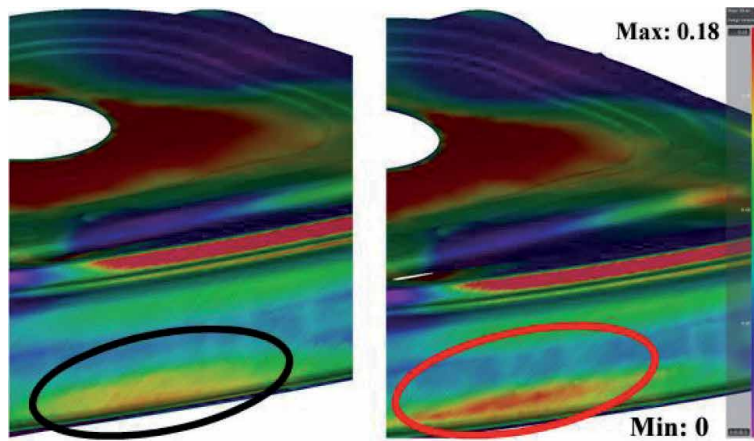


Figure 25. Variation of major strain for blank with constant lubrication (left) and the variable amount of lubrication (right). Source: Tatipala et al. [27].

Previously, it was enough to use constant friction in the simulations and the results for those materials were enough, so that a simple test could obtain the most adequate friction coefficient. However, with the advancement of new materials, such as advanced high strength steels, high plasticity aluminum alloys with high strength, magnesium alloys for cold forming, duplex stainless steels, dissimilar materials joined by welding, among others, have required that simulations be increasingly detailed in the amount of information to be collected. It is already possible, for example, to load in the software, information such as the topological profile of the surfaces in contact, the viscosity of the lubricant, the variation with pressure, temperature, sliding speed, level of strains and amount of lubricant applied in each region of the piece. This brings more accuracy to the failure prediction models, but also generates more work to be surveyed.

6. Final remarks and future trends

Tribology, including the study of surface phenomena such as contact, friction, lubrication and wear, plays a fundamental role in metal forming processes, as it directly influences the final quality of the parts produced and the useful life of the tools, which generally have a very high cost. In this sense, the use of mathematical models that represent the adequate friction conditions and the use of computational simulation tools play a fundamental role in reliably predicting the tribological aspects of the forming processes.

Generally, industrial case studies focused on sheet metal forming simulation using finite element methods, includes a constant coulombian friction model and cannot achieve good results when comparing numerical and experimental results, in terms of the prediction of wrinkling as well as ruptures, as presented in this work. However, further improvements are going towards spring back prediction, which includes surface texturing parameters and variable friction approach. All, aiming to a better reliability on tribological modeling of the friction influences for the metal forming process.

The present work shows that there is a growing concern regarding friction phenomena in metal forming. Numerical simulations are already at a very advanced stage in their ability to predict the behavior of the material being manufactured.

However, the amount of information that must be collected for the software to be able to simulate with precision is increasing and this will require a greater volume of data associated with the materials of the pieces, tools and metal interfaces. This may seem problematic in terms of costs, however, it must be taken into account that the failure and scrap rates will be practically zeroed, leading to more gains than the efforts to obtain all the necessary properties.

Author details


Luis Fernando Folle¹, Bruno Caetano dos Santos Silva¹, Gilmar Ferreira Batalha² and Rodrigo Santiago Coelho^{1*}

1 SENAI CIMATEC, SENAI Institute of Innovation for Forming and Joining of Materials, Salvador, BA, Brazil

2 Polytechnic School of Engineering, University of Sao Paulo, Sao Paulo, Brazil

*Address all correspondence to: rodrigo.coelho@fieb.org.br

IntechOpen

© 2022 The Author(s). Licensee IntechOpen. This chapter is distributed under the terms of the Creative Commons Attribution License (<http://creativecommons.org/licenses/by/3.0>), which permits unrestricted use, distribution, and reproduction in any medium, provided the original work is properly cited. 

References

- [1] Groover M. *Fundamentals of Modern Manufacturing Materials, Processes and Systems*. USA: John Wiley & Sons; 2010. p. 493
- [2] dos Santos C, Silva B, Mendes Rodrigues A, Mueller R, et al. Tribological investigations on tool surfaces for temperature-supported forming of Magnesium AZ31 sheets. *Materials*. 2020;**13**:1-14
- [3] Mousavi A, Schomäcker M, Brosius A. Macro and micro structuring of deep drawing tools for lubricant free forming. *Procedia Engineering*. 2014;**81**:1890-1895
- [4] Börner R, Scholz P, Kühn R, et al. Micro structuring of coated tools for dry sheet metal forming of aluminium alloys. *Proceedings of the 15th International Conference of the European Society for Precision Engineering and Nanotechnology, EUSPEN*; 2015. pp. 85-86
- [5] Klocke F. *Manufacturing Processes 4 - Forming (RWTH edition)*. Heidelberg, New York, London, Dordrecht: Springer; 2013. https://link.springer.com/chapter/10.1007/978-3-642-36772-4_4 http://https-link.springer.com.85d8bfe604.di-iranpaper.ir/chapter/10.1007/978-3-642-36772-4_4
- [6] Folle LF, Schaeffer L. Effect of surface roughness and lubrication on the friction coefficient in deep drawing processes of aluminum alloy aa1100 with fem analysis. *Revista Materia*. 2019;**24**:1. DOI: 10.1590/s1517-707620190001.0635
- [7] Orowan E. The Calculation of Roll Pressure in Hot and Cold Flat Rolling. *Proceedings of the Institution of Mechanical Engineers*. 1943;**150**(1):140-167. DOI: 10.1243/PIME_PROC_1943_150_025_02
- [8] Rodrigues J, Martins PAF. *Tecnologia da Deformação Plástica - Vol. I*. Lisboa: Escolar Editora 2005.
- [9] ALTAN T, Tekkaya AE. *Sheet metal forming - Fundamentals*. Ohio: ASM International; 2012. DOI: 10.1007/978-2-287-72143-4_10
- [10] Trzepieciński T, Lemu HG. Recent developments and trends in the friction testing for conventional sheet metal forming and incremental sheet forming. *Metals*. 2020;**10**:1. DOI: 10.3390/met10010047
- [11] Folle L, Schaeffer L. New proposal to calculate the friction in sheet metal forming through bending under tension test. *Materials Research*. 2019;**22**:1. DOI: 10.1590/1980-5373-MR-2019-0523
- [12] Lovell M, Higgs CF, Deshmukh P, et al. Increasing formability in sheet metal stamping operations using environmentally friendly lubricants. *Journal of Materials Processing Technology*. 2006;**177**:87-90. DOI: 10.1016/j.jmatprotec.2006.04.045
- [13] Hao S, Klamecki BE, Ramalingam S. Friction measurement apparatus for sheet metal forming. *Wear*. 1999;**224**:1-7
- [14] Trzepieciński T, Lemu HG. Proposal for an experimental-numerical method for friction description in sheet metal forming. *Strojnicki Vestnik/Journal of Mechanical Engineering*. 2015;**61**:383-391. DOI: 10.5545/sv-jme.2015.2404
- [15] Miguel V, Coello J, Calatayud A, et al. An approach to evaluation of sheet bending force under successive multiaxial stress condition. *Journal of Materials Processing Technology*. 2009;**209**:1588-1596
- [16] Duncan JL, Shabel BS, Gerbase Filho J. A Tensile Strip Test for Evaluating

Friction in Sheet Metal Forming. SAE Technical Paper. Detroit: Congress and Exposition Cobo Hall; 1978.

[17] Sniekers RJJM, Smits HAA. Experimental set-up and data processing of the radial strip-drawing friction test. *Journal of Materials Processing Technology*. 1997;**66**:216-223

[18] Andreasen JL, Olsson DD, Chodnikiewicz K, et al. Bending under tension test with direct friction measurement. *Proceedings of the Institution of Mechanical Engineers, Part B: Journal of Engineering Manufacture*. 2006;**220**(1):73-80. DOI: 10.1243/095440505X32913

[19] Tillmann W, Stangier D, Lopes-Dias NF, et al. Adjustment of friction by duplex-treated, bionic structures for Sheet-Bulk Metal Forming. *Tribology International*. 2017;**111**:9-17

[20] Fratini L, Casto S, lo, lo Valvo E. A technical note on an experimental device to measure friction coefficient in sheet metal forming. *Journal of Materials Processing Technology*. 2006;**172**:16-21

[21] Wang W, Zhao Y, Wang Z, et al. A study on variable friction model in sheet metal forming with advanced high strength steels. *Tribology International*. 2016;**93**:17-28

[22] Hol J, Cid Alfaro M, v., de Rooij MB, et al. Advanced friction modeling for sheet metal forming. *Wear*. 2012; **286-287**:66-78

[23] Shisode M, Hazrati J, Mishra T, et al. Mixed lubrication friction model including surface texture effects for sheet metal forming. *Journal of Materials Processing Technology*. 2021;**291**:1. DOI: 10.1016/j.jmatprotec.2020.117035

[24] Dou S, Xia J. Analysis of sheet metal forming (Stamping process): A study of the variable friction coefficient on 5052 aluminum alloy. *Metals*. 2019;**9**:1. DOI: 10.3390/met9080853

[25] Sigvant M, Pilthammar J, Hol J, et al. Friction and lubrication modeling in sheet metal forming simulations of a Volvo XC90 inner door. *IOP Conference Series: Materials Science and Engineering*. 2016;**159**:012021

[26] Zabala A, de Argandoña ES, Cañizares D, et al. Numerical study of advanced friction modelling for sheet metal forming: Influence of the die local roughness. *Tribology International*. 2022;**165**:1. DOI: 10.1016/j.triboint.2021.107259

[27] Tatipala S, Pilthammar J, Sigvant M, et al. Introductory study of sheet metal forming simulations to evaluate process robustness. *IOP Conference Series: Materials Science and Engineering*. 2018;**418**:1. DOI: 10.1088/1757-899X/418/1/012111

Groove Shape Optimization on Dry Gas Seals

Masayuki Ochiai and Yuki Sato

Abstract

In this paper, a topological optimum design for the shape of a groove in a dry gas seal is described. Dry gas seals are widely used in high speed and high pressure rotating machinery such as gas turbines, compressors, and so on because of their high reliability compared to other types of seals. However, recent requirements for reducing emission with further control of leakage are in order. With this background, we propose applying topological optimization to the groove shape in a dry gas seal to reduce its leakage while keeping its stiffness for safe operation. First, the method of topological optimum design as applied to the groove of a dry gas seal is explained via numerical analysis. Next, results of the topological optimization are shown via categorizing an optimum shape map. Finally, the mechanism of reducing the gas leakage with an optimized seal is discussed based on the prediction of the flow field using a CFD analysis.

Keywords: mechanical seals, dry gas seals, groove shape, optimization, gas lubrication

1. Introduction

Non-contact dry gas seals with a grooved pattern on a seal face can maintain a film thickness of just a few micrometers. Therefore, these seals have better sealing performance when compared to typical labyrinth seals [1]. Dry gas seals are used in many turbomachinery, such as in gas and steam turbines, turbochargers, and compressors. Moreover, they are applied to high-speed operation and under high-pressure differences.

Recently, to reduce energy consumption, more enhancements toward efficient turbomachinery are required. To solve this problem, one effective way is by enhancing the sealing characteristics of seals. Many types of grooved dry gas seals have been developed [1]. Spiral grooved seals are widely used because of their good sealing ability. Lately, a significant amount of research on spiral grooved dry gas seals focused on analytical methods [2–8], dynamic force characteristics [9–11], thermal effects considerations [12], and CFD analysis considering the turbulent flow [13] have been performed.

On the other hand, the optimum design of the grooves is one of the effective ways to enhance the seal characteristics. The optimum design methods have been also applied to gas film bearings. Lin and Satomi [14] and Hashimoto and Ochiai [15, 16] applied an optimum design method to spiral groove thrust bearing towards enhancing performance characteristics from variations in groove depth, groove angle, and so on. Moreover, an experimental verification was conducted comparing

the novel configuration against a conventional designed spiral groove bearing. However, it was found that the effectiveness of the optimization is limited because these studies have not been changed the groove shapes which were based on a spiral path.

Under this circumstance, Hashimoto and Ochiai [17] proposed a topological optimum design method for a grooved thrust gas bearing. In this method, the groove shape could be changed freely using a cubic spline function. Novel groove shapes were found in this study. The effectiveness and the applicability of the method were verified theoretically and experimentally. Moreover, Hashimoto and Namba [18] found the best groove shapes against various objective functions such as film thickness, friction torque, and dynamic axial stiffness. Also, the effect of the new groove shape on sealing characteristics of FDB(Fluid dynamic bearing) was studied previously and discussed by authors [19].

To date, many researchers have treated spirally grooved shape dry gas seals. On the other hand, recently, the optimum design of groove shape on the dry gas seal was proposed by authors, and comparison of the flow visualization was presented [21]. However, the process of the optimum design has not been mentioned and also it has not been studied for a wide range of operation conditions. Therefore, in this study, the application of the topological optimum design to the dry gas seal instead of the thrust bearings to find an optimum groove shape that enhances the seal leakage restriction and its dynamic stiffness is presented. Moreover, it is important to know the optimum groove shapes under various conditions, therefore, in this study, we tried to make a categorization map of the seal's optimum shape based on the results of the optimum design calculations under a wide range of operating conditions. Furthermore, CFD analysis is conducted and compared with the experimental flow visualizations for verification, while the rationale for reducing the gas leakage with an optimized seal is presented.

2. Topological optimization methods

Figure 1 shows the typical structure of a dry gas seal cartridge. It consists of a rotating shaft, a ring with grooves on its face, a stationary ring, support springs, and housing. The gas film is generated by the hydrodynamic effect induced on the

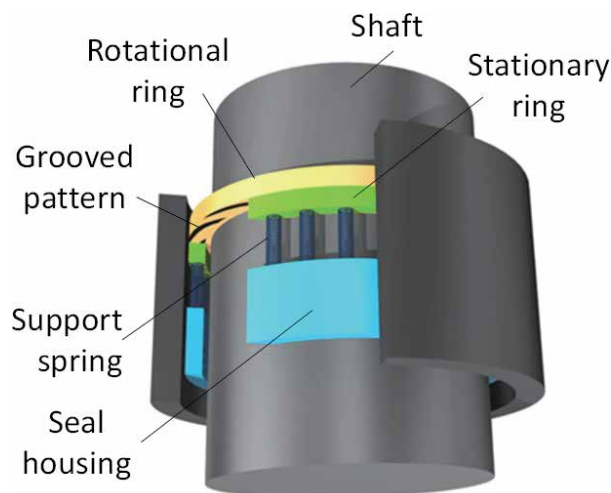


Figure 1.
Components of a non-contacting dry gas seal.

Parameter	Values
Stator mass m	1.0 kg
Support spring k	5.0×10^5 N/m
Steady-state clearance c_r	5 μ m
Assumed disturbance f	5 G
Viscosity of the air	1.82×10^{-5} Pa·s
Compressibility number $\Lambda = (6\mu\Lambda/P_a) * (r_1/h_r)^2$	100–750
Outer side pressure P_O	0.5–10 MPa
Inner side pressure P_I	0.1 MPa

Table 1.
 Dry gas seal physical parameters.

grooves of the face. The film thickness is determined by the force balance between the support springs and the hydrodynamic gas film force. The film thickness can be changed by changing the support springs. The seal leakage is a function of the film thickness, the gas pressure differential between the inner side and outer side of the seal chamber, the viscosity of the gas, and the groove shape mounted on the face.

In the design of dry gas seals, it is important to minimize the gas leakage towards enhancing the efficiency of turbomachinery. Simultaneously, enhancing the dynamic stiffness of a gas film is an important factor for its safe operation, at high speed in particular. Because turbomachinery is likely to be exposed to some outer disturbance such as earthquakes, a hard contact of the rotor on the seal surface leads to serious damage to the mechanical system.

Both a low gas leakage and a high gas film stiffness are trade-off relations, being difficult to optimize both parameters at the same time. Therefore, in this study, sufficient stiffness is selected for safety. The whole structure of the dry gas seal with the gas film is modeled as spring and damper as shown later. Therefore, from the calculation of a linear vibration waveform, the minimum film thickness is obtained. Under the conditions presented in **Table 1**, Ref. [19], the required gas lubricated film stiffness is defined. Because the leakage rate is strongly affected by film thickness, the value is fixed as 5 μ m in this optimization as shown in **Table 1**.

3. Optimum design formula

The optimization method in this study is based on Hashimoto and Ochiai's topological optimum design theory [17]. The outline of the method is as follows. The initial groove geometry is the usual spiral groove shape, and then, cubic spline interpolation functions are applied to the initial geometry with 4 grids. Moving the grids on the same circumferences changes the groove shape. Applying the optimum design method, an optimized seal groove shape is obtained. Simultaneously, the number of grooves N , the seal radius R_s , the groove depth h_g , and the groove width ratio α are set as the optimized design valuables in this study. Therefore, the design vector of parameters is

$$\mathbf{X} = (\varphi_1, \varphi_2, \varphi_3, \varphi_4, N, R_s, h_g, \alpha) \quad (1)$$

where, the φ_1 to φ_4 mean the angles from an initial spiral groove shape, shown in **Figure 2a**.

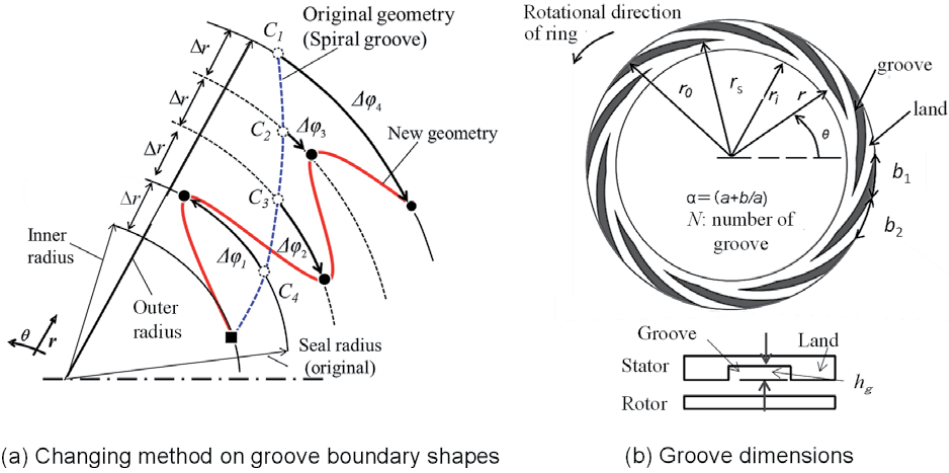


Figure 2.
Geometry of a seal and optimum design variables.

In the optimum design, the objective functions should be defined. Obviously, the most important one is to minimize the leakage q . Therefore, the objective function is set as

$$f_1(\mathbf{X}) = q \quad (2)$$

Moreover, even if a lesser leakage design is available, it is impractical to have a lesser dynamic stiffness simultaneously. Since dry gas seals are usually used under high speed and high-pressure differential conditions, sudden contact on the seal faces may lead to serious accidents. Therefore, the dynamic stiffness K must be used as the second objective function,

$$f_2(\mathbf{X}) = K \quad (3)$$

The constraint relationships in this optimization are

$$g_i(\mathbf{X}) \leq 0 (i = 1 \sim 19) \quad (4)$$

where

$$\left. \begin{aligned} g_1 &= \varphi_{1\min} - \varphi_1, g_2 = \varphi_1 - \varphi_{1\max}, g_3 = \varphi_{2\min} - \varphi_2, \\ g_4 &= \varphi_2 - \varphi_{2\max}, g_5 = \varphi_{3\min} - \varphi_3, g_6 = \varphi_3 - \varphi_{3\max}, \\ g_7 &= \varphi_{4\min} - \varphi_4, g_8 = \varphi_4 - \varphi_{4\max}, g_9 = N_{\min} - N, \\ g_{10} &= N - N_{\max}, g_{11} = R_{s\min} - R_s, g_{12} = R_s - R_{s\max}, \\ g_{13} &= h_{g\min} - h_g, g_{14} = h_g - h_{g\max}, g_{15} = \alpha_{\min} - \alpha, \\ g_{16} &= \alpha - \alpha_{\max}, g_{17} = -c, g_{18} = -k, g_{19} = -W \end{aligned} \right\} \quad (5)$$

The g_1 to g_{16} indicate the upper and lower limit of the design variables and the g_{17} is to avoid negative damping.

The optimum design problem is formulated as

$$\begin{aligned} & \text{Find } \mathbf{X} \text{ to minimize } f_1(\mathbf{X}) \text{ and maximize } f_2(\mathbf{X}) \\ & \text{subjected to } g_i(\mathbf{X}) \leq 0 (i = 1 \sim 19) \end{aligned} \quad (6)$$

4. Calculation method of seal characteristics

The analysis method to calculate the seal characteristics is shown below. During the optimum design calculations, the groove shape should be changed continuously from its original spiral groove shape into other shapes. Therefore, a boundary-fitted coordinate system is adopted as the numerical calculation method [15]. Moreover, a divergence formulation method is implemented. A Reynolds equivalent equation obtained from flow balance as shown in **Figure 3** is used to obtain the pressure distributions on the seal face. This is because the geometry has a step over which there is a discontinuous pressure gradient between the groove and the land areas.

The Reynolds equivalent equation [16] is

$$Q_{2I}^{\xi} + Q_{1III}^{\xi} - Q_{2II}^{\xi} - Q_{1IV}^{\xi} + Q_{2I}^{\eta} + Q_{1II}^{\eta} - Q_{2III}^{\eta} - Q_{1IV}^{\eta} = Q^I \quad (7)$$

Subscripts 1, 2, and *I* to *IV* indicate the areas in the control volume shown in **Figure 3**.

where the mass flow rates through the various boundaries are

$$Q^{\xi} = \int_{\eta_1}^{\eta_2} \rho \left(-A_0 \frac{\partial p}{\partial \xi} + B_0 \frac{\partial p}{\partial \eta} + D_0 + E_0 \right) d\eta \quad (8)$$

$$Q^{\eta} = \int_{\xi_1}^{\xi_2} \rho \left(B_0 \frac{\partial p}{\partial \xi} - C_0 \frac{\partial p}{\partial \eta} + F_0 + G_0 \right) d\xi \quad (9)$$

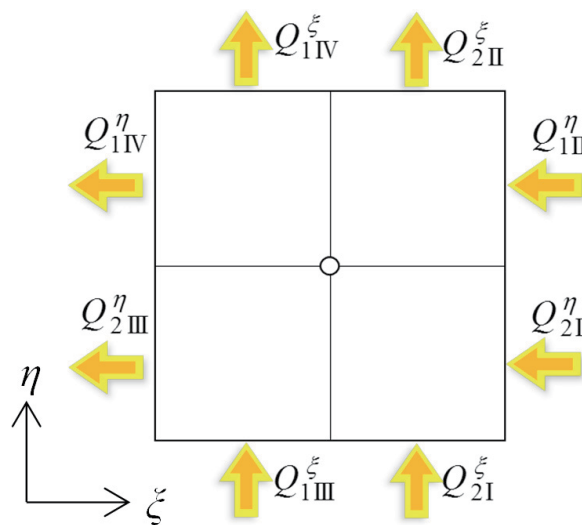


Figure 3.
Control volume and flow rates.

$$Q^r = \int_{\xi_1}^{\xi_2} \int_{\eta_1}^{\eta_2} \frac{\partial(\rho h)}{\partial t} \Big|_{J_0} |d\eta d\xi \quad (10)$$

The coefficients of A_o to J_o are

$$\left. \begin{aligned} A_o &= a_o \frac{h^3}{12\mu J}, B_o = b_o \frac{h^3}{12\mu J}, C_o = c_o \frac{h^3}{12\mu J}, D_o = -\frac{r\omega_s h}{2} r_\eta, \\ E_o &= \frac{\rho r \omega_s^2 h^3}{40\mu} r\theta_\eta, F_o = \frac{r\omega_s h}{2} r_\xi, G_o = \frac{\rho r \omega_s^2 h^3}{40\mu} r\theta_\xi, \\ a_o &= (r\theta_\xi)^2 + r_\eta^2, b_o = (r\theta_\xi)(r\theta_\eta) + r_\xi r_2, c_o = (r\theta_\xi)^2 + r_\xi^2, \\ J_o &= r_\xi(r\theta_\eta) - r_\eta(r\theta_\xi), r_\xi = \frac{\partial r}{\partial \xi}, r_\eta = \frac{\partial r}{\partial \eta}, \\ r\theta_\xi &= r \frac{\partial \theta}{\partial \xi}, r\theta_\eta = r \frac{\partial \theta}{\partial \eta} \end{aligned} \right\} \quad (11)$$

Assuming a small amplitude vibration of the seal with frequency ω_f , the gas film thickness and pressure are expressed as follows.

$$\left. \begin{aligned} h &= h_0 + \varepsilon e^{j\omega_f t} \\ p &= p_0 + \varepsilon p_t e^{j\omega_f t} \end{aligned} \right\} \quad (12)$$

where, ε is an amplitude of vibration and p_0 and p_t express a static component and dynamic pressure components, respectively.

Substituting Eq. (12) into Eq. (7) and neglecting seconds terms of ε , the following equations regarding the 0th field and 1st field ε are obtained.

$$F_0(p_0) = Q_{2I0}^\xi + Q_{1III0}^\xi - Q_{2II0}^\xi - Q_{1IV0}^\xi + Q_{2I0}^\eta + Q_{1II0}^\eta - Q_{2III0}^\eta - Q_{1IV0}^\eta \quad (13)$$

$$F_t(p_t, p_0) = Q_{2It}^\xi + Q_{1IIIIt}^\xi - Q_{2IIIt}^\xi - Q_{1IVIt}^\xi + Q_{2It}^\eta + Q_{1IIIt}^\eta - Q_{2IIIIt}^\eta - Q_{1IVIt}^\eta \quad (14)$$

Discretizing Eqs. (13) and (14), and then solving the equations numerically, the static and dynamic components of the gas pressure fields are obtained. Finally, the gas leakage rate q is calculated from the static pressure distributions as

$$q = \int_0^{2\pi} -\frac{\rho h^3}{12\mu} \frac{\partial p_0}{\partial r} \Big|_{r=r_i} r d\theta \quad (15)$$

Moreover, assuming the simple vibration model of a dry gas seal shown in **Figure 4**, the dynamic stiffness K is obtained from the calculated dynamic pressure distributions as,

$$K = \sqrt{k^2 + (\omega_f c)^2} \quad (16)$$

$$k = \int_0^{2\pi} \int_{r_i}^{r_o} \text{Re} \{ -p_t \} r dr d\theta \quad (17)$$

$$c = \int_0^{2\pi} \int_{r_i}^{r_o} \text{Im} \{ -p_t \} r dr d\theta \quad (18)$$

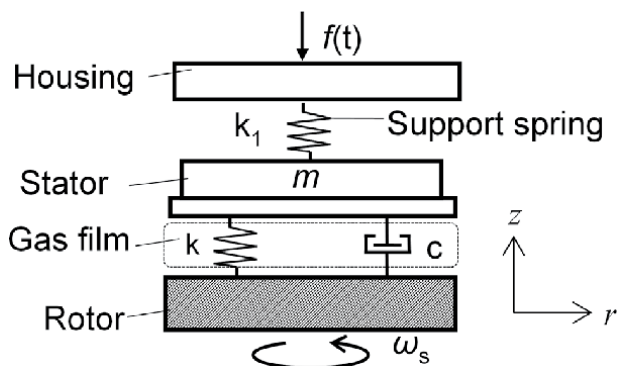


Figure 4.
 Simple vibration model of the dry gas seal.

5. Topological optimization results

Using the method mentioned above, topological optimum calculations were conducted. The calculation conditions are shown in **Tables 1** and **2**, and **Figure 2**. As shown in **Table 1**, the mass of stator $m = 1.0$ kg, the support spring $k = 5.0 \times 10^5$ N/m, the steady-state clearance $c_r = 5 \mu\text{m}$ are defined in the reference literature [19]. The assumed disturbance of $f = 5G$ is defined from the magnitude of earthquakes. The Compressibility number Λ and outer side pressure P_0 are set under a wide range of operation conditions. Because we would like to find the general optimum shape of the seal groove under various operating conditions, not a limited condition. The parameters for optimum design calculations are set as shown in **Table 2**. These set values are defined by representative of the dry gas seals. The groove numbers are discrete values. The other optimum design variables of the groove depth, the angle amount, the groove width, the inner and outer radius are continuous values, and their maximum and minimum values are set as concentration conditions.

By solving the above optimum design problem, a multi objective genetic algorithm is used as this in a multi objective optimization [20].

Figure 5 shows the optimization results for operation with a compressibility number $\Lambda = 500$ and inlet pressure $P_0 = 2.5$ MPa. The vertical axis shows the gas leakage flow rate as the 1st objective function and the horizontal axis shows the dynamic stiffness as the 2nd objective function. In this figure, the red line at the

Parameters	Values
Groove number	6,8,10,12,14,16,18,20,22,24
Minimum groove depth	$h_{g \min} = 5 \mu\text{m}$
Maximum groove depth	$h_{g \max} = 10 \mu\text{m}$
Minimum angle amount	$\phi_{i \min} = -\pi$ (i = 1-4)
Maximum angle amount	$\phi_{i \max} = \pi$ (i = 1-4)
Minimum groove width	$\alpha_{\min} = 0.4$
Maximum groove width	$\alpha_{\max} = 0.9$
Minimum seal radius to outer radius ratio	$R_s \min = 0.86$
Maximum seal radius to outer radius ratio	$R_s \max = 0.95$

Table 2.
 Parameters for optimum design study.

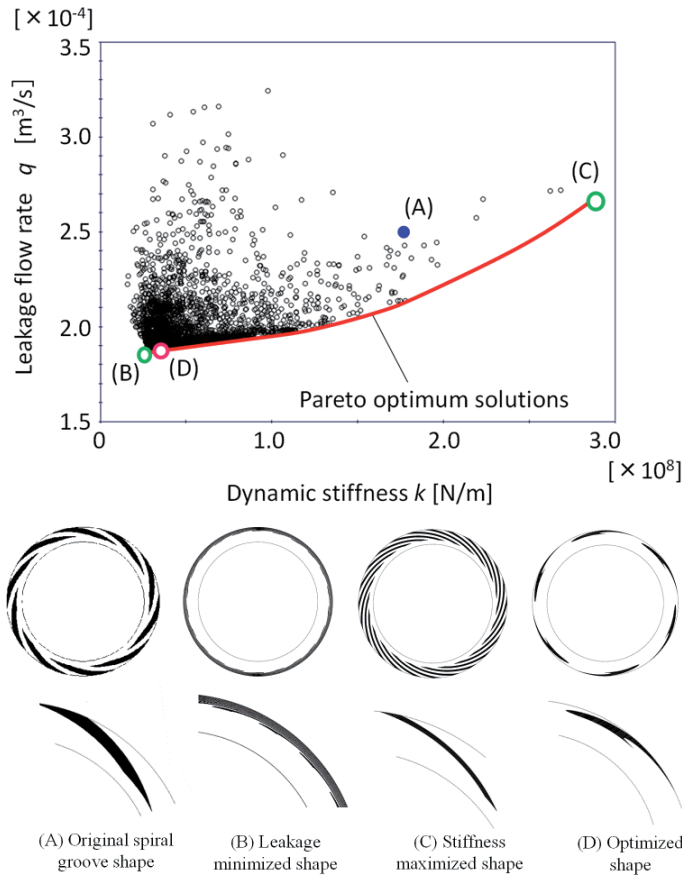


Figure 5.
The case of Pareto optimum solutions ($P_i = 2.5 \text{ MPa}$, $\Lambda = 500$).

Seal shapes	Leakage flow rate q (kg/s)	Dynamic stiffness K (MN/m)
Spiral groove	24.9×10^{-5}	177
Maximum stiffness	26.9×10^{-5}	286
Minimum leakage	18.8×10^{-5}	28.9
Optimized geometry	18.9×10^{-5}	30.5

Table 3.
Characteristic values.

bottom part denotes the Pareto solution curve. Here, the Pareto result means the cloud of optimum solutions from the multi-optimization results. From this result, it is confirmed that there is trade-off relations between the objective functions of gas leakage and the dynamic stiffness. The leakage minimized seal has less dynamic stiffness, whereas the dynamic stiffness maximized seal has inferior sealing characteristic. Therefore, in this study, the allowable dynamic stiffness which means avoiding the contact of the seal surface against the outer disturbance as criteria is set. Because the gas leakage should be reduced as much as possible under a safe operation. Comparing the gas film thickness and the linear impulse response by using the vibration model as shown in **Figure 4**, we can recognize whether the contact occurs or not by outer disturbance. The critical dynamic stiffness can be defined from the criteria. Moreover, in this study, we defined the allowable

dynamic stiffness adopting a safety factor of 3 which means three times of the critical dynamic stiffness. In this manner, the optimized groove shapes as shown in **Figure 5** were obtained and the characteristic values of optimized seals are shown in **Table 3**.

The initial shape of the spiral groove seal labeled (A) does not have the desired characteristics of both low gas leakage and high dynamic stiffness. Comparing the shapes of (A) through (D), from the point of view of minimizing the gas leakage, the shape of the groove is quite different from the initial spiral groove as shown in **Figure 5B**. The optimized shape has a bending curve in the vicinity of the outer diameter of the seal face. On the other hand, from the viewpoint of maximizing the dynamic stiffness, the shape of the groove, as shown in **Figure 5C** is similar to the spiral groove shape in **Figure 5A**. This is because a high positive dynamic pressure is required. It is well known that the spiral groove shape can effectively generate high positive pressure.

Thus, considering an allowable dynamic stiffness, the optimized shape as shown in **Figure 5D** is similar to the shape that minimizes gas leakage with a bending curve. However, the length of the bending curve is no longer that of the leakage minimized seal. This is due to gas flow around the outer vicinity of the gas seal face. The gas flow from the outer high pressure is retarded by the effect of the curved shape of the grooves. From these results, the most interesting thing is that quite a different shape is obtained for the case reducing gas leakage only. However, the results are valid only for the case of $\Lambda = 500$ and inlet pressure $P_o = 1.0$ MPa.

Figure 6 depicts the tendency of change in the shape of the dry gas seal face on the Pareto optimum solution. Orienting the low leakage design, the strong bending shape in the outer vicinity and the wide plane region in the inner side are obtained. This bending shape reduces the leakage to the inner side of the seal by pump-out effect from the inner to the outer circumference side. On the other hand, emphasizing the stiffness design, it is found that the bending tendency goes weak and finally the shape goes to the spiral shape gradually.

From the point of view of the actual seal design, a wider range of operations is required. Therefore, the optimum design calculations were conducted over a wide range of conditions $\Lambda = 100\text{--}750$, inlet pressure $P_o = 1.0\text{--}10.0$ MPa. The inlet pressure is the most important operating condition in a dry gas seal design. On the contrary, the range of compressibility numbers encompasses many operating conditions of rotational speed, film thickness, gas viscosity, and size of seal.

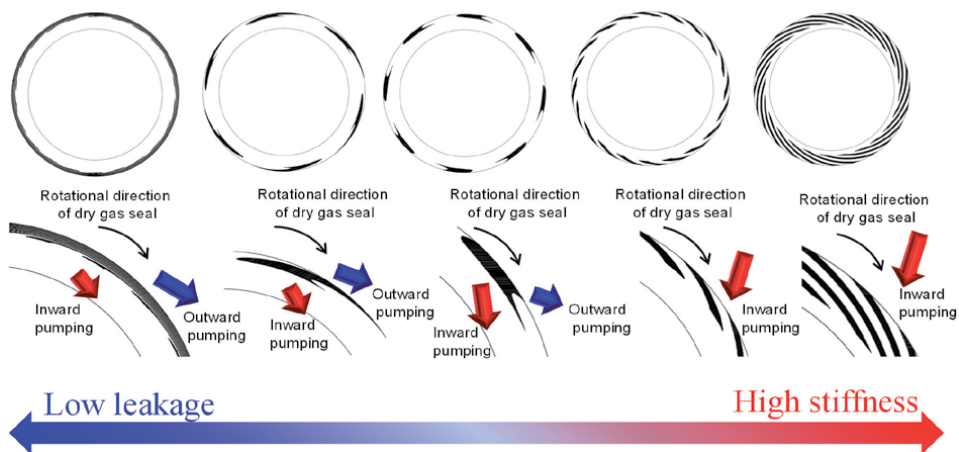


Figure 6.
Change in optimum shape tendency of the dry gas seal face.

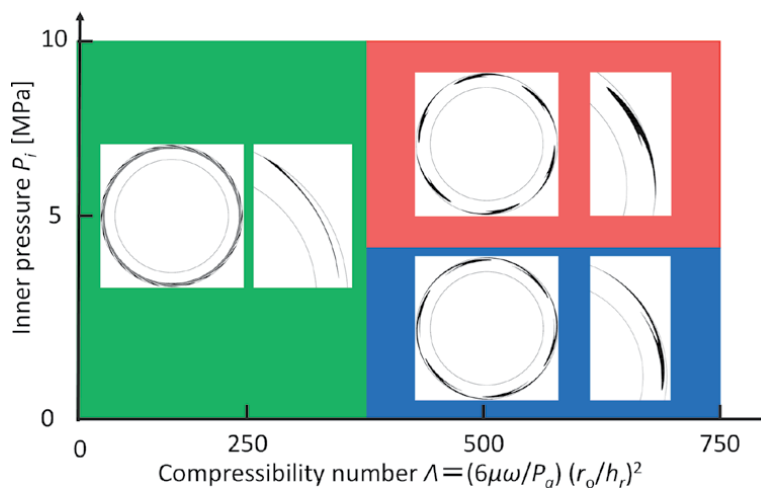


Figure 7.
Optimal design map under a wide range of conditions.

Figure 7 depicts the optimized shape map for a wide range of inner static pressure at the outside diameter and compressibility numbers. There are three types of shapes, one is quite similar to the spiral groove shape and applicable to a low inlet pressure range of $P_o = 1.0\text{--}4.0$ MPa and low compressibility number range of $\Lambda = 10$ to 350. Another shape has a slight bend curve like in **Figure 5B** in the range of $P_o = 1.0$ to 4.0 MPa and $\Lambda = 350$ to 750. The other is a shape having a strong bending curve like in **Figure 5D** for an inlet pressure range of $P_o = 4.0\text{--}10.0$ MPa and over the whole range of Λ .

From the results, in the case of low inner static pressure conditions and a low compressibility number ($\Lambda < 350$), shown in the green color area, it is a required feature of a dry gas seal to enhance its dynamic stiffness. This is due to the ability to generate a dynamic positive pressure on the seal face. Under the conditions of low inlet pressure and high compressibility number, shown in the blue color area, large film thickness, and low viscosity, etc., it is difficult to generate high dynamic pressure on the seal face. Therefore, the grooves are formed to maximize the seal dynamic stiffness.

On the other hand, for a high inlet pressure or a high compressibility number condition, shown in the red area, the allowable film stiffness could be obtained easily as its basic ability. Because the high inlet pressure condition is expected to deliver a hydrostatic effect and the high compressibility number leads to an enhancement of the hydrodynamic effect. Hence, the main object of topological optimization is to reduce gas leakage. However, for a low inner static pressure condition, the hydrostatic effect is not expected. Therefore, the bending curve shape is weak. In other words, it is found that the topological optimization for reducing gas leakage is effective in the case of a high inner static pressure condition.

6. CFD analysis of visualization of the flow and discussions

In order to consider the mechanism for reducing the gas leakage of the optimized shape, which is the interesting bending shape, a CFD analysis of the gas flow was conducted using commercial software (ANSYS FLUENT) which can solve the Navier-Stokes equation including the flow of outer side area of dry gas seal and considered to be obtained more accurate solution compared to usually used

Reynolds equation, which is neglecting the outer side flow of seals. In the past work of Hashimoto[18], a similar bending shape is obtained in the case of maximizing the bearing stiffness on a high-speed air bearing. However, as mentioned in the previous sections, another tendency is obtained in this case. That is, the bending shape is obtained in the case of minimizing the air leakage instead of maximizing the stiffness. Therefore, the reason why this shape is obtained is unclear.

Figure 8 and **Table 4** report the CFD calculation model and the specifications respectively. The inner and outer radii are same as our experimental equipment [21], Moreover, the groove depths and seal clearance of the seals are 60 μm and 30 μm respectively because of their mesh size limitations. The seal radius ratio (R_s/R_o) and Groove width ratios are chosen by representative values for each seal. In addition, **Table 4** indicates the calculation conditions of CFD analysis. The inlet pressure, it means the outer side of the dry gas seal, is set as 0.11 MPa, and the rotational speed is set as 5000 rpm. These values are the same as the previous experiment. The calculations are conducted under the area of one groove pattern by using a periodic boundary condition. In addition, the calculation does not use the turbulent model and concludes choked flow. Because the Reynolds number of the gas seal flow is approximately $Re = 26$, where the representative length is the clearance 30 μm , the representative speed is peripheral speed at an outer radius of 20 m/s. This setting reduces calculation costs. Consequently, the calculation area sizes are not identical (**Table 5**).

Figure 9 shows the predicted (I) pressure distribution and (II) velocity distribution from the CFD analysis on the middle plane of gas film thickness comparing the conventional spiral grooved seal(a) versus the optimized seal(b). In this study,

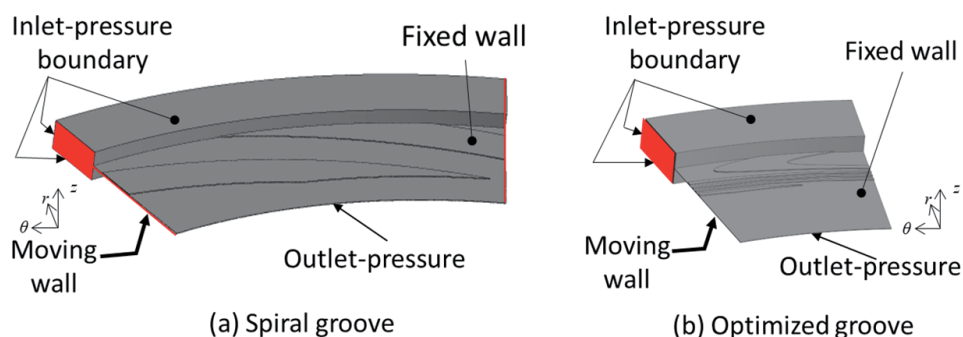


Figure 8.
 CFD analysis model.

	Spiral groove	Optimized groove
Outer radius R_o		32.0 mm
Inner radius R_i		25.6 mm
Groove depth		60 μm
Seal Clearance		30 μm
Seal radius ratio Seal radius ratio (R_s/R_o)	0.5	0.4
Groove width ratio	0.86 μm	0.93 μm
Number of groove	10	24

Table 4.
 Seal specifications of CFD analysis.

Operating conditions	
Inlet pressure	0.11 MPa
Outlet pressure	0.1 MPa
Rotational speed	5000 rpm
Air temperature	300 K
Dynamic viscosity of air	1.85×10^{-5} Pa·s

Table 5.
Calculation conditions of CFD analysis.

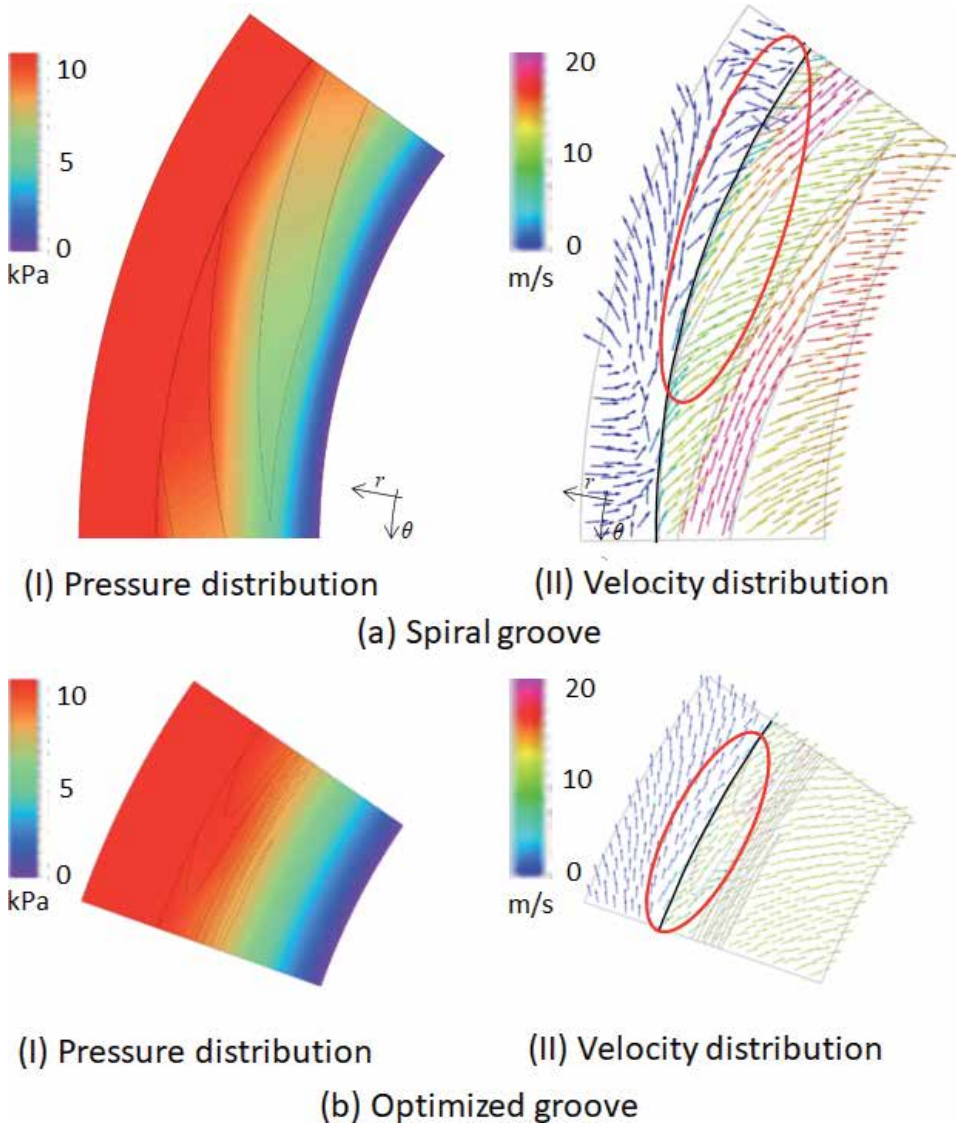


Figure 9.
CFD analysis results of pressure and velocity distributions on grooved seals.

the film thicknesses are common. Therefore, the closing forces are different. In addition, the visualization areas are different in the two seals because the calculation area depends on the groove shape intervals.

From the results in **Figure 9(I)**, high pressure is generated on the outer region of the seal caused by the hydrostatic effect. However, the high-pressure area in the optimized seal is narrow compared with that of the spiral grooved seal. Moreover, the velocities on the flow in the optimized seal are faster than those in the spiral grooved seal. This is due to groove shape in the outer radius vicinity. The groove shape of the spiral groove is formed along the rotational direction. Consequently, outer air is drawn into the seal and the air velocity is fast. On the other hand, with the optimized seal face, the gas flow velocity in the outer vicinity reduces because the inflow is suppressed by the pump effect of the bending shape groove. As mentioned earlier, reducing the gas inlet flow velocity on the optimized seal face leads to reduce the gas overall leakage.

Moreover, comparing both the Reynolds equation and the CFD results of load-carrying capacity and amount of leakage, are shown in **Table 6**. As shown in the Table, the load-carrying capacity is in very good agreement with both results. On the other hand, the amount of leakage, there is a little difference in both analytical solutions. This is because the amount of leakage is calculated using pressure difference and it is easy to include the numerical error. Besides, the load-carrying capacity is calculated by the integration of pressure distribution. Therefore, it is considered that the numerical error is very small. However, the difference in the amount of leakages is acceptable.

Finally, the experimental verification of flow visualization is mentioned. The experimental visualization results are picked up from our past research work [21, 22].

The experimental conditions are same as **Tables 4** and **5**, except the groove depth of 70 μm and the seal clearance of 50 μm . Here, the main purpose of the

		Reynolds Eq.	CFD
Load carrying capacity (kg)	Spiral	0.79	0.76
	Optimized	0.76	0.71
Amount of leakage (10^{-5} kg/s)	Spiral	7.87	8.19
	Optimized	5.70	5.81

Table 6.
 Comparison of Reynolds equation to CFD.

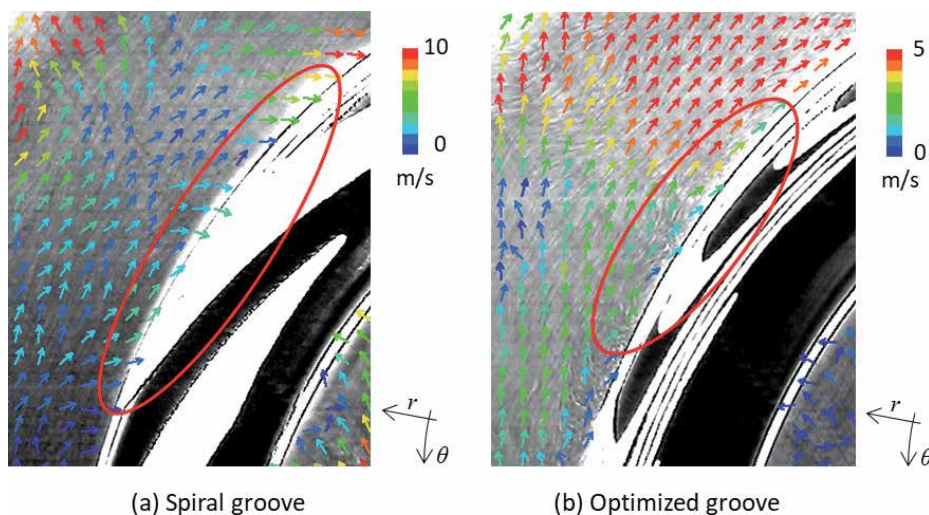


Figure 10.
 Experimental visualization results [21].

verification is to confirm the qualitative flow difference, therefore we think the comparison is meaningful even if the values between the CFD and experimental visualization are not the same. The specific visualization setup and spec are shown in the previous studies.

Figure 10 depicts the experimental visualization results of our previous study [21]. The velocity distributions are shown as color arrows. The outer side gas flows strongly into the spiral groove seal face through the boundary as shown in **Figure 10a**. On the other hand, in the case of optimized seal, the flows are very weak compared to that of spiral groove seal. The same tendencies are shown in the CFD analysis results, and the applicability of the optimization was verified experimentally.

7. Conclusions

In this study, a topological optimization of the groove shape on a dry gas seal is conducted to improve its sealing characteristics. The main conclusions are as follows:

1. The groove shape of the topological optimum design to minimize gas leakage has a bending curve near the outer radius of the rotating seal face. On the other hand, the optimum groove shape when maximizing the gas film stiffness becomes quite similar to that of a spiral grooved shape.
2. For the purpose of obtaining a workable solution over a wide range of operating conditions, an allowable gas film stiffness is adopted. As a result, the optimum shape pattern is similar to that of the spiral groove under conditions of low inner static pressure and low compressibility number. For high inner static pressure and high compressibility number conditions, the outer groove shape bends. The tendency of bending becomes stronger with an increase in the inner static pressure at the outside diameter and the compressibility number.
3. CFD analysis reveals that the inflow velocity in the optimized seal is low compared with that in a conventional spiral groove seal. The newly found outer bending curve shape of the groove leads to suppress the inflow. Moreover, the same tendency is shown in experimental visualization.

Acknowledgements

We would like to express our sincere gratitude to Professor Hiromu Hashimoto for his appropriate suggestions, Professor Luis San Andres for his polite advice, and all the students who have supported this research.

Nomenclature

a	a parameter related to the inflow angle β used to define a spiral curvature
b_1	width of groove [m]
b_2	width of land [m]
c	damping coefficient of gas film [N·s/m]

$f(X)$	objective function [N/m]
$g_i(X)$ ($i = 1 \sim 2n+2$)	constraint function
h_g	groove depth [m]
h_r	gas film thickness [m]
k	spring coefficient of gas film
k_1	spring coefficient of support spring
N	number of grooves
n_s	shaft angular speed [rpm]
p_0	static component of gas film pressure (absolute pressure) [Pa]
p_a	atmospheric pressure at inside diameter [Pa]
P_i	inner side pressure [Pa]
P_o	outer side pressure [Pa]
p_t	dynamic component of gas film pressure [Pa]
q	leakage gas mass flow rate [kg/s]
r	coordinate of radial direction [m]
r_i	inside radius of seal [m]
r_o	outside radius of seal [m]
r_s	inner radius of the grooves [m]
R_s	seal diameter ratio ($= r_s / r_o$)
R_r	ratio between inside radius and outside radius of seal ($= r_i / r_o$)
X	vector of variables used in calculations
α	groove width ratio $= b_1 / (b_1 + b_2)$
β	inflow angle [rad]
Δr	equipartition space of r [m]
θ	coordinate of circumferential direction [rad]
θ_i	angle of basic geometry (spiral curvature) at the i th nodal point [rad]
ϕ_i	extent of angle change from basic geometry (spiral curvature) at the i th nodal point [rad]
$\delta\phi_i$	extent of angle change during optimization at the i th nodal point [rad]
Λ	compressibility number $= 6\mu\omega_s / Pa) * (r_1/h_r)^2$
μ	viscosity of gas [Pa·s]
ρ	density of gas [kg/m ³]
ξ	coordinates of change based on boundary fitted coordinate system [m]
η	coordinates of change based on boundary fitted coordinate system [rad]
ω_f	angular velocity of squeeze motion [rad/s]
ω_s	angular velocity of shaft rotation [rad/s]

Subscripts:

max	maximum value of state variables
min	minimum value of state variables

Author details

Masayuki Ochiai* and Yuki Sato
Department of Mechanical System Engineering, Tokai University, Hiratsuka-shi,
Kanagawa, Japan

*Address all correspondence to: ochiai-m@tsc.u-tokai.ac.jp

IntechOpen

© 2022 The Author(s). Licensee IntechOpen. This chapter is distributed under the terms of the Creative Commons Attribution License (<http://creativecommons.org/licenses/by/3.0>), which permits unrestricted use, distribution, and reproduction in any medium, provided the original work is properly cited. 

References

- [1] Inoue H. State-of-the-art surface texturing on mechanical seals. *Journal of Japanese Society of Tribologists*. 2015; **60**(4):58-61
- [2] Chen HS, Castelli V, Chow CY. Performance characteristics of spiral-groove and shrouded Rayleigh step profiles for high-speed noncontacting gas seals. *Transactions on the ASME: Journal of Tribology*. 1969; **91**(1):60-68
- [3] Green I, Barnsby MR. A simulations numerical solution for lubrication and dynamic stability of noncontacting gas face seals. *Transactions on the ASME: Journal of Tribology*. 2001; **123**(1):388-394
- [4] Miller BA, Green I. Numerical techniques for computing rotordynamic properties of mechanical gas face seals. *Transactions on the ASME: Journal of Tribology*. 2002; **124**(1):755-761
- [5] Wang Y, Wang J, Yang H, Jiang N, Sun X. Theoretical analyses and design guidelines of oil-film-lubricated mechanical face seals with spiral grooves. *Tribology Transactions*. 2004; **47**:537-542
- [6] Faria MTC, San Andrés L. On the numerical modeling of high-speed hydrodynamic gas bearings. *ASME Journal of Tribology*. 2000; **122**:124-130
- [7] Faria MTC. An efficient finite element procedure for analysis of high-speed spiral groove gas face seals. *ASME Journal of Tribology*. 2001; **123**:205-210
- [8] Wang B, Zhang H. Numerical analysis of a spiral-groove dry-gas seal considering micro-scale effects. *Chinese Journal of Mechanical Engineering*. 2011; **24**:186-195
- [9] Harp SR, Salant RF. Analysis of mechanical seal behavior during transient operation. *Transactions on the ASME: Journal of Tribology*. 1998; **120**: 191-197
- [10] Zirkelback NL, San Andrés L. Effect of frequency excitation on the force coefficients of spiral groove gas seals. *ASME Journal of Tribology*. 1999; **121**: 853-863
- [11] Ruan B. Numerical modeling of dynamic sealing behaviors of spiral groove gas face seals. *Transactions on the ASME: Journal of Tribology*. 2002; **124**(1):186-195
- [12] Hong W, Baoshan Z, Jianshu L, Changliu Y. A thermohydrodynamic analysis of dry gas seals for high-temperature gas-cooled reactor. *Transactions on the ASME: Journal of Tribology*. 2013; **135**(2):021701-1-021701-9
- [13] Wang B, Zhang HQ, et al. The flow dynamics of a spiral groove dry gas seal. *Chinese Journal of Mechanical Engineering*. 2013; **26**:78-84
- [14] Lin G, Satomi T. Optimum design and analysis of characteristics of spiral groove thrust air bearing. *Journal of JSME Series C*. 1991; **57**(541):2971-2977
- [15] Hashimoto H, Ochiai M. Theoretical analysis and optimum design of high speed gas film thrust bearings (static and dynamic characteristic analysis with experimental verifications). *JSME Technical Journal, JAMDSM*. 2007; **1**(1): 102-112
- [16] Hashimoto H, Ochiai M. Theoretical analysis and optimum design of high speed gas film thrust bearings (application to optimum design problem). *JSME Technical Journal, JAMDSM*. 2007; **1**(3):306-318
- [17] Hashimoto H, Ochiai M. Optimization of groove geometry for thrust air bearing to maximize bearing stiffness. *Transactions on the ASME: Journal of Tribology*. 2008; **130**(3): 031101

[18] Hashimoto H, Namba T. Optimization of groove geometry for a thrust air bearing according to various objective functions. *Transactions on the ASME: Journal of Tribology*. 2009; **131**(4):1-10

[19] Tabata H, Sano M. Development of high-speed and high-pressure dry-gas-seal. *Design Engineering*. 2009; **44**(3): 45-54

[20] Papadopoulos CI, Efstathiou EE, Nikolakopoulos PG, Kaiktsis L. Geometry optimization of textured three-dimensional micro-thrust bearings. *Transactions on the ASME: Journal of Tribology*. 2011; **133**(4):1-10

[21] Suzuki D, Kodama S, Ochiai M, Sunami Y, Hashimoto H. Visualization experiment of gas flow in dry gas seals. *Journal of Advanced Science*. 2016; **28**: 11005-1-11005-5

[22] Ibrahim MD, Marusman N, Sunami Y, Amran SNA, Musa SS, Ochiai M, et al. Characteristics of modified spiral thrust bearing through geometries and dimension modifications. *Tribology*. 2018; **13**(6): 334-339

Surface Characterization after Blasting

Dagmar Draganovská, Janette Brezinová and Anna Guzanová

Abstract

Blasting modifies the surface state of materials in terms of surface irregularities too. Bearing in mind that the roughness characteristics affect the components functionality, it is essential to study and evaluate the surface state of pretreated materials. The chapter deals with evaluation of relation between individual surface roughness parameters of the blasted surfaces based on the measured values on the surfaces, which were blasted by various types of blasting materials. Based on the analysis of the results were also proposed sets of surface roughness parameters, which can be used in the assessment of the blasted surfaces. These allow you to effectively distinguish differences in roughness of blasted surfaces from the point of view of other follow-up technologies. It also lists the main factors that affect surface roughness.

Keywords: blasting, surface, roughness, blasting abrasive, surface roughness parameters, technological parameters

1. Introduction

The blasting process involves several simultaneously occurring processes. From the point of view of blasting effect on the base material, it is necessary to understand blasting process as the process of surface deformation or elastic-plastic deformation of metal in its full volume.

The quality of blasted surface is characterized by the following features, namely:

- a. The geometrical shape of the blasted surface, which involves the micro-geometry, a surface volume, and the real size of the surface;
- b. The condition of the blasted surface, which involves a plastic deformation, strengthening, a thermal effect, structural changes, changes of mechanical and technological properties, and the residual stresses;
- c. The cleanliness of the blasted surface.

From the point of view of a component function, geometrical properties of a surface are very important in many cases (e.g., in conditions of friction and wear). Therefore it is necessary to put a sufficient emphasis on evaluation of surfaces geometry and the determination of profile deviations from the defined plain [1–4].

From the micro-geometry point of view, surfaces can be divide into:

- oriented surface – in two perpendicular directions has notably different values of roughness (anisotropic surface) and
- non-oriented surface – the roughness and spacing of peaks in two perpendicular directions are not notably different (isotropic surface).

On the basis of the stated facts, it is possible to classify the blasted surface like non-oriented (isotropic) surface, while its creation is mainly conditioned by abrasive particle shape used, **Figure 1**. The selection of a type, size, and shape of blasting material depends on a purpose of newly created surface usage. This selection is the basic issue for the process of blasting.

Juvenile surface, obtained by a blasting process, has a specific character. The micro-geometry of a blasted surface depends on:

- blasted material properties (mainly hardness). A material with a higher roughness will not be during the blasting from the point of view of its surface micro-geometry affected in such amount, as a soft material;
- a type of used blasting material. Blasting abrasives with a high hardness and with a bigger particle size roughen a surface more intensively compared with fine-grained blasting materials. It is evident that during a blasting process with a demand for obtaining a specified roughness, it is necessary to select an adequate combination of blasted material hardness with hardness and particle

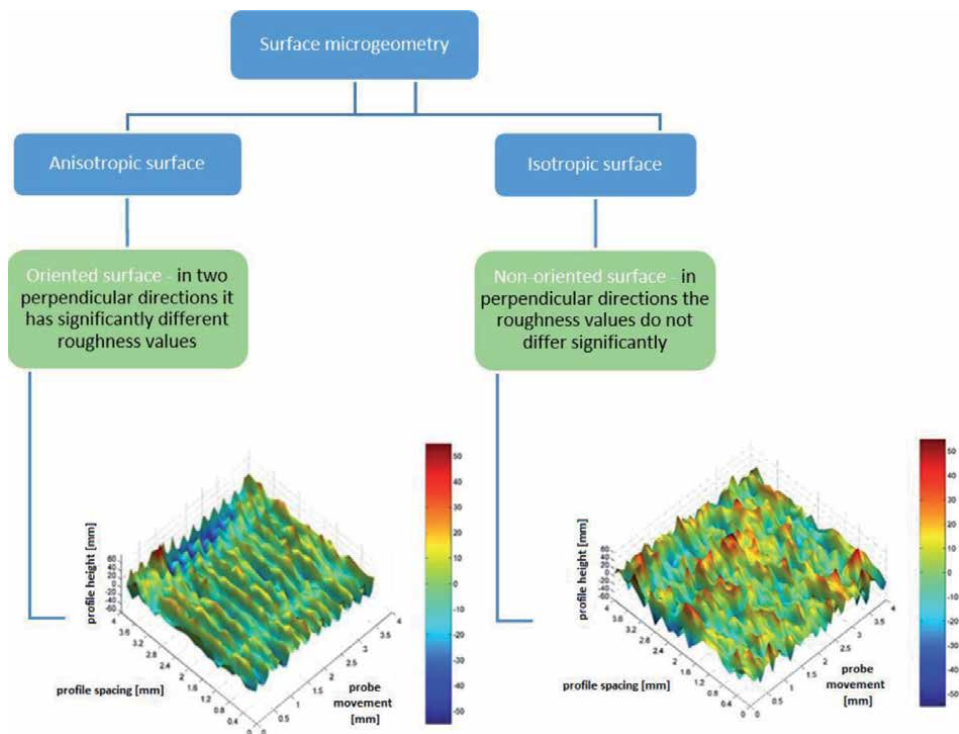


Figure 1.
The classification of surfaces in terms of microgeometry.

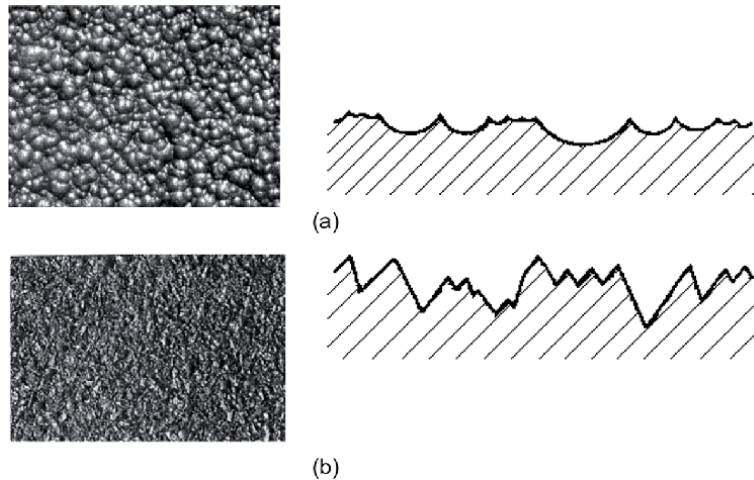


Figure 2.
The surface of metallic substrate blasted by polydispersed (a) shot, and (b) grit.

size of a blasting material. The ratio of hardness of blasting material to a hardness of blasted metal is important from the point of view of surface qualitative affection as well as in terms of removal of base material;

- blasting parameters. In selection of blasting material type, blasting parameters are also important. The same blasting material creates various surface roughnesses in the different blasting parameters (an abrasive speed, an impact angle, etc.) [5–7].

Blasting abrasives are loose materials of granular nature consisting of different large particles (polydispersion). There are mainly two types of blasting media used—metallic and nonmetallic ones. Metal blasting abrasives can be in three different forms:

- blasting abrasive of spherical shape, known as shot,
- blasting abrasive of irregular sharp shape – grit,
- blasting abrasive of a roller shape, its height is equal to its diameter – chopped wire.

The shape of particle of blasting abrasives used determines the resulting surface relief [4, 8, 9]. Surface has rounded small peaks after the blasting with grit or sharp notches after grit, **Figure 2**.

2. The evaluation of blasted surfaces roughness

Functional properties of areas are dependent on the various surface properties and subsurface layers of a base substrate. One of the criteria concerning the quality of products in terms of production genesis is their geometric and dimensional accuracy, then the surface quality, particularly its roughness. The ISO plan was created for such a purpose creating the structure of necessary norms and standards for the area of “Geometrical specification of products.”

From the point of view of a component function, geometrical properties of a surface are very important in many cases (e.g., in conditions of friction and wear). Therefore, it is necessary to put a sufficient emphasis on the evaluation of surfaces geometry and the determination of profile deviations from the defined plain [10–13].

The experimental analysis used various blasting materials [5]:

- steel grit (SG) – angular type blasting material is produced by crushing specially treated steel shot. The advantage of this abrasive lies in its durability and impact resistance. Chemical composition: C – 0.75–1.20%, Mn – 0.60–1.10%, Si – 0.60–1.10%, P – max 0.04%, S – max 0.04%.
- steel shot (SS) – is made from hypereutectoid specially processes steel. It has fine homogeneous structure of tempered martensite, which exhibits optimal resilience and resistance to fatigue. Chemical composition: C – 0.75–1.20%, Mn – 0.60–1.10%, Si – 0.60–1.10%, P – max 0.04%, S – max 0.04%.
- brown corundum (BC) – is very aggressive and hardest material used for blasting. It is made by fusing bauxite in the induction furnace at a temperature of 1600°C. It is used for cleaning steel or gray cast iron, the removal of the tip of refined steel, the processing of wood and plastic, rust removal, roughening, tarnishing. Despite its mineral nature it is not silicogenic. Chemical composition: Al_2O_3 – 95.50% min, SiO_2 – 1.40% max, Fe_2O_3 – 0.60% max, CaO – 0.40% max, TiO_2 – 1.80–2.80%.

The type of material whose surface has been subjected to the surface roughness analysis was the steel plate S235JRG2 (EN 10025), thickness 2 mm. It is a non-alloy high-quality structural steel, it can be cold formed and after subsequent normalization even in heat, it is suitable for welding. Chemical composition: C – 0.19% max, Mn – 1.50% max, P – 0.045% max, S – 0.045% max, N – 0.014% max. The dimensions of the testing samples were 100 × 30 mm.

The blasting was pneumatic air-blast device by equipment TJVP 320, producer Škoda, Plzeň, Czech Republic. The samples were blasted with abrasives at working pressure of 0.6 MPa, nozzle diameter was 1.2 mm, blasting angle 75° and the distance of the nozzle from the substrate was 200 mm.

2.1 2D surface roughness parameters and characteristics of blasting surface

The basis of measurement 2D surface roughness parameters and characteristics of surface – the planer evaluation (in direction x – y) is a unit of length (μm). ISO 4287:1997 standard – nowadays the valid international standard defines terms and surface roughness parameters. In this standard, the calculating system for the evaluation of surface roughness parameters is based on the system of the mean line of the roughness profile, the waviness, and the mean line of the primary profile.

2D roughness measurement is often performed using a contact profilometer SurfTest SJ – 301, Mitutoyo, Tokyo, Japan. Settings in roughness measurement:

- a measured profile: R,
- a filter: GAUSS,
- a sampling length l (λc): 2.5 mm,
- a number of sampling lengths: $N = 5$,

- an evaluation length l_n : 12.5 mm,
- a number of measured profiles: 20.

The probe stylus of a device is in direct contact with the evaluated surface, **Figure 3**.

The sharp stylus of the profilometer sensor converts the distribution on the surface roughness on mechanical movement, which is then processed by the sensor into an electrical signal and further interpreted as the numerical value of the selected surface roughness parameters of micro-geometry, as well as the graphic record of the surface roughness profile – profilograph.

The some important surface roughness parameters of ISO 4287:1997 are:

- R_a – Arithmetical mean deviation of the assessed profile—indicates the average of the absolute value along the sampling length, **Figure 4**.
- R_z – Maximum height of the profile—indicates the absolute vertical distance between the Maximum profile peak height and the Maximum profile valley depth along the sampling length, **Figure 5**.
- R_{Sm} – Mean width of the profile elements—indicates the average value of the length of the profile element along the sampling length, **Figure 6**. X_{si} is the length of a single profile element.

In **Table 1**, values of averages of selected surface roughness parameters of blasted surfaces using various blasting materials are listed as steel grit (SG) with

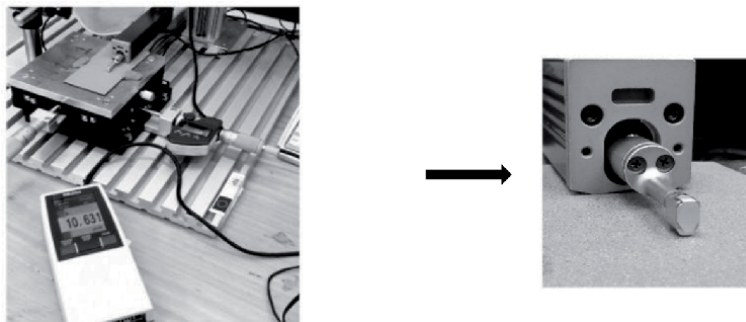


Figure 3.
The contact between a profilometer stylus and measured surface.

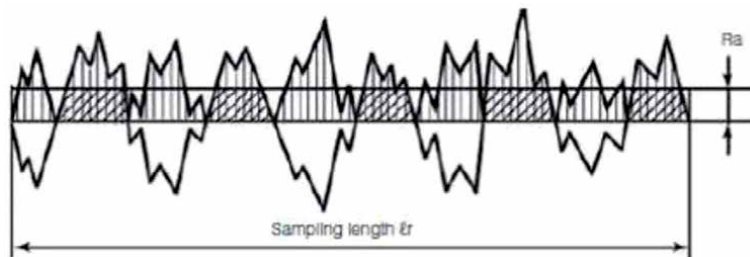


Figure 4.
Arithmetical mean deviation of the assessed profile R_a .

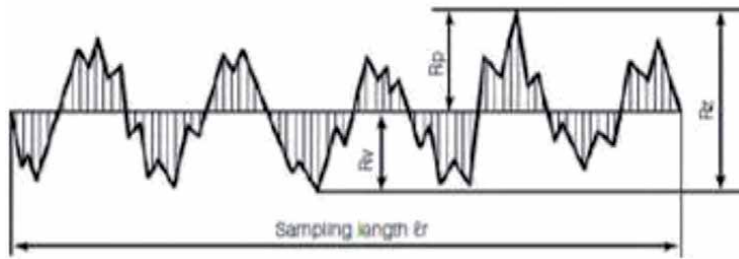


Figure 5.
Maximum height of the profile Rz .

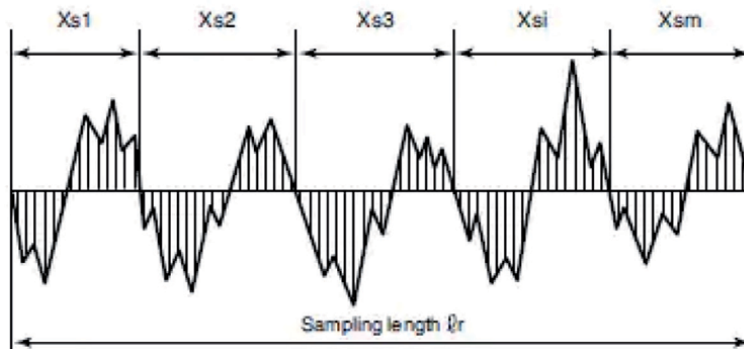


Figure 6.
Mean width of the profile elements RSm .

Blasting materials	Ra (μm)	Rz (μm)	RSm (μm)	RPc (–/cm)
SS 0.9	11.22 (± 0.87)	60.79 (± 4.54)	642.70 (± 72.27)	15.88 (± 2.15)
SG 0.71	10.91 (± 0.68)	68.70 (± 6.62)	355.05 (± 45.12)	28.60 (± 4.08)
BC 0.9	11.43 (± 0.96)	70.29 (± 7.12)	339.45 (± 39.25)	29.21 (± 3.95)

Table 1.
Arithmetic average of surface roughness parameters of blasted surfaces [5].

particle size $dz. = 0.71$ mm, brown corundum (BC) $dz. = 0.9$ mm, and steel shot (SS) $dz. = 0.9$ mm. The arithmetic average was calculated from 20 measured.

For all the evaluated surfaces, a comparable surface roughness parameter Ra was achieved; however, values of other surface roughness parameters (Rz – maximum height of profile, RSm – mean width of the profile elements, RPc – peak count per a length unit) are different, and it depends on used type of a blasting material. Individual profiles with material ratio curves of blasted surfaces also show differences between the surfaces, **Figure 7**.

Differences in the micro-geometry of surfaces blasted by BM of different shape (rounded and sharp-edged) are concisely expressed by profilographs and material ratio curves (Abbot Firrestone curves), **Figure 7**. By comparing the material ratio curves of the assessed profile it is possible to explain the difference between surfaces blasted by sharp-edged and rounded blasting material and therefore by the course of material ratio curve in upper level of cut (cca 40%). Bigger material portion in the

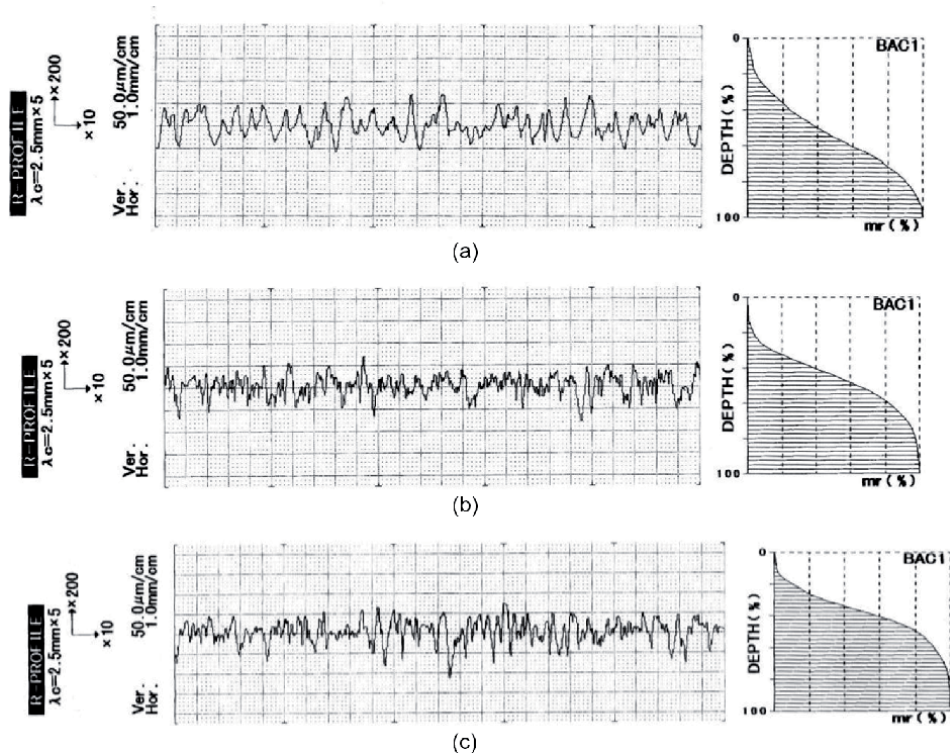


Figure 7.

The profiles of surfaces blasted with different blasting materials [5]. (a) the profilograph of a surface blasted by steel shot, (b) the profilograph of a surface blasted by steel grit, and (c) the profilograph of a surface blasted by brown corundum.

level is achieved at surfaces which are blasted by sharp-edged devices, what creates more suitable conditions for good anchoring of subsequently applied coatings.

The shape of valleys at surfaces blasted by sharp-edged blasting materials also play a notable role (formation of wedge or anchor profile elements) in anchoring the coatings into more rugged and more heterogeneous reliefs regarding the shape, which are achieved for those surfaces.

In the complex appraisal of the blasted surfaces micro-geometry an evaluation by a set of chosen surface roughness parameters is necessary. According to the analysis, the most suitable surface roughness parameters are:

- Ra – Arithmetical mean deviation of the assessed profile,
- Rz – Maximum height of the profile,
- RSm – Mean width of the profile elements (eventually RPC – the peak count per the unit of length),
- The material ratio curve of the profile (Abbot Firrestone curves).

By the combination of those surface roughness parameters it is possible to expertly distinguish differences in micro-geometry of blasted surfaces, what is important in terms of further technologies, which led to their creation [11, 14].

2.2 3D surface roughness parameters and characteristics of blasting surface

The complex information about a surface is possible to gain by three-dimensional, therefore spatial, measuring of the surface profile. Spatial 3D surface characteristics allow, compared with flat 2D characteristics, to evaluate and define a surface more detail.

Spatial measuring and evaluation of a surface 3D, brings very valuable and practically usable information about relations between geometrical characteristics of a surface and its functional properties. Fast development of measuring technique and control software will nowadays allow implementing advantages of 3D evaluation for a surface texture. Spatial measuring of a surface micro-geometry in comparison with 2D evaluation of a single profile assures more objective presentation of the whole surface with notably bigger statistical meaning of obtained characteristics. Individual spatial surface roughness parameters of a texture are calculated from considerably bigger amount of data.

Data for spatial evaluation of the surface texture are possible to obtain either by a contact measurement (scanning of a set of normally parallel profiles) or by the optical technique. Optical devices use scanning ray, which monitors a surface similarly as a contact scanner or defined viewing field of a microscope.

Nowadays a variety of devices are available (contact and optical) using which it is possible to measure also a surface texture. Differences in measurement are given by various principles of scanning systems, varied precision of measurement, and also interaction of devices and controlled surface. Difference in results is also affected by the methodology of verification of devices properties and their calibration.

ISO 25178 norm is a norm for spatial texture of 3D surface. Measuring and elaboration of notably bigger amount of data, which describe a spatial surface profile, bring a huge amount of information for a real presentation of the controlled surface.

Practical result of implementation of the norm is not only a contribution for the selection of suitable surface roughness parameters of surface structure evaluation, but also a preparation of measuring and analyzing devices of a quantitative control of surface structure. Advantages of spatial evaluation show that they are progressive metrological methods. Not only increasing requirements on precision and quality of existing production technologies, but also the development of new materials and technological methods will undoubtedly contribute for their wider practical utilization.

A 3D study of blasted surfaces of different types of blasting abrasives (shot and grit types) in a contact way is shown in **Figure 8**.

The creation of a 3D surface texture by the contact method was realized using the SurfTest SJ – 301 stylus profilometer, Mitutoyo, Japan. The measured research area was 4×4 mm. The resulting spatial image of the surface is then created in such a way that the profile curves and their data in the parallel direction at a defined scanning distance are recorded by the scanning tip of the profilometer and subsequently joined by the software. The method is applicable if the workplace has only a 2D roughness meter. The disadvantage of the method is its time-consuming compared to contactless evaluation.

3D imaging of blasted surfaces was performed by the non-contact method with a confocal laser microscope Olympus LEXT OLS 3000, **Figure 9**. The measured research area was 1.25×1 mm, the profile height is presented on the Z axis.

It is a highly accurate 3D measurement in real time and a reliable evaluation of profiles, which is based on the illumination of the sample with a laser beam,

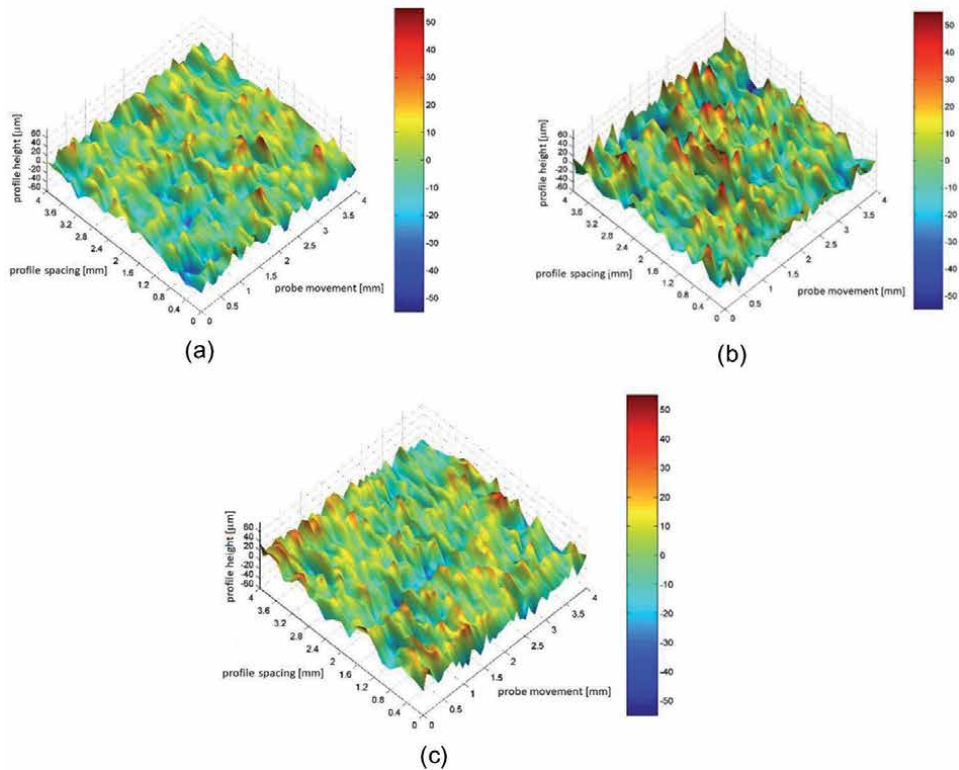


Figure 8. 3D imaging blasted surfaces by contact method. (a) 3D surface blasted by steel shot, (b) 3D surface blasted by steel grit, and (c) 3D surface blasted by brown corundum.

which is focused on one point. This eliminates noise caused by unwanted light, resulting in better image quality.

The performed measurements show that noncontact method is sensitive enough for imaging blasted surfaces. Compared with the contact method, the contactless method is less time-consuming, but the device itself is more expensive compared with the conventional roughness tester.

At a mutual visual comparing of assessed surfaces, **Figures 8** and **9**, a difference is visible in a character of surfaces blasted by various blasting materials. At such types an uneven surface is reached, resulting by an incidental fall of particles—blasting abrasives. A surface blasted by a sharp blasting abrasives—steel and corundum grit does not show such uniformity as at blasting by round particles—steel shot. Notches are on the surface in a various orientation, intersected mutually and a notable part of holes and juts is sharp. From utilized sharp blasting materials, the most segmented surface was detected at the surface blasted by a steel grit. At blasting by round blasting abrasives—a steel shot, more uniformed surface modification was achieved, which is created by intersected round juts.

By realized measurements and 3D visualization of blasted surfaces a presumption was proved that abrasive particles make after the fall in a base material their prints which are dependent on their shape and size, by which a detection of surface complexity was achieved—thus its various segmentation. The particle shape of blasting abrasives (round or angular) has thus a notable effect in the process of blasting and is one of the attributes for an achieved microgeometry of blasted surface and further characteristics as well.

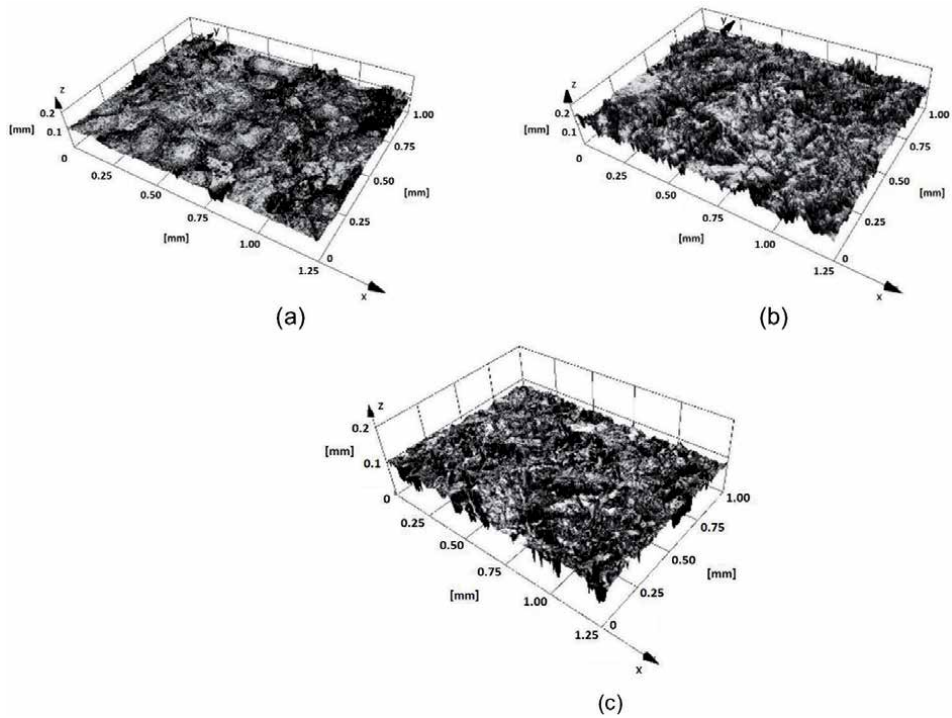


Figure 9. 3D imaging of blasted surfaces by the non-contact method. (a) 3D surface blasted by steel shot, (b) 3D surface blasted by steel grit, and (c) 3D surface blasted by brown corundum.

3. Influence of blasting abrasive and technological parameters on the roughness of blasted surface

The main factors that may affect the quality and thus the roughness of the blasted surface are as follows:

- the abrasive shape and particle size,
- the abrasive hardness,
- the abrasive particle size distribution,
- the blasting process parameters—abrasive velocity, blasting distance, impact angle, hardness of substrate [5].

3.1 Impact of abrasive shape

The nature of blasted surface depends on the shape of abrasive used. When using round particle of blasting abrasive (shot), relatively uniform deformation of the surface is achieved. The surface consists of intersecting spherical dimples, **Figure 18a**. Sharp angular particles of abrasive (grit) cause notches in the substrate whose orientation on the surface is stochastic. Particles in their random movement in the stream of abrasive can impact the surface by their edge, straight surface or tip, **Figure 10**.

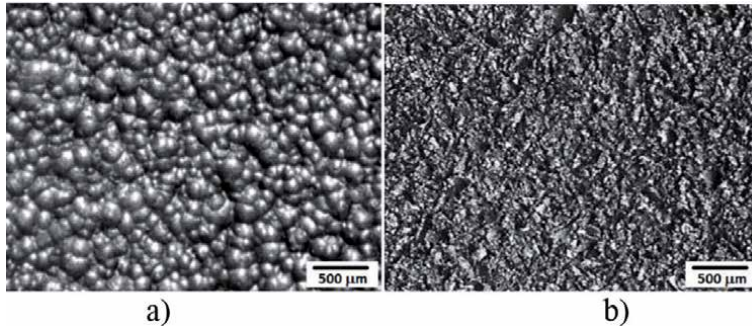


Figure 10.
Surface of mild steel after blasting after the impact of (a) round, and (b) sharp angular blasting abrasive.

3.2 Impact of abrasive particle size

Large particles concentrate significant impact energy at the point of impact while their effect depends on the use of this impact energy. Impacting particle causes not only local disintegration of oxide layer but also significantly hammers the substrate. The effect on the substrate is reflected mainly in its plastic deformation and corresponding work-hardening, or depending on the impact angle also the removal of the substrate occurs. With larger particles of abrasive a higher surface roughness is achieved, but also a greater amount of blasting abrasive is required for complete surface coverage.

Small particles, on the other hand, have smaller kinetic energy which is consumed mainly for removal of scale layer from the surface and it has less influence on the substrate. Smaller particles require lower necessary quantities and the surface is smoother and evenly covered. Surfaces blasted by different particle sizes of blasting abrasives are shown in **Figure 11**.

3.3 Impact of abrasive hardness

Impact of abrasive hardness on the substrate is reflected in character of blasted surface. Impact of substrate hardness is suppressed when blasting by very hard abrasives. When selecting blasting abrasive for pretreatment of the substrate, the following principle applies: selected abrasive must be softer than the material to be retained after blasting but it has to be harder than the material that is meant to be removed by blasting.

3.4 Impact of abrasive particle size distribution

The homogeneity of particle size distribution affects the appearance and roughness of the blasted surface. The narrower is the particle size distribution, the more marked is the surface relief. In wide particle size distribution the characteristic surface relief is not so marked.

The appearance of surfaces blasted by poly-dispersed mixtures of blasting abrasives (steel shot and chilled iron grit) is shown in **Figure 12** [5].

3.5 Impact of abrasive velocity

From **Figure 13**, it is clear that the higher the velocity of the particle, the higher the roughness of the substrate and the less the blasting abrasive necessary to cover

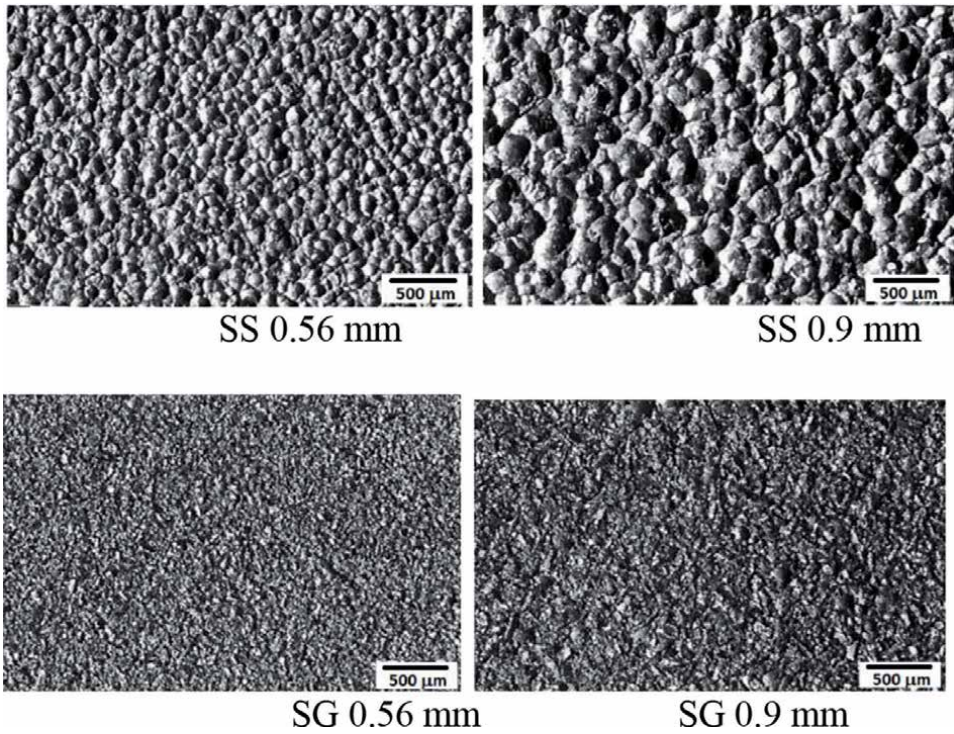


Figure 11. Surfaces of mild steel blasted by different particle sizes of blasting abrasives (SS – Steel shot, SG – Steel grit) [6].

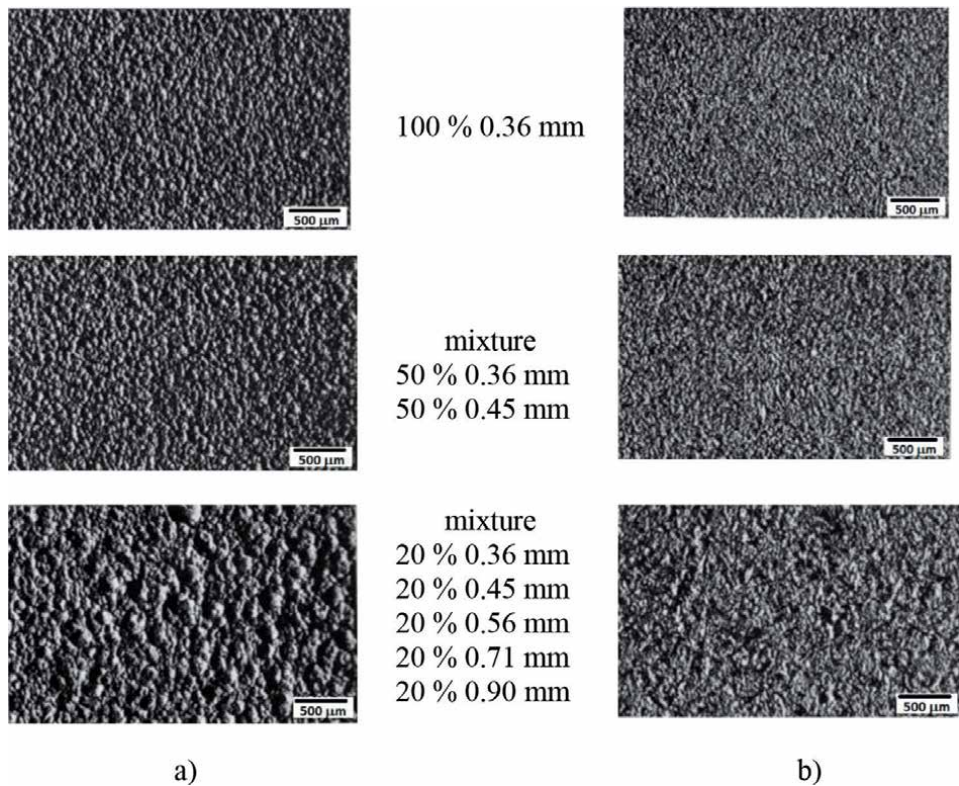


Figure 12. The appearance of mild steel surfaces blasted by polydispersed mixtures of (a) steel shot, and (b) iron grit [5].

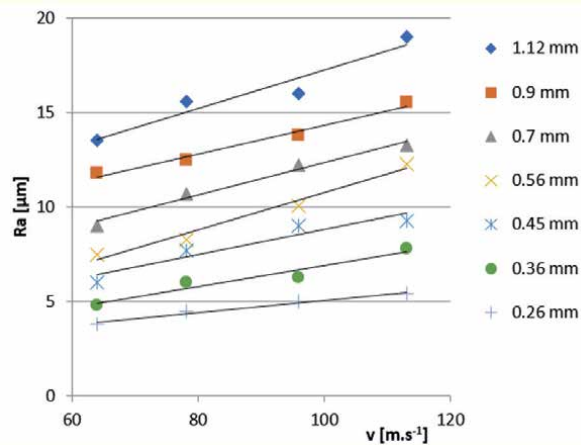


Figure 13.
Dependence of Ra on particle velocity v at various particle sizes [5].

a certain substrate area. To achieve high quality of surfaces one chooses greater blasting velocity for a larger abrasive particle size and less blasting speed for smaller particle size [5].

3.6 Impact of blasting distance

The effect of nozzle-substrate distance on surface roughness is not clearly determined. While some tend to believe that the distance of the nozzle from the surface does not affect the resulting surface roughness, others have found a clear, almost a linear, increase in roughness with an increasing nozzle-substrate distance. It has been found that nozzle-substrate distance affects the final roughness only when a specific distance is exceeded. The value of the specific distance depends on air pressure, for instance for a pressure of 0.4 MPa, the critical distance is 250 mm. It is possible to determine an optimal nozzle – substrate distance for achieving the maximal Ra. This optimal distance depends on the hardness of the substrate, **Figure 14**. As abrasive blasting material used corundum with grain size 1.4 mm. It is very aggressive and hardest material used for blasting (more than 9 Mohs scale).

For materials with higher hardness the optimal range of nozzle-substrate distance is wider. At a distance greater than the optimal, less kinetic energy of the impacting particles causes a decrease in roughness.

3.7 Impact of hardness of substrate

Figure 15 shows that with increasing hardness of substrate at constant blasting conditions a decrease in blasted surface roughness occurs [6].

Depending on the combination of substrate and abrasive hardness, four different states can occur:

- a. abrasive and substrate are relatively soft – deformation of both occurs,
- b. abrasive is relatively soft, substrate is relatively hard – abrasive deformation is significant, substrate will be polished,
- c. abrasive is relatively hard, substrate is relatively soft – substrate is fully covered by notches or dimples,

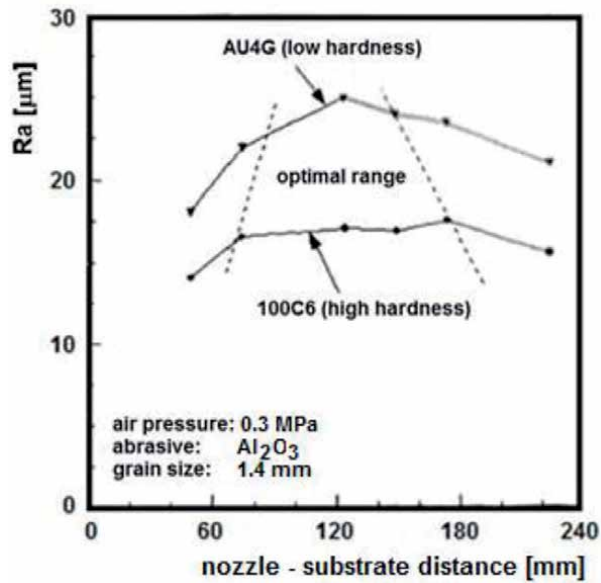


Figure 14. Influence of nozzle-substrate distance on surface roughness for substrates with low and high hardness; optimal range of blasting distance indicated by dotted line [5].

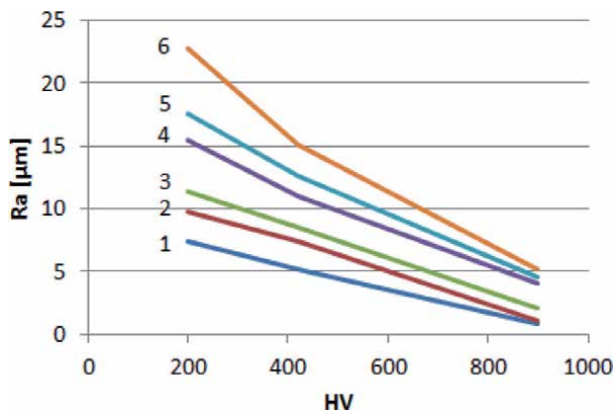


Figure 15. Dependence of blasted surface roughness Ra on the substrate Vickers hardness (HV) for different abrasive particle sizes [6] (1 – Low particle size, 6 – High particle size).

d. both abrasive and substrate are relatively hard – intense fragmentation of the blasting particle material occurs with only little roughening of substrate.

The resulting surface morphology is determined by the type of substrate, material of blasting abrasive and blasting conditions.

3.8 Impact of blasting angle

Blasting angle α for air blasting is characterized as the angle between the surface of the substrate and blasting stream (**Figure 16a**) or for a mechanical blasting it is the angle between the trajectory of particles flying out of blasting wheel and the substrate (**Figure 16b**).

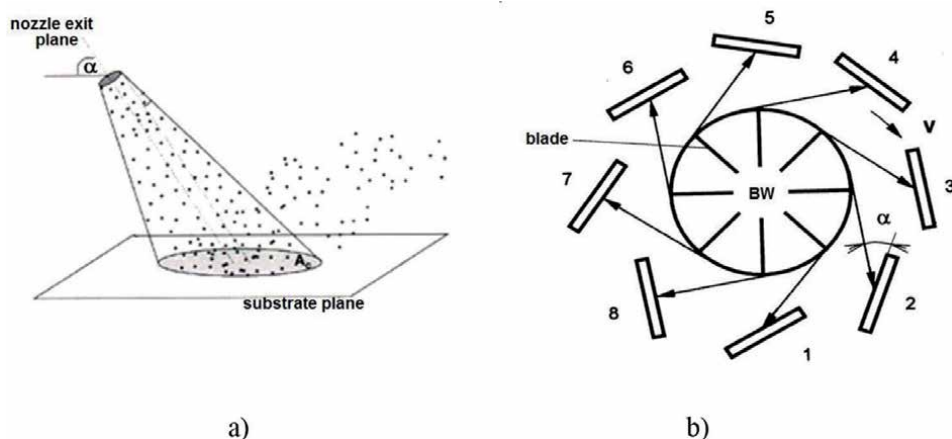


Figure 16. Depiction of blasting angle for (a) air blasting, and (b) mechanical blasting (BW – Blasting wheel, v – Abrasive speed, 1–8 blasted samples positioned around blasting wheel).

Blasting angle affects changes caused by the impact of blasting abrasive. During blasting, either mechanism of creating indentations or removal or grooving mechanism prevails. If the blasting angle is less than 45° , the grooving effect of abrasive prevails and the length of the grooves is higher, the smaller the blasting angle is. The surface of the substrate with grooves does not lead to good strength of bonded joints. At a blasting angle of 75° removal mechanisms prevail and the resulting surface is roughened containing many sites suitable for mechanical anchoring of the adhesive. At a blasting angle of 90° indentation mechanism prevails and the resulting surface is not suitable for mechanical anchoring of the adhesive.

Values of roughness along the blasted area are not constant. In the middle of the track, roughness reaches the highest value due to the fact that the stream of accelerated particles is stable there. At the periphery of the track, the particles are deflected from their trajectory by other particles bounced back from substrate, and moreover the roughness values are smaller **Figure 17**.

The change in surface roughness at different impact angles is shown in **Figure 18**. At an impact angle of 75° Ra value of the surface is maxim. The impact angle of 75° is an optimum angle at which the maximum material is removed, and cleaning and roughening occurs with minimum consumption of abrasive [5].

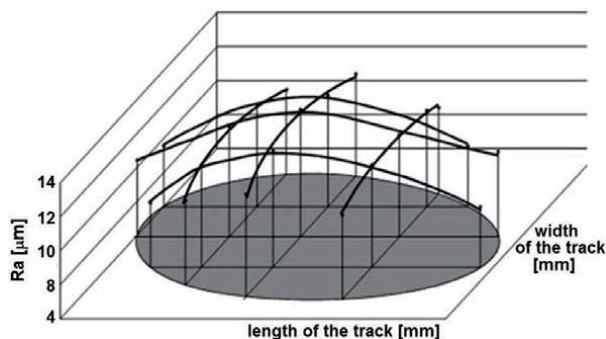


Figure 17. Distribution of surface roughness in affected area (steel grit, blasting angle 30° , particle size 0.9 mm).

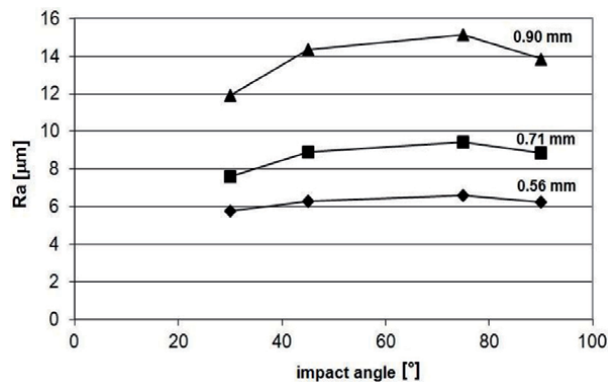


Figure 18.
Dependence of R_a on impact angle of steel grit with different particle sizes [5].

4. Conclusions


The production history of materials leaves characteristic features on the surface that affect their behavior during other technological processes. This chapter is focused on the issue of morphological changes that occur on surfaces after abrasive blasting. These changes in terms of roughness need to be monitored as accurately as possible with the whole set of surface roughness parameters, not only from a 2D but also a 3D perspective. This gives a comprehensive view of the blasted surface. At the same time, the factors that contribute to these changes must be taken into account. These are mainly the technological conditions of blasting and the type of blasting abrasive. By their suitable choice, it is possible to achieve the most suitable surface pretreatment by abrasive blasting with the required morphological, tribological, and other properties.

Author details

Dagmar Draganovská*, Janette Brezinová and Anna Guzanová
Faculty of Mechanical Engineering, Department of Technology, Materials and
Computer Supported Production, Technical University of Košice, Košice, Slovakia

*Address all correspondence to: dagmar.draganovska@tuke.sk

IntechOpen

© 2022 The Author(s). Licensee IntechOpen. This chapter is distributed under the terms of the Creative Commons Attribution License (<http://creativecommons.org/licenses/by/3.0>), which permits unrestricted use, distribution, and reproduction in any medium, provided the original work is properly cited. 

References

- [1] Draganovská D, Ižaríková G, Guzanová A, Brezinová J. General regression model for predicting surface topography after abrasive blasting. *Metals*. 2018;**11**:1-20. DOI: 10.3390/met8110938
- [2] Whitehouse DJ. A new look at surface metrology. *Wear*. 2009;**266**:560-565. DOI: 10.1016/j.wear.2008.04.058
- [3] Kirk D. Theoretical principles of shot peening coverage. *Shot Peener*. 2005;**19**:24-26
- [4] Nouguié-Lehon C, Zarwel M, Diviani C, Hertz D, Zahouani H, Hoc T. Surface impact analysis in shot peening process. *Wear*. 2013;**302**:1058-1063. DOI: 10.1016/j.wear.2012.11.031
- [5] Brezinová J, Guzanová A, Draganovská D. Pretreatment of Surface – Theory and Practice. 1st ed. Košice: Technical University of Košice; 2012. p. 240
- [6] Jankura D, Brezinová J, Ševčíková J, Draganovská D, Guzanová A. Materials in Mechanical Engineering and Technology of their Finalization. 1st ed. Košice: Technical University of Košice; 2011. p. 378
- [7] Momber A. Blast Cleaning Technology. 1st ed. Berlin Heidelberg: Springer-Verlag; 2008. p. 540. DOI: 10.1007/978-3-540-73645-5
- [8] Miao HY, Demers D, Larose S, Levesque M. Experimental study of shot peening and stress peen forming. *Journal of Materials Processing Technology*. 2010;**210**:2089-2102. DOI: 10.1016/j.jmatprotec.2010.07.016
- [9] Kirk D. Hardness matters. *Shot Peener*. 2019;**33**:28-38
- [10] Draganovská D, Ižaríková G, Guzanová A, Brezinová J. The study of parameters of surface roughness by the correlation analysis. *Materials Science Forum*. 2015;**818**:15-18. DOI: 10.4028/www.scientific.net/MSF.818.15
- [11] Bačová V, Draganovská D. Analyses of the quality of blasted surfaces. *Materials Science*. 2004;**1**:125-131. DOI: 10.1023/B:MASC.0000042795.54319.a5
- [12] Cammett J: Shot peening process optimization: A cost-effective means of improving component life and performance. *Shot Peener*. 2018;**32**: 10-14
- [13] Zhu H, Ge S, Huang X, Zhang D, Liu J. Experimental study on the characterization of worn surface topography with characteristic roughness parameter. *Wear*. 2003;**255**:309-314. DOI: 10.1016/S0043-1648(03)00215-1
- [14] Bagherifard S, Ghelichi R, Guagliano M. Numerical and experimental analysis of surface roughness generated by shot peening. *Applied Surface Science*. 2012;**258**: 6831-6840. DOI: 10.1016/j.apsusc.2012.03.111

Tribological Performance of Random Sinter Pores vs. Deterministic Laser Surface Textures: An Experimental and Machine Learning Approach

Guido Boidi, Philipp G. Grützmacher, Markus Varga, Márcio Rodrigues da Silva, Carsten Gachot, Daniele Dini, Francisco J. Profito and Izabel F. Machado

Abstract

This work critically scrutinizes and compares the tribological performance of randomly distributed surface pores in sintered materials and precisely tailored laser textures produced by different laser surface texturing techniques. The pore distributions and dimensions were modified by changing the sintering parameters, while the topological features of the laser textures were varied by changing the laser sources and structuring parameters. Ball-on-disc tribological experiments were carried out under lubricated combined sliding-rolling conditions. Film thickness was measured *in-situ* through a specific interferometry technique developed for the study of rough surfaces. Furthermore, a machine learning approach based on the radial basis function method was proposed to predict the frictional behavior of contact interfaces with surface irregularities. The main results show that both sintered and laser textured materials can reduce friction compared to the untextured material under certain operating conditions. Moreover, the machine learning model was shown to predict results with satisfactory accuracy. It was also found that the performance of sintered materials could lead to similar improvements as achieved by textured surfaces, even if surface pores are randomly distributed and not precisely controlled.

Keywords: lubrication, friction reduction, laser surface texturing, sintered material, machine learning

1. Introduction

The surface topography of mechanical components is often modified to improve their tribological performance, such as cylinder liner honing in internal combustion engines [1] and laser surface texturing in piston-rings [2, 3], rolling element bearings [4], and journal- and thrust bearing systems [5].

Surface textures can promote several tribological improvements. Surface cavities can reduce abrasive wear in harsh contact conditions by retaining wear and

contaminant particles (debris trapping effect), as well as work as micro-reservoirs and secondary oil suppliers (oil reservoir effect) [6]. Under mixed and (elasto) hydrodynamic lubrication, friction can be reduced by the interplay of different mechanisms, such as the (i) micro-hydrodynamic bearing (boosting in the fluid pressures due to the texture-induced cavitation at the divergent regions of the textures) [7], (ii) inlet suction (lubricant sucking into the interface due to the difference between the supply pressure and the cavitation pressure) [3, 8, 9], and (iii) shear-area variation (decrease of the fluid and contact shear stresses over the contact area) [10] mechanisms. Furthermore, under boundary and mixed lubrication regimes, textures can influence the sealing performance and percolation behavior. The reader is referred to the comprehensive reviews [4, 11–14] for a more in-depth evaluation of several aspects of surface texturing for tribological improvements.

The tribological effects of surface texturing were first studied in the 1960s by Hamilton's and Anno's research groups [15, 16]. Afterwards, this topic covered a marginal role in the tribological community until the 1990s, when Etsion and co-workers re-discovered its potential impact [17, 18], also in the context of improved manufacturing techniques. In recent years, the interest in research on surface texturing, mainly laser texturing, has significantly increased [11] as some texture configurations have shown significant tribological improvements in various machine elements [2, 19–21].

The design of effective surface textures requires a thorough understanding of the tribosystem's characteristics and the capabilities and limitations of the texturing techniques available. General guidelines for texture design could be found in [4, 12]. Nevertheless, further in-depth research is still required to reveal the precise mechanisms (and their interplay) responsible for the improvements in tribological performance due to the presence of optimally designed micro-textured surfaces; this is still not fully understood. This lack of understanding is mainly related to the design and manufacturing limitations of optimal texture geometries for different components, the influence of varying operating conditions in transient applications, and the evolution of the texture geometry over the components' lifetime. Additionally, there is a particular debate on the effect of surface textures on the behavior of lubricated non-conformal contacts under different sliding-rolling conditions. Finally, to successfully and economically implement surface texturing in practical applications and industrial scale, the gain in tribological performance must compensate for the additional manufacturing steps leading to longer processing times and costs.

Surface porosity in sintered materials could be potentially used as inherent surface texture and saving extra manufacturing. Pore characteristics can be controlled, to certain limits, by the sintering parameters and powder properties [22]. However, in contrast to deterministic laser textures – with a precisely tailored topography – surface pores are statistically distributed and have irregular shapes. The effect of pores on mechanical proprieties of sintered materials was extensively studied [23–26]; however, the influence of surface porosity on the tribological performance is sparsely investigated [27–29].

Advanced statistics, artificial intelligence (AI) and machine learning (ML) methods have gained increasing importance in describing and interpreting scientific findings. In tribology research, ML & AI approaches have already been used for online condition monitoring of bearings, design of material composition, lubricant formulations, lubrication and fluid film formation analysis, among other applications [30–32]. An ML method was also recently proposed to predict the frictional performance of textured and porous interfaces [33], whose methodology could be extended to support the optimum design of surface texturing.

This study aims to quantitatively compare random surface features of porous sintered materials with distinctly manufactured laser surface textures in the particular case of lubricated non-conformal contacts. Especially the sliding-rolling conditions as occurring in roller-bearings are tackled. Finally, the radial basis ML method was used to enhance results interpretation and build a general predictive model to support the design of new surface features for obtaining superior tribological performances.

2. Sample manufacturing and surface texturing

The geometries of the sintered and laser textured samples had either curved surfaces (ball-shape) or plain surfaces (face of the disc). The geometrical dimension of samples followed standard dimensions imposed by the tribometer manufacturer, see Section 3. Balls are $\varnothing 19.05$ mm and discs $\varnothing 46 \times 6$ mm.

Reference steel material (AISI 52100), defined as NP (Non-Porous), was used as the benchmark for comparing the results obtained from surface modifications (both from randomly distributed surface pores and deterministic laser textures). NP samples were purchased from the test rig manufacturer with controlled roughness ($Sq = 20$ nm) and dimensions; therefore, no further operations were needed. Samples with surface features (either pores or texture) were always tested against reference NP material (either ball or disc). Sintered against sintered (or textured against textured) condition was avoided to facilitate results interpretations and isolate the effect of surface features. The sintering process for powder metallurgy (PM) samples was followed by machining to obtain the final sample geometry, whereas laser texturing was directly applied on reference steel samples present in the final geometry for testing.

2.1 Powder metallurgy, sintering techniques and porosity

Powder metallurgy (PM) refers to the conjunction of processes and operations for obtaining components from powders mixtures through a sintering process. The drive for sintering is the reduction of free energy between particles and consequently diffusion during sintering [34, 35]. Details of conventional PM processes are out of the scope of this work and can be found in [22].

Besides them, Spark Plasma Sintering (SPS) [36] has attracted attention in the last decades [37–41] due to high densification achieved in reduced time and grain grow inhibition [42–44], as SPS is a pressure-assisted process. The powder mixtures are placed in an electrically conductive die (often graphite) that is mounted in a low vacuum chamber. Two graphite punches apply load on the die and permit a pulsed electric current passage that increases samples' temperature and enhances sintering. SPS also allows high heating rates (up to 100 °C/min), and is applied to reduce porosity and improve densification [45, 46]. SPS' monitoring and controlling system of temperature and pressure allow obtaining materials with a range of densifications and compositions. Hence, SPS makes it possible to tailor and prototype different materials [47].

Pores strongly influence mechanical and tribological properties of sintered samples [23, 26, 28, 41, 48]. Therefore, precise control and characterization of pores are required in PM. The quantity and characteristics of pores depend either on powder characteristics (shape, dimensions, distribution, particle mechanical properties) or on the sintering processes and parameters (pressure, sintering time and temperature) [36]. Particles with similar size distribution and irregular shape improve densification during the compacting phase and reduce porosity in the final

components [36]. Similarly, increasing the applied pressure reduces total porosity. Pore characteristics including area, size, perimeter, average distance between pores, distribution and shape can be controlled by sintering temperature and time. The increase of sintering temperature promotes diffusion and increases densification, reduces total porosity, pore dimensions and irregular shape [27, 49], and the occurrence of grain growth. Archimedes' method [50] can estimate the total porosity, and pore characteristics can be evaluated through image analysis. In this study, images were taken in five different areas on the sintered samples' surface and then processed using the freely available Image J software [51] to highlight and characterize the pores. Only pore size and circularity index were considered here as main factors [52]. The circularity index ranges between 0 (very irregular) and 1 (perfectly circular) [52].

Surface roughness is another crucial parameter that strongly influences the tribological performance of tribosystems. For PM materials, roughness evaluation is not trivial since pores represent geometrical depressions that significantly increase the root mean square roughness (Sq) of the surfaces. Alternatively, the *plateau* root mean square roughness (Spq) parameter generally used to characterize honed cylinder liner topographies [53–55] is adopted to quantify the roughness of PM samples. Besides, an *ad-hoc* measuring and postprocessing procedure, including the choice of the roughness filter and cut-off values), was developed to weakening pore contours' effects on roughness characterization. More details of this procedure can be found in previous publications [29, 56–58]. The surface roughness of the reference smooth material NP was evaluated using the Sq parameter.

For this study, a commercially available steel powder mixture (Astaloy85Mo) was used. The Fe-based mixture contains 0.85 wt.% Mo, 0.3 wt.% C. Ball-shape samples were manufactured via SPS, whereas disc-shaped samples via conventional sintering. As SPS only generates cylinders and conventional sintering produced some surface irregularities, ball and disc samples had to be machined to achieve the final geometry for testing. All sintered samples were water quenched at 850°C and polished.

Different sintering parameters were used for varying porosity, see **Table 1**. Only one sintering condition is presented for the ball-shaped samples as this set of parameters (Ball-Sint) was the only one where open surface pores could be observed after machining [29, 56]. Three different compacting pressures were used with the conventional sintering technique for obtaining disc samples with different porosity. The main characteristics of sintered materials are summarized in **Table 2**.

2.2 Laser texturing techniques

As laser surface texturing is the technique most successfully used to apply deterministic textures on engineering surfaces [59], it was chosen to compare

	Sintered balls		Sintered discs	
	SPS	Conventional Sintering		
	Ball-Sint	Disc-Si4	Disc-Si5	Disc-Si6
Compacting pressure (MPa)	35	400	500	600
Sintering temperature (°C)	800	1280	1280	1280
Holding time (min)	1	60	60	60

Table 1. Sintering parameters used to manufacture the ball (SPS technique) and disc samples (conventional sintering).

	Sintered balls		Sintered discs		Discs/balls
	Ball-Sint	Disc-Si4	Disc-Si5	Disc-Si6	NP
Density (g/cm ³)	6.6	6.7	6.9	7.0	7.8
Surface porosity (%)	2	14	12	11	NA*
Average surface pore size (µm)	2.0	7.1	6.5	5.4	NA
Average circularity index (-)	0.9 ± 0.1	0.7 ± 0.3	0.8 ± 0.2	0.8 ± 0.2	NA
Surface hardness (HV1)	600 ± 80	520 ± 85	520 ± 75	550 ± 55	750 ± 25
Surface roughness, S _q (nm)	180 ± 50	370 ± 85	280 ± 70	190 ± 60	20 ± 5

*NA = not applicable.

Table 2. Porosity characteristics, Vickers hardness and surface roughness values of sintered and NP samples.

against sintered samples with random textures. Laser texturing of ball samples demonstrates the feasibility of processing curved surfaces, which is highly interesting for a wide range of applications (*i.e.* ball bearings). The texture design in terms of shape and dimensions is inspired by the most promising solutions from the literature [4, 11–14].

Two different laser systems were used to texture ball samples, which are based on different mechanisms of texture generation: an Nd:YAG laser (Quanta Ray Pro 290, Newport Spectra Physics) with a pulse duration of 10 ns and a passively mode-locked ultrashort-pulsed Ti:Sapphire laser (Spitfire Pro XP, Newport Spectra Physics) with a pulse duration of 100 fs. Due to the different pulse durations of the laser systems, the ablation mechanism varies. In the case of the ns-system, the pulse duration is long enough to melt the material leading to a different texture morphology as it is the case for the fs-system, where the pulse duration is so short that the material is directly ablated, thereby preventing melt formation and keeping the heat-affected zone at a minimum [60]. The fs-Ti:Sapphire laser, having a wavelength of 800 nm and a repetition rate of 1 kHz, was used in a direct laser writing (DLW) process. In this process, the laser beam is focused by a collective lens with a focal length of 100 mm onto the sample surface. The sample is moved by a rotation stage, thereby scanning the laser beam over the surface and generating the desired texture shape. One single shot of the laser produces a circular dimple with a diameter of 50 µm and a depth of 0.1 µm. To generate dimples (Ball-Di) or grooves (Ball-LG), the rotation speed of the stage was adapted. For higher speeds, individual laser shots hit the surface (dimples), and for lower speeds, individual laser shots are overlapping by 50%, thus producing a homogenous line pattern (longitudinally oriented with respect to the sliding direction) [61]. The accumulated laser fluences were 3.87 and 5.57 J/cm² for the dimples and the grooves, respectively.

Grooves with an orientation perpendicular to the sliding direction were generated with the ns-Nd:YAG laser in a direct laser interference patterning (DLIP) process. The laser had a wavelength of 355 nm and a repetition rate of 10 Hz. In the DLIP process, the primary laser beam exiting the laser is split up into two sub-beams by a beam splitter, which are then traveling through an optical setup guiding both beams to the sample surface. Upon overlapping of the two laser beams, a sinusoidal intensity distribution results from the interference of the beams. At the intensity maxima positions, the material is molten and removed, whereas the material stays virtually unchanged at the intensity minima positions, thus forming a groove-like texture. The laser fluence was kept constant at 1.29 J/cm² for all experiments. Due to the nature of the texture formation, textures of much smaller feature

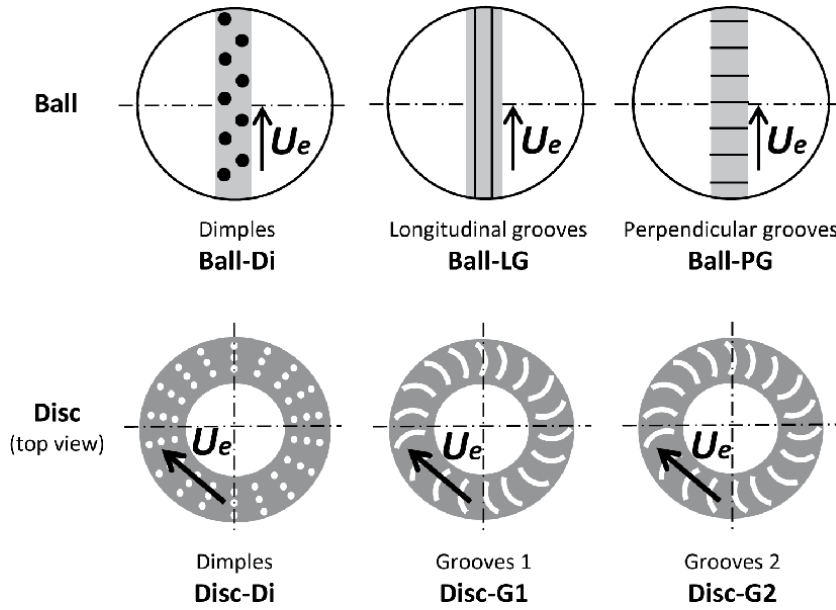


Figure 1.
Surface texture patterns on the ball and disc-shaped samples.

sizes are generated, and a higher processing speed can be achieved. Further details related to DLIP and the optical setup can be found in [62, 63].

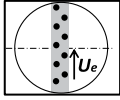
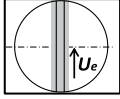
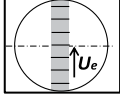
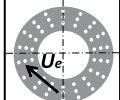
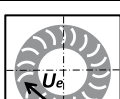

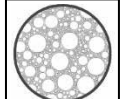

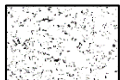

The flat surface of disc-shaped samples was textured using another fs-laser system. Radial lines of dimples were designed along the tested circumference of the discs, see **Figure 1**. The dimples have a diameter of $\sim 15 \mu\text{m}$ and a depth of $0.5 \mu\text{m}$. The radial distance between dimples was maintained at $10 \mu\text{m}$, and the circumferential distance between dimples is $\sim 300 \mu\text{m}$. Additionally, two configurations of curved radial grooves were designed on discs. One configuration of grooves had a shallow depth ($< 0.5 \mu\text{m}$) compared to the other one (depth $> 1 \mu\text{m}$). The groove width was around $20 \mu\text{m}$ for both cases.

A schematic view of texture design on ball and disc samples is presented in **Figure 1**. The main geometrical characteristics of textured and sintered features are summarized and schematically represented in **Table 3** to facilitate the input into the ML algorithm (Section 5). Note that the coverage area (Ca) represents the percentage of texture area to the tested surface. The parameter P was introduced to evaluate the shape and orientation of the texture, and it was arbitrary assigned the values of 1 for perpendicular features, 0 for dimples and -1 for longitudinal features.

3. Test rigs

3.1 Coefficient of friction measurements

The tribological tests were carried out in a ball-on-disc tribometer (MTM2 from PCS Instruments) under varying slide-to-roll ratio (SRR) conditions. In this tribometer, the ball and the disc are driven by two independent motors allowing continuous variations of SRR (see **Figure 2**). The coefficient of friction (COF) is calculated through the vertical load on the disc and the transversal force on the ball arm measured by load cells. The disc is mounted in a temperature-controlled bath, where a precise amount of lubricant is inserted. Another important feature of the test rig is the electric contact resistance (ECR) measurement. Although the ECR is

	Feature	Name	Schematic	W	D	C_a	C	P	Sq^*
				(μm)	(μm)	(%)	(%)	(-)	(μm)
Textured Ball	Dimples	Ball-Di		50	0.1	14	1	0	20
	Longitudinal Grooves	Ball-LG		35	0.1	21	0	-1	20
	Perpendicular Grooves	Ball-PG		7	0.4	47	0	1	20
Disc	Dimples	Disc-Di		15	0.5	1	1	0	20
	Grooves 1	Disc-G1		25	0.35	12.5	0	1	20
	Grooves 2	Disc-G2		20	1.35	10	0	1	20
Sintered Ball	Sintered	Ball-Sint		2	1	2	0.9	0	180
Disc	Sintered-400 MPa	Disc-Si4		7	3.5	14	0.5	0	370
	Sintered-500 MPa	Disc-Si5		6	3	12	0.6	0	280
	Sintered-600 MPa	Disc-Si6		5	2.5	11	0.6	0	190

*Note that Spq was considered for sintered materials, whereas Sq was used for the smooth and textured samples.

Table 3. Schematic configuration and geometric characteristics of sintered and textured samples. W is the feature width, D feature depth, C_a is the coverage area, C circularity, P perpendicularity, and Sq is the surface roughness.

not a direct film thickness measurement, it enables identifying the lift-off speed, *i.e.* the minimum speed from which the contact surfaces are entirely separated by a thin film of lubricant [64].

Stribeck-like curves (COF *vs.* entrainment speed U_e at fixed SRR) were obtained at different SRRs for the sintered and textured materials. All tests were performed with synthetic base oil PAO6 at the constant temperature of 40 °C and constant maximum Hertzian pressure of 0.6 GPa. Each test was repeated three times to

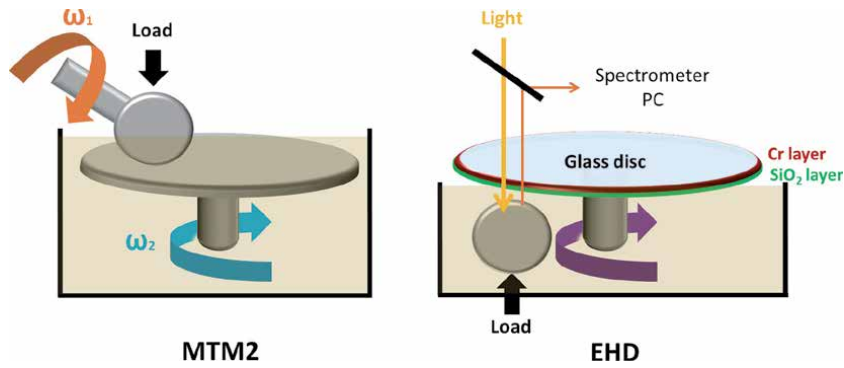


Figure 2. Schematics of tribometers used for the coefficient of friction (MTM₂) and film thickness measurements (EHD).

Parameter	MTM 2	EHD
Entrainment speed Ue (mm/s)	2000–10	2200–20
Side-to-roll-ratio SRR (%)	5–20 - 50 - 80 - 100 - 120 - 150 - 180	0
Temperature (°C)	40	40
Contact Pressure (GPa)	0.6	0.6
Lubricant	PAO6	PAO6

Table 4. Test parameters adopted for friction (MTM₂ rig) and film thickness (EHD rig) measurements.

assess repeatability. The detailed test parameters for the MTM₂ rig are summarized in **Table 4**.

3.2 Film thickness measurements

The optical interferometry technique based on the spacer layer imaging method (SLIM) [65–67] was used for film thickness measurements. A steel ball is loaded against a glass disc coated with a Cr layer and a SiO₂ spacer layer (see **Figure 2**). Light passing through the disc is reflected by the ball surface and recombined by the light reflected by the Cr layer. Differences in light wavelength are used to calculate the central EHD lubricant film thickness of non-conformal contacts.

The used EHD test rig (PCS Instruments) with the SLIM setup had to be slightly modified for measuring film thickness on rough surfaces, according to Guegan [68–70]. Basically, this is achieved by two LED light sources to obtain brighter images, and the measurement is triggered to a specific ball position to always measure the film in the same position. Besides measuring central film thickness, the contact area and the minimum and maximum film thickness of a specific area can be calculated [68–70].

Only pure rolling (SRR 0%) was tested with this setup (see **Table 4**) since the increase of sliding may cause premature damage of the spacer layer, and it was proved that film thickness depends mainly on the entrainment speeds and only marginally on the SRR [69–71].

4. Experimental results and discussion

The authors have already published most of the experimental work for sintered [29, 37, 41, 57, 58] and textured materials [33, 56, 72, 73] presented in the following

sections, and the main goal of this work is to provide a critical comparison between the different solutions. Hence, only the main results are reported and selected so that the tribological effects of surface pores and laser textures can be thoroughly evaluated and contrasted.

4.1 Sintered samples

Figure 3a shows the Stribeck-like curves of the sintered discs for SRR 100%. The results for distinct SRRs presented a similar trend. As can be observed, the decrease of total porosity and pore dimensions (**Table 2**) decreased the COF of the PM discs. The reduction of porosity goes conform with the decrement of surface roughness. As explained in Section 2.1, the alteration of surface pores is directly connected with surface morphology and, consequently, surface roughness. These parameters (surface roughness and porosity) should always be evaluated together when interpreting the friction results of PM materials.

Smooth reference samples NP showed significant lower COF when compared to the discs with pores. Again, this could be justified by the significant difference in surface roughness. For a better comparison between porous and NP samples, results can be evaluated in terms of the specific film thickness (Λ), see **Figure 3b**.

The sintered ball samples presented higher COF than NP for all SRRs and entrainment speeds, similarly to sintered discs. These outcomes are not explicitly

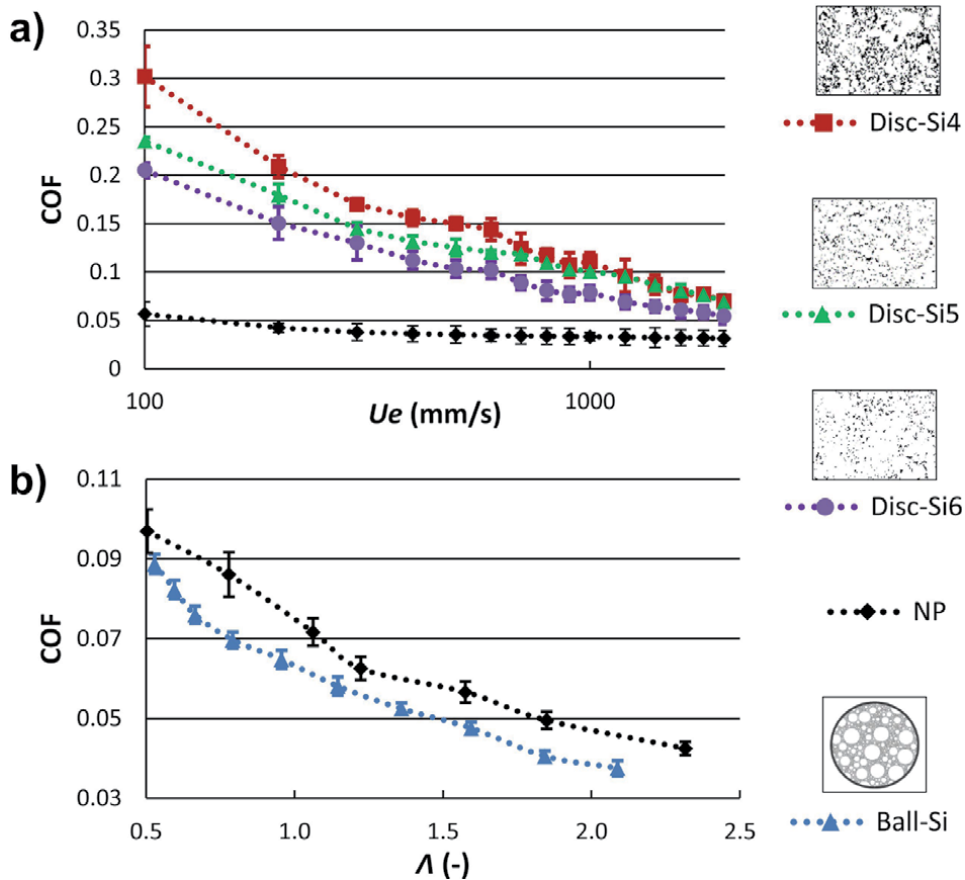


Figure 3. a) Stribeck-like curves in terms of entrainment speed (COF vs. U_e) of sintered discs for SRR 100% and b) in terms of measured specific film thickness (COF vs. Λ) of NP and sintered balls for SRR 100%.

reported here and the reader is referred to the original reference for a more in-depth result examination [29]. As for the sintered disc, the improved performance of NP compared to sintered balls could be attributed to the significant difference in surface roughness of almost one order of magnitude between the two sets of samples (see **Table 2**).

Film thickness was only evaluated for the sintered (Ball-Sint) and NP balls. The optical interferometry technique requires glass discs, which excludes the use of sintered discs. The central region of every interferogram was selected, and the mean film thickness was analysed. The COF results of NP and sintered balls were compared in **Figure 3b** as a function of Λ for SRR 100%. As can be seen, the COF of sintered balls was lower than the NP samples for all Λ values, indicating beneficial friction behavior promoted by the surface porosity. Although only results for SRR 100% are shown here, this trend was also confirmed for other SRRs. These results show how surface pores can potentially have a similar effect as classical surface texturing. It should be noted that NP was tested at lower speeds than Ball-Sint for obtaining the COF in the same ranges; therefore, the increase of porosity and roughness in porous samples increased the lift-off speed compared to smooth NP surfaces.

Previous work by Li *et al.* [74] proved that the tribological behavior of PM materials is not only dependent on the total surface porosity but also on the pore characteristics (morphology, shape, contour, area). When using sintered balls (Ball-Sint) with small and regular-shaped pores, the friction performance was similar to that of conventional dimple textured surfaces [75, 76]. Pores with dimensions smaller than the contact area and shallow depth (generally $<0.5 \mu\text{m}$) can also improve the hydrodynamic load-carrying capacity in non-conformal contacts due to the action of the so-called “micro-hydrodynamic bearing effect”. The passage of the counter-body over the convergent region of the pores or textures can promote a local increment of the lubricant viscosity and pressure, thus increasing the hydrodynamic load capacity [3]. In addition, lubricant can be “sucked” into the texture or pore when the inlet pressure in the diverging region is lower than the ambient pressure [8, 9].

4.2 Laser textured samples

The Stribeck-like curves of the laser textured samples for SRR 100% are shown in **Figure 4**. Similar trends were also obtained for distinct SRRs. Since film thickness could not be measured for textured discs, COF results were plotted together with ECR values to highlight different lubrication regimes and lift-off speed.

Dimple-textured discs (Disc-Di) promoted friction reduction compared to the reference disc NP, especially at low speeds ($<100 \text{ mm/s}$). Shallow radial grooves (Disc-G1) also slightly reduced friction compared to NP, whereas deeper textures (Disc-G2) produced significant higher COF. As previously demonstrated in [6, 75, 77] and observed in the present results, shallow features can boost the hydrodynamic load-carrying capacity in non-conformal EHD contacts due to the local increase in fluid pressure. On the contrary, deeper textures (Disc-G2) can disturb the lubricant film locally and, therefore, induce asperities contact and COF rise [77]. Considering the results of ECR and COF in **Figure 4**, this is following the behavior observed here. Boundary lubrication characterized by an ECR of 0% started roughly at the same speed for all samples (line “a” in **Figure 4**), whereas full-film EHD lubrication regime (ECR 100%) was achieved at different speeds (lines “b” and “c” in **Figure 4**). Dimples (Disc-Di) presented lower lift-off speed, having the steepest increase in ECR value and therefore film thickness and reaching hydrodynamic lubrication at the lowest speed. Dimples were followed by shallow radial grooves (Disc-G1), NP, and

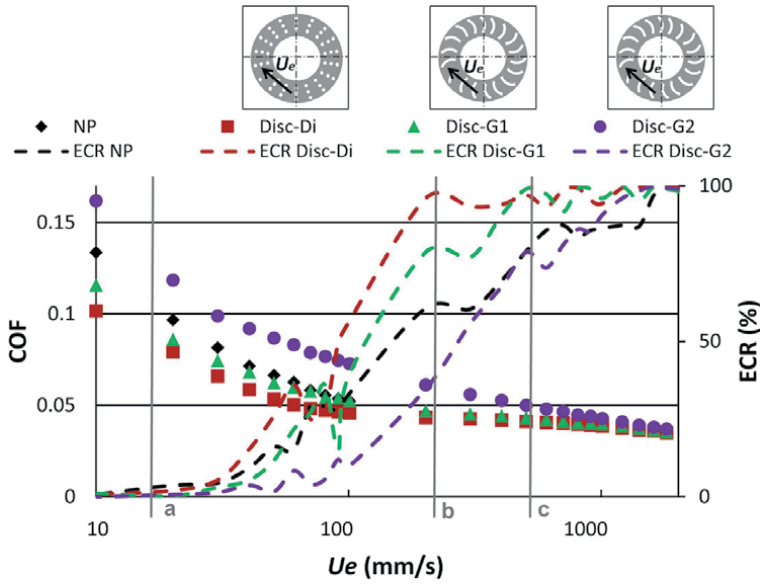


Figure 4. Friction and contact resistance results of textured disc samples tested at SRR 100%.

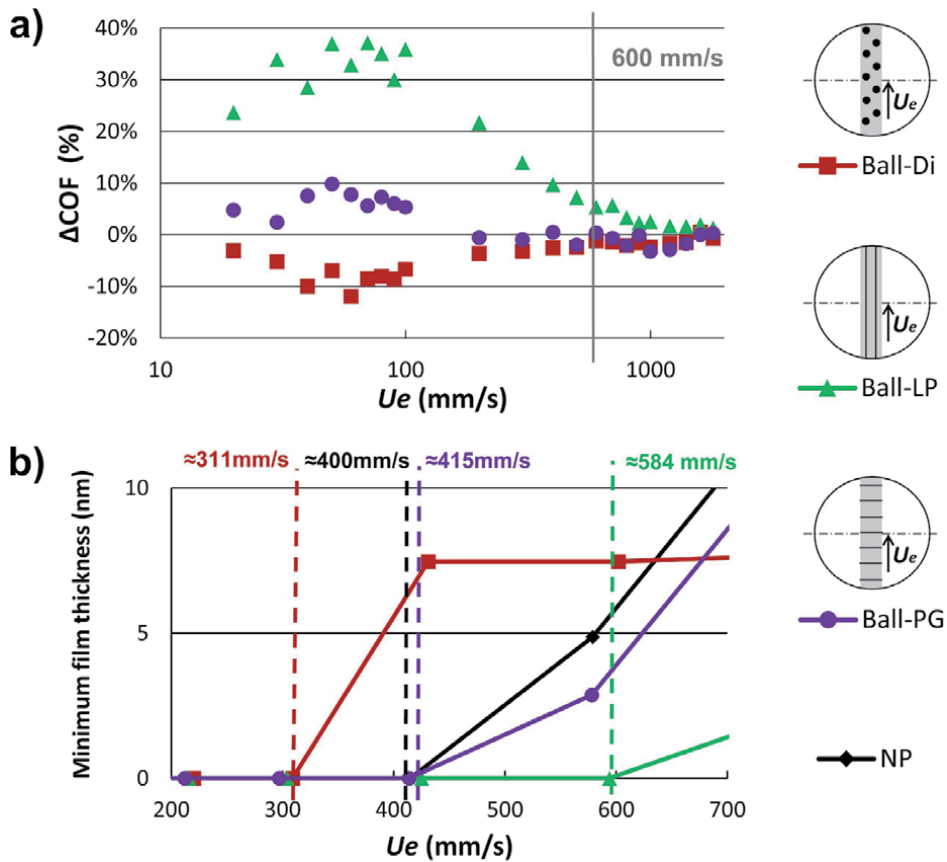


Figure 5. a) Relative differences in friction plotted as a function of U_e using SRR 100% and b) measured minimum film thickness for NP and textured balls at low-speed (< 800 mm/s) and lift-off speed values (vertical dashed lines).

finally deep radial grooves (Disc-G2). This trend proved that shallow configurations (Disc-Di and Disc-G1) had a micro-bearing effect under mixed lubrication, promoting full-film lubrication at lower speed than NP and Disc-G2, thus leading to reduced friction. This trend is also reflected in the COF *vs.* Ue dependence.

Results of textured balls were normalized using NP as a reference in **Figure 5a**, the negative values representing friction reduction. Differences between the samples are evident at Ue lower than 600 mm/s. Similarly to textured discs, the configuration of selected dimples (Ball-Di) improved frictional response. Perpendicular grooves (Ball-PG) generally behaved quite similarly to NP, whereas longitudinal grooves (Ball-LG) brought drawbacks and significantly increased COF. This behavior was observed for all the SRRs studied. To understand the reasons, film thickness results are presented in **Figure 5b**.

Particularly interesting are the values of minimum film thickness since the lift-off speed can be estimated from them. Comparing the different surface textures, dimples (Ball-Di) featured full-film conditions at a lower speed. Perpendicular grooves (Ball-PG) and NP showed similar lift-off speeds, whereas a complete separation between the rubbing surfaces was significantly delayed to higher speeds for longitudinal grooves (Ball-LG). COF and lift-off speed results are in good correlation, confirming the micro-bearing effect of dimples again. Perpendicular grooves did not significantly improve frictional performance, probably as a result of a great extent of the grooves in transversal direction (~ 1 mm) relative to the contact dimensions (~ 170 μm), leading to a reduction of pressure build-up as the lubricant flows transversally in the grooves upon contact with the counter body. Finally, longitudinal grooves (Ball-LG) did not improve the hydrodynamic load-carrying capacity, which can be traced back to a more effortless lubricant flow inside the grooves when the entrainment speed is in the direction of the textures. Upon contact, lubricant is thus squeezed out of the tribological contact, and the textures contribute to higher friction instead of local increment of pressure/viscosity and film thickness [2, 12].

Sintered and textured samples were compared both from a manufacturing, topographical, and tribological point of view. The manufacturing of sintered materials inherently entails surface features that can potentially improve tribological performance. However, pores are randomly distributed, and the geometrical characteristics of the single features can only be influenced but not precisely tailored by the sintering parameters (**Table 2**). Furthermore, surface pores in sintered material increased surface roughness, making the direct geometrical and tribological comparison with smooth samples challenging (see **Figure 3**). On the other hand, the manufacturing of laser texturing requires extra effort, but it ensures a very precise tuning of the feature's geometry and distribution.

The topographical comparison between sintered and textured materials is quite demanding since the geometrical and spatial distributions of the features are significantly different. A series of parameters was selected to statistically compare the two classes of features, *i.e.* width W and depth D for dimension, area coverage Ca for spatial distribution, perpendicularity P and circularity C for shape, see **Table 3**. Only main representative parameters were selected here to reduce the complexity since they were also used as inputs for the ML model in the next section.

The tribological improvements of textured materials were observed in **Figures 4** and **5**. Particularly, dimple-configurations (Ball-Di and Disc-Di) reduced both COF and lift-off speed, increasing the load-carrying capacity compared to NP. Surface pores in sintered balls decreased friction compared to NP only at the same specific film thicknesses, see **Figure 3b**. The large difference in COF at equal entrainment speed between sintered and NP (see **Figure 3a**) is due to the extensive difference in surface roughness, see **Table 2**. Therefore, it should be noted that the presented

pore configurations increased the lift-off speed since the increase of roughness requires higher speeds for reaching hydrodynamic conditions, see **Figure 3**. The tribological performances of dimples and pores in sintered balls can be comparable due to the geometrical similarities of surface features (see **Table 3**) and the small extent of cavities compared to the contact area.

A further comparison between sintered and textured materials is made in the following ML section. The geometrical parameters were used as inputs to characterize very different surfaces, and the COF was used as the output of the predicting model.

5. Machine learning approach

This preliminary model aims at predicting COF based on topographical characteristics of interfaces (surface pores and texture) rather than investigating the physical mechanisms associated to the tribological behavior.

The average coefficient of friction from 6228 experiments was organized in a training dataset of 1704 different combinations of geometric and operational parameters and, subsequently, used as inputs to a Hardy Multiquadric Radial Basis Function (RBF), as illustrated schematically in **Figure 6**. The mathematical development and detailed results are reported in [33]. Similar to several Artificial Neural Networks (ANN) methods, the RBF approach can produce a correct input–output mapping even for noisy and dispersed data. The RBF and experimental COF output were compared using the coefficient of determination (R^2) evaluation to avoid that the variation among the tribological experiments could be wrongly assessed as a surface feature or test parameter (*i.e.* overfitting). The results were considered satisfactory under this perspective because the error percentage was not significantly different from the maximum relative standard deviation of the dataset.

A summary of the model fitting capacity is shown in **Figure 7**, where the RBF and experimental COF results were plotted together. Overall, results from all the

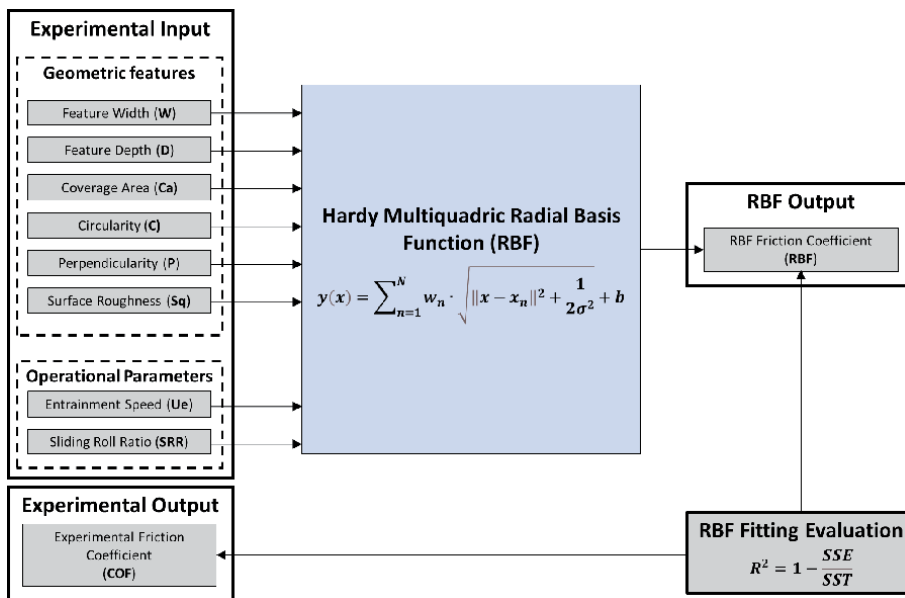


Figure 6. Schematic of the machine learning model proposed to predict the frictional behavior of porous and textured interfaces from the experimental dataset.

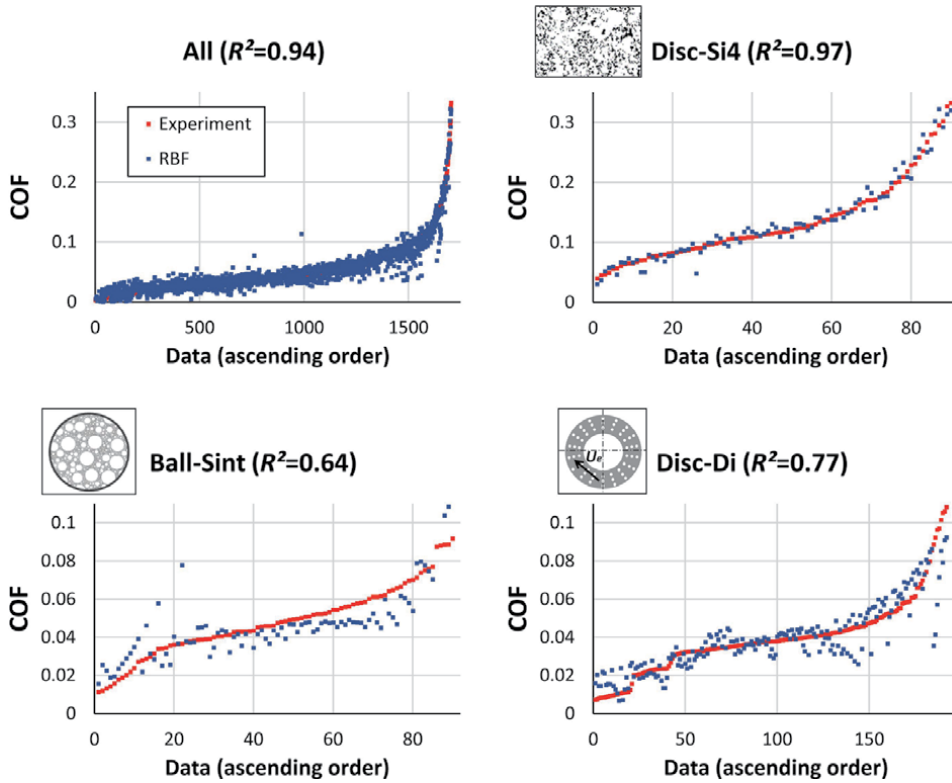


Figure 7. Comparative plots for some surface features. Each number in the horizontal axis represents a single experimental test (single combination of surface and test parameters) sorted in ascending order according to friction results rather than in chronological order for improving readability.

different samples presented a high fitting capacity ($R^2 \approx 0.94$), being the worst Ball-Sint (≈ 0.64) and the best fitting Disc-Si4 (≈ 0.97). The R^2 values from the other surface configurations are distributed between these two extremity values.

The proposed model is more sensitive to high values of W , D and Ca . Low values of W and D for shallow configurations could be difficult to be interpreted by the model since the overall topography is not mathematically significantly different from the smooth samples NP. Furthermore, shallow features in Ball-Sint and Disc-Di also occupied a very small area (low Ca values), making it even more challenging to discern between NP and shallow features.

Together with the continuous improvement of the mathematical model and expansion of the dataset to shallow and less dense surfaces, these results indicate that the RBF methodology can be an effective tool for designing novel surface features for tribological applications.

6. Conclusions

The frictional performance of textured discs and balls containing surface pores or laser textures was assessed carrying out a wide range of experiments under lubricated non-conformal contact and varying kinematic conditions (speed and slide-to-roll-ratio).

Between the different texture geometries studied, dimples generally performed best, demonstrating the lowest COFs and lowest lift-off speed, which can be traced

back to the increment of the hydrodynamic load-carrying capacity at lower speeds, further separating the rubbing surfaces and consequently reducing asperity contact. This was proven by film thickness and electric contact resistance measurements. Perpendicular grooves demonstrated beneficial performance compared with polished reference samples, depending on depth and transversal dimension. Potential beneficial effects of perpendicular grooves were partially mitigated by textures' excessive transversal dimension or depth. Longitudinal grooves led to unbeneficial tribological behavior, as equal entrainment and groove direction probably promoted lubricant migration out of the contact.

Sintering parameter tuning permitted to obtain different porosities and pore characteristics. The pore configuration achieved by machining the sintered ball samples reduced friction compared to the unstructured reference at the same specific film thickness.

Deterministic laser textures seem to outperform surface pores with random distribution and size despite the difficulties of comparing sintered with laser textured samples. This is particularly evident when considering the entrainment speed, showing that laser textures can significantly decrease the lift-off speed, after which full-film lubrication prevails by generating additional hydrodynamic pressure. Both textures have in common that textures of small dimensions being smaller than the contact area yielded the best results. However, it should be noted that laser texturing requires an additional manufacturing step, thus making the production process more complex.

Finally, considering that using advanced machine learning methods to describe tribological problems is still in its infancy, the proposed radial bias function approach showcased promising results that open new perspectives for its extension to support the optimum design of surface texturing for tribological applications in the future.

Acknowledgements

The State of São Paulo Research Foundation, Brazil (FAPESP grant N. 2016/25067-9), the Brazilian National Council for Scientific and Technological Development (CNPq) and the "Austrian COMET Program" (project InTribology, no. 872176) via the Austrian Research Promotion Agency (FFG) and the federal states of Niederösterreich and Vorarlberg are acknowledged for funding this work. Part of this work was carried out within the "Excellence Centre of Tribology" (AC2T research GmbH). C. Gachot acknowledges the government of Lower Austria for financially supporting the endowed professorship tribology at the TU Wien (Grant No. WST3-F-5031370/001-2017) in collaboration with AC2T research GmbH. D. Dini also acknowledges the support received from the Engineering and Physical Sciences Research Council (EPSRC) via his Established Career Fellowship EP/N025954/1. M. Roudrigues da Silva thanks the Centro Educacional da Fundação Salvador Arena and Termomecanica São Paulo S.A. for the financial support.

Author details

Guido Boidi^{1*}, Philipp G. Grützmacher², Markus Varga¹,
Márcio Rodrigues da Silva^{3,4}, Carsten Gachot², Daniele Dini⁵, Francisco J. Profito³
and Izabel F. Machado³

1 AC2T research GmbH, Wiener Neustadt, Austria

2 Department of Engineering Design and Product Development, TU Wien, Austria


3 Polytechnic School, University of São Paulo – USP, São Paulo, Brazil

4 Faculdade de Tecnologia Termomecanica, São Bernardo do Campo, SP, Brazil

5 Department of Mechanical Engineering, Imperial College London, London, UK

*Address all correspondence to: guido.boidi@ac2t.at

IntechOpen

© 2021 The Author(s). Licensee IntechOpen. This chapter is distributed under the terms of the Creative Commons Attribution License (<http://creativecommons.org/licenses/by/3.0>), which permits unrestricted use, distribution, and reproduction in any medium, provided the original work is properly cited. 

References

- [1] Lawrence KD, Ramamoorthy B. Multi-surface topography targeted plateau honing for the processing of cylinder liner surfaces of automotive engines. *Appl Surf Sci* 2016;365:19–30. <https://doi.org/10.1016/j.apsusc.2015.12.245>.
- [2] Vlădescu SC, Olver A V., Pegg IG, Reddyhoff T. The effects of surface texture in reciprocating contacts - An experimental study. *Tribol Int* 2015;82: 28–42. <https://doi.org/10.1016/j.triboint.2014.09.015>.
- [3] Profito FJ, Vlădescu SC, Reddyhoff T, Dini D. Transient experimental and modeling studies of laser-textured micro-grooved surfaces with a focus on piston-ring cylinder liner contacts. *Tribol Int* 2017;113:125–136. <https://doi.org/10.1016/j.triboint.2016.12.003>.
- [4] Rosenkranz A, Grützmacher PG, Gachot C, Costa HL. Surface Texturing in Machine Elements – A Critical Discussion for Rolling and Sliding Contacts. *Adv Eng Mater* 2019;1900194: 1900194. <https://doi.org/10.1002/ade.m.201900194>.
- [5] Rosenkranz A, Costa HL, Profito F, Gachot C, Medina S, Dini D. Influence of surface texturing on hydrodynamic friction in plane converging bearings - An experimental and numerical approach. *Tribol Int* 2019;134:190–204. <https://doi.org/10.1016/j.triboint.2019.01.042>.
- [6] Wang X., Zhang H., Hsu SM. The Effects of dimple size and depth on friction reduction under boundary lubrication pressure 2007:24–26.
- [7] Yu H, Wang X, Zhou F. Geometric shape effects of surface texture on the generation of hydrodynamic pressure between conformal contacting surfaces. *Tribol Lett* 2010;37:123–130. <https://doi.org/10.1007/s11249-009-9497-4>.
- [8] Fowell M, Olver A V., Gosman AD, Spikes HA, Pegg I. Entrainment and inlet suction: Two mechanisms of hydrodynamic lubrication in textured bearings. *J Tribol* 2007;129: 336–347. <https://doi.org/10.1115/1.2540089>.
- [9] Olver A V., Fowell MT, Spikes HA, Pegg IG. “Inlet suction”, a load support mechanism in non-convergent, pocketed, hydrodynamic bearings. *Proc Inst Mech Eng Part J J Eng Tribol* 2006; 220:105–108. <https://doi.org/10.1243/13506501JET168>.
- [10] Zimmer M, Vlădescu S-C, Mattsson L, Fowell M, Reddyhoff T. Shear-area variation: A mechanism that reduces hydrodynamic friction in macro-textured piston ring liner contacts. *Tribol Int* 2021;161:107067. <https://doi.org/10.1016/j.triboint.2021.107067>.
- [11] Gropper D, Wang L, Harvey TJ. Hydrodynamic lubrication of textured surfaces: A review of modeling techniques and key findings. *Tribol Int* 2016;94:509–529. <https://doi.org/10.1016/j.triboint.2015.10.009>.
- [12] Gachot C, Rosenkranz A, Hsu SM, Costa HL. A critical assessment of surface texturing for friction and wear improvement. *Wear* 2017;372–373:21–41. <https://doi.org/10.1016/j.wear.2016.11.020>.
- [13] Sudeep U, Tandon N, Pandey RK. Performance of Lubricated Rolling/ Sliding Concentrated Contacts With Surface Textures: A Review. *J Tribol* 2015;137:031501. <https://doi.org/10.1115/1.4029770>.
- [14] Grützmacher PG, Profito FJ, Rosenkranz A. Multi-Scale Surface Texturing in Tribology — Current Knowledge and Future Perspectives. *Lubricants* 2019;7.

- [15] Hamilton DB, Walowit JA, Allen CM. A Theory of Lubrication by Microirregularities. *J Basic Eng* 1966;88: 177–185. <https://doi.org/10.1115/1.3645799>.
- [16] Anno JN, Walowit JA, Allen CM. Load Support and Leakage from Microasperity-Lubricated Face Seals. *J Lubr Technol* 1969;91:726–731. <https://doi.org/10.1115/1.3555030>.
- [17] Etsion I, Burstein L. A Model for Mechanical Seals with Regular Microsurface Structure. *Tribol Trans* 1996;39:677–683. <https://doi.org/10.1080/10402009608983582>.
- [18] Etsion I, Kligerman Y, Halperin G. Analytical and Experimental Investigation of Laser-Textured Mechanical Seal Faces. *Tribol Trans* 1999;42:511–516. <https://doi.org/10.1080/10402009908982248>.
- [19] Kovalchenko A, Ajayi O, Erdemir A, Fenske G, Etsion I. The Effect of Laser Texturing of Steel Surfaces and Speed-Load Parameters on the Transition of Lubrication Regime from Boundary to Hydrodynamic. *Tribol Trans* 2004;47: 299–307. <https://doi.org/10.1080/05698190490440902>.
- [20] Kovalchenko A, Ajayi O, Erdemir A, Fenske G, Etsion I. The effect of laser surface texturing on transitions in lubrication regimes during unidirectional sliding contact. *Tribol Int* 2005;38:219–225. <https://doi.org/10.1016/j.triboint.2004.08.004>.
- [21] Pettersson U, Jacobson S. Influence of surface texture on boundary lubricated sliding contacts. *Tribol Int* 2003;36:857–864. [https://doi.org/10.1016/S0301-679X\(03\)00104-X](https://doi.org/10.1016/S0301-679X(03)00104-X).
- [22] Upadhyaya A, Upadhyaya GS. *Powder Metallurgy: Science, Technology and Materials*. First. Boca Raton, FL 33487, USA: CRC Press LLC, Taylor and Francis Group; 2011.
- [23] Carabajar S, Verdu C, Hamel A, Fougères R. Fatigue behavior of a nickel alloyed sintered steel. *Mater Sci Eng A* 1998;257:225–234. [https://doi.org/10.1016/S0921-5093\(98\)00846-6](https://doi.org/10.1016/S0921-5093(98)00846-6).
- [24] Carabajar S, Verdu C, Fougères R. Damage mechanisms of a nickel alloyed sintered steel during tensile tests. *Mater Sci Eng A* 1997;232:80–87. [https://doi.org/10.1016/S0921-5093\(97\)00100-7](https://doi.org/10.1016/S0921-5093(97)00100-7).
- [25] Straffelini G, Molinari A, Danninger H. Impact notch toughness of high-strength porous steels. *Mater Sci Eng A* 1999;272:300–309. [https://doi.org/10.1016/S0921-5093\(99\)00491-8](https://doi.org/10.1016/S0921-5093(99)00491-8).
- [26] Straffelini G, Fontanari V, Molinari A. True and apparent Young's modulus in ferrous porous alloys. *Mater Sci Eng A* 1999;260:197–202. [https://doi.org/10.1016/S0921-5093\(98\)00960-5](https://doi.org/10.1016/S0921-5093(98)00960-5).
- [27] Martin F, García C, Blanco Y. Influence of residual porosity on the dry and lubricated sliding wear of a powder metallurgy austenitic stainless steel. *Wear* 2015;328–329:1–7. <https://doi.org/10.1016/j.wear.2015.01.025>.
- [28] Li X, Olofsson U. A study on friction and wear reduction due to porosity in powder metallurgic gear materials. *Tribol Int* 2017;110:86–95. <https://doi.org/10.1016/j.triboint.2017.02.008>.
- [29] Boidi G, Profito FJ, Kadirci A, Machado IF, Dini D. The use of Powder Metallurgy for promoting friction reduction under sliding-rolling lubricated conditions. *Tribol Int* 2021; 157:106892. <https://doi.org/10.1016/j.triboint.2021.106892>.
- [30] Rosenkranz A, Marian M, Profito FJ, Aragon N, Shah R. The Use of Artificial Intelligence in Tribology—A Perspective. *Lubricants* 2020;9:2. <https://doi.org/10.3390/lubricants9010002>.
- [31] Prost J, Cihak-Bayr U, Neacșu IA, Grundtner R, Pirker F, Vorlauffer G.

- Semi-Supervised Classification of the State of Operation in Self-Lubricating Journal Bearings Using a Random Forest Classifier. *Lubricants* 2021;9:50. <https://doi.org/10.3390/lubricants9050050>.
- [32] Pandiyan V, Prost J, Vorlaufer G, Varga M, Wasmer K. Identification of abnormal tribological regimes using a microphone and semi-supervised machine-learning algorithm. *Friction* 2021. <https://doi.org/10.1007/s40544-021-0518-0>.
- [33] Boidi G, da Silva MR, Profito FJ, Machado IF. Using Machine Learning Radial Basis Function (RBF) Method for Predicting Lubricated Friction on Textured and Porous Surfaces. *Surf Topogr Metrol Prop* 2020;8:044002. <https://doi.org/10.1088/2051-672X/abae13>.
- [34] German RM. *Sintering Theory and Practice*. Ed. John Wiley and Sons: 1996.
- [35] Barsoum MW. *Fundamentals of ceramics*. The Mc Graw-Hill Companies Inc.: 2003.
- [36] Chen W, Anselmi-Tamburini U, Garay JE, Groza JR, Munir ZA. Fundamental investigations on the spark plasma sintering/synthesis process: I. Effect of dc pulsing on reactivity. *Mater Sci Eng A* 2005;394:132–138. <https://doi.org/10.1016/j.msea.2004.11.020>.
- [37] Fukumasu NK, Boidi G, Seriacopi V, Machado GAA, Souza RM, Machado IF. Numerical analyses of stress induced damage during a reciprocating lubricated test of fecmo sps sintered alloy. *Tribol Int* 2017;113:443–447. <https://doi.org/10.1016/j.triboint.2016.12.025>.
- [38] Balima F, Largeteau A. Phase transformation of alumina induced by high pressure spark plasma sintering (HP-SPS). *Scr Mater* 2019;158:20–23. <https://doi.org/10.1016/j.scriptamat.2018.08.016>.
- [39] Fu L, Wu C, Grandfield K, Unosson E, Chang J, Engqvist H, et al. Transparent single crystalline ZrO₂-SiO₂ glass nanoceramic sintered by SPS. *J Eur Ceram Soc* 2016;36:3487–3494. <https://doi.org/10.1016/j.jeurceramsoc.2016.05.016>.
- [40] Xuan CJ, Zhao Z, Jönsson PG. Wettability and corrosion of spark plasma sintered (SPS) ZrN by liquid iron and steel. *J Eur Ceram Soc* 2016;36:2435–2442. <https://doi.org/10.1016/j.jeurceramsoc.2016.03.006>.
- [41] Boidi G, Fukumasu NK, Machado IF. Wear and friction performance under lubricated reciprocating tests of steel powder mixtures sintered by Spark Plasma Sintering. *Tribol Int* 2018;121:139–147. <https://doi.org/10.1016/j.triboint.2018.01.032>.
- [42] Zhan G-D, Kuntz J, Wan J, Garay J, Mukherjee AK. A Novel Processing Route to Develop a Dense Nanocrystalline Alumina Matrix (<100 nm) Nanocomposite Material. *J Am Ceram Soc* 2003;86:200–2002. <https://doi.org/10.1111/j.1151-2916.2003.tb03306.x>.
- [43] Omori M. Sintering, consolidation, reaction and crystal growth by the spark plasma system (SPS). *Mater Sci Eng A* 2000;287:183–188. [https://doi.org/10.1016/s0921-5093\(00\)00773-5](https://doi.org/10.1016/s0921-5093(00)00773-5).
- [44] Li W, Gao L. Fabrication of HAp-ZrO₂ (3Y) nano-composite by SPS. *Biomaterials* 2003;24:937–940. [https://doi.org/10.1016/S0142-9612\(02\)00428-3](https://doi.org/10.1016/S0142-9612(02)00428-3).
- [45] Zarebski K, Putyra P. Iron powder-based graded products sintered by conventional method and by SPS. *Adv Powder Technol* 2015;26:401–408. <https://doi.org/10.1016/j.apt.2014.11.010>.
- [46] Orrù R, Licheri R, Locci AM, Cincotti A, Cao G. Consolidation/synthesis of materials by electric current

- activated/assisted sintering. *Mater Sci Eng R Reports* 2009;63:127–287. <https://doi.org/10.1016/j.mser.2008.09.003>.
- [47] Machado IF, Girardini L, Lonardelli I, Molinari A. The study of ternary carbides formation during SPS consolidation process in the WC–Co–steel system. *Int J Refract Met Hard Mater* 2009;27:883–891. <https://doi.org/10.1016/J.IJRMHM.2009.05.001>.
- [48] Li X, Olofsson U, Bergseth E. Pin-on-Disc Study of Tribological Performance of Standard and Sintered Gear Materials Treated with Triboconditioning Process: Pretreatment by Pressure-Induced Tribofilm Formation. *Tribol Trans* 2017; 60:47–57. <https://doi.org/10.1080/10402004.2016.1146379>.
- [49] Li X, Sosa M, Olofsson U. A pin-on-disc study of the tribology characteristics of sintered versus standard steel gear materials. *Wear* 2014;340–341:31–40. <https://doi.org/10.1016/j.wear.2015.01.032>.
- [50] Dlapka M, Danninger H, Gierl C, Lindqvist B. Defining the pores in PM components. *Met Powder Rep* 2010;65: 30–33. [https://doi.org/10.1016/S0026-0657\(10\)70093-X](https://doi.org/10.1016/S0026-0657(10)70093-X).
- [51] Schneider CA, Rasband WS, Eliceiri KW. NIH Image to ImageJ: 25 years of image analysis. *Nat Methods* 2012;9:671–675. <https://doi.org/10.1038/nmeth.2089>.
- [52] Seville J.P.K., Wu CY. *Particle Technology and Engineering: an Engineer's Guide to Particles and Powders: Fundamentals and Computational Approaches*. 2016.
- [53] Grabon W, Pawlus P, Wos S, Koszela W, Wieczorowski M. Effects of cylinder liner surface topography on friction and wear of liner-ring system at low temperature. *Tribol Int* 2018;121: 148–160. <https://doi.org/10.1016/j.triboint.2018.01.050>.
- [54] Reizer R, Pawlus P. 3D surface topography of cylinder liner forecasting during plateau honing process. *J Phys Conf Ser* 2011;311:012021. <https://doi.org/10.1088/1742-6596/311/1/012021>.
- [55] Grabon W, Pawlus P, Wos S, Koszela W, Wieczorowski M. Effects of honed cylinder liner surface texture on tribological properties of piston ring-liner assembly in short time tests. *Tribol Int* 2017;113:137–148. <https://doi.org/10.1016/j.triboint.2016.11.025>.
- [56] Boidi G. An experimental assessment of surface micro irregularities (porosity and texture) effects on tribological behavior under lubricated conditions. Doctorate Thesis, Universidade de São Paulo, 2019. <https://doi.org/10.11606/T.3.2019.tde-22102019-091137>.
- [57] Boidi G, Tertuliano IS, Cano MF, Machado GAA, Souza RM, Machado IF. Tribological Evaluation of Sintered and Conventional Gear Materials, 2017. <https://doi.org/10.4271/2017-36-0153>.
- [58] Boidi G, Tertuliano IS, Lima LGBS, Profito FJ, Machado IF. Porosity Effect of Sintered Steel on the Frictional Performance of Conformal and Nonconformal Lubricated Contacts. *Tribol Trans* 2019;62:1029–1040. <https://doi.org/10.1080/10402004.2019.1640917>.
- [59] Costa H, Hutchings I. Some innovative surface texturing techniques for tribological purposes. *Proc Inst Mech Eng Part J J Eng Tribol* 2015;229:429–448. <https://doi.org/10.1177/1350650114539936>.
- [60] Chichkov BN, Momma C, Nolte S, Alvensleben F, Tünnermann A. Femtosecond, picosecond and nanosecond laser ablation of solids. *Appl Phys A Mater Sci Process* 1996;63:109–115. <https://doi.org/10.1007/BF01567637>.
- [61] Grützmacher PG, Rosenkranz A, Szurdak A, Gachot C, Hirt G,

Mücklich F. Lubricant migration on stainless steel induced by bio-inspired multi-scale surface patterns. *Mater Des* 2018;150:55–63. <https://doi.org/10.1016/j.matdes.2018.04.035>.

[62] Grützmacher PG, Rosenkranz A, Szurdak A, König F, Jacobs G, Hirt G, et al. From lab to application - Improved frictional performance of journal bearings induced by single- and multi-scale surface patterns. *Tribol Int* 2018; 127:500–508. <https://doi.org/10.1016/j.triboint.2018.06.036>.

[63] Mücklich F, Lasagni A, Daniel C. Laser Interference Metallurgy – using interference as a tool for micro/nano structuring. *Int J Mater Res* 2006;97: 1337–1344. <https://doi.org/10.3139/146.101375>.

[64] Heemskerk RS, Vermeiren KN, Dolfmsma H. Measurement of Lubrication Condition in Rolling Element Bearings. *A S L E Trans* 1982;25:519–527. <https://doi.org/10.1080/05698198208983121>.

[65] Luo J, Wen S, Huang P. Thin film lubrication. Part I. Study on the transition between EHL and thin film lubrication using a relative optical interference intensity technique. *Wear* 1996;194:107–115. [https://doi.org/10.1016/0043-1648\(95\)06799-X](https://doi.org/10.1016/0043-1648(95)06799-X).

[66] Cann PM, Spikes HA, Hutchinson J. The development of a spacer layer imaging method (slim) for mapping elastohydrodynamic contacts. *Tribol Trans* 1996;39:915–921. <https://doi.org/10.1080/10402009608983612>.

[67] Johnston GJ, Wayte R, Spikes HA. The measurement and study of very thin lubricant films in concentrated contacts. *Tribol Trans* 1991;34:187–194. <https://doi.org/10.1080/10402009108982026>.

[68] Guégan J. Experimental Investigation into the Influence of Roughness on Friction and Film

Thickness in EHD Contacts. Imperial College London, 2015. <https://doi.org/10.25560/53388>.

[69] Guegan J, Kadiric A, Spikes H. A Study of the Lubrication of EHL Point Contact in the Presence of Longitudinal Roughness. *Tribol Lett* 2015;59:1–18. <https://doi.org/10.1007/s11249-015-0549-7>.

[70] Guegan J, Kadiric A, Gabelli A, Spikes H. The Relationship Between Friction and Film Thickness in EHD Point Contacts in the Presence of Longitudinal Roughness. *Tribol Lett* 2016;64:1–15. <https://doi.org/10.1007/s11249-016-0768-6>.

[71] Rycerz P, Kadiric A. The Influence of Slide–Roll Ratio on the Extent of Micropitting Damage in Rolling–Sliding Contacts Pertinent to Gear Applications. *Tribol Lett* 2019;67:63. <https://doi.org/10.1007/s11249-019-1174-7>.

[72] Boidi G, Grützmacher PG, Kadiric A, Profito FJ, Machado IF, Gachot C, et al. Fast laser surface texturing of spherical samples to improve the frictional performance of elasto-hydrodynamic lubricated contacts. *Friction* 2021;9:1227–1241. <https://doi.org/10.1007/s40544-020-0462-4>.

[73] Boidi G, Tertuliano IS, Profito FJ, de Rossi W, Machado IF. Effect of laser surface texturing on friction behavior in elastohydrodynamically lubricated point contacts under different sliding-rolling conditions. *Tribol Int* 2020;149: 105613. <https://doi.org/10.1016/j.triboint.2019.02.021>.

[74] Li S, Parmar U. The Effects of Microdimple Texture on the Friction and Thermal Behavior of a Point Contact. *J Tribol* 2018;140:041503. <https://doi.org/10.1115/1.4039228>.

[75] Krupka I, Hartl M, Zimmerman M, Houska P, Jang S. Effect of surface

texturing on elastohydrodynamically lubricated contact under transient speed conditions. *Tribol Int* 2011;44:1144–1150. <https://doi.org/10.1016/j.triboint.2011.05.005>.

[76] Mourier L, Mazuyer D, Ninove FP, Lubrecht AA. Lubrication mechanisms with laser-surface-textured surfaces in elastohydrodynamic regime. *Proc Inst Mech Eng Part J J Eng Tribol* 2010;224:697–711. <https://doi.org/10.1243/13506501JET771>.

[77] Mourier L, Mazuyer D, Lubrecht AA, Donnet C. Transient increase of film thickness in micro-textured EHL contacts. *Tribol Int* 2006;39:1745–1756. <https://doi.org/10.1016/j.triboint.2006.02.037>.

Tribological Behavior of Atmospheric Plasma Sprayed HA-CNT Coatings of Biomaterials

Mahesh M. Sonekar and Walmik S. Rathod

Abstract

A MWCNT-induced hydroxyapatite, air plasma spray coatings were produced on SS-316 L, CoCrMo, and Ti6Al4V alloys at varied weight percent ratios. The shape, thickness, adhesion, structure, and content of the APS-treated samples, as well as particle distribution, were studied using an X-ray diffraction, scanning electron microscope, Fourier transform infrared, and 3D-profilometer. The study looks at dry and wet unidirectional sliding wear behaviors, as well as the influence of incorporating carbon nanotubes in different weight percent to hydroxyapatite by plasma spraying on its tribological properties in physiological condition. In-vitro investigation was conducted in controlled environment to model complicated interactions among cells growth factors. Both CNT and HA particles were absorbed into the APS layers, as evidenced by the results. Crystallinity and volume percent with open porosity were substantially higher in the APS-CNT imposed HA coating than in the control. When compared to pure HA coating, the enhanced hardness ranged from 2.4 to 5.6 GPa, the modulus of elasticity ranged from 105 to 172 GPa, and the fracture toughness from 0.6 to 2.4 MPa.m^{1/2}, with a reduced wear rate of 50.2 × 10⁻⁵ mm³ to 4.2 × 10⁻⁵ mm³ N⁻¹ m⁻¹. CNT addition has no negative effect on osteoblast proliferation and cell viability.

Keywords: hydroxyapatite, carbon nanotube, air plasma spraying, biocoating, tribology, biocompatibility

1. Introduction

The fundamental requirement of bio implant should be its biocompatibility with the biological system, high mechanical properties to withstand various stresses induced, and excellent corrosion resistance in the body fluid [1]. Materials used for bio-implants are categorized as Metals and alloys, Polymers, ceramics, and reinforced composites. Advanced materials like Surgical stainless steel, CoCrMo alloys, and different Titanium grades are the most commonly used implant material due to their good biomechanical properties. But their main limitation is that these materials may not always be biocompatible with the body fluids, and tissues may not grow on these materials after they are implanted in the body [2]. The recurring failure of traditional materials used in orthopedic implant manufacturing was due to a lack of or inadequate integration of implant materials to the juxtaposed bone & stress-strain imbalance between the interface of tissue and implant material [3].

Ceramics are commonly used for bio implant applications due to their superior biocompatibility in the body environment. Due to their similarity with human bone natural tissues easily grow on their surfaces [4]. Few bioceramic materials are HA, tri-calcium phosphates (TCP), and bioactive glasses. But uses of ceramics are limited due to their poor mechanical properties.

Polymers are soft materials that can be easily formed into complex shapes; however, they have poor mechanical properties and cannot be used in heavy load-bearing applications such as knee and hip prostheses [5]. Composite materials are typically created by joining two or more distinct material phases, such as metallic-ceramic, polymer-ceramic, and metallic-polymer [6]. These materials have good mechanical properties and biocompatibility, but it is extremely difficult to make composite parts biocompatible [7].

Hydroxyapatite (HA) coating is an excellent aspirant for bio-implants in order to improve their biocompatibility in body fluid [8]. Because the chemical structure of HA is very similar to the structure of natural bone, it can form new tissues on it in body fluids, which is critical for the fixation of bio-implants inside the body and also protects the body from any harmful metal ion released by the metallic implant [9]. It has lower mechanical properties, such as low bending strength, fracture toughness, and impact strength, and thus cannot be used in pure form for load-bearing applications [10]. The coating of HAP alters the dispersion behavior of MWCNTC in the PP matrix, causing variations in the tensile and thermomechanical characteristics of MWCNTs/PP composites [11].

Hence it is a good idea to overcome these mechanical limitations to coat this material on the metallic substrates which have good mechanical properties. From the previous work [12] it has been found that pure HA coating results in poor adhesion, bonding strength, and other mechanical properties. Hence to improve these properties reinforced materials like zirconia, silica, titania, alumina, carbon, and boron nanotubes are added in bulk HA. Particularly there must be sufficient adhesion strength between HA coating and metallic implants to avoid spalling, cracking and wearing of the coating [13]. Many techniques like electrophoretic, sol-gel, and thermal spraying (plasma and HVOF), etc. are used for HA deposition on metallic substrates. Among these, the air plasma technique is widely used because of its excellent adhesion strength, better process control, crystal structure, and thickness of the coating as compared with other such coating techniques [14]. This technique is recommended and approved by Food and Drug Administration (FDA) in the USA for clinical trials [15].

Despite the many advantages of hydroxyapatite coating on metallic substrates, the brittle nature and low strength of hydroxyapatite delay clinical trials under varying loading conditions [16]. Because HA is brittle, secondary reinforcement materials such as Zirconia, Ni3Al, Alumina (Al_2O_3), carbon nanotubes (CNTs), boron nitride nanotubes (BNNTs), Silica, yttria-stabilized zirconia (YSZ), and Ti-grade-alloys are commonly used to improve mechanical properties such as fracture toughness and Young's modulus [17]. CNT reinforced composites outperformed other composites in terms of biological and tribo mechanical properties. The addition of CNTs increases the crystallinity, shape, and biological characteristics of HAP [18]. The COF of a composite can be reduced by varying the rate of CNT. The inclusion of CNTs boosts cell growth and adhesion. Wear-related mass loss is reduced by 13.33%, 66.67%, and 83.33% [19]. To understand the functionalization of CNTs to increase their hydrophobic qualities, the intrinsic nature of CNTs, including their physical and chemical properties, is explained. CNTs are often functionalized with different functional groups (such as -OH and -COOH) using covalent and non-covalent approaches to increase dispersity in aqueous conditions and limit toxicity [20]. The specimens' corrosion resistance reveals

the biocompatibility of Ti-Co-Cr as being more unique due to the presence of titanium metal [21]. Many corrosion, wear, and abrasion resistant applications exist for plasma sprayed $\text{Al}_2\text{O}_3\text{-TiO}_2$ ceramics in industries such as aircraft, textile, and automotive [22]. Gell et al. [23] investigated plasma-sprayed nanostructured 13 wt% $\text{Al}_2\text{O}_3\text{-TiO}_2$ coatings and reported that these coatings had been approved for submarine and shipboard applications by the US Navy.

It is well understood that with HA coating wear indicates the possibility of orthopedic implant degradation failure. According to previous research, the main issue that affects the total joint replacement longevity is “worn particle-induced osteolysis, particularly adjacent to acetabular components” [24]. Wear particles are generated by the articulating surface and migrate along the implant interface, causing osteolysis, implant loosening, and, eventually, implant failure. However, there was no detailed information on the mechanism of microstructural failure. As a result, investigating the tribological behavior of HA-CNT coated specimens at the microstructure level requires considerable effort. The effect of CNTs on the human body and the environment is not well established, owing to a lack of standardization of toxicological tests, which leads to discrepancies in the results [25]. The current work will investigate the microstructural properties of applied coatings and investigate the potential of HA-CNT coating by plasma spray for bio implant applications. In this work, an attempt was made to deposit HA with 10% and 5% CNT on surgical grade SS 316L, CoCrMo, and Ti6Al4V substrates and to establish their suitability for in vivo applications.

2. Experimental procedure

2.1 Preparation of substrates and feedstock powder coating processes

The alloy samples of SS 316L, CoCrMo & Ti6Al4V were cut to form an approximate disc having 40x5 mm diameter size. The surface of coated samples is prepared using alumina (Al_2O_3) of size 65–90 μm in a grit blaster within a blasting pressure range of 0.50 MPa for better adhesion of coating powders. After grit blasting the samples were air blasted to clean the surface from alumina contamination before final coating. **Table 1** shows the chemical composition of HA-CNT powder for coating substrate materials. Commercially available HA powder was used for coating deposition which was procured from Xi'an Prius Biological Engineering Co., Ltd. XS province, China, and MWCNT procured from Adnano Technologies Pvt. Ltd., Karnataka, India was used as reinforcing material. Reinforcing material was mixed in pure hydroxyapatite Powder in 10% and 5% by weight using laboratory ball mill up to 10 hours for uniform mixing of reinforced HA coating at Plasma Spray Coats, Bangalore, India. Particle size, composition (wt.%) with powder designation are shown in **Table 1**.

Morphological studies of bare hydroxyapatite powder with carbon nanotube reinforcement on coated alloy substrates have been carried out using scanning electron micrographs. These powders were also characterized by the XRD technique

Coating powder	Composition (wt. %)	Particle size	Designation
Pure HA	$\text{Ca}_{10}(\text{PO}_4)_6\text{OH}_2$	100–160 μm	Pure HA
Reinforced HA	$\text{Ca}_{10}(\text{PO}_4)_6\text{OH}_2$ —MWCNT (10 wt% & 5 wt%) mixed in laboratory ball mill for 8 h.	Reinforcement 10–45 μm	Reinforced HA-C

Table 1.
 Chemical composition and other details of HA-CNT coating powder.

using the Xta-LABmini™ Benchtop X-ray Diffraction/Crystallography system from Rigaku Americas Corporation in the angle range of 20°–90°. **Figures 1** and **2** depict the micrographs and EDX analysis of (10 wt% and 5 wt%) reinforced HA-C coating. SEM micrograph shows that reinforced material has crushed angular and ball shape.

2.2 Wear analysis

Ball/Pin on disc tribo tester (Ducom Instruments, model TR-20LE) was used for bare and HA-CNT coated samples under dry and wet (SBF) sliding conditions for analyzing the abrasive wear. The samples were prepared as per G95-99a. The effect of the counter body of Steel Ball SAE52100, H = 9.46 GPa was studied to analyze the counterparts. The roughness (Ra) values of testing samples were made in the range of 0.8 μm or less. A varying speed of 100 RPM with a 25 mm circular track radius with a total traveling distance of 90–200 m was used to study the wear at a macro level. A specific linear speed of the tribo probe was set to 10 mm/s. The counter

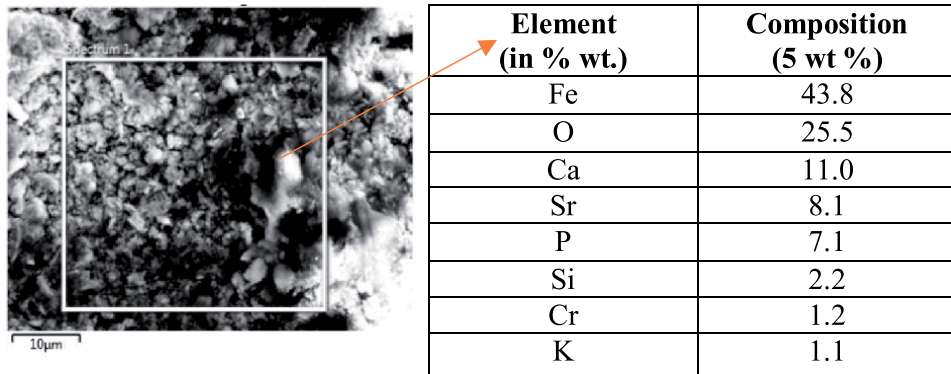


Figure 1. Scanning electron micrograph showing morphology of 10 wt% reinforced HA-CNT powder with element composition from EDX analysis.

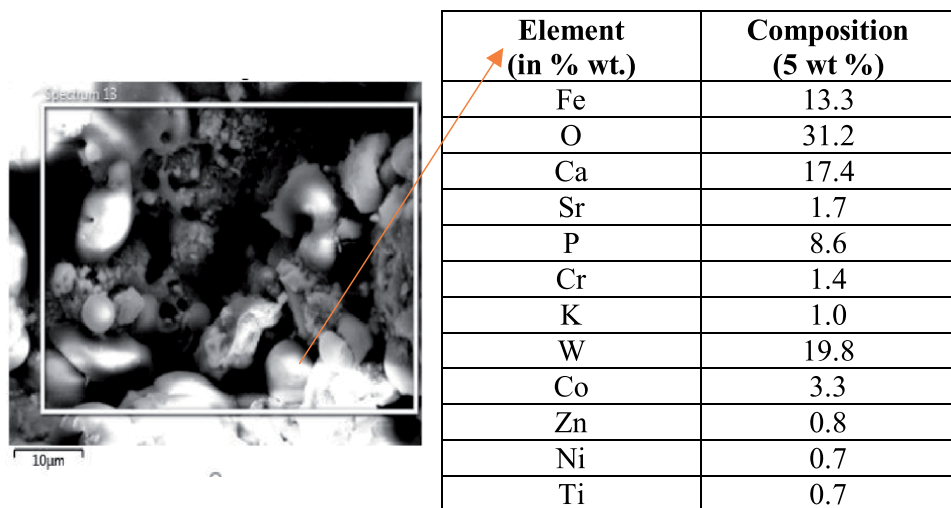


Figure 2. Scanning electron micrograph showing morphology of 5 wt% reinforced HA-CNT powder with element composition from EDX analysis.

body (probe) used was an 8 mm diametric steel ball. The inbuilt LVDT sensor gives the value of linear force in between the coated surface and steel probe under the depth of wear track. The coefficient of frictional data is acquired at the 17 Hz frequency level. Alicona 3D profilometer was used to obtain the profiles of wear track on tested samples. The value of wear volume is computed using the wear track depth profile.

Figure 3 shows the pictorial view of wear (tribological) study in physiological conditions. The tests were performed with samples immersed in externally supplied simulated body fluid (SBF), in the tribo tester with the same test parameters and conditions as was used during the dry wear test. The SBF is prepared and purchased from KET's Scientific Research Centre Mumbai, India using Takadama Hiroaki [26] with the same ion concentration of chemicals as compared with human blood. The chloride ions are the cause of corrosion biomaterials, so these fluids are suitable for analyzing the corrosion resistance [27].

2.3 Coating characterization

The critical evaluation of SS 316 L, CoCrMo, and Ti6Al4V substrates coated by 10 wt% and 5 wt% CNT and worn-out surfaces are done. The metallographic study of as-sprayed coatings on these substrates is examined under ZEISS Gemini field emission scanning electron microscope (FE-SEM), operating at 18 kV. To have high-resolution imaging, gold is used as the sputter coating material before analyzing in SEM. It can be seen from the optical micrograph **Figure 4** that the top surface of the coating is free from cracks and macro-level porosity. Most of the splats are well-formed without any sign of disintegration. Some melted grains are also visible on the surface of coatings in most of the micrographs. Further, it can be observed from the SEM/EDX analysis that a whitish appearance somewhere in the coating in SEM micrographs indicates Ca-rich HA particles. In reinforced HA coatings some streaks are detected whose EDX analysis confirms the presence of reinforcing content which is distributed in the matrix of the HA-C coatings [28, 29]. EDS spectroscopy indicated a Ca/p ratio of 1.62 in calcium phosphate deposits, which is similar to the ratio of 1.64 in natural bone [30].

Figure 5 shows an insight on the FTIR analysis of HA-CNT reinforced coated samples in the range of 4000 cm^{-1} to 500 cm^{-1} . OH⁻ group at 3568 cm^{-1} and 652 cm^{-1} can be seen with the presence of PO₄³⁻ group at 960 cm^{-1} , 1033 cm^{-1} and

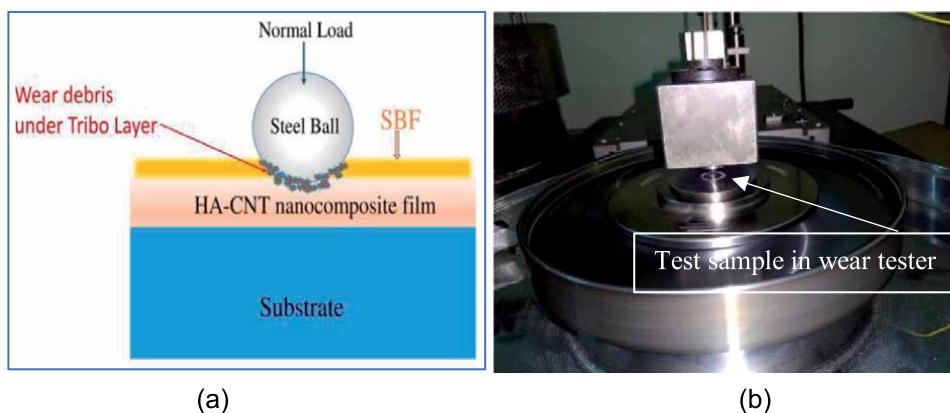


Figure 3. Experimental set-ups for tribological wear test (a) wear test mechanism under SBF (b) wear test sample in physiological condition.

558 cm^{-1} . CO_2 molecules which were not visible in the original powder are now can be observed at 2360 cm^{-1} . The intensity of OH^- group has become comparatively weaker after coatings in the case of reinforced HA-C coatings in all alloy substrates.

The basic mechanical property of HA-C coating is microhardness, which may play an important role in bio implant application. At the coating interface, the microhardness of coatings on alloy substrates was measured. Profiles for microhardness with distance from the coating substrate interface are shown in **Figure 6**. The hardness of both (10 wt% & 5 wt%) reinforced HA-C coating is lowest (310 Hv, 340 Hv, and 402 Hv in case of uncoated SS 316 l, CoCrMo, and Ti6Al4V, whereas 322 Hv, 352 Hv, and 418 Hv in case of reinforced HA-C respectively) at the interface in case of all the three alloy substrates. Slight improvement in hardness was observed with

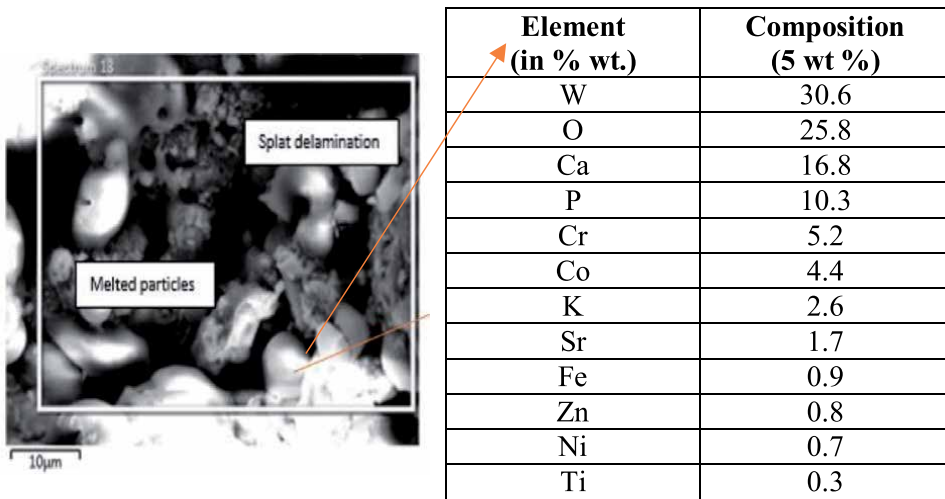


Figure 4. Optical micrograph of reinforced HA-C coating on Ti6Al4V alloy with element composition from EDX analysis.

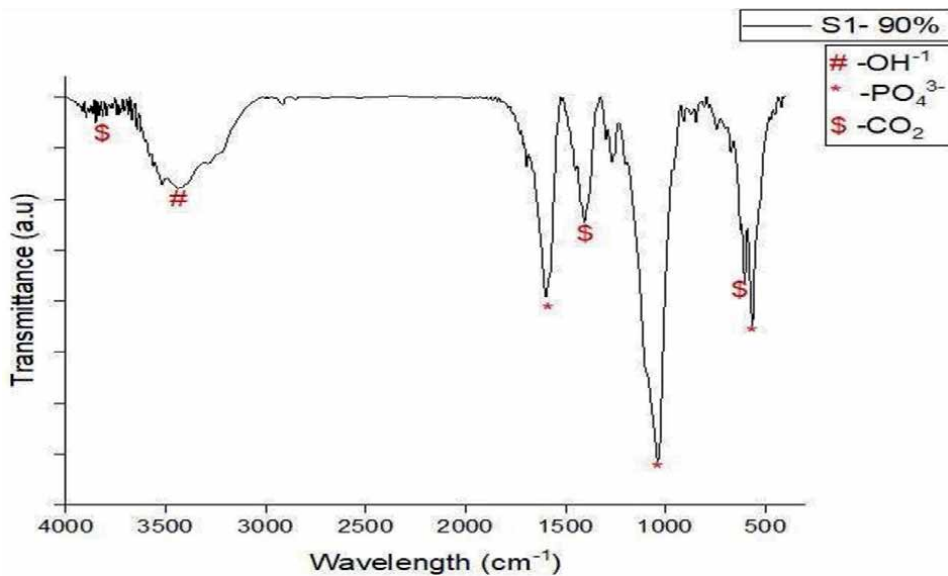


Figure 5. FTIR spectroscopy for plasma sprayed reinforced HA-C coating powder (a) 10 wt% CNT

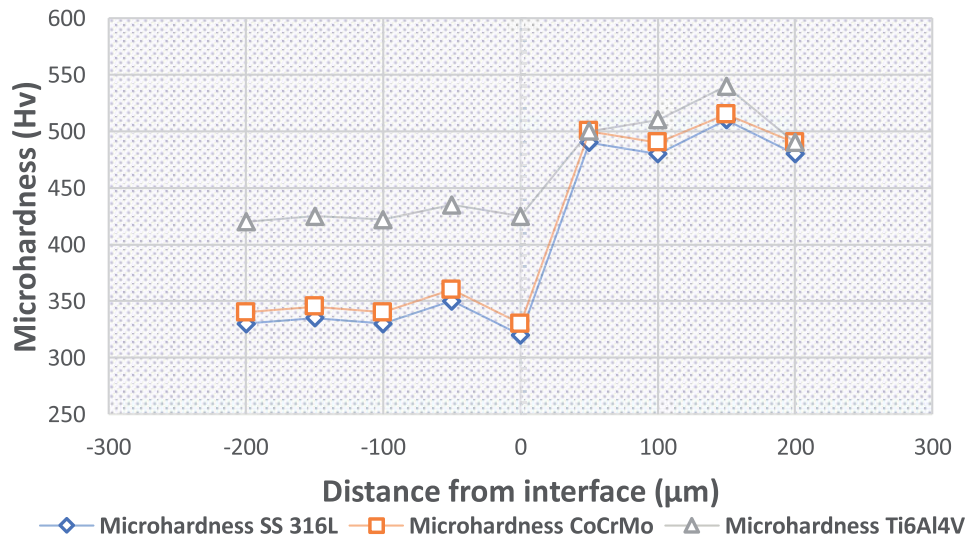


Figure 6.
Micro hardness profiles of reinforced HA-C coatings on SS 316L, CoCrMo, and Ti6Al4V alloy along the cross-section.

the reinforcement content. Enhanced Vickers hardness resulted in improved hydrophobicity for a 5% HAP/MWCNT coating [31]. The impression of Vickers indent **Figure 7** was observed under SEM for an accurate radial crack length measurement.

2.4 Bio-compatibility test of the coating

A direct contact method was used to perform cytotoxicity test with test samples. Samples of Pure SS-316L, CoCrMo, and Ti6Al4V, 5 wt% coatings, and 10 wt% coatings as per ISO 10993-5 are prepared. The test was done on 6 well plates. A fresh medium is used to replace the culture medium from the 3T3-L1 monolayer. On the cells test samples, negative & positive controls in triplicate were placed. After incubation at 38°C for 2, 15, and 30 days, the cell monolayer was examined



Figure 7.
Radial cracks on HA-CNT coating caused by microindentation.

microscopically for the response around the test samples. The reactivity was based on the zone of lysis, vacuolization, detachment, and membrane disintegration as per norms. Hemocytometer was used for viable cell count as shown in with cell suspension >90% viability for each experiment. MTT experiments revealed that graphene-doped hydroxyapatite composite had a substantial influence on 293T cell growth and excellent biomimetic mineralization, as demonstrated by in vitro bioactivity studies.

3. Results and discussion

3.1 Characterization of uncoated and plasma sprayed HA-C reinforced coating

Figure 8a revealed the microstructure study of surgical stainless steel SS-316 L, as equiaxed austenite grains which are as per the grade of this steel [32]. Annealing twins are also present in the structure which reveals the resemblance of the structure discussed in the handbook. SS-316 L is austenitic stainless steel where ‘L’ denotes low carbon content which is limited to 0.03%. A carbide-free austenitic and strain-free microstructure is produced in this steel that retains in the soluble carbon at an annealing temperature of 1010–1065°C (1700–1850°F) due to rapid quenching. **Figure 8b** depicts that there exists a hexagonal close-packed and face-centered cubic crystalline structure with CoCrMo alloy. Typically, at normal temperature, the face-centered cubic phase is predominant causing fcc to hcp transformation. The microstructural grain consists of bigger Co dendrites having an hcp structure with the smaller surrounding zones correspond to the embedded carbides which are recognized as M23C6 type. The analysis suggests that there is uniformity in porosity with fine grain structure. The microstructure of Ti6Al4V **Figure 8c** is compared with the standard microstructures from Metals Handbook (1975) and ASM Handbook (1992, 2001). The microstructure consists of equiaxed α grains (light) and intergranular β (gray), which corresponds to the grade of this alloy. EDAX analysis confirms the CA/P ratio in between 1.67–2.4 which is the desired ratio for long-term applications of the implant [33]. CNT-HA composites can generate bone-like apatite on the surface of the sample due to greater calcium ion concentration in SBF and higher negative charge, as well as more accessible nucleation sites.

It has been reported in the earlier research work [34] that thicker coatings have been more durable when implanted in the body environment. But thickness

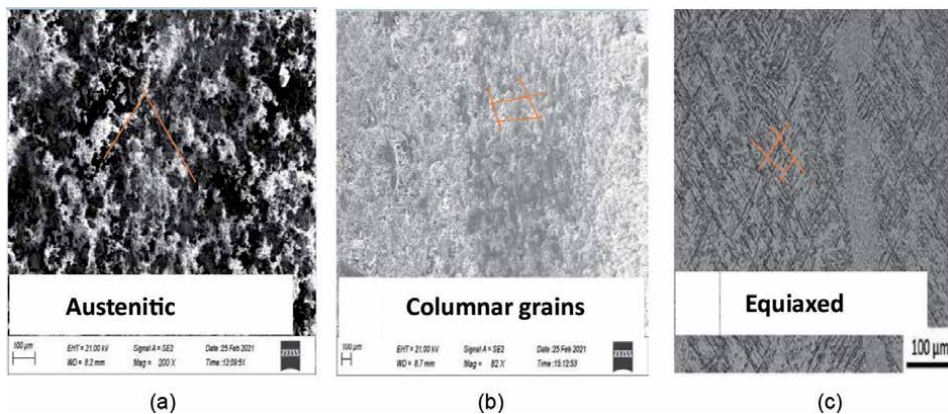


Figure 8. Optical micrograph of HA-C coating on (a) SS 316L, (b) CoCrMo, (c) Ti6Al4V.

more than the critical limit leads to self-disintegration of the coatings and this would lead to the problem of increased mechanical competence of coating [35]. High crystalline coating with higher thickness may lead to the formation of brittle material causing cracking under shear or bending forces. So it was aimed to produce coatings having thickness of 150–200 μm . Some randomly selected coated samples were measured along the cross-section for determining the coating thickness and reported in **Table 2**.

The porosity of the coating in bio implant application has an important role. Earlier literature proposed that the surface of the coating should be free from porosity and coating should act as a railing between the substrate and body fluid environment to avoid metal ion release in the body [36]. A slight decrease in porosity is observed with the addition of reinforcement of 10 wt% and 5 wt%. This decrease in porosity is due to the small size of reinforcement. The slight reduction is in agreement with the findings of Morks, [37, 38]. APS coated Ti samples have 0.40%–1.35% porosity, and in contrast to the higher side, the SS & CO samples exhibited marginally more porosity of the range 0.45%–1.40%. The surface of the bio implant must be rough enough for easy cell growth which improves the fixation of the bio implant in a physiological environment. Both Ra and Rz values of the reinforced HA-C coating on ally substrates are measured. Average values of surface roughness (i.e. Ra and Rz) of HA-C coatings on SS-316 L are 6.32 μm and 33.83 μm respectively, whereas for Ti6Al4V these are 6.06 and 39.41 μm respectively. It can be seen from the results that the average value of surface roughness (Ra) for uncoated samples is slightly lower than that of reinforced coatings on all the alloy substrates.

Figure 9 represents XRD spectra of HA-C coatings of samples tested under wet (SBF) conditions. All peaks in the case of coating correspond to HA. One small broad peak of CaO is observed in all reinforced HA coatings which confirms the presence of amorphous CaO in a very minute amount. An important observation shows the presence of tricalcium phosphate (α -TCP, β -TCP) and tetra calcium phosphate (TTCP) peaks between 29° to 32° angle range on all as-sprayed coatings. As the original powders do not have these phases. The severe failure and destruction of the implant were caused due to the rapid solubility of the amorphous phase in the human body’s physiological environment. The XRD analysis also depicts the sharp HA peaks which turn to be broader after coatings indicating the corrosion of crystalline materials to the amorphous phase during spray coating.

Coating Crystallinity was calculated at a 20° to 90° angle. Random HA-C coated samples were analyzed for average values and presented in **Table 3**. The fraction percentage of the amorphous (TCP & TTCP) phase was also shown.

Sr. No	Coating (APS)	Substrate	Coating thickness (μm)
1	Reinforced HA-C (10 wt%)	SS 316 L	178
2	Reinforced HA-C (5 wt%)	SS 316 L	184
3	Reinforced HA-C (10 wt%)	CoCrMo	188
4	Reinforced HA-C (5 wt%)	CoCrMo	190
5	Reinforced HA-C (10 wt%)	Ti6Al4V	190
6	Reinforced HA-C (5 wt%)	Ti6Al4V	193

Table 2.
Average coating thickness of plasma sprayed HA-C coatings.

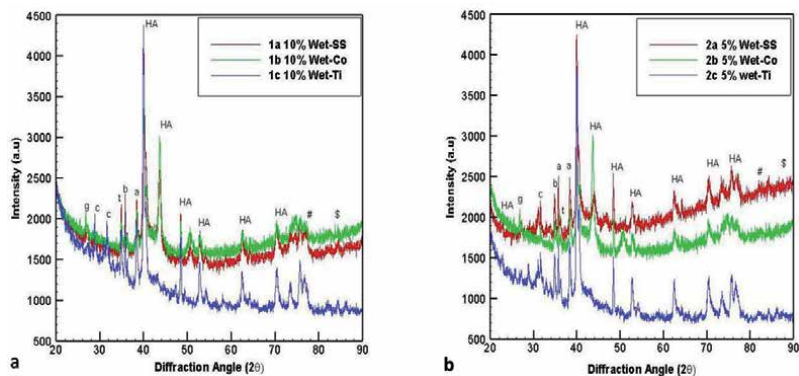


Figure 9.

XRD pattern for plasma sprayed reinforced HA-C coated wet samples. (a- 10 wt% & b- 5 wt% wet) HA, α -TCP, β -TCP, t-TTCP, c-CaO, g-graphene, #-Al₂O₃, \$-TiO₂.

Sr. no	Coating	Substrate	Crystallinity (%)	TCP, TTCP phases (%)
1	Reinforced HA-C	SS 316L	66.8	14.45
2	Reinforced HA-C	CoCrMo	66.9	14.24
3	Reinforced HA-C	Ti6Al4V	68.5	14.12

Table 3.

Crystallinity, TCP and TTCP phases in reinforced HA-C coatings.

3.2 Corrosion and sliding wear performance

3.2.1 Corrosion (electrochemical polarization) test

Corrosion behavior of all coated samples are evaluated by electrochemical polarization test in simulated fluid as proposed by Kokubo and Takadama [39]. The primary reason to use Tafel polarization was to evaluate corrosion current density of all HA-CNT coatings in simulated body fluids whereas Potentiodynamic measurement were carried out to study the passive behavior of the coatings. Tafel polarization measurement were carried out starting from -250_{OCP} mV to $+250_{\text{OCP}}$ mV with a scan rate of 1 mV/s, whereas Potentiodynamic polarization were carried out starting from -250_{OCP} mV to 1600_{SCE} mV. **Table 4** represents the polarization test results. The corrosion current in the case of SS 316 L is more as compared to that of CoCrMo and Ti6Al4V, hence it can be inferred that corrosion resistance of Co and Ti-based alloy is more than that of SS. Also, the passivation range of Ti alloy obtained from potentiodynamic curves is comparatively larger than that of SS and Co alloy, which supports the results of the Tafel polarization method. The results obtained from Potentiodynamic polarizer suggests that all as sprayed HA-CNT coatings show passive behavior in simulated body fluids which support the low current density presented by Tafel polarization method.

3.2.2 Wear (Abrasive wear) and friction mechanism of bare and APS-coated specimens against steel

Morphological structure and hardness are the two main parameters affecting the wear resistance of any coatings. **Figure 10a** and **b** represents the micrograph image of the wear mechanism of the Ti sample during uniform directional sliding of HA-C coated specimen. SEM micrograph after wear test exposure shows uniform and continuous wear. It can be observed that wear tracks are visible due to abrasive

Specimen	E corr. (mv)	I corr. (μ A)	β a (mv)	β c (mv)
SS 316L	-497.814	1.432	102.432	40.870
CoCrMo	-420.122	1.477	102.490	40.015
Ti ₆ Al ₄ V	-247.365	1.598	105.415	133.322

Table 4. Result of Tafel polarization test of reinforced HA-C coating on SS 316L, CoCrMo and TTTi6Al4V in SBF solution.

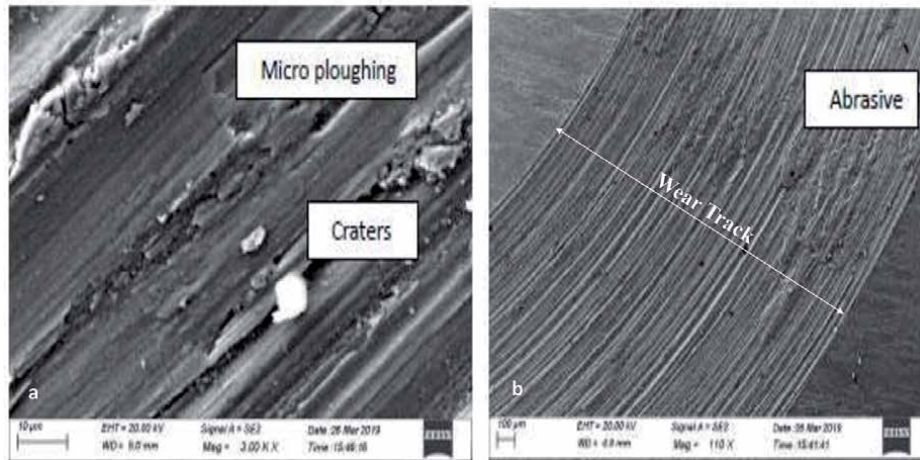


Figure 10. Wear scar micrograph of APS- sprayed HA-C coatings against steel ball (a- wear mechanism & b- wear path).

action on the both uncoated and coated surface. The micrograph also shows the small debris by abrasion. SEM images revealed the presence of areas of cracks and fractures due to plastic deformation, which is attributed to abrasive wear [40]. In the HA-CNT wear track, the image depicts smaller craters and a huge area of abraded surface. Fracture and chipping form the crater, while abrasive wear results in the rough surface.

Average Weight loss (kg/m^2) of uncoated samples was 0.14, 0.12 and 0.09 kg/m^2 respectively whereas for reinforced HA-C coating it was 0.24, 0.22 and 0.18 kg/m^2 respectively. It may be observed from the wear results that weight loss of metallic substrates is comparatively lower than that of all as-sprayed coatings on alloy substrates. It can be observed from the plotted results from **Figure 11** that, the wear volume was reduced up to 75% with the improvement in the wear resistance of reinforced HA-C coatings with 10 wt% and 5 wt% reinforcement. This improvement is because of the increased fracture toughness and elastic modulus.

The average wear rate and friction coefficient fall into a near mild wear regime, with values ranging from 10 to 7 to 10⁻⁴ mm^3/Nm [41]. The tribological test parameters were chosen with the conditions of medical implants working inside the human body, specifically the failure of the femoral head within the acetabular cup of the hip joint. Normally 0.8–2.5 MPa of stress is considered in a hip joint while walking [42]. The HA-C coating has to withstand a maximum frictional force for a minimum period of 20 years [43]. To compensate the entire working life a high value of 10 N load is kept during the entire test.

Surface hardness, toughness, spraying technique, and contact pressure are considered as the significant effecting factors on the coefficient of friction value. **Figure 12** represents the accumulated mean CoF from 0.35 to 0.42 due to the

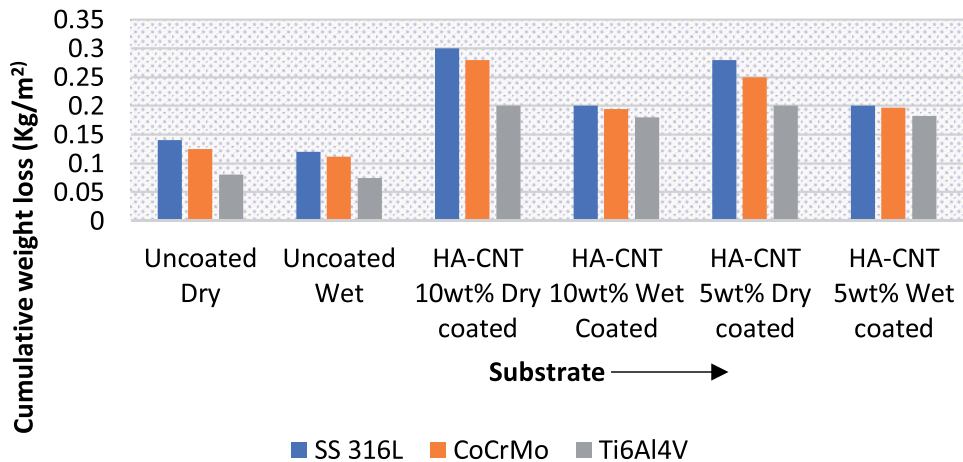


Figure 11. Variation in wear loss (kg/m^2) of uncoated, 10 wt% and 5 wt% HA-C coatings alloy in dry and wet (SBF) condition.

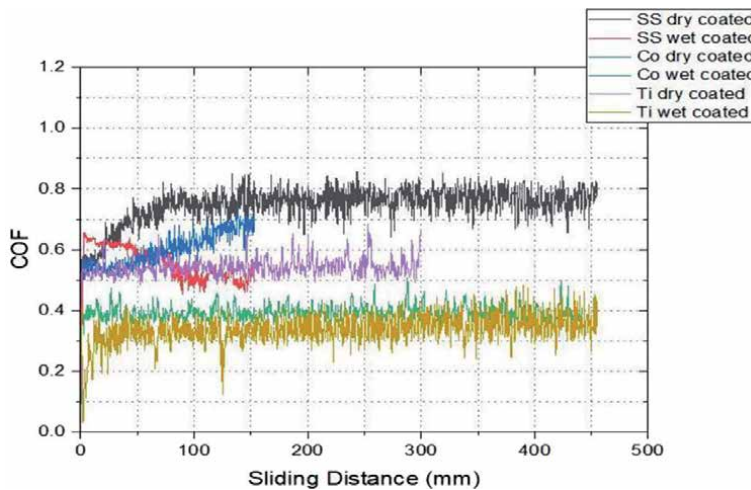


Figure 12. Average CoF curves for APS coating against steel ball SAE 52100 at contact pressure of 2000 MPa. (a- sliding distance vs CoF & b- time vs CoF curve).

varying contact pressure of the steel ball. The effect of the spray technique is the drop in mean CoF up to 0.37 for the Ti coated samples in wet (SBF) conditions. The total mass loss study demonstrated that the presence of PBS in the electrolyte solution tended to exacerbate the deterioration of the alloy under the circumstances examined, which was also verified by the 3D analysis of the wear track geometry [44]. As hardness of counter body governs the tribological failure, so it primarily influences the specific wear rate. Ti6Al4V alloy has shown maximum wear resistance among all uncoated and coated specimens. Improvement in wear resistance may be observed with the incorporation of reinforcement in the case of HA coatings. There is a slight decrease in CoF from 0.8 to 0.6 with the addition of reinforced CNT into the HA matrix. As the graphene layer is peeled off from the CNT surface it offers lubrication causing the decrement in CoF value.

A tensile force ≥ 11 GPa is required to remove the single graphite layer from multi-walled CNT along its axial direction [39]. The evaluated tensile stress in the wear track in the current study was ~ 12 GPa, which was found to be sufficient for the removal of

the graphene layer from CNT. Similar results were seen when the test was carried out under SBF immersed solution. As the body fluid would offer additional lubrication on the implant surface it would decrease the amount of wear debris thus, expecting better performance of coating inside the human body. Tribo Mechanical wear is the most common wear mechanism, as seen by abrasion, adhesion, and cracking [45].

Figure 13 represents the wear depth profile and 3D topography of HA-C coating against SAE 52100 steel. The wear volume against the track was calculated (using average value of cross-section area from three variable experimental sets with track diameter) from the profile and found to be 0.25 mm^3 for HA-CNT coating. With CNT addition it decreases up to 75% resulting in a “reduced probability of disturbance in the biological environment around the implant”. The $15.70 \text{ }\mu\text{m}$ of wear depth is recorded which is maximum for both types of coatings versus a steel ball.

3.3 Bio-compatibility evaluation of HA-CNT coatings

MTT assay was used to determine the mitochondrial activity and cellular viability of 3T3-L1 viable cells on uncoated and reinforced HA-CNT coatings. When incubated with viable cells, the reduction reaction of MTT reagent causes it to be reduced into purple formazan crystal. The cell viability is indirectly reflected by the absorbed formazan crystal. As a positive control, cells seeded on tissue culture plates are used.

3.3.1 Cell viability study

Morphology of cell-seeded on bare SS-316 L, CoCrMo, and Ti6Al4V substrates after 2 days were analyzed. Cell viability (%) is shown in the histogram presented in **Figure 14**, after 2, 15, and 30 days of incubation. It may be observed that cell viability on Ti6Al4V substrate was 72%, 81%, and 88% respectively whereas it was 68%, 78%, and 85% on CoCrMo and 66%, 78%, and 84% respectively on SS-316 L. Further, cells were comparatively less viable initially on all the three alloy substrates than that of the grown cells on the tissue-cultured plate ($p, 0.05$), but viability increased with exposure time duration.

The morphology of 3T3-L1 cells seeded on reinforced HA-CNT with 10 wt% and 5 wt% coatings (as-sprayed) on all Ti6Al4V alloy samples is shown in micrographs presented in **Figure 15a–d**, respectively. According to the viability results, cell viability of 5 wt% reinforced HA-CNT coatings is lower than that of 10 wt%

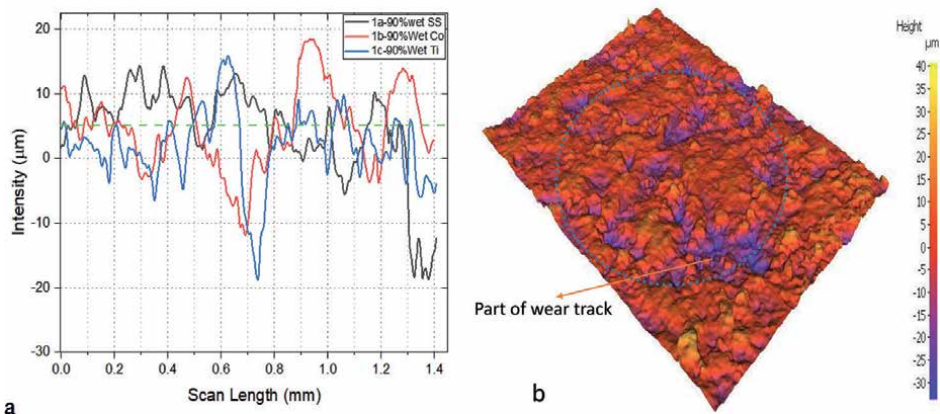


Figure 13.
(a) Wear depth profile and (b) 3D topography for APS coated sample.

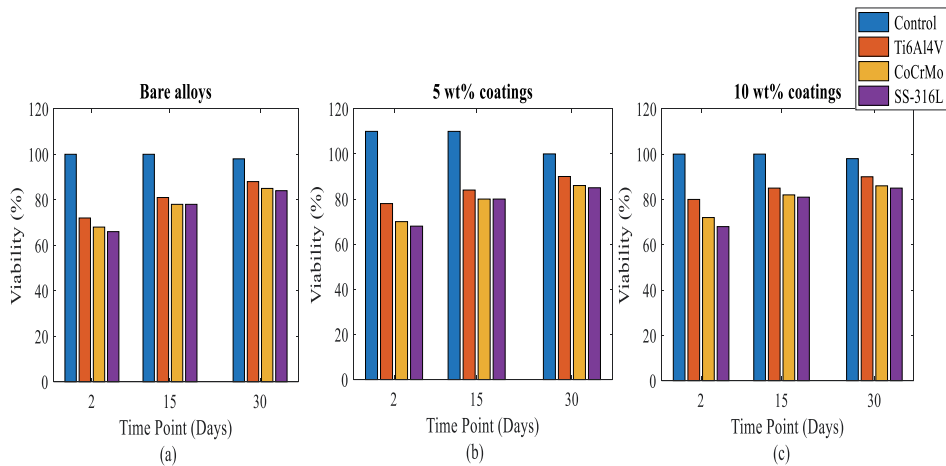


Figure 14. Viability of 3T3-L1 cells on Ti6Al4V, CoCrMo and SS-316L alloy from 2 to 30 days.

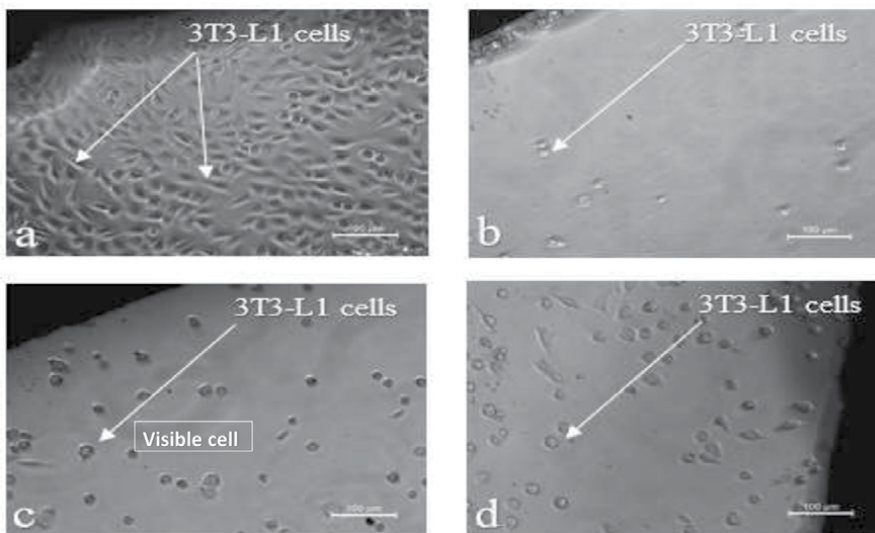


Figure 15. SEM (BSE) image of 3T3-L1 cells seeded on (a) control (b) bare Ti6Al4V (c) 5 wt% Ti6Al4V (d) 10 wt% Ti6Al4V.

coatings after 2 and 15 days of exposure, respectively. However, after 30 days of exposure, the viability of all as-sprayed coatings was comparable.

3.3.2 Cell proliferation study

Following the Cellular viability study viable cell count of 3T3-L1 cells on bare and coated substrates, the alloy was determined by staining them with 0.4% trypan blue at 1:5 ratios and counting them using a hemocytometer for cell proliferation study. Each experiment used a cell suspension with greater than 95% viability, as discussed in the experimental procedure. The difference in proliferation rates was found to be significant for alloy substrates and tissue culture plates ($p < 0.05$). Cell count on tissue culture plate (i.e. 110, 500, and 1500) was remarkably greater than that of alloy substrates (i.e. 48, 288, 365 for Ti6Al4V, 40, 218, 320 for CoCrMo and 32, 216, 310 for SS-316 L) after 2, 15 and 30 days respectively. A similar pattern with

a slight increase in cell count was also seen in reinforced HA-CNT coatings with different wt% ratios. The *in vivo* bone creation of CNT-coated Nanofillers was dramatically accelerated by greater bone mineral density and up-regulated osteogenic signs (ODN, OCN, BMP2) of bone-forming cells [46].

The reason for higher proliferation on HA-CNT coating as compared to the uncoated metallic substrate is justified by previous researchers that “hydroxyapatite once implanted into the body can easily react with physiological fluids and form a tenacious bond to hard and soft tissues through cellular activity”. Another cause that gives an idea about the superior proliferation rate of coatings is the difference in surface roughness between porous HA-CNT coating and smooth bare metallic alloy substrates. Cytocompatibility and Osseointegration of the bone cement can be controlled by adjusting the MWCNT coating [47]. Furthermore, it may be observed from the results of this study that the proliferation rate on a tissue culture plate was comparatively higher than on all HA coatings due to their special design to enhance cell growth.

4. Conclusions

The HA-CNT coatings with different wt.% was processed by air plasma spray on alloy samples. The characterization and tribological properties comparatively were investigated:

HA-CNT composites could be successfully synthesized using the air plasma spraying method. Reinforced CNT has not shown any adverse effect on densification. The uniform and improved densification of hydroxyapatite microstructure are because of the high electrical and thermal conductivity of nanotubes.

The computed tensile stress in the wear track was ~12 GPa which, was achieved because of the well retained peeled off graphene layers. Both the 10 wt% and 5 wt% HA-C coatings form dense morphological structures. Due to high interstitial bonding of HA with CNT matrix the cracks were properly bridged and fracture energy was fully absorbed causing a better hardening mechanism.

The wear mechanisms revealed by APS-sprayed HA-C coating on SS 316 L and CoCrMo that, due to higher contact stress a small amount of carbon adhesion with minor plastic deformation of austenitic grains took place. However, in the case of Ti6Al4V coatings exhibited brittle cracking, spalling and abrasive grooves.

An improved wear resistance by 75% with the lesser volume of wear debris generation was seen as the 10 wt% and 5 wt% CNT reinforcement was added to plasma spray HA coating. The lubrication provided by peeled off graphene layer from CNT decreases the CoF on the coated surface. CNTs content reduces the wear particle size (HA-CNT: 0.15–3.4 μm).

Contact pressure, hardness of counter body, spraying technique, and coating reinforcement with Hydroxyapatite are the major influencing parameters from the investigation.

Biocompatibility of all HA-CNT coatings was improved and is relatively higher than that of bare alloys.

Control > as sprayed reinforced 10 wt% HA-CNT coatings > as sprayed reinforced 5 wt% HA-CNT coatings > Bare Ti6Al4V > CoCrMo > SS-316L.

Therefore, the outcome of the present research work could be used to improve the efficacy with enhanced service life of medical implants and other such applied components. A very attractive solution to existing problem of HA with different reinforcement material could be established by HA-CNT composites and coatings. The process of HA-CNT coatings with different wt% compositions are user friendly and capable to provide alternative solutions to other high end coating techniques and reinforcement materials.

Acknowledgements

The authors would like to express their gratitude to Plasma Spray Coats in Bangalore, India, for providing the coating facility. The authors would like to thank VJTI, Mumbai, as well as IIT Bombay, India, for providing testing facilities such as SEM, EDX, XRD, Nano-indentation, and Non-contact profilometer. A special extended thanks to Sree Chitra Tirunal Institute of Medical Science and Technology, Kerala for helping in performing the in-vitro biocompatibility test. This research is not supported by any financial grant from a public or private funding agency.

Disclosure statement


No potential conflict of interest was reported by the author(s).

Author details

Mahesh M. Sonekar* and Walmik S. Rathod
Department of Mechanical Engineering, Veermata Jijabai Technological Institute,
Mumbai, India

*Address all correspondence to: mmsonekar_p16@me.vjti.ac.in

IntechOpen

© 2022 The Author(s). Licensee IntechOpen. This chapter is distributed under the terms of the Creative Commons Attribution License (<http://creativecommons.org/licenses/by/3.0>), which permits unrestricted use, distribution, and reproduction in any medium, provided the original work is properly cited. 

References

- [1] Hansen Douglas C. Metal corrosion in human body: The ultimate bio corrosion scenario. *The Electrochemical Society Interface*. Summer. 2008;**17**(2):17-31. DOI: 10.1149/2.f04082if Corpus ID: 45331227
- [2] Kamachimudali U, Sridhar TM, et al. Corrosion of bio implants. *Sadhana Academy Proceedings in Engineering Science*. August 2003;**28**(3&4):601-637. ISSN: 0256-2499@printed in India
- [3] Arumugam S, Ju Y. Carbon nanotubes reinforced with natural/synthetic polymers to mimic the extracellular matrices of bone: A review. *Material Today Chemistry*. 2021;**20**:1004-1020
- [4] Murugan NC, Sathishkumar M, et al. Novel graphene-based reinforced hydroxyapatite composite coatings on titanium with enhanced anti-bacterial, anti-corrosive and biocompatible properties for improved orthopedic applications. *International Journal of Pharmaceutical, Chemical & Biological Sciences*. 2016;**6**(4):432-442
- [5] Paital SR, Dahotre NB. Calcium phosphate coatings for bio-implant applications: Materials, performance factors, and methodologies. *Materials Science and Engineering: R: Reports*. 2009;**66**(1-3):1-70
- [6] Wang M. Developing bioactive composite materials for tissue replacement. *Biomaterials*. 2003;**24**: 2133-2151
- [7] Shi G, Rouabhia M, et al. A novel electrically conductive and biodegradable composite made of polypyrrole nanoparticles and polylactide. *Biomaterials*. 2004;**25**(13):2477-2488
- [8] Morks M, Kobayashi F. Influence of spray parameters on the microstructure and mechanical properties of gas-tunnel plasma sprayed hydroxyapatite coatings. *Materials Science and Engineering: B*. 2007;**139**(2-3):209-215
- [9] Senraa MR, de Limaa RB, et al. Thermal characterization of hydroxyapatite or carbonated hydroxyapatite hybrid composites with distinguished collagens for bone graft. *Materials Research and Technology*. 2020;**9**(4):7190-7200
- [10] Habibovic P, Kruyt MC, et al. Comparative in vivo study of six hydroxyapatite-based bone graft substitutes. *Journal of Orthopaedic Research*. 2008;**26**(10):1363-1370
- [11] Chaudhary B, Panwar V, et al. Effect of addition of hydroxyapatite as secondary filler in CNT-reinforced polypropylene hybrid composites. *Polymers and Polymer Composites*. 2021;**29**:888-896
- [12] Khor KA, Dong AL, et al. Microstructure investigation of plasma sprayed HA/Ti6Al4V composites by TEM. *Material Science and Engineering-A*. 2000;**281**:221-228
- [13] Prodana M, Stoian AB, Burnei C, Ionita D. Innovative coatings of metallic alloys used as bioactive surfaces in implantology: A review. *Coatings*. 2021;**11**(649):1-20
- [14] Tsuia YC, Doyleb C, et al. Plasma sprayed hydroxyapatite coatings on titanium substrates Part 1: Mechanical properties and residual stress levels. *Biomaterials*. 1998;**19**(22):2015-2029
- [15] Kantesh B, Yao C, et al. Tribological behaviour of plasma-sprayed carbon nanotube reinforced hydroxyapatite coating in physiological solution. *Acta Biomaterialia*. 2007;**3**:944-951
- [16] Zheng X, Huang M, Ding C. Bond strength of plasma sprayed

- hydroxyapatite/Ti composite coatings. *Biomaterials*. 2000;**31**(8):841-849
- [17] Kantesh B, Rebecca A, et al. Plasma sprayed carbon nanotube reinforced hydroxyapatite coating and their interaction with human osteoblasts in-vitro. *Biomaterials*. 2007;**28**:618-624
- [18] Gopi D, Shinyjoy E, et al. Development of carbon nanotubes reinforced hydroxyapatite composite coatings on titanium by electrodeposition method. *Corrosion Science*. 2013;**73**: 321-330
- [19] Zalnezhad E, Musharavati F, et al. Tribo-mechanical properties evaluation of HA/TiO₂/CNT nanocomposite. *Nature Research Scientific Reports*. 2021;**11**:1867
- [20] Huang B. Carbon nanotubes and their polymeric composites: The applications in tissue engineering. *Bio manufacturing Reviews*. 2020;**5**: 3105-3117
- [21] Godwina G, Julyes Jaisingh S, et al. Wear and corrosion behaviour of Ti-based coating on biomedical implants. In: *Surface Engineering*. Vol. 37, No. 1. Taylor & Francis; 2020. pp. 32-41
- [22] Yourong L, Fischer TE. Comparison of HVOF and plasma-sprayed alumina-titania coatings microstructure, mechanical properties and abrasion behaviour. *Surface and Coatings Technology*. 2003;**167**:68-76
- [23] Gell M, Jordan EH, et al. Development and implementation of plasma sprayed nanostructured ceramic coatings. *Surface and Coatings Technology*. 2001;**146-147**:48-54
- [24] Coathup MJ, Burn JB, et al. Role of Hydroxyapatite coating in resisting wear particle migration and osteolysis around acetabular components. *Biomaterials*. 2005;**26**:4161-4169
- [25] Canuto BR, de Menezes K, Rodrigues F, et al. Recent advances in the use of carbon nanotubes as smart biomaterials. *Journal of Materials Chemistry B*. 2019;**7**:1343-1360
- [26] Tadashi K, Hiroaki T. How useful is SBF in predicting in vivo bone bioactivity. *Biomaterials*. 2006;**27**:2907-2915
- [27] Awwaluddin M, Prajitno DH, et al. Mechanical properties and corrosion behavior of novel β -type biomaterial Zr-6Mo-4Ti-xY alloys in simulated body fluid Ringer's lactate solution for implant applications. *AIMS Materials Science*. 2020;**7**(6):887-901
- [28] Dey A, Mukhopadhyay AK. Characterization of Microplasma sprayed hydroxyapatite coating. *Journal of Thermal Spray Technology*. 2009;**18**: 578-592
- [29] Dey A, Mukhopadhyay AK, et al. Development of hydroxyapatite coating by microplasma spraying. *Materials and Manufacturing*. 2009;**24**:1321-1330
- [30] Yang Z, Liu J, et al. Investigation on physicochemical properties of graphene oxide/nano-hydroxyapatite composites and its biomedical applications. *Journal of the Australian Ceramic Society*. 2021;**57**:625-633
- [31] Stango AX, Vijayalakshmi U, et al. Electrochemically grown functionalized -Multi-walled carbon nanotubes/ hydroxyapatite hybrids on surgical grade 316L SS with enhanced corrosion resistance and bioactivity. *Colloids and Surfaces B: Biointerfaces*. 2018;**171**: 186-196
- [32] ASM Handbook. Properties and Selection: Irons, Steels and High Performance Alloys. Vol. 1. Materials Park: ASM Publication; 2001

- [33] Balagna C, Spriano S, Faga MG. Characterization of CoCrMo alloys after a thermal treatment for high wear resistance. *Materials Science and Engineering*. 2012;**32**:1868-1877
- [34] Levingstone Tany J, Optimization of plasma sprayed hydroxyapatite coatings, PhD thesis, 2006; School of Mechanical and Manufacturing Engineering, Dublin City University, Ireland.
- [35] Tranquilli AL, Lucino E, Garzetti GG, Romanini C. Calcium, phosphorus and magnesium intakes correlate with bone mineral content in postmenopausal women. *Gynecological Endocrinology*. 1994;**8**(1):55-58
- [36] Sergey VD. Calcium orthophosphate coatings, films and layers. *Progress in Biomaterials*. 2012;**10**(2). DOI: 10.1186/2194-0517-1-1. Published online 26 Sep 2012
- [37] Kwok CT, Wong PK, Cheng FT, Man H. C, Characterization and corrosion behaviour of hydroxyapatite coatings on Ti6Al4V fabricated by electrophoretic deposition. *Applied Surface Science*. 2009;**255**:6736-6744
- [38] Bansiddhi A, Sargeant TD, Stupp SI, Dunand DC. Porous NiTi for bone implants: A review. *Acta Biomaterialia*. 2008;**4**(4):773-782
- [39] Kokubo T, Kushitani HT, Sakka S, Kitsugu T, Yamanuro T. Solution able to reproduce in vivo surface structure changes in bioactive A-W glass ceramics. *Journal of Biomedical Material Research*. 1990;**81**:1705-1728
- [40] Solanke SG, Gaval VR, et al. Tribological studies of different bioimplant materials for orthopaedic application. *ASM Science Journal*. 2020;**38**(3&4):4-14
- [41] Kato K. *Friction and Wear of Passive Metals and Coatings*. Amsterdam: Woodhead Publishing; 2011. pp. 65-99
- [42] Ipavec M, Igljic A, Igljic VK, Sarkar K. Stress distribution on the hip joint articular surface during gait. *European Journal of Physiology*. 1996;**431**: R275-R276
- [43] Jorge Rituerto Sin, Investigation of the corrosion and tribocorrosion behaviour of metallic biomaterials, 2015, PhD thesis, Luleå University of Technology.
- [44] Neumann L, Freund KG, Sorenson KH. Long-term results of Chernley total hip replacement. *Journal of Bone Joint and Surgery*. 1994;**76**:245-251
- [45] Yu MF, Lourie O, Dyer MJ, Moloni K, Kelly TF, Rouff RS. Strength and breaking mechanism of multiwalled carbon nanotube under tensile load. *Science*. 2000;**287**:637-640
- [46] Fellah M, Labaiz M, et al. Tribological behavior of biomaterial for total hip prosthesis. *EDP Sciences*. 2017;**102**:1-8
- [47] Wang C, Yu B, et al. Incorporation of multi-walled carbon nanotubes to PMMA bone cement improves cytocompatibility and osseointegration. *Materials Science and Engineering: C*. 2019;**103**:109-123

Estimation of the Grain Trajectory and Engaging on the Material

Takenori Ono

Abstract

In this chapter, a numerical estimation of the grain trajectory in the grinding process is introduced. The topic describes a fundamental of the numerical theory of the grain trajectory, the estimation of the grain trajectory in the hemispherical grinding stone in the micro grooving process as an application of the numerical estimation.

Keywords: grinding process, grain trajectory, numerical model, hemispherical grinding stone, tool posture

1. Introduction

In this chapter, a theoretical evaluation method of the grain trajectory and its engaging process onto the material in the grinding is introduced. In the first topic, the geometric relationship between the abrasive grain and the material in the cylindrical grinding process, that is, the movement of the abrasive grain and the cutting distance to the material will be described using a mathematical model. In the next topic, we will explain how to theoretically evaluate the resistance generated in the entire working surface of the grindstone, starting from the model of cutting with one abrasive grain for grinding force. In the next topic, to introduce the application of the above topics, a theoretical model of the grain trajectory and engaging depth on the material in the curve generation grinding by the spherical grinding stone will be described. Finally, an evaluation method using a statistical method for basic grinding parameters (Ex. length of successive grains, depth of grain engaging) will be described briefly.

2. Basic theory of the grain engaging in the grinding process

In this section, a geometric relationship between the abrasive grain and the material in the cylindrical grinding is introduced [1]. **Figure 1** shows the schematic of the cylindrical grinding process. In this figure, a cylindrical grinding stone which has a radius of R engages onto the side surface of the cylindrical workpiece of which the radius r with a depth of engaging of Δ . Also, the prior abrasive grain of Q on the workpiece processes a grinding mark of SPR , and the subsequent grain of P in the same cross-section of the axis which contains the Q processes the mark of PBC to follow the prior mark. And the grain P removes the region of “BRC” which is filled by the hatching in the figure. In general, the P is named the “successive grinding grain (or cutting point)”, and the distance between QP is called “length of the

From this formula, since $r = \infty$ when replaced in the case of planner grinding and " $r < 0$ " in the case of internal cylindrical grinding, the maximum depth of each cases g_p and g_i can be expressed by following formulas, respectively.

$$g_p = \frac{v}{V} a \sqrt{\frac{2\Delta}{R}} \quad g_i = \frac{v}{V} a \sqrt{\frac{r-R}{Rr}} \quad (7)$$

In general, in various grindings, the maximum depth g is an indicator for the grinding force applied to an abrasive grain. If the binding degree (intensity) of the abrasive grain is constant during grinding, when g becomes large, excessive grinding force applies to the abrasive grain, the abrasive grain is easy to leave out from the working surface of stone ("shedding"). And conversely, when the g is small, the abrasive grain is difficult to leave out, and the chips are deposited in the vacancy of the working surface ("loading") and abrasive grains are worn out and the escape surface land (in cutting) expands ("glazing"). In general, the binding degree does not only depend on the material properties, but also depends on the conditions of stone and process including g .

In the next topic, the average depth of grain engaging is introduced. In this section, the average depth of cut is called " g' ", it may be considered to the average in the diagonal region that consloses the removal region PRCU which is described in **Figure 2**. However, in this discussion, the region is divided into curved triangles PRU and CRU, respectively. In the first step, the g' is considered in the PRU region. The PUC and PR are obtained by the following formula.

$$\begin{aligned} PUC : x^2 + y^2 &= R^2 \\ PR : \{x - (r + R - \Delta)(1 - \cos \gamma)\}^2 + \{y - (r + R - \Delta) \sin \gamma\}^2 &= R^2 \end{aligned} \quad (8)$$

In this region, two intersections between the arcs (PUC, PR) and the dashed line " $y = -x \tan \phi$ " (it is shown in **Figure 2**) are called H (x_1, y_1) and G (x_2, y_2). To approximate as $\cos \gamma \sim 1 - \gamma^2/2$, $\sin \gamma \sim \gamma$, $\tan \phi \sim \phi$, the x coordinates of each intersection (x_1, x_2) are obtained by the following formulas.

$$\begin{cases} x_1 = R \left(1 - \frac{\phi^2}{2}\right) - \frac{(r+R)^2}{2R} \gamma^2 + \frac{r+R}{2} (\gamma^2 + 2\gamma\phi) \\ x_2 = R \left(1 - \frac{\phi^2}{2}\right) \end{cases} \quad (9)$$

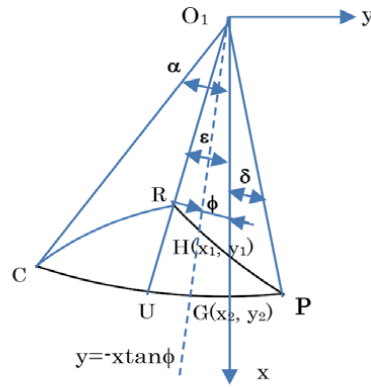
In **Figure 2**, the length of HG is a grinding depth at the angle of ϕ . However, therefore the angle of $\alpha + \beta$ is small enough in this figure, HG can be approximated as " $x_2 - x_1$ ", The engaging depth $g_1(\phi)$ at the angle of ϕ can be expressed as follows.

$$g_1(\phi) = x_2 - x_1 = \frac{r(r+R)}{2R} \gamma^2 - (r+R)\gamma\phi \quad (10)$$

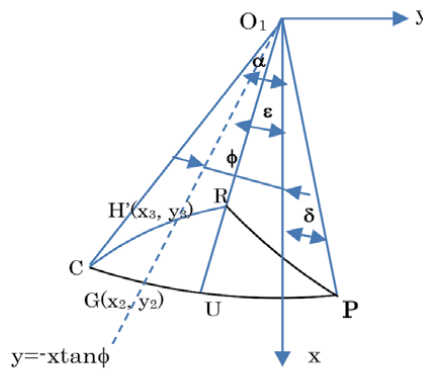
In the next step, g in the CRU region is considered. The RC can be expressed by the following formula.

$$RC : \{x - (r + R - \Delta)\}^2 + y^2 = r^2 \quad (11)$$

The x coordinate of the intersection of this arc and the line " $y = -x \tan \phi$ " x_3 which is the x coordinate of point H' can be obtained by the following formula.



(a) region PRU



(b) region CRU

Figure 2.
Schematics of the grain engaging depth.

$$x_3 = R - \Delta + \frac{R^2}{2r} \phi^2 \quad (12)$$

Therefore, the engaging depth $g_2(\phi)$ in this region is obtained by the following formula.

$$g_2(\phi) = x_2 - x_3 = \Delta - \frac{R(r+R)}{2r} \phi^2 \quad (13)$$

If the average depth g' is obtained using the above formulas (12) and (13), the following formula is obtained.

$$g' = \frac{1}{\alpha + \delta} \left[\frac{r(r+R)}{2R} \gamma^2 \int_{-\epsilon}^{\delta} d\phi - (r+R)\gamma \int_{-\epsilon}^{\delta} \phi d\phi + \Delta \int_{-\alpha}^{\epsilon} d\phi - \frac{R(r+R)}{2r} \int_{-\alpha}^{\epsilon} \phi^2 d\phi \right] \quad (14)$$

However, in **Figure 2**, if it can be approximated as $PB \sim SB/2$, and $\gamma = (2R/r)\delta$, and $PBC = SPR + SB + PBU$, the angle of ϵ can be placed with “ $\epsilon = \alpha - 2\delta$ ”. When the g' and ϵ are assigned to formula (15) and integrated the formula, the g' is obtained by the following formula.

$$\bar{g} = \frac{\delta}{\alpha + \delta} \left[2\Delta - \frac{R(r+R)}{r} \frac{\delta^2}{3} \right] \quad (15)$$

From of this formula (2):

$$\overline{O_2C} = \overline{O_1^2O_2^2} + \overline{O_1C^2} - 2\overline{O_1^2O_2^2} \cdot \overline{O_1C} \cos \alpha \quad (16)$$

the angle of α which is described in **Figure 1** can be obtained by following formula, with approximation as “ $\cos \alpha \sim 1 - \alpha^2/2$ ”

$$\alpha = \sqrt{\frac{2r\Delta}{R(r+R-\Delta)}} \cong \sqrt{\frac{2r\Delta}{R(r+R)}} \quad (17)$$

In addition, δ can be obtained from the following formula because $(av / V) / 2 \sim R\delta$.

$$\delta = \frac{a v}{2RV} \quad (18)$$

Finally, a formula of the length of the successive grains “a” is introduced. Although, grains on the working surface of the stone are arranged randomly, it is considered that they are arranged regularly at the average abrasive grain pitch w for simplifying discussion. In this case, since there are $1/w^2$ grains per unit area, w can be obtained if the number of particles per unit area is measured on the grinding wheel work surface. **Figure 3** shows an example of the arrangement of a grinding stone. In this figure, grains are regularly arranged on the lines A_1A_m and B_1B_m in parallel at the distance of w , and the same numbered abrasive grains on each line are arranged vertically. The grain A_m in this figure is feed to the prior grain B_1 to follow the line A_mB_1 by the relative motion during the grinding stone rotation and the material. In this situation, the line A_mB_1 coincides with the average of the length of the successive grains “a”. Before A_m passes through B_1 , abrasive grains A_1 to A_{m-1} on the line A_1A_m are pass through the same point. In this case, if the average width of the scrape marks generated in the workpiece finishing surface is b ($= (w/m) \cos \theta$). On the other hand, because $a = m w / \cos \theta$, the “a” can be obtained by the following simple formula with b and w .

$$a = \frac{w^2}{b} \quad (19)$$

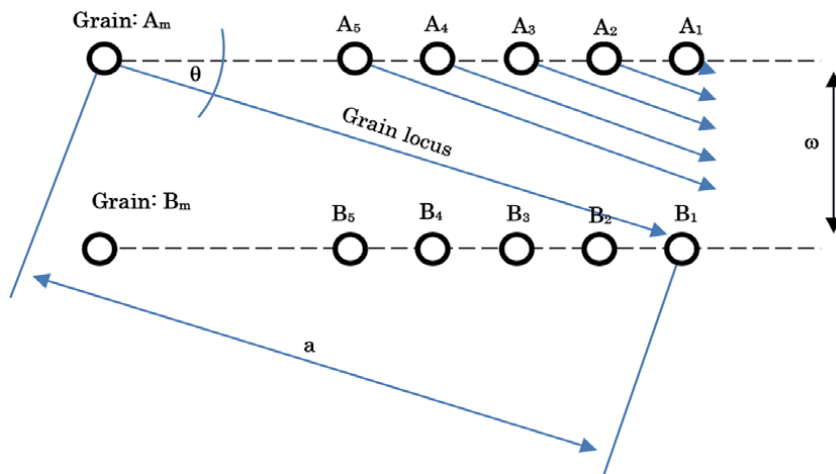


Figure 3. Successive grain engaging and concerned parameters a , w .

Based on this formula, if w and b can be obtained by actual measurement, also the a can be obtained.

3. Example: curve generation by the spheric grinding stone

In this section, to show the application of the previous section, a theoretical grain engaging model of the curve generation process by the spheric grinding stone is introduced. For example, an electro-plated micro-spherical grinding stone is shown in **Figure 4**. The spherical grinding stones are widely used for grooving or free form shapes of glass materials, optical lenses, and in recent years for processing joint parts (bone heads, etc.) of implants such as hip joints and knee joints. A trajectory of the abrasive grain draws a trochoid during the grinding process. However, its movement is changed by the tool posture and grinding conditions (Ex. rotational speed, feed rate, etc.). In this topic, to simplify the discussion, the theoretical model of a grain trajectory is illustrated. However, it is assumed that grains have the same profile (Ex. cone) and size are arranged with the periodic length of successive grains a and pitch “ w ” on the working surface.

Figure 5 shows the motion of a grinding stone in the grinding process. In this situation, the stone is fixed on the coordinate system of the machine tool (described as X, Y, Z) at any posture and the tool attitude changes by the grain locus. As shown in **Figure 5**, the fixed stone inclines to the $+X$ direction of the coordinate system of the machine tool $Y-Z$ at a lead angle of θ and to $+Y$ direction at a tilt angle of ϕ , respectively. The grinding stone with the nose radius ρ is then fed to the $+X$ direction of the machine tool coordinate system at a feed rate of f and rotational speed of ω , respectively. In this situation, the tool attitude in machine coordinate (X_t, Y_t, Z_t) is described by the following formulas:

$$\begin{cases} X_t = \sin \theta \\ Y_t = \cos \theta \sin \phi \\ Z_t = \cos \theta \cos \phi \end{cases} \quad (20)$$

If the center of the ball nose moves from point $A (X_A, Y_A, Z_A)$ to point $B (X_B, Y_B, Z_B)$ as shown in **Figure 5**, the angles of grain locus (vector AB) α and β are described by the following formulas:

$$\begin{cases} \alpha = \tan^{-1} \left(\frac{Z_B - Z_A}{\sqrt{(X_B - X_A)^2 + (Y_B - Y_A)^2}} \right) \\ \beta = \tan^{-1} \left(\frac{Y_B - Y_A}{X_B - X_A} \right) \end{cases} \quad (21)$$

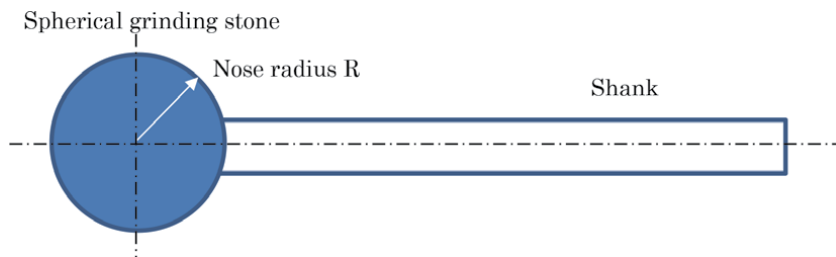
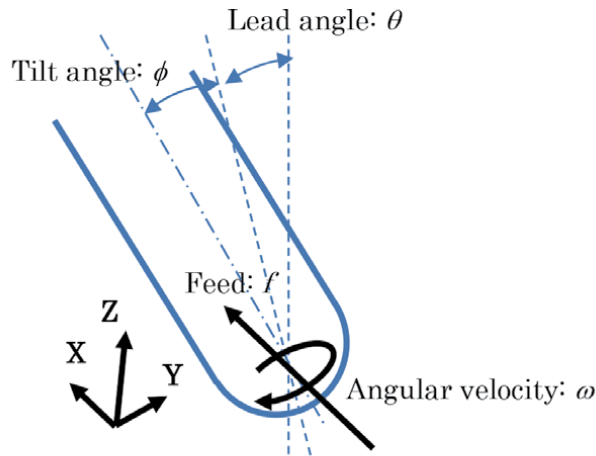
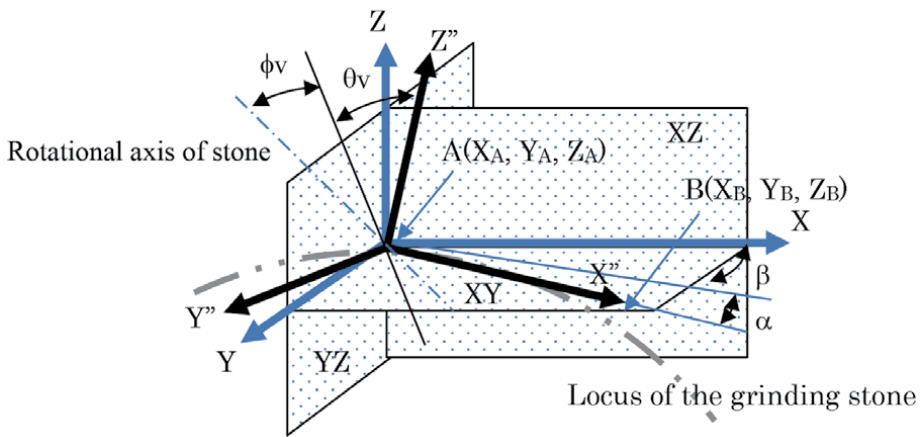


Figure 4.
An example of the (hemi) spherical grinding stone.



(a) Stone posture in global coordinate (X-Y-Z)



(b) Tool attitude on its locus

Figure 5.
 Changing of the stone attitude on its locus.

According to these formulas, the tool attitude in the coordinate of tool locus (X'' , Y'' , Z'') as shown in **Figure 5** can be described as follows:

$$\begin{cases} X''_t = \cos \alpha \cdot \cos \beta \cdot X_t + \cos \alpha \cdot \sin \beta \cdot Y_t - \sin \alpha \cdot Z_t \\ Y''_t = -\sin \beta \cdot X_t + \cos \beta \cdot Y_t \\ Z''_t = \sin \alpha \cdot \cos \beta \cdot X_t + \sin \alpha \cdot \sin \beta \cdot Y_t + \cos \alpha \cdot Z_t \end{cases} \quad (22)$$

Based on the formula (22), a lead angle of θ_v and a tilt angle of ϕ_v of grinding stone in a coordinate of grain locus are described as follows:

$$\theta_v = \tan^{-1} \left(\frac{X''_t}{Z''_t} \right) \quad (23)$$

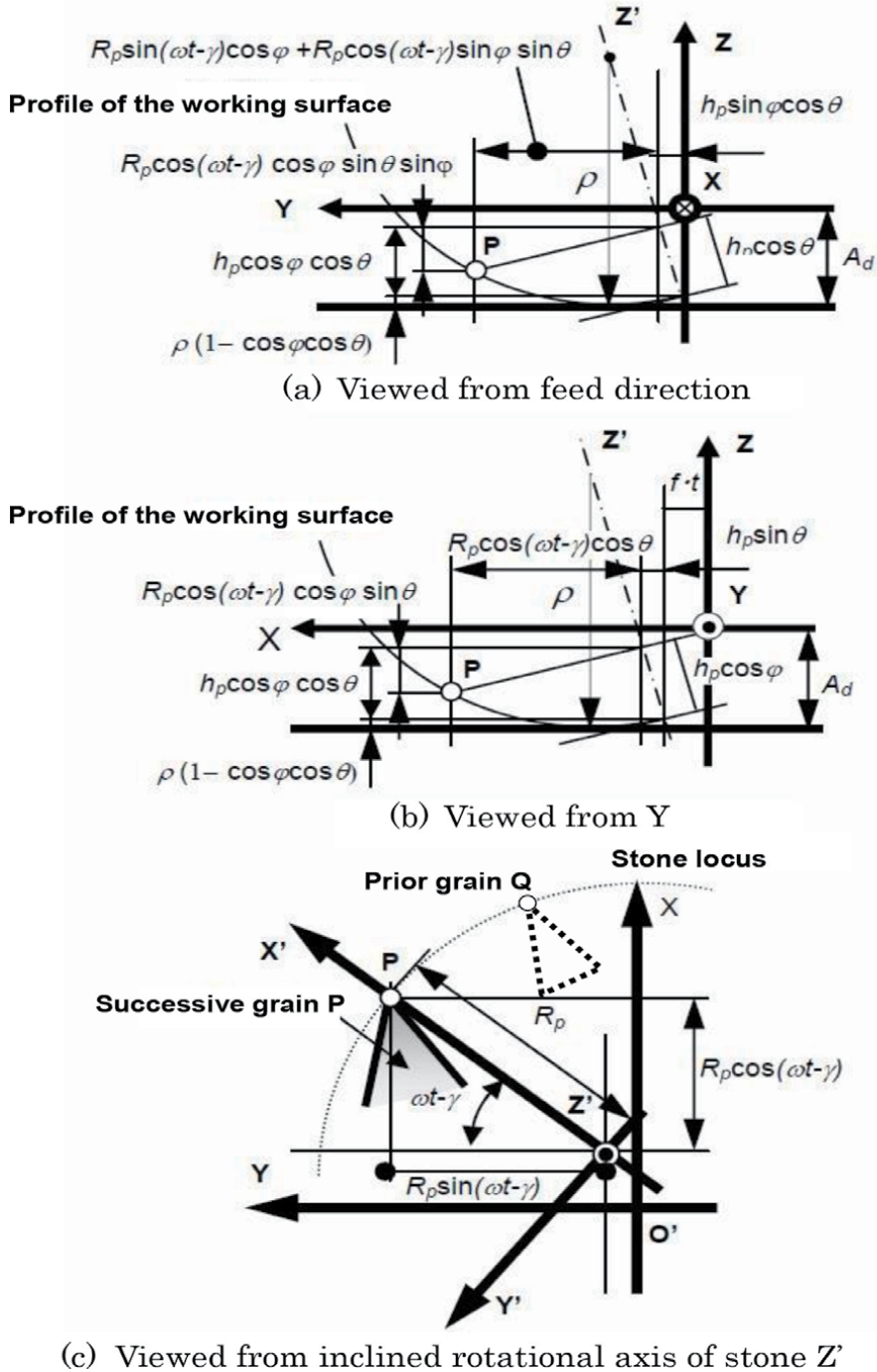


Figure 6.
 Geometry of the grain locus in curve generation.

small segments. The rotational radius R_p in each segment is determined with the actual (or theoretical) shape of the cutting edge. By calculating the engaging depth at each time step with calculated stone posture (inclination and tilting angles), the time series of the engaging depth can be calculated in any stone locus and attitude.

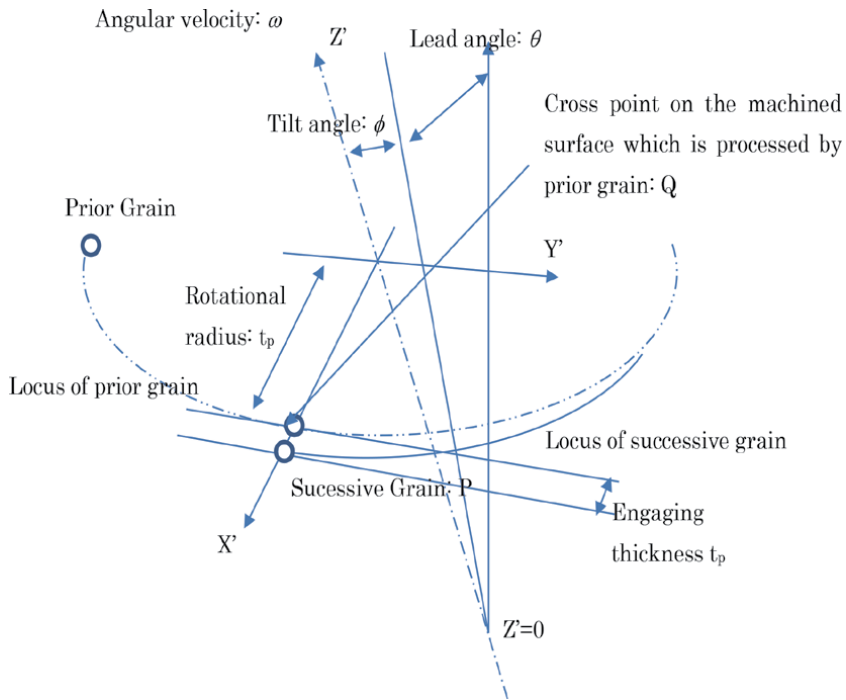


Figure 7. Schematics of the successive grain engaging by the spherical stone.

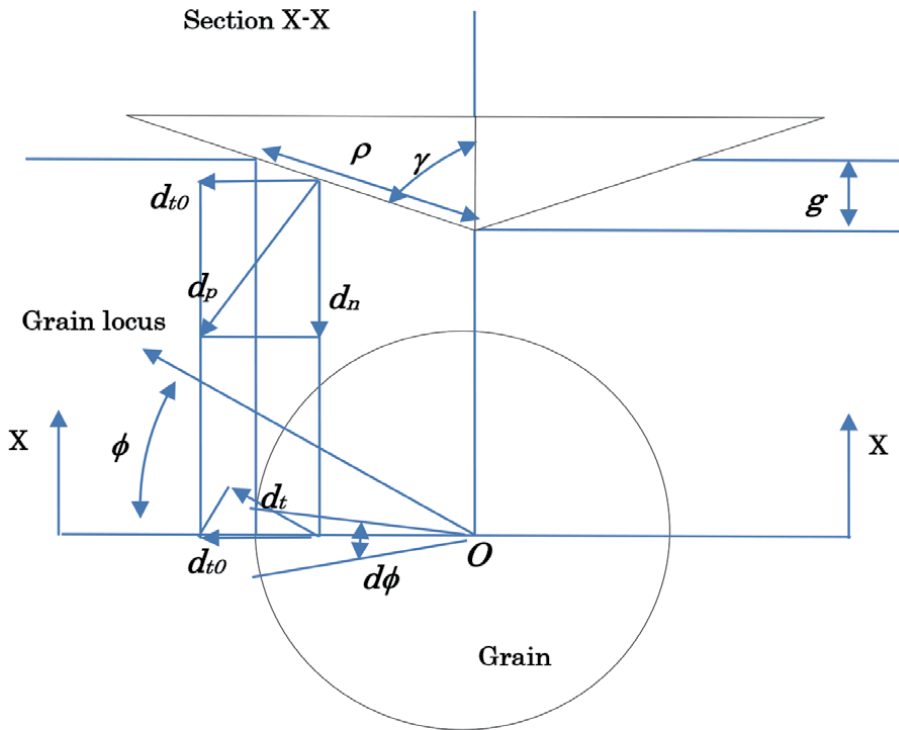
4. Estimation of the grinding force

In this section, a theoretical model of the grinding force in the grinding process is introduced. Generally, the profile of abrasive grains varies on the working surface with the nonperiodic arrangement. However, in this topic, to simplify the illustration, it is assumed that the grinding force is applied on only one abrasive grain (which is arranged on the work surface as periodic successive length and pitch) during grinding, and the conical grain which has the vertex angle of “ 2γ ” ($= 120$ deg.) as shown in **Figure 8**. In addition, each grain tip faces the radial direction of the cylindrical grinding stone. Although, a strict solution cannot be obtained, the above assumption can make to approximate the grinding force which is applied on one conical abrasive grain when the engaging on the material surface at the average abrasive depth of g' (which is described by formula (15)). In **Figure 8**, considering the region OAB (of which area: “ d_s ”) inclined only by φ from the abrasive grain feed direction, the grinding force d_p applied on grain’s conical surface. Assuming that there is no friction between the abrasive grain and the material for simplicity, d_p acts perpendicularly on the conical surface, and the rubbing direction dt of the abrasive grain shown in the figure and its vertical component dn can be decomposed into components as follows.

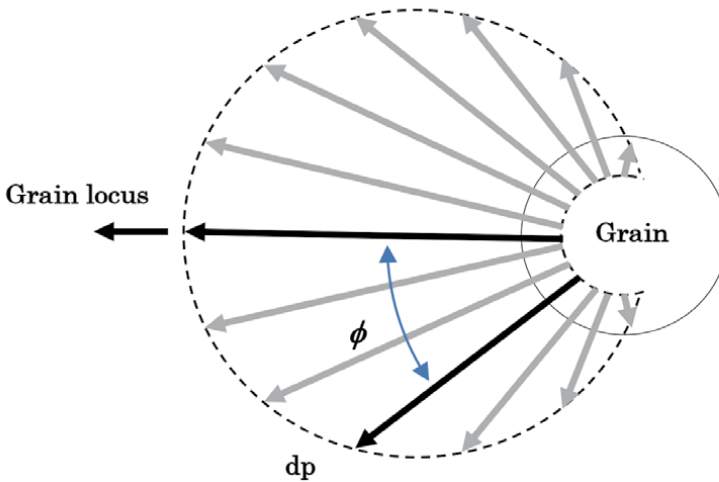
$$\begin{cases} dt = dp \cos \gamma \cos \phi \\ dn = dp \sin \gamma \end{cases} \quad (28)$$

The force per area (per perpendicular) to the abrasive grain’s feed direction is placed as the specific grinding force σ , and assuming that this is constant, d_p is obtained by the following formula.

$$dp = \sigma d_s \cos \gamma \cos \phi \quad (29)$$



(a) Tangential and normal components of the grinding force



(b) Relation between the d_p and ϕ

Figure 8.
 Grinding force which apply on an ideal (conical) grain.

The above formula shows that the distribution of d_p is circular as shown by the wavy lines of **Figure 8b**. As shown in **Figure 8a**, when a conical generatrix ρ in the grain profile, the conical surface d_s of the grain can be described as the following formula.

$$ds = \frac{\rho^2}{2} \sin \gamma d\phi \quad (30)$$

To assign this formula onto formula (29), also d_p can be obtained by the following formula.

$$dp = \frac{\rho^2 \sigma}{2} \sin \gamma \cos \gamma \cos \phi d\phi \quad (31)$$

And, to substitute this formula onto the formula (28) the two components of the grinding force d_t , d_n can be obtained by the following formula.

$$\left(\begin{array}{l} dt = \frac{\rho^2 \sigma}{2} \sin \gamma \cos^2 \gamma \cos^2 \phi d\phi \\ dn = \frac{\rho^2 \sigma}{2} \sin^2 \gamma \cos \gamma \cos \phi d\phi \end{array} \right) \quad (32)$$

And, to integrate these two formulas by angle ϕ , the tangential component t and its vertical component n of the grinding force are obtained from the following formulas.

$$\left(\begin{array}{l} \bar{t} = \int_{-\pi/2}^{\pi/2} \frac{dt}{d\phi} d\phi = \frac{\pi \rho^2 \sigma}{4} \sin \gamma \cos^2 \gamma = \frac{\pi \sigma}{4} \bar{g} \sin \gamma \\ \bar{n} = \int_{-\pi/2}^{\pi/2} \frac{dn}{d\phi} d\phi = \rho^2 \sigma \sin^2 \gamma \cos \gamma = \sigma \bar{g}^2 \sin \gamma \tan \gamma \end{array} \right) \quad (33)$$

The number of grains j in the grinding region PBC (described in **Figure 1**) can be obtained by the following formula.

$$j = \frac{R(\alpha + \delta)f}{\omega^2} \quad (34)$$

By three formulas, (15), (33), and (34), the tangential component F_t and its vertical component F_n of the total grinding force applied on the working surface can be obtained by the following formula.

$$\left(\begin{array}{l} Ft = j\bar{t} = \frac{\pi \sigma Rf}{4 \omega^2} \frac{\delta^2}{\alpha + \delta} \left[2\Delta - \frac{R(r+R)\delta^2}{r} \frac{\delta^2}{3} \right]^2 \sin \gamma \\ Fn = j\bar{n} = \sigma \frac{Rf}{\omega^2} \frac{\delta^2}{\alpha + \delta} \left[2\Delta - \frac{R(r+R)\delta^2}{r} \frac{\delta^2}{3} \right]^2 \sin \gamma \tan \gamma \end{array} \right) \quad (35)$$

If the above components of the grinding force are measured with experiments, and the half vertex angle γ is assumed of 60 deg., the experimental formula of σ can be obtained with a converse solution of the formula (35) [2].

5. Remarks: Statistical approaches

In the final section of this chapter, an evaluation of the grain locus by a statistical approach is discussed. During the previous sections, it was obtained based on (like a) “fly-cutter” model in which abrasive grains are arranged with “equal heights” at

equal length and pitch. However, this model cannot duplicate a profile in the actual grinding stone correctly, also the length of the successive grains and pitch are different from that on the actual working surface. Generally, these parameters have a statistical distribution. Therefore, to understand this phenomenon, an attempt to evaluate grinding parameters by statistical considerations has been reported from about 1960's [3–8]. For example, Matsui and Shoji, they proposed the statistically model for length and engaging depth of the successive grains (for more details, refer to their reports [6, 7]). However, generally, it is required the highly calculation cost in the numerical simulation with the statistical method [8, 9]. In addition, to obtain the reasonable solutions of the simulation, the optimal statistical model must be chosen for evaluation of the actual problems. If an inadequate model is selected, the incorrect solution is obtained in the numerical simulation. Therefore, it is necessary to understand the problems to solve, and chose the optimal calculation method to solve the problem with consideration of the calculation cost in numerical simulations.

6. Conclusions

In this chapter, a theoretical evaluation method of the grain trajectory and its engaging process onto the material in the grinding was introduced. The basic theory of the grain locus in grinding process and its example: spherical grinding stone for curve generation were introduced. And the numerical model of the grinding force applied on one grain and working surface is illustrated. Finally, the statistical approaches for evaluating the actual grinding stone were discussed.

Author details

Takenori Ono
Teikyo University, Utsunomiya-shi, Tochigi, Japan

*Address all correspondence to: tono@mps.teikyo-u.ac.jp

IntechOpen

© 2022 The Author(s). Licensee IntechOpen. This chapter is distributed under the terms of the Creative Commons Attribution License (<http://creativecommons.org/licenses/by/3.0>), which permits unrestricted use, distribution, and reproduction in any medium, provided the original work is properly cited. 

References

[1] Sato K. Grinding theory (A numerical modeling of the grinding force). *Journal of the Japan Society of Precision Engineering*. 1951;17(196):88-93

[2] Sato K. Grinding theory (A measurement of the grinding force and evaluate the specific force). *Journal of the Japan Society of Precision Engineering*. 1951;17(198):173-177

[3] Orioka T. Theory of Probability on Generating Process of Finished Surface in Grinding Operation. *Journal of the Japan Society of Mechanical Engineering*. 1960;63(499):1185-1193

[4] Peklenik J. Versuchsergebnisse zur Ausbildung der Schneid- mente an Schleifwerkzeugen. *IndustrieAnzeiger*. 1961;83(97):1929–1936

[5] Bruckner K. Die Schneidfläche der Schleifscheibe und ihr Einfluss auf die Schnittkräfte beim Aussenrundeinstechschleifen. *IndustrieAnzeiger*. 1964;86(11):173

[6] Matsui S, Syoji K. A Statistical Approach to Grinding Mechanism. *Journal of the Japan Society of Precision Engineering*. 1970;36(421):115-120

[7] Matsui S, Syoji K. Statistical Approach to Grinding Mechanism (2nd Report). *Journal of the Japan Society of Precision Engineering*. 1970;36(422):196-201

[8] Usui E et al. Study on Edge Fracture of Abrasive Grain during Grinding with Applying the Theory of Markov Process (1st Report). *Journal of the Japan Society of Precision Engineering*. 1984; 50(10):1652-1658

[9] Obikawa T et al. Study on Edge Fracture of Abrasive Grain during Grinding with Applying the Theory of Markov Process (3rd Report). *Journal of the Japan Society of Precision Engineering*. 1986;52(4):685-691



*Edited by Giuseppe Pintaude,
Tiago Cousseau and Anna Rudawska*

Tribology is a branch of science that deals with machine elements and their friction, wear, and lubrication. *Tribology of Machine Elements - Fundamentals and Applications* presents the fundamentals of tribology, with chapters on its applications in engines, metal forming, seals, blasting, sintering, laser texture, biomaterials, and grinding.

Published in London, UK

© 2022 IntechOpen
© FedotovAnatoly / iStock

IntechOpen

ISBN 978-1-83969-895-8



9 781839 698958

